

# การปลูกและการวัดลักษณะสมบัติของ ZnO

นางสาว ยุพาวดี ดีศิริพัฒน์

วิทยานิพนธ์นี้เป็นส่วนหนึ่งของการศึกษาตามหลักสูตรปริญญาวิศวกรรมศาสตรดุษฎีบัณฑิต

สาขาวิชาวิศวกรรมไฟฟ้า ภาควิชาวิศวกรรมไฟฟ้า

คณะวิศวกรรมศาสตร์ จุฬาลงกรณ์มหาวิทยาลัย

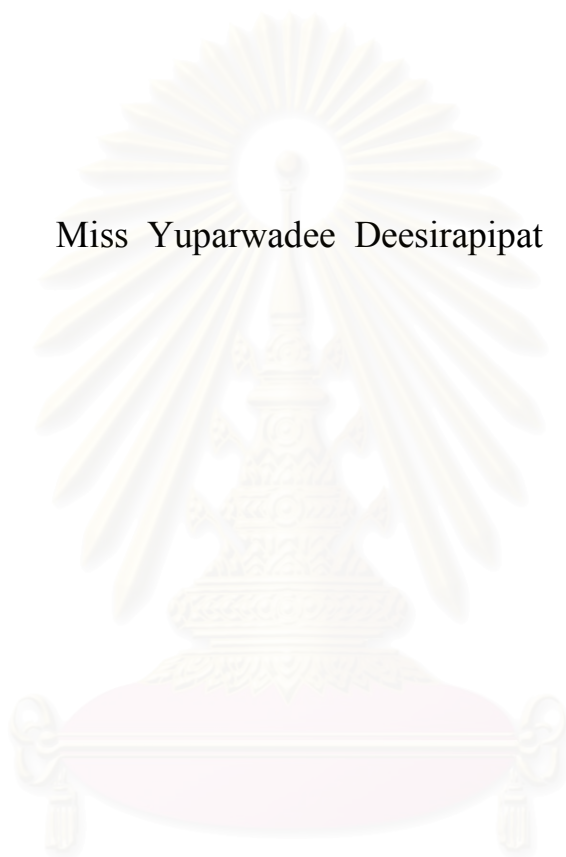
ปีการศึกษา 2548

ISBN 974-53-23756

ลิขสิทธิ์ของจุฬาลงกรณ์มหาวิทยาลัย

# GROWTH AND CHARACTERIZATION OF ZnO

Miss Yuparwadee Deesirapipat



A Dissertation Submitted in Partial Fulfillment of the Requirements  
for the Degree of Doctor of Engineering Program in Electrical Engineering

Department of Electrical Engineering

Faculty of Engineering  
Chulalongkorn University


Academic year 2005

ISBN 974-53-2375-6


Thesis Title                      GROWTH AND CHARACTERIZATION OF ZnO  
By                                      Miss Yuparwadee Deesirapipat  
Field of Study                      Electrical Engineering  
Thesis Advisor                      Associate Professor Choopol Antarasena, D.Ing.  
Thesis Co-advisor                      Professor Yoshiji Horikoshi, Ph.D.


---


Accepted by the Faculty of Engineering, Chulalongkorn University in  
Partial Fulfillment of the Requirements for the Doctor's Degree


.....Dean of the Faculty of Engineering  
( Professor Direk Lavansiri, Ph.D. )


THESIS COMMITTEE


..... Chairman  
( Professor Somsak Panyakeow , D.Eng. )

..... Thesis Advisor  
( Associate Professor Choopol Antarasena , D.Ing. )

..... Thesis Co-advisor  
( Professor Yoshiji Horikoshi , Ph.D. )

..... Member  
( Associate Professor Montri Sawadsaringkarn , D.Ing. )

..... Member  
( Associate Professor Koarakot Wattanavichean , D.Eng. )

..... Member  
( Associate Professor Somchai Rattanatammapan , D.Eng. )

อุทาวดี ดิสิริพิพัฒน์ : การปลูกและการวัดลักษณะสมบัติของ ZnO. (GROWTH AND

CHARACTERIZATION OF ZnO) อ. ที่ปรึกษา : รศ.ดร. ชุมพล อัครเสน, อ. ที่ปรึกษาร่วม : PROF.

Yoshiji Horikoshi, Dr. 130 หน้า. ISBN 974-53-2375-6.

วิทยานิพนธ์นี้นำเสนอการปลูกฟิล์มซิงค์ออกไซด์ (ZnO) บนแผ่นฐานต่างชนิดโดยอาศัยเทคนิคการปลูกผลึกด้วยลำโมเลกุล แผ่นฐานที่นำมาประยุกต์ใช้ในงานวิจัยนี้ได้แก่ ซิลิกอน แสฟไฟร์ และแก้ว โดยแผ่นฐานซิลิกอนและแอสฟไฟร์เป็นผลึกเดี่ยว ในขณะที่แผ่นฐานแก้วเป็นอสัณฐาน โดยในวิทยานิพนธ์นี้จะเน้นศึกษาวิจัยคุณสมบัติของฟิล์มซิงค์ออกไซด์ที่ปลูกบนแผ่นฐานแก้วเป็นหลักด้วยวิธีวัดต่างๆ ดังนี้ การวัดด้วยสแกนนิ่งอิเล็กตรอนไมโครสโคป (Scanning Electron Microscope) การวัดการเลี้ยวเบนของรังสีเอ็กซ์ (X-ray Diffraction) การวัดด้วยแรงอะตอม (Atomic Force Microscopy) การวัดโฟโตลูมิเนสเซนซ์ (Photoluminescence) ที่อุณหภูมิห้อง (10 เคลวิน) และ การวัดฮอลล์ (Hall Measurement)

ฟิล์มซิงค์ออกไซด์ที่ปลูกบนแผ่นฐานแก้วนี้มีความหนาประมาณ 800 นาโนเมตร โดยอัตราเร็วในการปลูกประมาณ 7 นาโนเมตรต่อวินาที หลังจากปลูกพบปัญหารอยแตกร้าว (crack) อันเนื่องมาจากความแตกต่างของค่าสัมประสิทธิ์การขยายตัวทางความร้อนระหว่างแก้วและซิงค์ออกไซด์มีค่ามาก (สำหรับแก้วมีค่า  $5.5 \times 10^{-7} \text{ K}^{-1}$  และสำหรับซิงค์ออกไซด์มีค่า  $4.75 \times 10^{-6} \text{ K}^{-1}$ ) เพื่อหลีกเลี่ยงปัญหานี้จึงปลูกชั้นแมกนีเซียมออกไซด์ (MgO) เป็นชั้นบัฟเฟอร์ (Buffer) อย่างไรก็ตามอัตราเร็วในการปลูกผลึกจะลดลงประมาณครึ่งหนึ่ง (3.4 นาโนเมตรต่อวินาที) เมื่อความหนาของชั้นแมกนีเซียมออกไซด์บัฟเฟอร์อยู่ในช่วง 130 ถึง 170 นาโนเมตร โดยในการทดลองนี้ อุณหภูมิปลูกชั้นซิงค์ออกไซด์คงที่ที่ 530 องศาเซลเซียส และ ความดันของปริมาณแก๊สสังกะสีและอัตราการไหลของออกซิเจนพลาสมาที่ปลูกคงที่เท่ากับ  $4.0 \times 10^{-6}$  ทอร์ และ 1.07 ลูกบาศก์เซนติเมตรต่อวินาที (sccm) ตามลำดับ

ผลการศึกษาความหนาชั้นแมกนีเซียมออกไซด์ พบว่า ชั้นงานที่มีความหนาชั้นบัฟเฟอร์น้อยกว่า 170 นาโนเมตร จะไม่พบปัญหารอยแตกร้าวในผลึก ในขณะที่พบปัญหาดังกล่าวจากชั้นงานที่มีความหนาชั้นบัฟเฟอร์ตั้งแต่ 170 นาโนเมตรขึ้นไป แต่สำหรับความหนาชั้นบัฟเฟอร์ที่น้อยกว่า 130 นาโนเมตร ถึงแม้จะไม่ปรากฏปัญหารอยแตกร้าวบนชั้นซิงค์ออกไซด์หลังการปลูกก็ตาม คุณสมบัติทางแสงมีผลตอบสนองทางแสงต่ำ คุณสมบัติทางไฟฟ้าไม่ดีพอ รวมถึงไม่มีการปรับปรุงคุณสมบัติทางโครงสร้างและการเรียงตัวของผลึก ในขณะที่ชั้นงานที่มีความหนาชั้นบัฟเฟอร์อยู่ระหว่าง 130 ถึง 170 นาโนเมตร ความแรงของสเปกตรัมโฟโตลูมิเนสเซนซ์ดีขึ้นอย่างมากเปรียบเทียบกับชั้นงานอื่น คิดเป็นประมาณ 20 เท่า อย่างไรก็ตามการเรียงตัวของผลึกในทิศทางการปลูกมีความเป็นระเบียบลดลง (c-orientation) ผลการทดลองนี้ชี้ให้เห็นว่า ความหนาของชั้นบัฟเฟอร์ที่เหมาะสมมีค่าประมาณ 130 ถึง 150 นาโนเมตร

นอกจากนี้ การเพิ่มปริมาณสังกะสีขณะทำการปลูกซิงค์ออกไซด์ ( $5.0 \times 10^{-6}$  ทอร์) หรือการเพิ่มอุณหภูมิการปลูก (600 องศาเซลเซียส) ยังสามารถปรับปรุงคุณสมบัติทางโครงสร้างให้มีความเป็นระเบียบมากขึ้น ในขณะที่ยังคงคุณสมบัติทางแสงที่ดีและไม่มีปัญหาการแตกร้าว

ภาควิชา .....วิศวกรรมไฟฟ้า..... ลายมือชื่อนิสิต .....อุทาวดี.....

สาขาวิชา .....วิศวกรรมไฟฟ้า..... ลายมือชื่ออาจารย์ที่ปรึกษา .....*Yoshi Horikoshi*.....

ปีการศึกษา ..... 2548 ..... ลายมือชื่ออาจารย์ที่ปรึกษาร่วม .....*Yoshi Horikoshi*.....

## 4571818321 : MAJOR ELECTRICAL ENGINEERING

KEY WORD: POLYCRYSTALLINE ZnO / LT-MgO BUFFER LAYER/ DOTLIKE SURFACE / SURFACE CRACK / MOLECULAR BEAM EPITAXY

YUPARWADEE DEESIRAPIPAT : GROWTH AND CHARACTERIZATION OF ZnO. THESIS ADVISOR : ASSOC. PROF. CHOOMPOL ANTARASENA, DR., THESIS CO-ADVISOR : PROF. YOSHIJI HORIKOSHI, DR. , 130 pp. ISBN 974-53-2375-6.

ZnO films grown on different substrates by molecular beam epitaxy have been investigated in this work. The substrates, composed of silicon, sapphire and quartz glass, were applied in this research. Silicon and sapphire are single crystal substrates, whereas the quartz glass is an amorphous one. In this work, we emphasized mainly on the study of the properties of ZnO films grown on quartz glass substrates. The characteristics of the grown samples were measured by scanning electron microscope (SEM), x-ray diffraction (XRD), *ex-situ* atomic force microscopy (AFM), 10K photoluminescence (PL) and hall measurement.

The investigated thickness of ZnO film grown on glass with the growth rate of 7 nm/s was about 800 nm. After the ZnO film growth, the surface-crack problem appeared due to the very high difference of the thermal expansion coefficient between glass and ZnO ( $5.5 \times 10^{-7} \text{ K}^{-1}$  and  $4.75 \times 10^{-6} \text{ K}^{-1}$ , respectively). To avoid this problem, MgO-buffer-layer growth is necessary. However, the growth rate of ZnO film approximately reduced to 3.4 nm/s when MgO-buffer-layer thickness was varied from 130 to 170 nm. The ZnO growth temperature was fixed at 530°C and the amount of deposited zinc pressure and oxygen plasma flow rate were  $4.0 \times 10^{-6}$  Torr and 1.07 sccm, respectively.

We found that no cracks was observed for the samples with MgO-buffer-layer thickness less than 170 nm, while the surface cracks appeared with the buffer layer thickness of 170 nm or more. However, the structural and optical properties of the samples with the buffer layer thinner than 130 nm were not improved, even though no cracks appeared, and also the electrical property was not good. For the samples with the buffer layer from 130 to 170 nm, the PL intensity was much improvement, approximately 20-time improvement. Anyway, no c-orientation existed. This experiment indicated that the optimum buffer layer thickness was around 130-150 nm.

Finally, via increasing zinc amount ( $5.0 \times 10^{-6}$ ) or increasing temperature (600°C) during ZnO film growth, the structural property with the very good optical property and no cracks can be improved.

Department .... Electrical Engineering ..

Field of study .. Electrical Engineering ..

Academic year ..... 2005 .....

Student's signature *Yuparwadee* .....

Advisor's signature *C. Antarasena* .....

Co-advisor's signature *Yoshiji Horikoshi* .....

## Acknowledgements

The author would like to give special thanks to her family for endless and encouraging support throughout this work.

The author gratefully acknowledges all those who provided invaluable help and encouragement during the research both at the Semiconductor Device Research Laboratory (SDRL), Department of Electrical Engineering, Faculty of Engineering, Chulalongkorn University, Bangkok, Thailand and at the Horikoshi Laboratory, Waseda University, Tokyo, Japan. In particular, the author would like to express her greatest gratitude to Associate Professor Dr. Choompol Antarasena, and Professor Dr. Yoshiji Horikoshi, who are the advisor and co-advisor; as well as the Thesis committee: Professor Dr. Somsak Panyakaew, Associate Professor Dr. Montri Sawadsaringkarn, Associate Professor Dr. Koarakot Wattanavichean, and Associate Professor Dr. Somchai Ratanathammaphan.

As always, this thesis could not have been completed without special helps of colleagues and members in the ZnO group and the SDRL. These are colleagues at Waseda University: Mr. Miki Fujita, Mr. Masanori Sasajima, Mr. Ryotaro Suzuki, Mr. Jiro Nishinaka, Ms. Tosaporn Chavanapranee, and colleagues at Chulalongkorn University: Mr. Supachok Thainoi, Mr. Pornchai Chuangmuang, and Mrs. Kwanruan Thainoi. In addition, the author would like to thank to Mr. Worapol Satirakul for endless and encouraging support throughout this work.

Special thanks go to the Royal Golden Jubilee (RGJ) scholarship for the research fund in Thailand and the short-program research fund at Waseda University, Tokyo, Japan, and Waseda exchange student scholarship with Monbukagakusho scholarship for funding of the research program at Waseda University, Tokyo, Japan.

# CONTENTS

|   | Page |
|---|------|
| Abstract (Thai) .....   | iv   |
| Abstract (English) .....  | v    |
| Acknowledgements .....  | vi   |
| Contents .....  | vii  |
| List of Figures .....   | x    |
| List of Tables .....  | xix  |
| List of Symbols .....   | xx   |
| <br>  |      |
| Chapter I    Introduction .....   | 1    |
| 1.1    Historical Background .....  | 1    |
| 1.2    Objective .....  | 3    |
| 1.3    Overview .....   | 4    |
| <br>  |      |
| Chapter II    ZnO Crystal Structure and Strain of Epilayers .....                 | 5    |
| 2.1    ZnO Crystal Structure .....  | 5    |
| 2.2    Strain and energies of epilayers .....                                     | 9    |
| 2.2.1    Misfit Strain .....  | 9    |
| 2.2.2    Dislocation and Strain Energies:<br>Periodic arrays of dislocation ..... | 11   |
| 2.2.3    Non-Periodic Arrays of Dislocation .....                                 | 14   |
| 2.3    Critical Thickness .....   | 16   |
| 2.4    Variation of Strain with Thickness .....                                   | 19   |
| <br>  |      |
| Chapter III    Experimental Details .....   | 22   |
| 3.1    Molecular Beam Epitaxy .....   | 22   |
| 3.2    RHEED Pattern Observation .....  | 24   |
| 3.3    Optical Microscope .....   | 26   |
| 3.4    Field Emission-Scanning Electron Microscope .....                          | 27   |
| 3.5    X-ray Diffraction .....  | 28   |
| 3.6    Atomic Force Microscopy .....  | 30   |

|             | Page  |
|-------------|---|
| Chapter III | Experimental Details (continued)  |
| 3.7         | Photoluminescence Spectroscopy ..... 31                                 |
| 3.8         | Absorption Spectroscopy ..... 33  |
| 3.9         | Hall Measurement ..... 35   |
| Chapter IV  | ZnO Film on Silicon and Sapphire Substrates ..... 39                    |
| 4.1         | ZnO film on silicon substrate ..... 39                                  |
| 4.1.1       | Initial Zn layer with ozone source ..... 40                             |
| 4.1.2       | Initial Zn layer with oxygen plasma and<br>LT-ZnO buffer layer ..... 46 |
| 4.1.3       | MgO buffer layer ..... 51   |
| 4.2         | ZnO film on sapphire substrate ..... 55                                 |
| 4.2.1       | Growth procedure ..... 55   |
| 4.2.2       | Experimental result ..... 55  |
| Chapter V   | ZnO Film on Glass Substrate ..... 65                                    |
| 5.1         | Growth Parameter Optimization ..... 65                                  |
| 5.1.1       | Growth Temperature ..... 65   |
| 5.1.2       | Zn Flux and Oxygen Quantity with Growth Rate ..... 66                   |
| 5.2         | Growth Procedure ..... 69   |
| 5.3         | <i>In Situ</i> RHEED Observation ..... 70                               |
| 5.4         | Surface Morphology ..... 71   |
| 5.5         | Structural Property ..... 73  |
| 5.6         | Optical Property ..... 74   |
| 5.7         | Electrical Property ..... 76  |
| 5.8         | Nitrogen Doped Effect ..... 77  |
| 5.8.1       | Growth Procedure ..... 77   |
| 5.8.2       | <i>In Situ</i> RHEED Observation ..... 78                               |
| 5.8.3       | Surface Morphology ..... 79   |
| 5.8.4       | Structural Property ..... 80  |



|   | Page |
|---|------|
| Chapter V ZnO Film on Glass Substrate (continued) |      |
| 5.8.5 Optical Property .....                      | 82   |
| 5.8.6 Impurity Measurement .....                  | 83   |
| 5.8.7 Electrical Property .....                   | 83   |
| Chapter VI MgO Buffer Layer Effect .....          | 86   |
| 6.1 Growth Procedure .....                        | 87   |
| 6.2 <i>In Situ</i> RHEED Observation .....        | 91   |
| 6.3 Surface Morphology .....                      | 92   |
| 6.4 Structural Property .....                     | 96   |
| 6.5 Optical Property .....                        | 99   |
| 6.6 Electrical Property .....                     | 104  |
| 6.7 ZnO Quality Improvement .....                 | 105  |
| 6.7.1 O <sub>2</sub> flow rate variation .....    | 105  |
| 6.7.2 Zn flux variation .....                     | 107  |
| 6.7.3 ZnO growth temperature variation .....      | 110  |
| Chapter VII Conclusion .....                      | 116  |
| References .....                                  | 118  |
| Appendix .....                                    | 124  |
| List of Publications .....                        | 125  |
| List of Presentations .....                       | 127  |
| Vitae .....                                       | 130  |

## LIST OF FIGURES

|            | Page  |
|------------|---|
| Figure 2.1 | Schematic representation of atomic arrangement in different solids: (a) monocrystalline, (b) polycrystalline, and (c) amorphous. The first two are characterized by complete or partial ordering whereas amorphous materials have no periodicity at all. .... 6   |
| Figure 2.2 | Representation of lattice atoms and unit-cells in crystalline materials: (a) two-dimensional arrangement of atoms in which the basis vectors and translational property are illustrated and (b) parallelepiped indicating the basis vectors $a$ , $b$ , $c$ and angles $\alpha$ , $\beta$ , and $\gamma$ . .... 7 |
| Figure 2.3 | Schematic representation of hexagonal close-packed structure ZnO. .... 9  |
| Figure 2.4 | Structure of an epilayer. The layer is under biaxial compression: (a) The layer is pseudomorphic layer and (b) the layer is relaxed by creation of misfit dislocations. .... 10   |
| Figure 2.5 | Schematic representation of (a) $60^\circ$ dislocations in an uncapped layer and (b) $60^\circ$ dipoles in a capped layer. .... 13  |
| Figure 2.6 | Critical thickness of II-VI semiconductor lattice mismatched layers. Dashed and solid lines give the calculated values of $h_c$ for the layers with free surface and for the capped layers, respectively. The description of the samples for symbols 1 to 11 is given in Table 2.1 by the items 1 to 12. .... 18  |
| Figure 2.7 | Plots of in-plane stress $\sigma$ vs layers thickness $h$ are shown for CdTe layers grown on a (111) $\text{Cd}_{0.96}\text{Zn}_{0.04}\text{Te}$ substrate. .... 20   |
| Figure 2.8 | Plots of in-plane strain $\epsilon_{//}$ in ZnSe layers grown on GaAs. Curve 1 is drawn through the experimental points shown by symbols as an aid to eye; Curve 2 is calculated using equation (2.11) and curve 3 is calculated using equation (2.12) for the total energy. .... 21                              |

|             | Page  |
|-------------|---|
| Figure 3.1  | Schematic drawing of the growth chamber of the modified MBE system modified with <i>in situ</i> RF plasma-assisted system. The growth chamber is cooled by a closed circuit liquid Ethylene Glycol. It is pumped by a rotary pump, an turbo-molecular pump, and an ion pump. The base pressure is around $1 \times 10^{-9}$ mbar. .... 23 |
| Figure 3.2  | (a) Schematic representation of the RHEED observation system (Mohammed Samir Hegazy, 2002) and (b) Ewald sphere construction for a reconstructed surface in $[-1\ 1\ 0]$ azimuth (Herman and Sitter, 1989). .... 25   |
| Figure 3.3  | Schematic diagram of the optical microscope. .... 26  |
| Figure 3.4  | (a) Bragg's Law factors and (b) Schematic representation of the X-Ray Diffraction $2\theta$ - $\omega$ measurement system. .... 28  |
| Figure 3.5  | Representation of the X-Ray diffraction pole figure system. .... 29   |
| Figure 3.6  | Schematic representation of AFM system. .... 30   |
| Figure 3.7  | Schematic of the PL experimental setup. .... 32   |
| Figure 3.8  | The absorption basic diagram. .... 33   |
| Figure 3.9  | Absorption spectroscopy system. .... 34   |
| Figure 3.10 | Hall measurement principle. .... 35   |
| Figure 3.11 | Schematic of a rectangular van der Pauw. .... 36  |
| Figure 3.12 | Representation of Hall measurement system with van der Pauw method of this work. .... 37  |
| Figure 4.1  | RHEED patterns along Si $[1\bar{1}\bar{2}]$ direction and Si $[\bar{1}\bar{1}0]$ direction in different stages of ZnO growth: (a) before growth, (b) the initial Zn layer is deposited, (c) oxidation is started, (d) the oxidation is continued, and (e) the growth of ZnO film is performed. .... 42                                    |

|             | Page   |
|-------------|--|
| Figure 4.2  | Relationship of the crystal orientation among Si, Zn and ZnO. The initial Zn layer and ZnO film are rotated by 30° with respect to the Si substrate orientation. The [1000] direction of Zn and ZnO are parallel to the $[11\bar{2}]$ direction of Si. .... 43       |
| Figure 4.3  | Effect of 30° rotation on lattice mismatch between Si (111) and initial Zn layer: (a) orientation-matched case, and (b) 30° rotation. .... 43  |
| Figure 4.4  | AFM images of the grown surfaces: (a) before oxidation of the initial Zn layer, and (b) after oxidation of the initial Zn layer. The grain size and the surface roughness increase with oxidation. .... 44   |
| Figure 4.5  | XRD 2θ-ω scan measurement of the as-grown and the annealed sample. The ZnO (10 $\bar{1}1$ ) diffraction peak disappears upon annealing. .... 44  |
| Figure 4.6  | {10 $\bar{1}1$ } XRD pole figure of the annealed sample. The sixfold symmetry about the surface normal is indicated. No rotational domain of ZnO (0001) exists in ZnO film. .... 45  |
| Figure 4.7  | PL spectra of the as-grown and the annealed samples. The bound exciton emission becomes dominant after annealing. Its peak intensity increases by a factor of 10 upon annealing. The FWHM of the exciton peak changes from 20 meV to 11 meV after annealing. .... 46 |
| Figure 4.8  | XRD result of a φ scan of the (10 $\bar{1}0$ ) planes of the ZnO film with the initial Zn layer. .... 48   |
| Figure 4.9  | Surface roughness of oxidized initial Zn layer surface. The RMS values are plotted as a function of growth temperature. .... 49  |
| Figure 4.10 | XRD rocking curves of the ZnO epitaxial layers with and without the LT-ZnO buffer layer. .... 49   |

|             | Page   |    |
|-------------|--|----|
| Figure 4.11 | Microscopic images of the films with and without the LT-ZnO layer. Straight cracks along the principal axes of Si (111) surface can be clearly observed. (a) ZnO film without LT-ZnO buffer layer (b) ZnO film with LT-ZnO buffer layer. ....          | 50 |
| Figure 4.12 | PL spectra of the ZnO film with and without the LT-ZnO buffer layer measured at 10 K. ....   | 51 |
| Figure 4.13 | RHEED patterns along Si $[1\bar{1}2]$ and Si $[\bar{1}10]$ direction in different stages of ZnO growth by using a MgO buffer layer: (a) before growth, (b) a Mg evaporated surface, (c) a MgO buffer layer, and (d) a ZnO layer. ....                  | 52 |
| Figure 4.14 | Microscopic images of the ZnO films grown by using (a) initial a Zn layer and (b) a MgO buffer layer. ....   | 53 |
| Figure 4.15 | Comparison of ZnO (0002) XRD spectra for the samples grown by using initial a Zn layer and a MgO buffer layer (a) $2\theta$ - $\omega$ scan spectra and (b) $\omega$ scan spectra. ....  | 54 |
| Figure 4.16 | PL spectra of ZnO films grown by using an initial Zn layer and a MgO buffer layer. ....  | 54 |
| Figure 4.17 | Growth rate as a function of Zn BEP for the samples grown at 575°C. The straight line indicates the linear relationship. ....  | 56 |
| Figure 4.18 | Depth profiles of Zn, O, and other impurities measured by AES. Al peak is caused by noise. ....  | 57 |
| Figure 4.19 | Depth profiles measured by SIMS. Both Al and Si in the layer are at the background level. ....   | 57 |
| Figure 4.20 | The typical PL spectrum of ZnO film measured at 10 K. The PL peaks at 3.358 eV and 3.362 eV are caused by the donor-bound excitons. Emissions due to free exciton and their second excited state are observed at 3.376 and 3.42 eV, respectively. .... | 58 |

|             | Page   |    |
|-------------|--|----|
| Figure 4.21 | Electron concentration as a function of annealing temperature when ZnO films are annealed in O <sub>2</sub> atmosphere (1 atm) for 5 min. The electron concentration is measured at room temperature. .... | 59 |
| Figure 4.22 | The typical PL spectra measured at 10 K for the samples grown at 315°C and 575°C. ....   | 60 |
| Figure 4.23 | The PL spectra of the sample grown at 315°C and those measured after thermal annealing in N <sub>2</sub> atmosphere at 700°C for 10 min and 20 min. ....   | 60 |
| Figure 4.24 | The PL spectra of the sample grown at 315°C, and that measured after thermal annealing in O <sub>2</sub> atmosphere at 600°C for 5 min. ....   | 61 |
| Figure 4.25 | The PL spectra around band edge for as-grown and annealed samples. The annealing is performed in O <sub>2</sub> at 1000°C for 10 min. ....   | 61 |
| Figure 4.26 | The PL spectra at around 2.3 eV for as-grown and annealed samples. The annealing is performed in O <sub>2</sub> at 1000°C for 10 min. ....   | 62 |
| Figure 4.27 | The PL spectra at around 2.3 eV for as-grown and annealed samples. The annealing is performed in N <sub>2</sub> at 700°C for 5 min. ....   | 63 |
| Figure 4.28 | The PL spectra at around 2.3 eV for ZnO films grown at 575°C under different Zn fluxes. ....   | 63 |
| Figure 5.1  | RHEED pattern of ZnO grown on sapphire (a) at 450°C (b) at 500°C (c) at 550°C. ....  | 66 |
| Figure 5.2  | Relation between ZnO growth rate (nm/hr) on glass substrate and Zn BEP (Torr) with growth mode details. ....   | 67 |
| Figure 5.3  | FWHM of ZnO film grown on sapphire substrate by XRD 2θ-ω scan with various Zn BEP. ....  | 68 |

|             | Page  |
|-------------|---|
| Figure 5.4  | Hall mobility and Carrier concentration of ZnO film grown on sapphire substrate with various Zn BEP. .... 68  |
| Figure 5.5  | Schematic diagram of the sample structure grown in this work. The growth conditions are given in the text. .... 69  |
| Figure 5.6  | (a) RHEED pattern before ZnO growth (hallo pattern).<br>(b) RHEED pattern after 10-nm ZnO growth (ring pattern).<br>(c) RHEED pattern after 800-nm ZnO growth (fixed-spotty pattern). .... 70                           |
| Figure 5.7  | Surface morphology of undoped ZnO film grown on glass substrate without buffer layer. .... 71   |
| Figure 5.8  | Surface investigation by FE-SEM. .... 72  |
| Figure 5.9  | 5×5 μm <sup>2</sup> AFM images of undoped ZnO surface.<br>(a) Surface roughness analysis (b) 3D image. .... 72  |
| Figure 5.10 | (a) XRD spectral: 2θ-ω scan of ZnO film without buffer layer (b) XRD spectral: pole figure of ZnO film without buffer layer. .... 73  |
| Figure 5.11 | Energy band gap estimation measured at room temperature of undoped ZnO film grown on glass substrate. .... 75   |
| Figure 5.12 | PL spectral response measured at 10 K of undoped ZnO film grown on glass substrate. .... 75   |
| Figure 5.13 | (a) RHEED pattern before ZnO with 0.1 sccm N <sub>2</sub> growth (hallo pattern) (b) RHEED pattern after 10-nm ZnO growth (ring pattern) (c) RHEED pattern after 600-nm ZnO growth (fixed-spotty pattern). .... 78      |
| Figure 5.14 | (a) RHEED pattern after 20-nm ZnO with 0.5 sccm N <sub>2</sub> growth (ring pattern) (b) RHEED pattern after 600-nm ZnO growth (ring pattern) (c) RHEED pattern after 900-nm ZnO growth (ring-to-spot pattern). .... 79 |

|             | Page  |
|-------------|---|
| Figure 5.15 | Surface morphology of ZnO film grown on glass substrate with N <sub>2</sub> (a) 0 sccm (b) 0.3 sccm (c) 0.5 sccm. .... 79   |
| Figure 5.16 | Growth rate of ZnO film grown on glass substrate with various N <sub>2</sub> quantities. .... 80  |
| Figure 5.17 | XRD 2θ-ω scan spectral response of ZnO film with N <sub>2</sub> flow rate of 0, 0.1, 0.3 and 0.5 sccm. .... 81  |
| Figure 5.18 | XRD 2θ-ω scan spectral response of ZnO film with N <sub>2</sub> flow rate of 0, 0.1, 0.3 and 0.5 sccm. .... 82  |
| Figure 5.19 | (a) PL spectral response around main peaks measured at 10 K of ZnO film with 0.3 sccm N <sub>2</sub> grown on glass substrate (b) PL spectral response in wide range of the same sample measured at 10 K. .... 83 |
| Figure 5.20 | XPS result of ZnO film with 0.3 sccm applied nitrogen (a) all material in the film (b) Zn, O, N and C components. .... 84   |
| Figure 6.1  | Schematic diagram of the sample structure grown in this work. The growth conditions are given in the text. .... 88  |
| Figure 6.2  | Comparison of PL spectra of the ZnO films with oxygen annealing and without oxygen annealing after 20-nm MgO buffer layer growth. .... 89   |
| Figure 6.3  | Comparison of PL spectra of the ZnO films with 10-min and 40-min oxygen annealing after 145-nm MgO buffer layer growth. .... 89   |
| Figure 6.4  | Surface morphology by 100,000-time FE-SEM as a function of the oxygen annealing period of 145-nm MgO buffer layer: (a) 10 min (b) 40 min. .... 90   |



|             | Page   |
|-------------|--|
| Figure 6.5  | (a) RHEED pattern of MgO buffer layer growth start (ring pattern). (b) RHEED pattern of 10-nm ZnO growth (ring pattern). (c) RHEED pattern of 800-nm ZnO growth (fixed-spotty pattern). ..... 91 |
| Figure 6.6  | RHEED patterns of the ZnO films as a function of the MgO buffer layer thickness: (a) 0 nm (b) 20 nm (c) 100 nm (d) 120 nm (e) 130 nm (f) 145 nm (g) 170 nm (h) 240 nm and (i) 300 nm. .... 92    |
| Figure 6.7  | ZnO surface images by optical microscope: (a) without MgO buffer layer (b) 145-nm MgO buffer layer (c) 170-nm MgO buffer layer. .... 93  |
| Figure 6.8  | Surface morphology by 100,000-time FE-SEM as a function of the MgO buffer layer thickness: (a) 0 nm (b) 145 nm (c) 300 nm. .... 93   |
| Figure 6.9  | Relation of ZnO thickness and MgO buffer layer thickness grown on glass substrate. .... 94   |
| Figure 6.10 | $5 \times 5 \mu\text{m}^2$ AFM images of ZnO surface with 130-nm MgO buffer layer. (a) Surface roughness analysis (b) 3D image. .... 95  |
| Figure 6.11 | RMS value of surface roughness of the samples with various MgO buffer layer thicknesses. .... 95   |
| Figure 6.12 | XRD $2\theta$ - $\omega$ scan spectral response of ZnO film with 120-nm MgO buffer layer (normal surface group) and with 145-nm MgO buffer layer (dot-like surface group). .... 97               |
| Figure 6.13 | XRD pole figure spectral response of ZnO film with 120-nm MgO buffer layer (normal surface group) and with 145-nm MgO buffer layer (dot-like surface group). .... 97                             |

|   | Page |
|---|------|
| Figure 6.14 Intensity of $2\theta$ - $\omega$ scan spectral response of ZnO film with various MgO buffer layer thicknesses in normal surface group. ....  | 98   |
| Figure 6.15 (a) PL spectra of the annealed MgO buffer layer samples with various buffer layer thickness.<br>(b) Relationship of the PL intensity of emission peaks at 3.358 eV and 3.368 eV. .... | 100  |
| Figure 6.16 RMS result by AFM and PL intensity of both dominant peaks, 3.358 eV and 3.368 eV, with various MgO buffer layer thicknesses. ....   | 102  |
| Figure 6.17 Absorption coefficient spectral response of ZnO thin films with various MgO buffer layer measured at room temperature. ....   | 102  |
| Figure 6.18 Estimated energy band gap of ZnO films with MgO buffer layer thickness at room temperature. ....  | 103  |
| Figure 6.19 Hall measurement result of the ZnO thin film with 20-nm MgO buffer layer. ....  | 104  |

## LIST OF TABLES

|           |   | Page |
|-----------|---|------|
| Table 2.1 | Observed values of critical thickness. The –ve sign indicates that $f_m$ is negative, the lattice constants of the epilayer is smaller and the in-plane strain $\epsilon_{  }$ is positive, see equation (2.2) and (2.3). The abbreviation used in the table are, x: x-ray diffraction, Ch: Channeling, R: RHEED, RO: RHEED Oscillations and T: TEM. .... | 17   |



สถาบันวิทยบริการ  
จุฬาลงกรณ์มหาวิทยาลัย

## LIST OF SYMBOLS

|                 |  |
|-----------------|--|
| $\alpha$        | absorption coefficient                                 |
| $a$             | basis vector   |
| $a_1$           | lattice constant of deposited material                 |
| $a_{Sub}$       | lattice constant of substrate material                 |
| $A$             | absorbance   |
| $A^*$           | adjustable parameter                                   |
| $Al_2O_3$       | sapphire   |
| AFM             | atomic force microscopy                                |
| AlGaAs          | aluminium gallium arsenide                             |
| AlGaN           | aluminium gallium nitride                              |
| AlN             | aluminum nitride                                       |
| $\beta$         | angle  |
| $b$             | path length of the absorbing species                   |
| $b_1$           | strain relaxation                                      |
| $B$             | magnetic field   |
| BEP             | beam equivalent pressure                               |
| $\theta$        | diffraction angle                                      |
| $c$             | concentration of the absorbing species                 |
| CCD             | Charge-Coupled Device                                  |
| Cd              | cadmium  |
| CdSe            | cadmium selenide                                       |
| CdTe            | cadmium telluride                                      |
| CdZnTe          | cadmium zinc telluride                                 |
| $d$             | interatomic spacing                                    |
| DI              | de-ion water   |
| $e$             | absorbitivity  |
| $\epsilon_{//}$ | in-plane homogeneous strain in the pseudomorphic layer |
| $E$             | Young's moduli of elasticity                           |
| $E_g$           | band gap energy  |
| $E_D^\infty$    | energy of a single isolated dislocation                |

|                        |  |
|------------------------|--|
| $E_D^{array}$          | energy of the arrays contained in a unit area of the layer                                 |
| $E_D^{pcap}$           | total energy of the arrays in a capped layer   |
| $E_H$                  | total homogeneous strain energy  |
| $E_I(h, p)$            | energy of interaction (per unit length of the dislocation lines) of a pair of dislocations |
| $E_{I\perp}^{\bar{p}}$ | energy of interaction between the two perpendicular arrays                                 |
| $E_T$                  | total energy   |
| $E_T^m$                | total misfit strain energy   |
| $f_m$                  | misfit parameter   |
| FE-SEM                 | field-emission scanning electron microscopy  |
| FWHM                   | full width at half maximum   |
| $\gamma$               | angle  |
| $\mathbf{G}$           | reciprocal lattice vector  |
| Ga                     | gallium  |
| GaAs                   | gallium arsenide   |
| GaAs                   | gallium arsenide   |
| GaN                    | gallium nitride  |
| GaP                    | gallium phosphide  |
| GeSi                   | germanium silicon  |
| $h$                    | thickness of epilayer  |
| $h_c$                  | critical thickness   |
| $h_{cc}$               | critical thickness of the capped layer   |
| H <sub>2</sub> O       | water  |
| $I$                    | current  |
| InP                    | indium phosphide   |
| InSb                   | indium sterbide  |
| IPA                    | isopropyl alcohol  |
| $k$                    | integer  |
| $\mathbf{k}'$          | wavevector of the diffracted electron  |
| $\mathbf{k}_0$         | wavevector of the incident electron  |
| $\lambda$              | wavelength   |

|            |   |
|------------|---|
| $l$        | integer   |
| $L$        | length  |
| LED        | light emitting diodes                                   |
| $\mu$      | mobility  |
| MBE        | molecular beam epitaxy                                  |
| MFC        | flow controller   |
| Mg         | magnesium   |
| MgO        | magnesium oxide   |
| MgZnO      | magnesium zinc oxide                                    |
| MOCVD      | metal organic chemical vapor deposition                 |
| MOVPE      | metal organic vapor phase epitaxy                       |
| MSM        | metal semiconductor metal                               |
| $n$        | integer   |
| $n_s$      | sheet density of charge carriers                        |
| N          | nitrogen  |
| $N$        | number of dislocations                                  |
| O          | oxygen  |
| $\rho_c$   | non-elastic part of the core energy of the dislocations |
| $p$        | inter-dislocation space                                 |
| $p_i$      | distribution of spacing                                 |
| $\bar{p}$  | average inter-dislocation distance in the array         |
| $P$        | beam of radiation leaving the sample of radiant power   |
| $P_0$      | beam of monochromatic radiation of radiant power        |
| PL         | photoluminescence                                       |
| PLD        | pulse laser deposition                                  |
| $q$        | electric charge   |
| $Q$        | core radius of the dislocation line                     |
| $\sigma$   | in-plane stress   |
| $\sigma_0$ | stress in a pseudomorphic layer                         |
| $r$        | translational vector                                    |

|          |   |
|----------|---|
| RF       | radio frequency                             |
| RHEED    | reflection high-electron energy diffraction |
| RMS      | root mean square roughness                  |
| sccm     | standard cubic centimeter per second        |
| Si       | silicon                                     |
| SiC      | silicon carbide                             |
| <i>T</i> | transmittance                               |
| UV       | ultraviolet                                 |
| $\nu$    | Poisson's ratio                             |
| $V_H$    | Hall voltage                                |
| XPS      | x-ray photoelectron spectroscopy            |
| XRD      | x-ray diffraction                           |
| Zn       | zinc  |
| ZnO      | zinc oxide                                  |
| ZnS      | zinc sulfide                                |
| ZnSe     | zinc selenide                               |
| ZnTe     | zinc telluride                              |



สถาบันวิทยบริการ  
จุฬาลงกรณ์มหาวิทยาลัย

# CHAPTER I

## INTRODUCTION

### 1.1 Historical Background

In present day, semiconductor technology has been rapidly developed and resulted in many applications owing to tunable electronic properties of semiconductors and several novel device concepts, especially in electronic and optoelectronic fields. With a semiconductor material (e.g. silicon (Si), gallium arsenide (GaAs)), elaborate processing yields a number of useful electronic devices. The foundation for a multi-electronics industry has been provided. Si is currently and will remain the material of choice for the foreseeable future due to the low cost, readily availability and established device technology and infrastructure. If a device can be made with Si, it will.

Recent development advances have allowed Si semiconductor technology to approach the theoretical limits of the Si material, however, power device requirements for many utility applications of power electronics are at a point that the present Si-based power devices cannot handle because of its limitation with respect to temperature, frequency operation and voltage blocking capabilities. Higher blocking voltages, switching frequencies, efficiency and reliability are really necessary for the requirement. To overcome this limitation, new semiconductor materials for power device applications are needed. Wide band gap semiconductors like silicon carbide (SiC), gallium nitride (GaN) and aluminum nitride (AlN) with superior electrical properties are likely candidates to replace Si in the near future for these high power requirements. Also, they hold promise for continuing revolutionary improvements in the size, cost, weight and performance of a broad range for military, and commercial microelectronic and optoelectronic applications. The inherent material properties of SiC, GaN and AlN make them ideal candidates for high-power, high-temperature electronics, power amplifiers, switches and short-wavelength light sources and detectors. Among these, SiC is the forerunner as the only wide band gap semiconductor with several commercially available power devices. GaN based on



semiconductor technology has provided the fundamental basis for a new class of optoelectronics. New electronic device structures based on SiC and/or GaN have demonstrated remarkable performance and are being considered for next generation military radar and commercial wireless applications. Additionally, SiC devices have been demonstrated that exhibit superior high-efficiency power switching capability, potentially leading to new capabilities in power distribution as well as electric vehicle technology.

On the other hand, another wide band gap semiconductor, wurtzitic zinc oxide (ZnO) with direct band gap of 3.37 eV at room temperature has not received the same attention. This is probably because this material has been perceived as being useful only in its polycrystalline form. Indeed, polycrystalline ZnO has found numerous applications in such device areas as facial powders, piezoelectric transducers, varistors, phosphors and optical transparency in the visible range-conducting films. Recently, however, large-area bulk growth has been achieved. Furthermore, several epitaxial methods have produced excellent material. Also, quantum wells have been successfully grown, by alloying with magnesium (Mg) or cadmium (Cd). Thus, ZnO is now being proposed for the same applications as those for GaN and SiC. In fact, ZnO has several fundamental advantages over its chief competitors, as the following:

- (1) Its free exciton is bound with 60 meV, much higher than that of GaN (21-25 meV)
- (2) It has a native substrate.
- (3) Wet chemical processing is possible.
- (4) It is more resistant to radiation damage compared to Si and GaAs.

The new interest in ZnO has recently culminated in the First International Workshop on ZnO, held in Dayton, Ohio, on 7-8 October, 1999. Recent success in producing large-area single crystals have opened up the possibility of producing blue and (ultraviolet) UV light emitters and high-temperature, high-power transistors. The main advantages of ZnO as a light emitter are its large exciton binding energy and the existence of well-developed bulk and epitaxial growth process; for electronic applications, its attractiveness lies in having high breakdown strength and high thermal saturation velocity. Optical UV lasing, at both low and high temperatures, has already been demonstrated, although efficient electrical lasing must await the further development of good, p-type material.

Although ZnO-based photonic and electronic devices show great promise for the future, still there are some severe problems which must be overcome before the most attractive devices can be produced. One problem is that Schottky barrier is not easy to fabricate, although some groups have been successful. Another, more serious problem, is that usable, reproducible p-type ZnO has not yet been reported, even though several laboratories have measured weak p-type conduction in acceptor-doped materials. Indeed, diode-like behavior and light emission have been measured, but the mechanism is not clear. One device, which does not require p-type material, is a photoconductive detector. Liu et al. have fabricated a ZnO metal semiconductor metal (MSM) detector with a low-frequency response of 400 A/W at 5 V bias and a response time of about 1  $\mu$ s. The cutoff frequency is quite sharp, at 373 nm, although a small tail does exist, probably due to gap states. These characteristics are better than those of GaN detectors, so that ZnO stands a good chance of being a material of choice for UV detectors in the future. However, other devices, such as blue and UV light emitting diodes (LED) and lasers, will require much more development. Also, lattice-matched substrate is very necessary to grow epitaxial ZnO layer due to the high cost of its own substrate. Then, the method, for example molecular beam epitaxy (MBE), pulse laser deposition (PLD) and metal organic chemical vapor deposition (MOCVD), to grow high optical and electrical properties of ZnO on different types of material substrate, such as Si, GaN, sapphire ( $\text{Al}_2\text{O}_3$ ) and glass, is needed to find out. Although some might argue that ZnO stands where GaN did ten years ago, the learning curve will be much faster, primarily because of what we have learned in the GaN area.

## 1.2 Objective

The objective of this work is to study the characteristic of ZnO films grown on different substrates, namely Si,  $\text{Al}_2\text{O}_3$  and especially glass owing to their characteristics as a promising material for optoelectronic applications in the blue and ultraviolet ranges. Also, the growth condition has been studied to improve the quality of ZnO film grown on glass substrate. Furthermore, a serious problem due to ZnO film directly grown on glass substrate, a high density of surface cracks, should be

solved. Then, we focus on the growth conditions, especially ZnO film growth with various MgO buffer layer thicknesses, and on the characteristics of the ZnO film after their growth.

### 1.3 Overview

This thesis presents a detailed study of the growth of ZnO film on quartz glass substrate by plasma-assisted MBE. The main purpose is to explore the properties of the growth film, to solve the surface-crack problem and to improve the quality of these ZnO films.

The thesis is organized as follows: The basic of ZnO crystal structure will be reviewed in chapter 2. This also includes the theories of strain of epilayers. Chapter 3 gives the experimental details including the plasma-assisted MBE technique. In chapter 4, results from experiments on the ZnO growth on single-crystal silicon and sapphire substrates are presented. These data will lead to the main experiments of the ZnO growth on amorphous quartz glass substrate shown in chapter 5. However, a serious problem, a high density of surface cracks, occurs when ZnO film grown directly on glass substrate. One way to solve this problem and also may make a p-type ZnO, which is really essential for the optoelectronic application, is nitrogen doping (N-doped). The study of N-doped ZnO will be also presented in chapter 5. However, the properties of the ZnO films cannot be improved by this doping method, even though the crack problem disappear. Then, a new method of MgO buffer layer application to both solve the crack problem and improve the film's quality, will be presented in chapter 6. The effects of MgO buffer layer on the structural and optical properties of polycrystalline ZnO film grown on amorphous glass substrate including other results will be also presented in this chapter. Furthermore, after we can determine and set the optimum MgO buffer layer thickness to the next step, other parameters including Zn flux, O<sub>2</sub> quantity and ZnO growth temperature have been adjusted to improve the quality of ZnO film. The studies are based on optical microscopy, field-emission scanning electron microscopy (FE-SEM), x-ray diffraction (XRD) of both  $2\theta$ - $\omega$  scan and pole figure, atomic force microscopy (AFM), photoluminescence (PL) and Hall measurement with van der Pauw method results. Finally, chapter 7 concludes this work.

## CHAPTER II

### ZnO CRYSTAL STRUCTURE AND STRAIN OF EPILAYERS

The basic concepts of crystal structure including ZnO structure are reviewed in this chapter. Also, the theory of strain and energies of the epilayers are reviewed because of their importance for the description of ZnO growth condition. In another part of this chapter, the strain relaxation in epilayers is presented based on variation of the layer thickness.

#### 2.1 ZnO Crystal Structure

A crystal or crystalline solid is distinguished from any other form of solid or condensed matter by two important facts: (1) the periodic arrangement of the atoms and (2) the binding forces that hold the atoms together. In a crystalline solid, the periodic arrangements of the atoms, usually in three dimensions, are repeated over the entire crystal. A unique feature of such a crystal is the translational symmetry of the atoms. In other words, the crystal appears identical at several equivalent regions defined by a basic periodicity. Such solids are termed single crystals. In contrast, solids that exhibit crystalline behavior over a small region and are divided by boundaries from other regions exhibiting a different periodicity and arrangement of atoms are called polycrystalline. Solids that have no periodic structure at all are called amorphous. The three types of solids are illustrated in Figure 2.1. While single crystal materials have long-range order, polycrystalline and amorphous materials have short-range order. The periodic array of points, generally in three dimensions, representing the positions occupied by the atoms of the crystal is called a lattice. Normally, the growth layer on the single crystal substrate with proper condition is also single crystal such as ZnO growth on silicon and sapphire substrates. In other improper growth condition the quality of the crystal may be poor and the growth layer becomes polycrystalline or amorphous. Also, the growth layer on amorphous substrate with proper growth condition is polycrystalline layer such as ZnO grown on quartz glass

substrate. To grow single crystal layer on poor amorphous substrate, we have to find out the best growth condition which may be impossible.

A unit cell is a region of a crystal defined by vectors  $a$ ,  $b$ ,  $c$  and angles  $\alpha$ ,  $\beta$ , and  $\gamma$ , which when translated by integral multiples of those vectors, reproduce a similar region of the crystal. This is the translational property mentioned above and is expressed by

$$r = ha + kb + lc \quad (2.1)$$

where  $h$ ,  $k$ , and  $l$  are integers. The set of linearly independent vectors  $a$ ,  $b$ ,  $c$ , which can be used to define a unit cell are called basis vectors. The vector  $r$  is sometimes called the translational vector.  $a$ ,  $b$  and  $c$  can be interatomic distances, in which case they are called the lattice constant. They usually have slightly different values because of microscopic differences in the binding forces. Figure 2.2 (a) illustrates a two-dimensional arrangement of atoms in which the atoms, basis vectors and the translational property are illustrated. The unit cell in this case is defined as the smallest unit cell in volume that can be independent vectors that define a primitive unit cell.

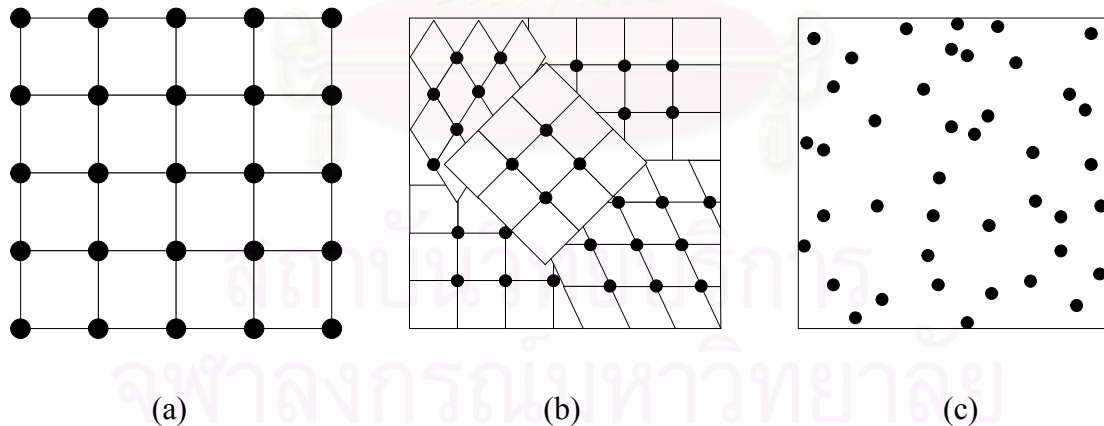


Figure 2.1 Schematic representation of atomic arrangement in different solids: (a) monocrystalline, (b) polycrystalline, and (c) amorphous. The first two are characterized by complete or partial ordering whereas amorphous materials have no periodicity at all.

The vectors  $a$ ,  $b$ ,  $c$  and angles  $\alpha$ ,  $\beta$ , and  $\gamma$  define, in general, the parallelepiped shown in Figure 2.2 (b). Different combinations of  $a$ ,  $b$ ,  $c$  and  $\alpha$ ,  $\beta$ ,  $\gamma$  give 14 different three-dimensional space lattices, called Bravais lattices. These are 1 triclinic, 2 monoclinic, 4 rhombic, 2 tetragonal, 1 hexagonal, 1 trigonal and 3 cubic. ZnO, which is a II-VI compound, crystallizes in the hexagonal or wurtzite form as shown in Figure 2.3. The unit cell of ZnO contains two Zn cations and two oxygen (O) anions. The ZnO crystal thus can be viewed as a sequence of O-Zn double layers stacked along the  $c$ -axis or (0001) direction as shown in Figure 2.3. The lattice parameters are the second nearest neighbor distance  $a = 3.253 \text{ \AA}$  and the ratio  $c/a = 1.602$ . This structure is well known to show piezoelectric properties with a large electromechanical coupling factor and a low dielectric constant. The crystal structure is strongly dependent on the deposition parameters (Pallab, 1997).

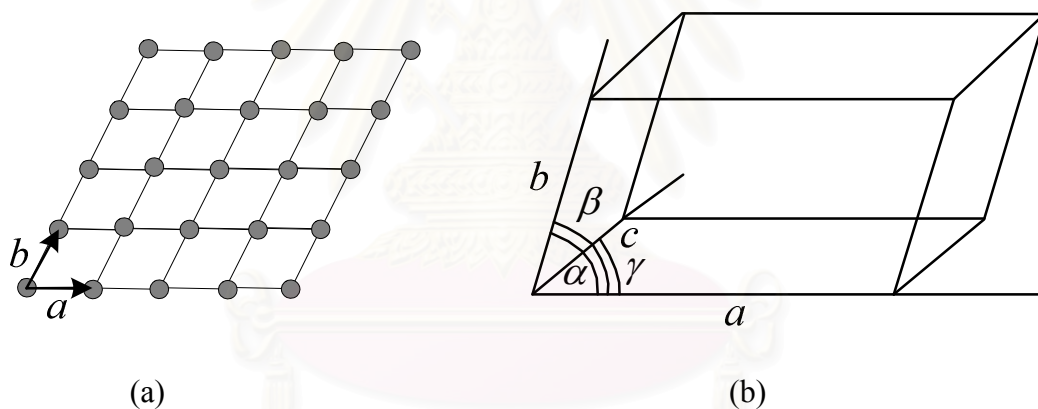


Figure 2.2 Representation of lattice atoms and unit-cells in crystalline materials: (a) two-dimensional arrangement of atoms in which the basis vectors and translational property are illustrated and (b) parallelepiped indicating the basis vectors  $a$ ,  $b$ ,  $c$  and angles  $\alpha$ ,  $\beta$ , and  $\gamma$ .

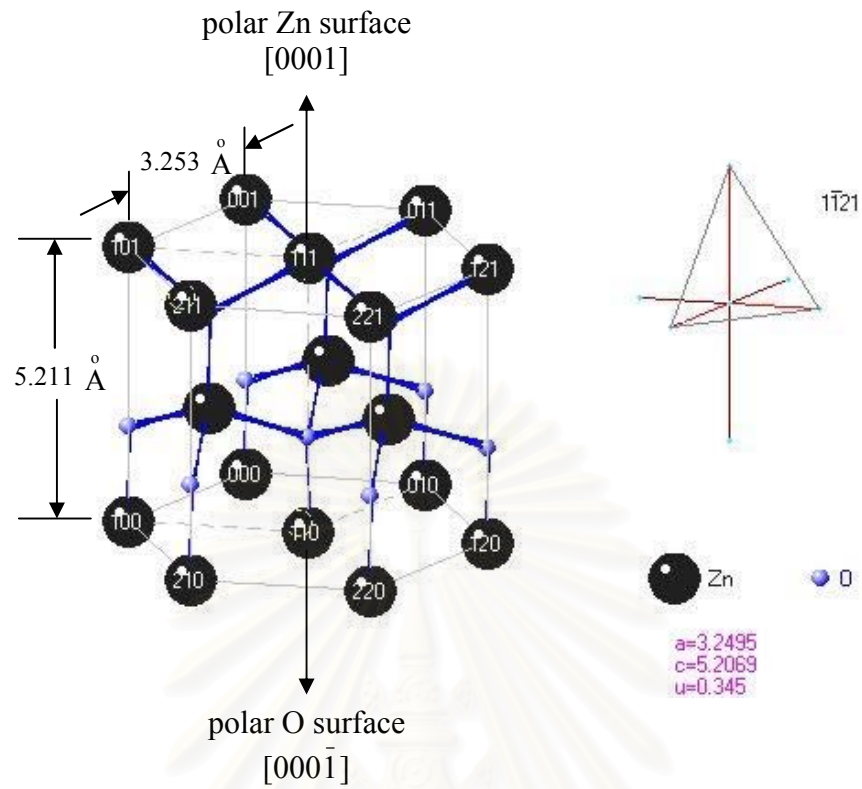


Figure 2.3 Schematic representation of hexagonal close-packed structure ZnO.

สถาบันวิทยบริการ  
จุฬาลงกรณ์มหาวิทยาลัย

## 2.2 Strain and Energies of Epilayers

One of the constraints in heterojunction technology for optoelectronics is the lack of suitable lattice-matched substrates. Even careful growth of an epitaxial layer whose lattice constant is close, but not equal to the lattice constant of the substrate can result in a coherent strain, as opposed to polycrystalline or amorphous incoherent growth. Furthermore, a strain caused by the different thermal expansion coefficients is also very important.

### 2.2.1 Misfit Strain

Consider an epilayer of a semiconductor with lattice constant  $a_l$  grown on a thick substrate with lattice constant  $a_{sub}$  (illustrated in Figure 2.4). The lattice mismatch is measured by the misfit parameter  $f_m$  defined below.

$$f_m = \frac{a_l - a_{sub}}{a_{sub}} \quad (2.2)$$

If both misfit parameter  $f_m$  and thickness  $h$  of the epilayer are small, the layer remains pseudomorphic. For the thermal expansion, we can expect the misfit parameter equal to the difference of the expansion coefficient between both materials. Misfit between two semiconductors is accumulated by the tetragonal strain in the epilayer as shown in Figure 2.4 (a). The strain is homogeneous and is known as the misfit strain. The in-plane homogeneous strain in the pseudomorphic layer is given by equation (2.3).

$$\epsilon_{//} = -f_m \quad (2.3)$$

If the thickness  $h$  of the epilayer exceeds a certain thickness, known as critical thickness  $h_c$ , misfit dislocations are created. Now the strain is partly accommodated by the misfit dislocations as shown in Figure 2.4 (b). The value of  $h_c$  decreases as  $f_m$  increases. If the epilayer contains dislocations with average inter-dislocation space  $p$ ,



each dislocation relaxes the strain by an amount  $b_l$ .  $b_l$  is equal to the active component of the Burgers vector  $b$ . Expression for the strain becomes

$$\epsilon_{//} = -\left(f_m + \frac{b_l}{p}\right) \quad (2.4)$$

where  $b_l = -b \sin \alpha \sin \beta$  and  $b$  is the Burgers vector. The value of  $b$  is  $3.84 \text{ \AA}$  for silicon and  $\sim 4.0 \text{ \AA}$  for compound semiconductors. For  $60^\circ$  dislocations,

$$\alpha = \arctan \frac{1}{\sqrt{2}}, \beta = \frac{\pi}{3} \quad (2.5)$$

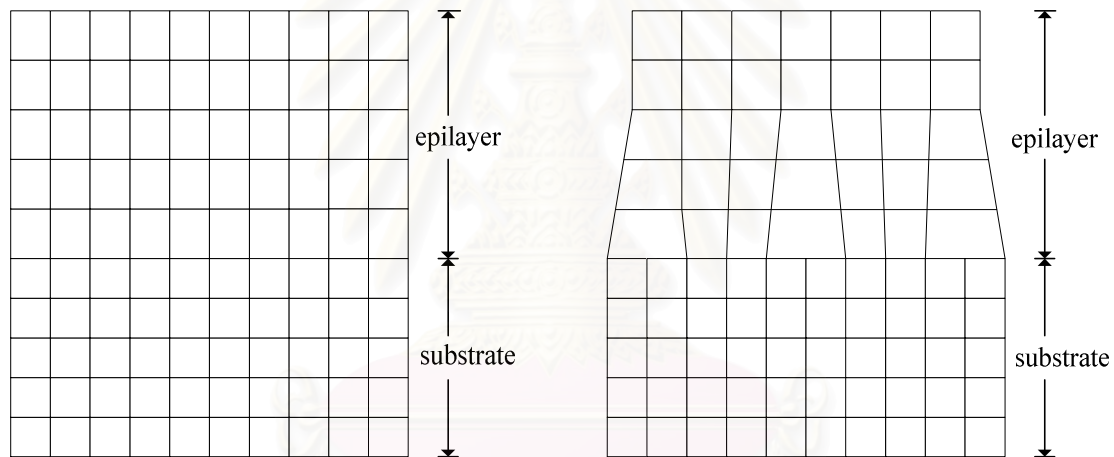


Figure 2.4 Structure of an epilayer. The layer is under biaxial compression: (a) The layer is pseudomorphic layer and (b) the layer is relaxed by creation of misfit dislocations.

Some authors have used  $(f_m - b_l/p)$  instead of  $(f_m + b_l/p)$  in equation (2.4). The +ve or the -ve sign depends on the sign convention used for the Burgers vector. Numerically the value of  $b_l/p$  is always subtracted from  $f_m$  in this equation. If the lattice constant of the layer is smaller than that of the substrate,  $f_m$  is negative, the strain is tensile and  $\epsilon_{//}$  is positive. According to convention, tensile strain and stress are positive and compressive strain and stress are negative.

The normal stress  $\sigma_0$  in a pseudomorphic layer grown on a (100) surface is given by

$$\sigma_0 = -2\mu \frac{\nu+1}{\nu-1} f_m = \frac{E}{1-\nu} \epsilon \quad (2.6)$$

where  $E$  and  $\mu$  are the Young's and shear moduli of elasticity and  $\nu$  is Poisson's ratio.

### 2.2.2 Dislocation and Strain Energies: Periodic Arrays of Dislocations

The energy of a single isolated dislocation is given by

$$E_D^\infty = \frac{\mu b^2}{4\pi(1-\nu)} [(1-\nu \cos^2 \beta) \ln \frac{\rho_c h}{q}] \quad (2.7)$$

The parameter  $\rho_c$  is introduced to account for the non-elastic part of the core energy of the dislocations and  $q$  is the core radius of the dislocation line, usually taken to be equal to  $b$ .

Two perpendicular arrays of interacting dislocations with a periodic distribution are then considered. Their strain field consists of an average homogeneous part and a fluctuating part with average equal to 0. The energy of the arrays contained in a unit area of the layer is given by

$$E_D^{array} = Bh \left( \frac{b_1}{p} \right)^2 + \frac{2}{p} E_{DS} \quad (2.8)$$

where

$$B = 2\mu \frac{1+\nu}{1-\nu} \quad (2.9)$$

The first term in equation (2.8) is the energy associated with the average homogeneous strain and the second term is the energy due to the fluctuating part of the strain of dislocations in the arrays.  $E_{DS}$  is the energy per unit length of a dislocation due to the fluctuating strain. A part of the energy due to average strain

caused by the dislocation network is included as  $Bh(b_1/p)^2$  in equation (2.8). Therefore  $E_{DS} < E_D^\infty$ , the difference  $E_D^\infty - E_{DS}$  is large for small values of  $p$ .

The homogeneous strain energy consists of  $Bhf_m^2$  due to misfit strain, the energy  $Bh(b_1/p)^2$  due to the average strain of the dislocation arrays and the product of these two terms due to interaction between the two strains. The expression for the total homogeneous strain energy  $E_H$  is,

$$E_H = Bh \left( f_m + \frac{b_1}{p} \right)^2 \quad (2.10)$$

Total energy  $E_T$  of a partially relaxed layer is the sum of the energy  $E_H$  and  $\frac{2}{p}E_{DS}$ ,

$$E_T = E_H + \frac{2}{p}E_{DS} \quad (2.11)$$

For large  $p$ ,  $E_{DS} \approx E_D^\infty$  and  $E_T$  can be written as

$$E_T^m = E_H + \frac{2}{p}E_D^\infty \quad (2.12)$$

If the layer under consideration has a thick cap-layer on the top, the above expressions for energies are not valid. If the cap is sufficiently thick, dislocation dipoles instead of dislocations are formed. A dipole consists of a pair of dislocations, one at the upper interface and the other one at lower interface. Figure 2.5 shows a schematic representation of a  $60^\circ$  array of dislocations in an uncapped layer and dipoles in a capped layer. Both dislocations of the dipole are  $60^\circ$  type and  $\alpha$  is the same as for the uncapped layers. The dislocations at the lower interface have a Burgers vector  $b$  and at the upper interface, a Burgers vector  $-b$ . The dipole spacing  $p$  is the spacing both in the upper and the lower array of dislocations as shown in Figure 2.5. The angle  $\theta$  is the angle between the line joining the two dislocations of a dipole and the line perpendicular to the interface.

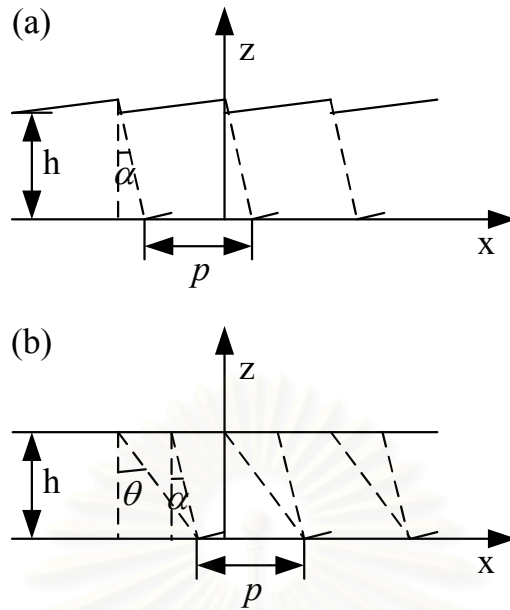


Figure 2.5 Schematic representation of (a)  $60^\circ$  dislocations in an uncapped layer and (b)  $60^\circ$  dipoles in a capped layer.

For obtaining the total energy  $E_D^{pcap}$  of the arrays in a capped layer,  $E_{DS}$  in equation (2.11) is replaced by  $E_{DS}^{cap}$ ,

$$E_D^{pcap} = Bh \frac{b_1^2}{p^2} + \frac{2}{p} E_{DS}^{cap} \quad (2.13)$$

The total energy of the capped layer is given by,

$$E_T^{cap} = Bh \left( f_m + \frac{b_1}{p} \right)^2 + \frac{2}{p} E_{DS}^{cap} \quad (2.14)$$

The energy of an array of dipoles in a capped layer is considerably larger than the energy of the array of dislocations in an uncapped layer. If interactions between the dipoles or between dislocations are neglected, the energy of a dipole in the capped layer is approximately twice as large as the energy of a dislocation in an uncapped layer.

### 2.2.3 Non-Periodic Arrays of Dislocations

The energy of an array of dislocations is lowest if the distribution is periodic. However, dislocations generally nucleate at heterogeneous sources (defects, impurities, ledges, etc.) and then they are clustered. Therefore, the energy of the arrays with irregular distribution of dislocations is considered. The energy of interaction  $E_I(h, p)$  (per unit length of the dislocation lines) of a pair of dislocations is given by,

$$\begin{aligned}
 E_I(h, p) = & Ab_1^2 \left[ \ln(4(h/p)^2 + 1) + \frac{4(h/p)^2(4(h/p)^2 + 3)}{(4(h/p)^2 + 1)^2} \right] \\
 & + Ab_2^2 \left[ \ln(4(h/p)^2 + 1) - \frac{4(h/p)^2(12(h/p)^2 + 1)}{(4(h/p)^2 + 1)^2} \right] \\
 & + Ab_3^2 [\ln(4(h/p)^2 + 1)(1 - \nu)]
 \end{aligned} \tag{2.15}$$

Let the number of dislocations be  $N+1$  with  $p_i$  as the inter-dislocation spacing between the  $i^{\text{th}}$  and  $(i+1)^{\text{th}}$  dislocations. The total interaction energy of the array is given by,

$$\begin{aligned}
 E_I^{\text{irr}}(N, h, \{p\}) = & \frac{2}{Np} \left[ \sum_{i=1}^N E_I(h, p_i) + \sum_{i=1}^{N-1} E_I(h, p_i + p_{i+1}) \right. \\
 & + \sum_{i=1}^{N-2} E_I(h, p_i + p_{i+1} + p_{i+2}) + \sum_{i=1}^{N-3} E_I(h, p_i + p_{i+1} + p_{i+2} + p_{i+3}) \\
 & + \dots + \left. \sum_{i=1}^{N-(N-1)} E_I(h, p_i + p_{i+1} + \dots + p_{i+(N-1)}) \right]
 \end{aligned} \tag{2.16}$$

To obtain the energy of the two perpendicular arrays per unit area of the layer, the interaction energy given above (1) the self-energy  $(2/\bar{p})E_D^\infty$  ( $\bar{p}$  is the average inter-dislocation distance in the array) of the dislocations and (2) the energy of interaction  $E_{I\perp}^{\bar{p}}$  between the two perpendicular arrays must be added. The energy of interaction  $E_{I\perp}^{\bar{p}}$  is given by,

$$E_{i\perp}^{\bar{p}} = \frac{2\mu h}{p} \left[ \frac{\nu b_1^2}{1-\nu} - \frac{b_3^2}{2} \right] \quad (2.17)$$

It has been assumed in writing the above equation that this energy depends only on the average spacing  $\bar{p}$  and not on the details of the distribution of spacing,  $p_i$ .



สถาบันวิทยบริการ  
จุฬาลงกรณ์มหาวิทยาลัย

### 2.3 Critical Thickness

The principle of energy minimization states that in thermal equilibrium the total energy of the epilayer is minimum with respect to the concentration of dislocations. By equating to zero the first derivative of the total energy  $E_T$  with respect to  $1/p$  ( $1/p$  is equal to the concentration of dislocations per unit length) and letting  $p \rightarrow \infty$  in equation (2.12), the following expression for  $h_c$  can be obtained by,

$$h_c = \frac{b^2(1-\nu \cos^2 \beta)}{8\pi f_m(1+\nu)b_1} \ln \frac{\rho_c h_c}{q} \quad (2.18)$$

If the layer is covered with a thick cap layer of the same material as the substrate, the energy  $E_D^{cap}$  for a dislocation in the capped layer should be used. The critical thickness of the capped epilayer increases by a factor of about 2 for  $f_m < 0.8$ .

Cohen-Solal et al. have proposed a new model for calculating the critical thickness. They supposed that the critical thickness is the thickness at which the homogeneous strain energy and the energy of the totally relaxed layer are equal. The energies were calculated using Keating's valence force field approximation. They found that the critical layer thickness can be written as

$$h_c = A^* f_m^{-3/2} \quad (2.19)$$

where  $A^*$  is an adjustable parameter. At  $h = h_c$ , there is a considerable strain in the layer and the arguments leading to this equation are not correct. However by adjusting the parameter  $A^*$ , fit of equation (2.19) (with  $A^* = 0.45 \text{ \AA}$ ) with experiments on II-VI semiconductor epilayers is reasonable.

Pinardi et al. have compiled experimental values of  $h_c$  of II-VI semiconductor and alloy epilayers as shown in Table 2.1. The experimental data from Table 2.1 are plotted in Figure 2.6.  $h_{cc}$  for capped layers of Figure 2.5 (b) is calculated. The results of these calculations are shown by the solid curve. If the correct theory is used (i.e., if interactions between the dislocations are taken into account), the values of  $h_c$  come out to be smaller. As mentioned earlier, the difference between the values of  $h_c$

calculated using the correct and the approximate theories is small, the maximum difference being 0.3% at low mismatch. Figure 2.6 shows that the experimental values of  $h_c$  are larger than the calculated values. The discrepancy is very large for small values of  $f_m$ , e.g., for the ZnSe layers. The difference between the calculated and the observed critical thickness is explained by assuming that there is an energy barrier for the creation of the misfit dislocations.

|    | Sample, $f_m$ (%)                                   | Method    | $h_c$ (nm)              | $T$ (°C) |
|----|---|-----------|-------------------------|----------|
| 1  | ZnSe/GaAs, 0.272                                    | x         | 150                     | -        |
| 2  | ZnSe/GaAs, 0.27                                     | x, T      | 150                     |          |
| 3  | ZnSe/ZnS, 5   | x         | 5 <sup>a</sup>          | -        |
| 4  | ZnTe/GaAs, 7.5                                      | R         | 1.2                     | 250      |
| 5  | CdSe/ZnSe (symmetrical SLS), 6.8                    | x, PL     | 0.91 (3mL)              |          |
| 6  | ZnSe/CdSe (symmetrical SLS), -6.3                   | x, PL     | 0.28 (1mL)              |          |
| 7  | CdTe/Cd <sub>0.97</sub> Zn <sub>0.03</sub> Te, 0.18 | Ch        | 390                     | -        |
| 8  | CdTe/ZnTe, 6  | RO, PL, T | 1.6 (5 mL)              | 250, 320 |
| 9  | CdTe/Cd <sub>0.96</sub> Zn <sub>0.04</sub> Te, 0.23 | x         | 513 <sup>a</sup>        |          |
| 10 | CdTe/InSb, 0.04                                     | x         | 2950 <sup>a</sup>       |          |
| 11 | CdTe/Cd <sub>1-x</sub> Zn <sub>x</sub> Te           |           | see Figure 2.6          |          |
| 12 | ZnTe/CdTe, -5.8                                     | R         | 2.1 (7 mL) <sup>b</sup> | 260      |

Table 2.1 Observed values of critical thickness. The –ve sign indicates that  $f_m$  is negative, the lattice constants of the epilayer is smaller and the in-plane strain  $\epsilon_{//}$  is positive, see equation (2.2) and (2.3). The abbreviation used in the table are, x: x-ray diffraction, Ch: Channeling, R: RHEED, RO: RHEED Oscillations and T: TEM.

<sup>a</sup>Values in (111) orientation were somewhat smaller.

<sup>b</sup>Relaxed buffer.

The value of  $h_c$  of ZnSe/GaAs has been determined by many workers. Yologawa et al. measured the lattice constants of ZnSe layers grown on GaAs substrates by metal organic vapor phase epitaxy (MOVPE). The calculated critical thickness is 21 nm as compared to the observed value of 150 nm. Other authors have also observed  $h_c = 150$  nm for ZnSe layers grown on GaAs. On the other extreme, the measured critical thickness of ZnSe on ZnS (mismatch 5%) buffer is 5 nm. The



experimental values of  $h_c$  of II-VI layers, particularly for low mismatch are quite reproducible.

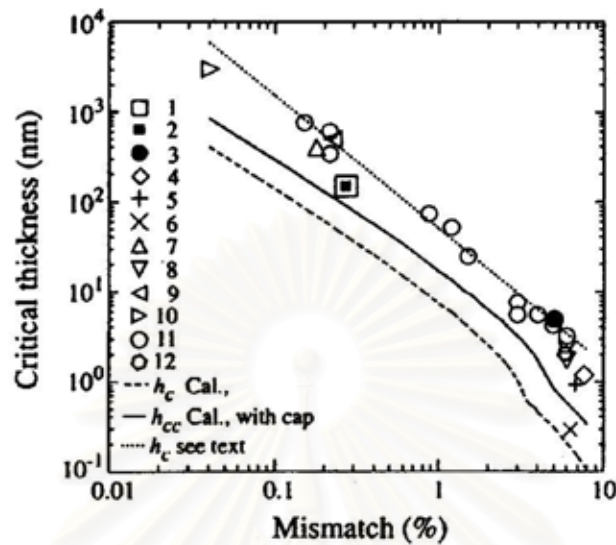


Figure 2.6 Critical thickness of II-VI semiconductor lattice mismatched layers. Dashed and solid lines give the calculated values of  $h_c$  for the layers with free surface and for the capped layers, respectively. The description of the samples for symbols 1 to 11 is given in Table 2.1 by the items 1 to 12.

Considering that the experimental values of  $h_c$  in Table 2.1 are for many different II-VI semiconductor and alloy layers and that the experiments have been done in different laboratories using different techniques of measurements, the scatter in the experiment values is small. The scatter in the values of  $h_c$  for InGaAs/GaAs and GeSi/Si is very large. The main reason for the different behavior of II-VI semiconductors is the fact that the II-VI semiconductors have weak bond strength. The dislocation energy in these semiconductors is much smaller than that in GeSi or III-V semiconductors. Dislocations are more easily produced in these semiconductors (Suresh, 2000).

## 2.4 Variation of Strain with Thickness

Lu et al. have grown ZnSe layer on InGaP buffers deposited on GaAs substrates by gas source MBE. By varying the composition of the buffer layer, its lattice constant can be changed from that of GaP to that of InP. The buffer layers containing 50% to 55% indium were pseudomorphic with GaAs if their thickness was less than 1  $\mu\text{m}$ . Thicker layers showed partial relaxation of strain. The layers were not completely relaxed even when their thickness was increased to more than 4  $\mu\text{m}$ . If the growth temperature was below 350  $^{\circ}\text{C}$ , the ZnSe layers grew in the 2D mode. X-ray diffraction studies of 1.9  $\mu\text{m}$  ZnSe layer grown on 1.15  $\mu\text{m}$   $\text{In}_{0.5}\text{Ga}_{0.5}\text{P}$  showed that the buffer layer was pseudomorphic. Due to the lattice mismatch of 0.27% between ZnSe and the pseudomorphic buffer layer, ZnSe layer was nearly fully relaxed.

Fortaine et al. have studied the strain relaxation in thick uncapped CdTe epilayers grown on (111)  $\text{Cd}_{0.96}\text{Zn}_{0.04}\text{Te}$  substrates. Lattice mismatch for this system is 0.23%. Experimental values of stress as a function of thickness  $h$  are shown in Figure 2.7. Pinari et al. have calculated relaxation of strain in thick layers using the equilibrium theory. According to the equilibrium theory, the number of dislocations introduced and the amount of strain relaxed in a layer of thickness  $h$  is such that the total energy  $E_T$  of the layer as a function of dislocation concentration is minimum. They have made plots of  $E_T$  vs  $1/p$  ( $p$  is the average interdislocation spacing) using equation (2.11) and (2.12) for several values of  $h$ . The value of  $1/p$  at the minimum in  $E_T$  gives the equilibrium dislocation concentration for each thickness  $h$ . Strain relaxation  $b_1/p$  is then calculated, converted into stress and plotted in Figure 2.7. Curve 1 uses the old theory based on equation (2.12). Curve 2 is obtained using equation (2.11) which takes into account the interactions properly for the total energy of the layer. The discrepancy between the theoretical curves and the experimental data is large.

Petruzzello et al. have investigated the structure of ZnSe layers grown on (100) GaAs (mismatch 0.27%) substrate by MBE. High resolution transmission electron microscopy (HRTEM) studies showed that there was complete registry of the lattice across the interface. The surface was wavy with amplitude of about 5 nm. In thin layers ( $h = 50$  and 87 nm), stacking faults were observed but there were no misfit dislocations. As the layer thickness increased beyond its experimental value of 150

nm, strain relaxation by the introduction of misfit dislocations began. The measured residual strain in the epilayers of different thicknesses is shown in Figure 2.8. The theoretical curves are also shown. The calculated curves have been moved down by  $0.4 \times 10^{-3}$  to take into account the thermal strain due to difference in the thermal coefficients of ZnSe and GaAs. They have been moved to the right by  $0.11 \mu\text{m}$  to take into account the difference between the calculated critical thickness (40 nm) and the observed thickness (150 nm). The agreement between the theory and experiment is quite reasonable in this case.

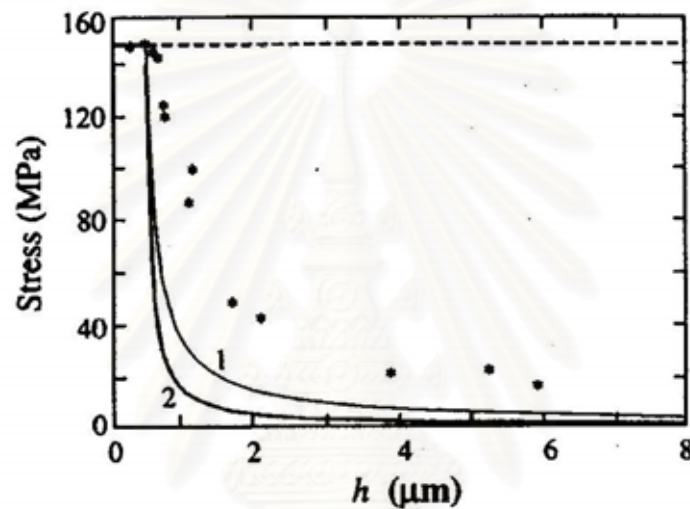


Figure 2.7 Plots of in-plane stress  $\sigma$  vs layers thickness  $h$  are shown for CdTe layers grown on a (111)  $\text{Cd}_{0.96}\text{Zn}_{0.04}\text{Te}$  substrate.

Yao et al. have measured lattice constant of ZnSe grown on (100) GaAs substrate. As the thickness of the epilayer increased, the layers relaxed by the creation of misfit dislocations at the growth temperature. At the same time on cooling, the in-plane lattice constant increased and lattice constant in the growth direction decreased due to tensile strain caused by the thermal mismatch. The strain has been determined by using the observed values of lattice constants and plotted by open circles in Figure 2.8. For this case, also agreement between theory and experiments is quite good. It is noted that ZnSe/GaAs (100) is the only known case where a reasonable agreement between theory and experiments exists. The discrepancy between the measured and calculated strain relaxation in the thick GeSi/Si and InGaAs/GaAs epilayers is very large (Pinaridi, 1998).

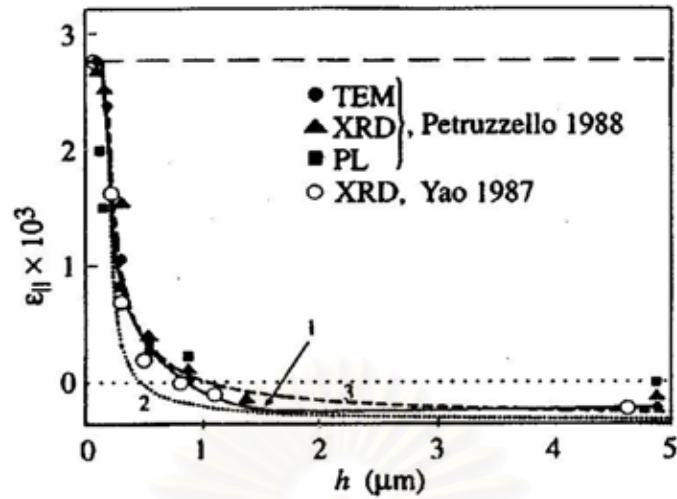


Figure 2.8 Plots of in-plane strain  $\epsilon_{||}$  in ZnSe layers grown on GaAs. Curve 1 is drawn through the experimental points shown by symbols as an aid to eye; Curve 2 is calculated using equation (2.11) and curve 3 is calculated using equation (2.12) for the total energy.

## CHAPTER III

### EXPERIMENTAL DETAILS

ZnO growth details in this work by plasma-assisted molecular beam epitaxy (MBE) including the characterization techniques are explained in this chapter. The rough segregation of the crystal quality is inspected by *in situ* reflection high-energy diffraction (RHEED) observation, while the surface morphology of all samples are characterized by *ex situ* optical microscopy, field emission-scanning electron microscope (FE-SEM) and atomic force microscopy (AFM). The structural, optical and electrical properties are observed by x-ray diffraction (XRD)  $2\theta$ - $\omega$  scan and pole figure, photoluminescence (PL) spectroscopy and Hall measurement with van der Pauw method, respectively.

#### 3.1 Molecular Beam Epitaxy

In this work, all samples are grown by a modified solid and gas source MBE machine. The MBE system consists of three chambers, which are composed of introduction chamber, transfer chamber, and growth chamber. A schematic drawing of the modified MBE growth chamber is shown in Figure 3.1.

The group II elements (Zn and Mg) and group III or V element for impurity implement (Ga or InP) are contained in PBN crucibles installed in separated effusion cells. All cells are heated by heaters and the temperatures are controlled by feedback from standard thermocouples through a controller. The special radio frequency (RF) cell is installed for plasma generation with VI gas source ( $O_2$ ). The flow rate of the gas is controlled by a mass flow controller (MFC) (STEC INC SEC-4400SP-MO-UC). The beam flux is turned on and turned off by controlling of the tantalum shutter position in front of each cell.

The equipments for RHEED experiment are a 15 kV electron gun, a fluorescent screen, and a CCD camera.

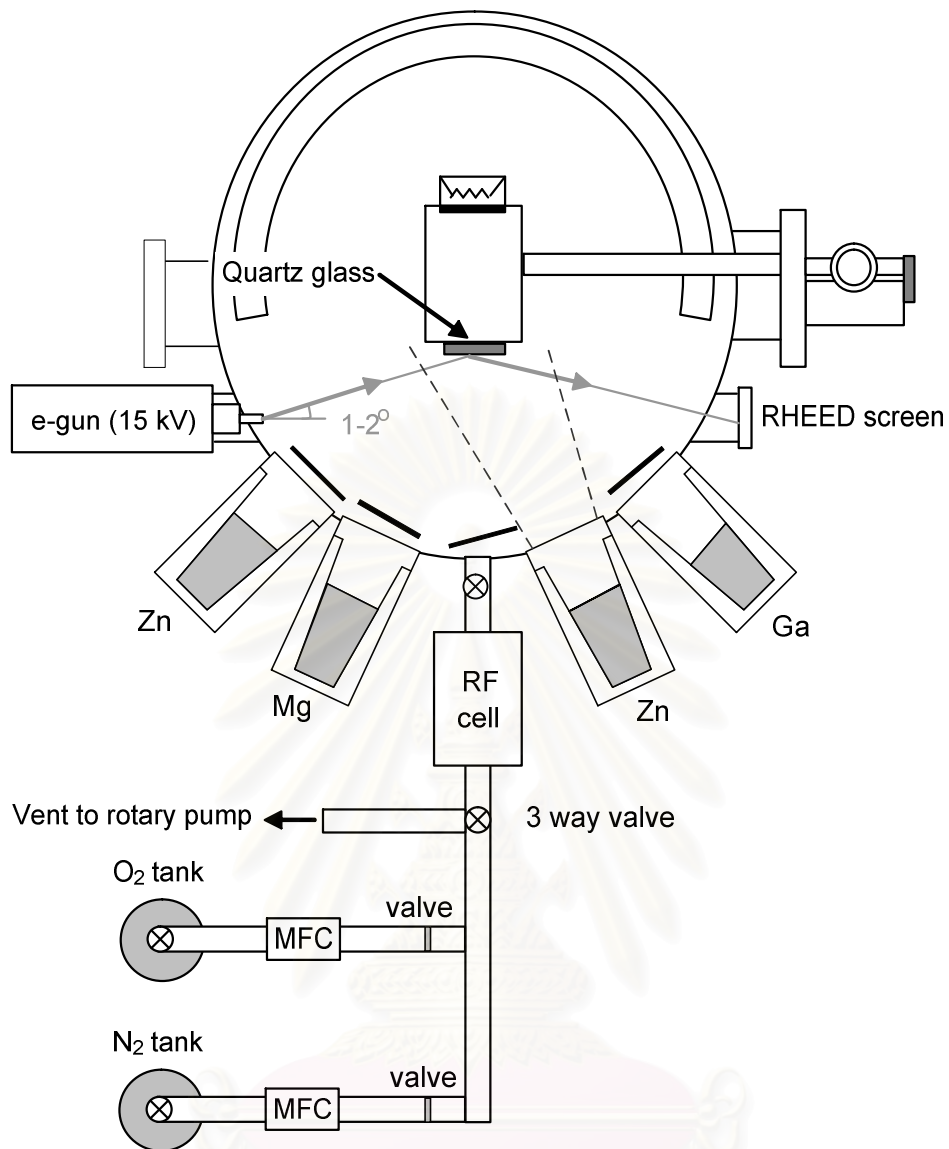


Figure 3.1 Schematic drawing of the growth chamber of the modified MBE system modified with *in situ* RF plasma-assisted system. The growth chamber is cooled by a closed circuit liquid Ethylene Glycol. It is pumped by a rotary pump, a turbo-molecular pump, and an ion pump. The base pressure is around  $1 \times 10^{-9}$  mbar.

### 3.2 RHEED Pattern Observation

RHEED is an important tool of surface science. It is highly surface-sensitive and is compatible with a wide range of other instruments and processes. The equipment is simple and robust, and it instantly provides information about a crystal surface. Diffraction techniques generally provide good measures of average long-range order.

A beam of energetic electrons strikes a crystal surface at a grazing incidence to produce a diffraction pattern on a phosphor screen. This process is shown schematically in Figure 3.2 (a). The electrons are nearly monoenergetic with a mean energy typically tens of kiloelectron-volts (15 KeV in this work.). Both the incident and diffracted beams travel nearly parallel to the surface ( $\theta \sim 1\text{-}2^\circ$ ). These electrons are scattered by the periodic potential of the crystal surface, which function as a grating, giving rise to the diffraction pattern. Because the RHEED pattern depends on the surface atomic configuration and can be performed *in situ*, this observation is crucial for MBE growth.

RHEED diffraction patterns are produced when the momentum of the incident beam and that of the diffracted beam differ by a reciprocal lattice vector of the surface. This is often represented by the Ewald sphere construction as shown in Figure 3.2 (b). The condition for imaging on the phosphor screen is called the *Laue diffraction condition* (Kittel, 1996):

$$\mathbf{k}' - \mathbf{k}_0 = \mathbf{G} \quad (3.1)$$

where  $\mathbf{k}_0$  and  $\mathbf{k}'$  are the wavevectors of the incident and diffracted electrons, respectively, and  $\mathbf{G}$  is the reciprocal lattice vector. This condition corresponds to Bragg's law in the simple diffraction theory. The pattern position can be graphically determined by the Laue method - intersection of Ewald sphere in reciprocal lattice space (see Figure 3.2(b)). Because the electron beam is restricted to the topmost atomic layers, diffracted electrons at the flat surface are images onto the screen. Therefore, the surface layer is represented by reciprocal lattice space rods, which are normal to the real surface. If the surface has roughness in the order of an atomic scale, the surface layer in the reciprocal space will be represented by a three-dimensional

point array. Therefore, the RHEED pattern can be simplified as the reciprocal lattice representation of the sample surface, which reflects the surface morphology on the atomic scale. In this work, we use RHEED to observe the development of the surface structure since the beginning of the MgO buffer layer growth. The transition of the reconstruction pattern shows the improvement of the crystal quality during the growth.

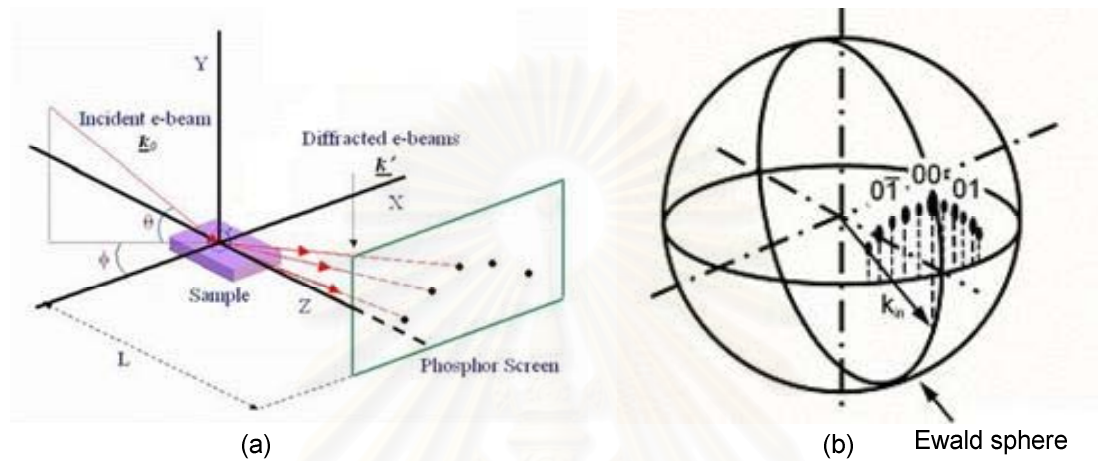


Figure 3.2 (a) Schematic representation of the RHEED observation system (Mohammed Samir Hegazy, 2002) and (b) Ewald sphere construction for a reconstructed surface in  $[-1\ 1\ 0]$  azimuth (Herman and Sitter, 1989).

สถาบันวิทยบริการ  
จุฬาลงกรณ์มหาวิทยาลัย



### 3.3 Optical Microscopy

The optical microscope remains the fundamental tool for phase identification. The optical microscope magnifies an image by sending a beam of light through the object as seen in the schematic diagram of Figure 3.3. The condenser lens focuses the light on the sample and the objective lenses (10X, 20X,..., 1000X) magnifies the beam, which contains the image, to the projector lens so the image can be viewed by the observer. In this work, the optical microscope (OLYMPUS AX70) is used to roughly observe the surface of samples with/without MgO buffer layer after growth.

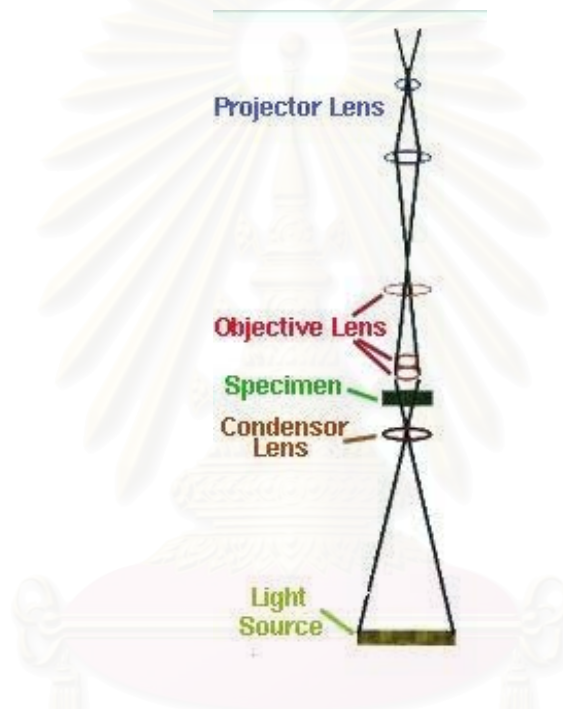


Figure 3.3 Schematic diagram of the optical microscope

สถาบันวิทยบริการ  
จุฬาลงกรณ์มหาวิทยาลัย

### 3.4 Field Emission-Scanning Electron Microscope

Both MgO buffer layer and ZnO layer thickness is measured by FE-SEM (JEOL Technology JSM 6500F), which is a high-resolution imaging technique providing topographical and structural information in plan view or in cross-section. The surface morphology of all samples is also investigated. For the sample preparation, because the FE-SEM is a state-of-the-art instrument that is capable of analytical microscopy at very high spatial resolution, it can only do this if the samples and holders are kept clean. The contamination rate increases approximately exponentially as the spot size decreases, so this effect is more important on these new SEMs than it was on the old ones. Before samples can be inserted into the microscope they must be mounted onto one of the available SEM stages. According to the non-conductive samples, a thin layer of metal or carbon before they are imaged in the microscope is normally needed. This prevents charge build-up on the surface of the sample. In this work, gold is applied to get through this problem as mentioned above.



### 3.5 X-ray Diffraction

Basically, diffraction occurs as waves interact with a regular structure whose repeat distance is about the same as the wavelength. X-rays have wavelengths on the order of a few angstroms, which are the same as typical interatomic distances in crystalline solids. That means X-rays can be diffracted from minerals, which, by definition, are crystalline and have regularly repeating atomic structures. When certain geometric requirements are met, X-rays scattered from a crystalline solid can constructively interfere, producing a diffracted beam. In 1912, W. L. Bragg recognized a predictable relationship among several factors, which are a distance between similar atomic planes in a mineral (the interatomic spacing) called the d-spacing and measure in angstroms, an angle of diffraction called the theta angle ( $\theta$ ) and measure in degrees (For practical reasons the diffractometer measures an angle twice that of the theta angle.) and a wavelength of the incident X-radiation, symbolized by the Greek letter lambda and, in this case, equal to 1.54 angstroms. These factors are combined in *Bragg's Law*:

$$2d \sin\theta = n\lambda \quad (3.2)$$

where  $d$  (d-spacing) and  $\theta$  are interatomic spacing in angstroms and diffraction angle in degrees, respectively. Besides,  $n$  and  $\lambda$  are integer 1,2,3,...,etc and wavelength in angstroms ( $1.54 \text{ \AA}$  for copper), respectively. The details are as shown in Figure 3.4.

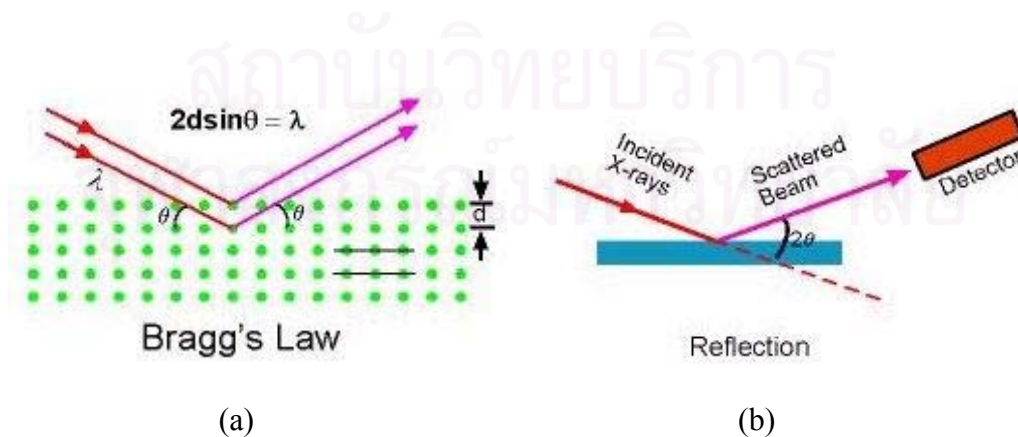


Figure 3.4 (a) Bragg's Law factors and (b) Schematic representation of the X-Ray Diffraction  $2\theta$ - $\omega$  measurement system

Moreover, texture measurements are used to determine the orientation distribution of crystalline grains in a polycrystalline sample. A material is termed textured if the grains are aligned in a preferred orientation along certain lattice planes. One can view the textured state of a material (typically in the form of thin films) as an intermediate state in between a completely randomly oriented polycrystalline powder and a completely oriented single crystal. The texture is usually introduced in the fabrication process (e.g. rolling of thin sheet metal, deposition, etc.) and affects the material properties by introducing structural anisotropy. A texture measurement is also referred to as a pole figure as it is often plotted in polar coordinates consisting of the tilt and rotation angles with respect to a given crystallographic orientation. A pole figure is measured at a fixed scattering angle (constant  $d$  spacing) and consists of a series of  $\psi$ -scans (in-plane rotation around the center of the sample) at different tilt or  $\Psi$ -(azimuth) angles, as shown in Figure 3.5.

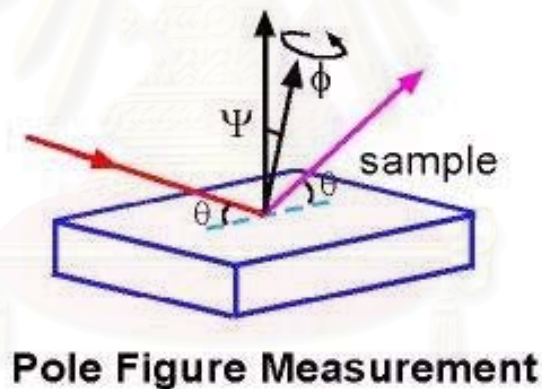


Figure 3.5 Representation of the X-Ray diffraction pole figure system

The structural property of all samples is characterized by X-ray diffraction  $2\theta$ - $\omega$  scan and pole figure (Philips X'pert MRD). Due to ZnO lattice constant, the  $2\theta$  value is around 34.42 degrees, whereas the common orientation of the grown ZnO layer is c-plane.

### 3.6 Atomic Force Microscopy

Atomic force microscope (AFM) provides pictures of atoms on or in surfaces. The AFM works by scanning a fine ceramic or semiconductor tip over a surface much the same way as a phonograph needle scans a record. The tip is positioned at the end of a cantilever beam shaped much like a diving board. As the tip is repelled by or attracted to the surface, the cantilever beam deflects. The magnitude of the deflection is captured by a laser that reflects at an oblique angle from the very end of the cantilever. A plot of the laser deflection versus tip position on the sample surface provides the resolution of the hills and valleys that constitute the topography of the surface. The AFM can work with the tip touching the sample (contact mode), or the tip can tap across the surface (tapping mode) much like the cane of a blind person. Figure 3.6 shows the schematic representation of AFM system.

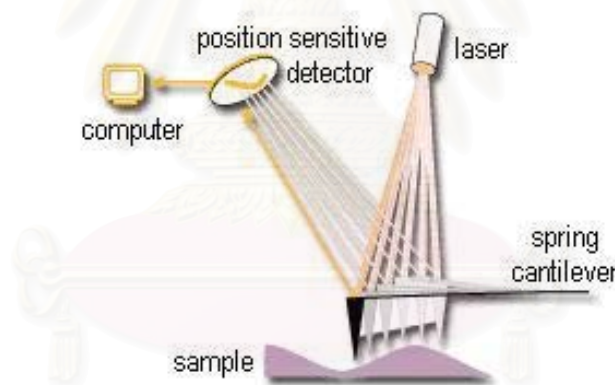


Figure 3.6 Schematic representation of AFM system

All samples are measured by AFM (JEOL Technology JSPM 4210) including computer program analyzation to investigate the surface morphology. The AFM is operated in the tapping mode. The scan rate is  $\sim 3$  Hz and the scan size is usually  $5 \times 5 \mu\text{m}^2$ . The number of data points per scan line is 512.

### 3.7 Photoluminescence Spectroscopy

Photoluminescence (PL) spectroscopy is a contactless, nondestructive method of probing the electronic structure of materials. Specifically, light is directed onto a sample, where it is absorbed and imparts excess energy into the material in a process called *photo-excitation*. One way this excess energy can be dissipated by the sample is through the emission of light, or luminescence. In the case of photo-excitation, this luminescence is called photoluminescence. The intensity and spectral content of this photoluminescence is a direct measure of various important material properties. More specifically, photo-excitation causes electrons within the material to move into permissible excited states. When these electrons return to their equilibrium states, the excess energy is released and may include the emission of light (a radiative process) or may not (a nonradiative process). The energy of the emitted light photoluminescence related to the difference in energy levels between the two electron states involved in the transition between the excited state and the equilibrium state. The quantity of the emitted light is related to the relative contribution of the radiative process.

The applications through PL measurement are composed of band gap determination, impurity levels and defect detection, recombination mechanisms and material quality. The most common radiative transition in semiconductors is between states in the conduction and valence bands, with the energy difference being known as the band gap. However, The PL energy associated with localized defect levels, which the radiative transitions in semiconductors also involve, can be used to specific defects, and the amount of PL can be used to determine their concentration. As mentioned above, the recombination involves both radiative and nonradiative processes. The amount of PL and its dependence on the level of photo-excitation and temperature are directly related to the dominant recombination process. Also, analysis of these results helps to understand the recombination mechanism. Generally, nonradiative processes are associated with localized defect levels, whose presence is detrimental to material quality and subsequent device performance. Thus, material quality can be measured by qualifying the amount of radiative recombination.

To investigate the optical property of all samples, photoluminescence (PL) spectroscopy is applied. A schematic of the PL experimental setup is shown in Figure 3.7. The 325-nm line of a He-Cd laser (KIMMON) excites the samples. The

integrated laser power is 1 mW. The laser beam is chopped and focused to the sample by a 10-cm focal length lens. An 30-cm focal length and a 40-cm focal length lens are used to collect the PL signal. The light signal is resolved by a 1-m photomultiplier (SPEX 500M). Typically, the entrance and exit slit widths are 2 mm. A high-pass filter is used to filter noise and the reflected laser beam signal. The resolved light signal is detected by a detector system (Hamamatsu C2761 No.300089). A chopper and the lock-in amplifier (NF Electronic Instruments Inc. 5610B Two-phase) are used to enhance the signal by the standard lock-in technique. The temperature of samples during measurement is cooled down to 10 K by Temperature controller (Scientific Instruments Inc. 9600-1 Silicon Diode).

In this work, the PL data lead to the information about the structural quality of the sample and excitonic levels. According to the wide direct bandgap as well as the high exciton binding energy of ZnO, the remarkable excitonic properties are clearly shown. The obvious result is the intensity of excitonic emissions due to the strain-induced structure and energy band bending. The misfit dislocations in the epitaxial film also create a high concentration of centers of nonradiative recombination and significantly reduce the integrated intensity of the PL spectrum. Therefore, the structural quality of the sample can be roughly estimated and the defect density can be compared among various samples by the PL intensity. Also, for the PL line width, the inhomogeneously broaden distribution of the emission centers make the line width wider.

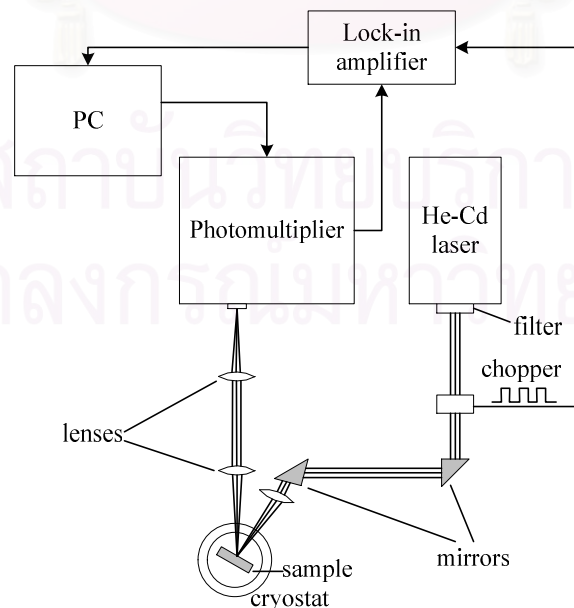


Figure 3.7 Schematic of the PL experimental setup.

### 3.8 Absorption Spectroscopy

Due to the strain-induced influence resulted by the balancing the compressive-tensile strain, energy band gap of the samples are estimated by absorption spectroscopy method at room temperature. The absorption spectrophotometer consists of a light source (hallow cathode lamp), a sample compartment for both sample and glass substrate reference, and a detector (photomultiplier).

Generally, molecules absorb ultraviolet or visible light. The absorbance of a sample increases as attenuation of the beam increases. Absorbance is directly proportional to the path length,  $b$ , and the concentration,  $c$ , of the absorbing species. *Beer's Law* states that

$$A = ebc \quad (3.3)$$

where  $e$  is a constant of proportionality, called the absorbtivity. Different molecules absorb radiation of different wavelengths. An absorption spectrum will show a number of absorption bands corresponding to structural groups within the molecule.

The spectral analysis depends on this law through the equation (3.4) and a diagram in Figure 3.8. The diagram shows a beam of monochromatic radiation of radiant power  $P_0$ , directed at a sample solution. Absorption takes place and the beam of radiation leaving the sample has radiant power  $P$ .

$$\begin{aligned} T \text{ (Transmittance)} &= P / P_0 \\ A \text{ (Absorbance)} &= \log_{10} P_0 / P \\ &= 2 - \log_{10} \%T \end{aligned} \quad (3.4)$$

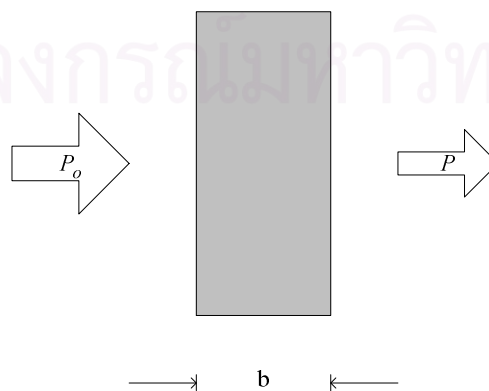


Figure 3.8 The absorption basic diagram



According to this technique, it is based on the measurement of the transmitted light through the sample, preferably under normal incidence. As the wavelength of the photons decreases, there will be a value for which the transmitted light will be abruptly reduced in the case of direct semiconductors. The onset of absorption is directly related to the band gap energy. However, large errors can be made by simple inspection of the absorption edge of the transmittance spectrum. Errors can be magnified if the sample is not thin enough, causing absorbance saturation or zero transmittance around the band gap, or in the case of presence of interference effects. A reliable analysis requires the determination of the absorption coefficient ( $\alpha$ ) as a function of photon energy and this is not a straightforward process. The reduction in the intensity of the transmitted beam is due to reflection at the sample interfaces, roughness scattering and other losses. Knowing  $\alpha$  as a function of energy around the absorption edge, the direct band gap is determined by equation (3.5).

$$\alpha(h\nu) = \frac{A}{h\nu} (h\nu - E_g)^{1/2} \quad (3.5)$$

where  $A$  is a prefactor which can be considered constant around the band gap region,  $h$  is the Planck constant and  $\nu$  is the frequency of the photons in vacuum. The typical procedure is to plot  $[\alpha(h\nu)h\nu]^2$  vs.  $h\nu$  and the intercept with the photon energy axis (for  $\alpha = 0$ ) defines the energy gap. (Optoelectronic Properties of Semiconductors and Superlattices, M.O. Manasreh) A schematic of the absorption experimental setup is shown in Figure 3.9.

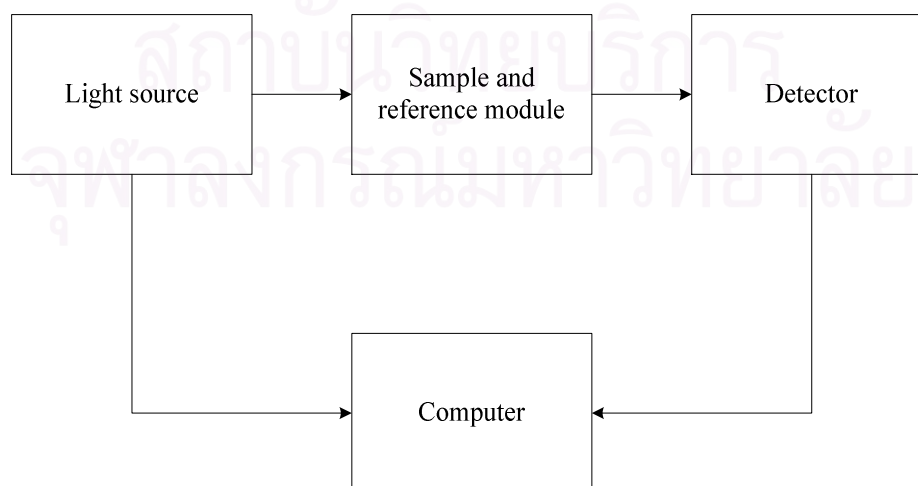


Figure 3.9 Absorption spectroscopy system

### 3.9 Hall Measurement

The basic physical principle underlying the Hall effect is the Lorentz force. When an electron moves along a direction perpendicular to an applied magnetic field, it experiences a force acting normal to both directions and moves in response to this force and the force results in the internal electric field. For an  $n$ -type, bar-shaped semiconductor shown in Figure 3.10, the carriers are predominately electrons of bulk density  $n$ . A constant current  $I$  is assumed to flow along the  $x$ -axis from left to right in the presence of a  $z$ -directed magnetic field. Electrons subject to the Lorentz force initially drift away from the current line toward the negative  $y$ -axis, resulting in an excess surface electrical charge on the side of the sample. This charge results in the Hall voltage, a potential drop across the two sides of the sample. Note that the force on holes is toward the same side because of their opposite velocity and positive charge. This transverse voltage is the Hall voltage  $V_H$  and its magnitude is equal to  $IB/qnd$ , where  $I$  is the current,  $B$  is the magnetic field,  $d$  is the sample thickness, and  $q$  ( $1.602 \times 10^{-19}$  C) is the elementary charge. In some cases, it is convenient to use layer or sheet density ( $n_s = nd$ ) instead of bulk density. One then obtains the equation (3.6).

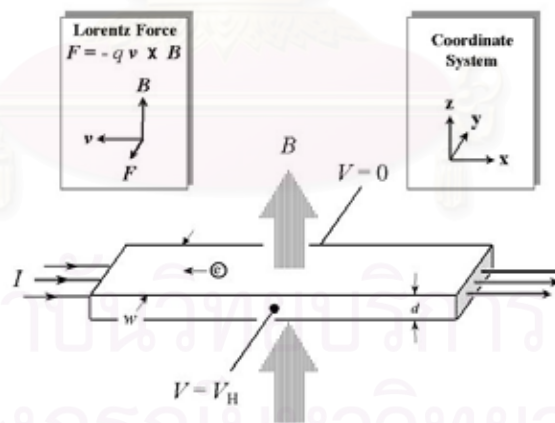


Figure 3.10 Hall measurement principle

$$n_s = \frac{IB}{q|V_H|} \quad (3.6)$$

Thus, by measuring the Hall voltage  $V_H$  and from the known values of  $I$ ,  $B$ , and  $q$ , one can determine the sheet density  $n_s$  of charge carriers in semiconductors.

In order to determine both the mobility  $\mu$  and the sheet density  $n_s$ , a combination of a resistivity measurement and a Hall measurement is needed. Van der Pauw technique is widely used in the semiconductor industry to determine the resistivity of uniform samples due to its convenience. A schematic of a rectangular van der Pauw configuration is shown in Figure 3.11.

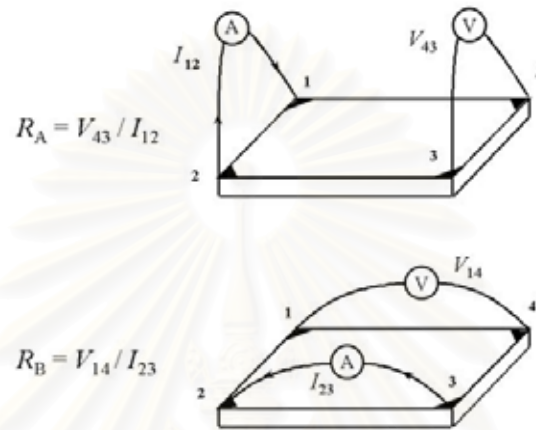


Figure 3.11 Schematic of a rectangular van der Pauw

The objective of the Hall measurement in the van der Pauw technique is to determine the sheet carrier density  $n_s$  by measuring the Hall voltage  $V_H$ . The Hall voltage measurement consists of a series of voltage measurements with a constant current  $I$  and a constant magnetic field  $B$  applied perpendicular to the plane of the sample. Conveniently, the same sample, shown again in Figure 3.12, can also be used for the Hall measurement. To measure the Hall voltage  $V_H$ , a current  $I$  is forced through the opposing pair of contacts 1 and 3 and the Hall voltage  $V_H$  ( $= V_{24}$ ) is measured across the remaining pair of contacts 2 and 4. Once the Hall voltage  $V_H$  is acquired, the sheet carrier density  $n_s$  can be calculated via equation (3.6) from the known values of  $I$ ,  $B$ , and  $q$ .

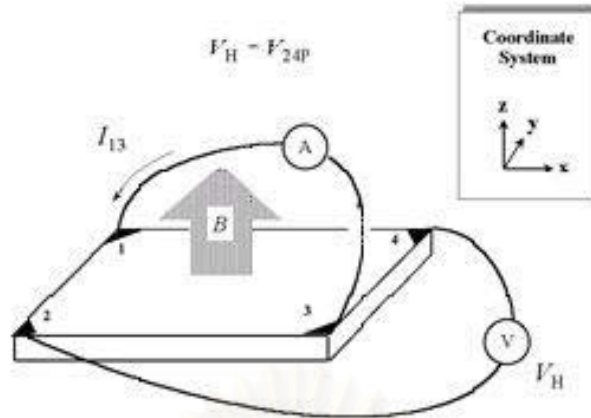


Figure 3.12 Representation of Hall measurement system with van der Pauw method of this work

To inspect the electrical property, all samples except the samples with cracks can be measured by Hall measurement with van der Pauw method. The preparation of the sample before characterization is necessary. The 4-contact with the symmetry shape of the sample is needed to avoid the current leakage during measurement due to an insulating glass substrate. Thus, the preparation process is as the following procedure.

1. Cut a sample with square size of  $0.5 \times 0.5 \text{ cm}^2$  due to a little smaller mask size of  $0.4 \times 0.4 \text{ cm}^2$ .
2. To clean attaching In at the backside, the ZnO surface is waxed and In is etched by HCl. Then, the sample is drained by De-ion (DI) water. Next, remove the wax by heated Ethanol and DI water.
3. Cut 2-cm Au wire and clean by Acetone with ultrasonic for 10 min. Then, clean in DI water with 10-min ultrasonic. Dry by nitrogen gas.
4. Evaporate Au to make the 4 contacts to the sample.

In this work, we mainly use the RHEED pattern, and XRD  $2\theta$ - $\omega$  scan and pole figure to investigate the crystal orientation and structural property. Also, optical microscope, FE-SEM and AFM are applied to observe the surface morphology and layer thickness. PL measurement and absorption coefficient are applied to measure the optical property including the ZnO energy band gap. For the electrical property,

all samples are measured by Hall measurement with van der Pauw method. Furthermore, some measurements such as X-ray Photoemission Spectroscopy (XPS) and Transmission Electron Microscopy (TEM) are partly used to investigate the impurity concentration and crystal quality, respectively.



สถาบันวิทยบริการ  
จุฬาลงกรณ์มหาวิทยาลัย

## CHAPTER IV

### ZnO FILM ON SILICON AND SAPPHIRE SUBSTRATES

According to the application device in blue and ultraviolet regions, the interest in ZnO, one of the promising materials, recently increases because of its wide energy gap, 3.37 eV at room temperature, and outstanding properties, especially excitonic properties. Then, the ZnO growth condition including relating application has been studied. One of the serious problems is the dislocation around the boundary of ZnO and the substrate due to the lattice mismatch. To grow high-quality ZnO layer, ZnO substrate is certainly the best choice, however, the price of the ZnO substrate is very expensive. Therefore, other cheaper substrates such as Si and sapphire with acceptable lattice mismatch are necessary.

#### 4.1 ZnO film on silicon substrate

There have been many reports on the growth of ZnO by MBE, and highly luminescent ZnO crystals have been grown on sapphire substrates. However, electrically insulating substrates such as sapphire make the device fabrication processes more complex, when the grown crystal is applied to injection light-emitting devices. In addition, the crystal quality of the Si substrate is expected to be remarkably higher than that of the sapphire substrate. Anyway, the growth of epitaxial ZnO films on Si is known to be very difficult because the Si substrate surface is easily oxidized and covered with a resulting amorphous SiO<sub>x</sub> layer when it is exposed to reactive oxygen sources. This amorphous SiO<sub>x</sub> layer degrades the crystal quality of ZnO grown on the Si substrate. Recently, a few works of ZnO grown on Si substrates have been reported. For example, Iwata et al. reported ZnO growth on Si (111) substrate, applying NH<sub>3</sub> plasma nitridation of the Si surface prior to the growth. They found that the nitridation process was effective in preventing surface oxidation, and obtained (0001)-oriented ZnO layers. However, the grown layers suffered from rotational domains which make the lateral orientation random. Also, the growth of ZnO on Si and SiO<sub>2</sub> has been investigated by Choi et al. using pulse laser deposition.

Although the grown surface grains were preferentially oriented in the (0001) direction (normal to the surface), lateral orientation was found to be random. This is probably caused by the SiO<sub>2</sub> film, formed on the Si surface. Therefore, the prevention method from the oxidation of Si substrate surface in the initial stage of ZnO growth is the most important issue for the ZnO grown on Si. The studies of ZnO grown on Si substrates have been investigated by some members in our group. The detail is as the following.

#### **4.1.1 Initial Zn layer with ozone source**

To hinder the oxidation of the Si substrate surface as the important problem mentioned above, Miki et al. proposes the introduction of an initial Zn layer followed by its oxidation before the ZnO growth. The growth procedure and experimental result are shown, respectively.

##### *4.1.1.1 Growth procedure*

The detailed steps for sample preparation are as following. First, a substrate surface is clean by chemical solution. The substrate is degreased in Isopropyl alcohol (IPA) with ultrasonic for 10 min. Then, the substrate is soaked in DI water. The substrate is next etched in 5% HF solution and a solution of HCl:H<sub>2</sub>O<sub>2</sub>:H<sub>2</sub>O (3:3:5). Finally, it is soaked in DI water again and dried by nitrogen gas. Then, the substrate is then mounted onto a molybdenum block by Titanium lock. The substrate is inserted into the MBE chamber. Before growth, the sample is heated to decontaminate the substrate surface from water (H<sub>2</sub>O) at 800°C until the streaky (7×7) RHEED pattern appeared. After the desorption at 800°C, the substrate is cooled down to 100°C. Then, the initial Zn layer is deposited at a Zn Beam Equivalent Pressure (BEP) of 1×10<sup>-7</sup> Torr for 2 min. After the Zn deposition, ozone is supplied to oxidize the initial Zn layer. The background pressure during oxidation is approximately 1×10<sup>-4</sup> Torr. At the same time, the substrate temperature is increased. The increase of the substrate temperature under ozone supply is continued until the substrate temperature reaches 200°C. The temperature is then held at this value for the subsequent ZnO growth. A 250-nm-thick ZnO film is grown using Zn BEP of 1×10<sup>-6</sup> Torr. The ozone flow rate is

lowered so as to produce the background of  $1 \times 10^{-5}$  Torr. After growth, the sample is annealed at  $1,100^\circ\text{C}$  for 1 min in nitrogen atmosphere.

#### 4.1.1.2 Experimental result

RHEED patterns obtained using electron beam incident azimuths along Si  $[\bar{1}\bar{1}0]$  and Si  $[1\bar{1}\bar{2}]$  directions in different stages of ZnO growth are shown in Figure 4.1. A clear  $(7 \times 7)$  pattern appears at  $800^\circ\text{C}$  as shown in Figure 4.1(a), which indicates the appearance of an atomically clean Si (111) surface. While the initial Zn layer is deposited, the  $(7 \times 7)$  Si pattern gradually disappears and a streaky pattern emerges as shown in Figure 4.1(b). However, the streaky pattern easily changes to a ring pattern when the deposition time is increased. When the initial Zn layer showing the ring pattern is oxidized and subsequent ZnO growth is performed, polycrystalline ZnO film with non-orientation is grown. This film shows very poor PL characteristic. When the initial Zn layer shows streaky pattern, however, c-axis-oriented ZnO film is obtained. These results suggest that the crystal quality of ZnO epitaxial film depends strongly on the quality of the initial Zn layer. Without the initial Zn layer, no ZnO growth takes place, probably due to the surface oxidation of the Si substrate. Then, the initial Zn layer is useful for protecting the Si substrate surface from oxidation. Also, the initial Zn layer with a streaky RHEED pattern provides a good template for further ZnO growth. Thus, the initial Zn layer with the streaky RHEED pattern is chosen to provide the improvement of the ZnO film. The thickness of the initial Zn layer is estimated to be approximately 0.5 nm by AFM measurement.

The streaky RHEED pattern of the initial Zn layer is ascribed to Zn  $(1 \times 1)$  because the spacing between the diffraction spots coincides well with the hexagonal Zn lattice arrangement. The observed RHEED pattern also shows that the initial Zn layer is rotated by  $30^\circ$  with respect to the Si substrate, as shown in Figure 4.2. Also, the  $[1000]$  direction of Zn is parallel to the  $[1\bar{1}\bar{2}]$  direction of the Si surface and the  $[1\bar{1}\bar{2}0]$  direction of Zn is parallel to the  $[\bar{1}\bar{1}0]$  direction of the Si surface. The ratio of the diffraction spot spacing of the Si substrate to that of the deposited Zn layer is 10:25 when the electron beam azimuth is  $[\bar{1}\bar{1}0]$  of the Si surface, while it is 17:14 when the azimuth is  $[1\bar{1}\bar{2}]$  direction. These results with the sixfold-symmetry streaky pattern indicate that the initial Zn layer is rotated by  $30^\circ$  with respect to the Si substrate surface. When ozone supply is started, the RHEED pattern changes from the



Zn (1×1) to the ZnO (1×1) streaky pattern, indicating the formation of fairly flat ZnO surface, illustrated in Figure 4.1(c). However, near the end of the oxidation process of the initial Zn layer, a spotty RHEED pattern appears as shown in Figure 4.1(d). This spotty pattern is essentially unchanged during the subsequent growth of ZnO films as shown in Figure 4.1(e). It should be noted that the lateral crystal orientation is kept unchanged during the oxidation process of the initial Zn layer and the subsequent ZnO layer deposition process, illustrated in Figure 4.2.

Both the initial Zn layer and the ZnO epitaxial layer grown on it have crystallographic orientation rotated by 30° with respect to the Si substrate. The mechanism, which controls the observed 30° rotation of the initial Zn layer, is not clearly understood, however, the observed 30° rotation could relieve the strain caused by lattice mismatch between the Si (111) substrate and the initial Zn layer. The schematic lattice arrangements between the Si (111) substrate and the initial Zn layer with and without 30° rotation are shown in Figure 4.3. When the hexagonal Zn layer is deposited on the Si (111) surface without rotation, the lattice mismatch should be 30.6%. However, when the Zn layer is rotated by 30° on the Si (111) surface, the corresponding lattice mismatch is reduced to 20.2%, which may alleviate the strain caused by lattice mismatched between these materials.

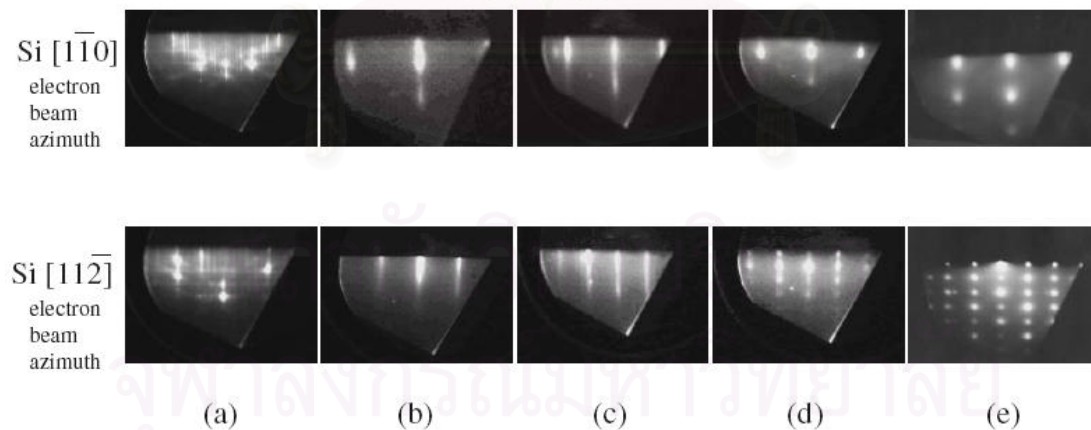


Figure 4.1 RHEED patterns along Si  $[11\bar{2}]$  direction and Si  $[\bar{1}10]$  direction in different stages of ZnO growth: (a) before growth, (b) the initial Zn layer is deposited, (c) oxidation is started, (d) the oxidation is continued, and (e) the growth of ZnO film is performed.

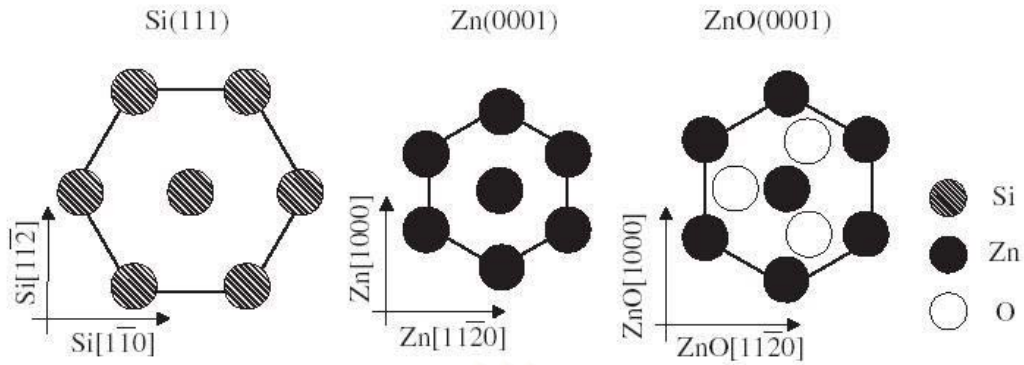


Figure 4.2 Relationship of the crystal orientation among Si, Zn and ZnO. The initial Zn layer and ZnO film are rotated by  $30^\circ$  with respect to the Si substrate orientation. The  $[1000]$  direction of Zn and ZnO are parallel to the  $[11\bar{2}]$  direction of Si.

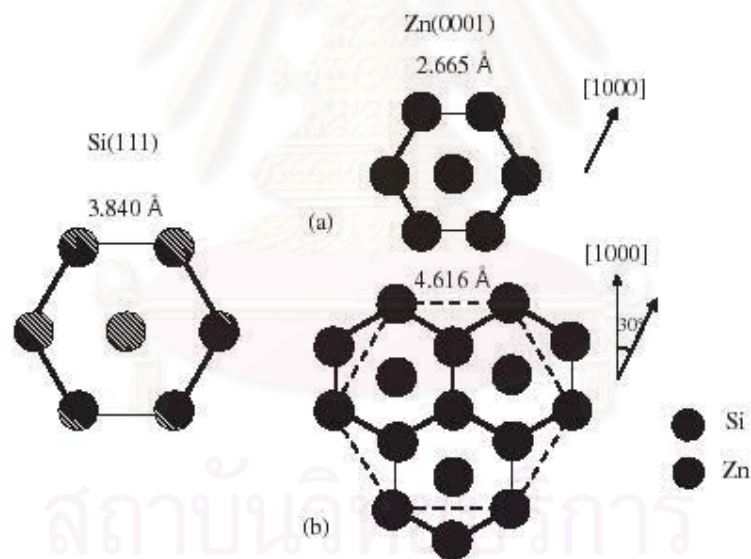


Figure 4.3 Effect of  $30^\circ$  rotation on lattice mismatch between Si (111) and initial Zn layer: (a) orientation-matched case, and (b)  $30^\circ$  rotation.

Figure 4.4 shows the AFM images of the Zn-deposited surface with the surface after oxidation. The observed AFM images show that the grain size and the surface roughness increase with oxidation.

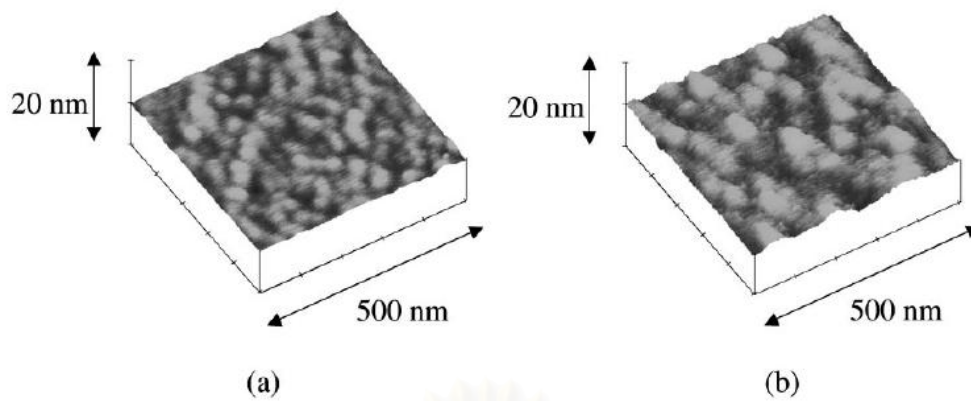


Figure 4.4 AFM images of the grown surfaces: (a) before oxidation of the initial Zn layer, and (b) after oxidation of the initial Zn layer. The grain size and the surface roughness increase with oxidation.

The results of the XRD  $2\theta$ - $\omega$  scan measurement of the as-grown and the annealed sample are shown in Figure 4.5. The as-grown ZnO film is found to be strongly c-oriented. Although a weak diffraction signal, which is probably due to the ZnO  $(10\bar{1}1)$  planes, appears in a higher diffraction angle region, it completely disappears after annealing at 1100 °C. No change is observed for the ZnO (0002) diffraction peak width after annealing. Figure 4.6 shows a  $\{10\bar{1}1\}$  x-ray pole figure of the annealed sample. It clearly shows the sixfold symmetry about the surface normal, indicating that no rotational domain of ZnO (0001) exists in this ZnO film. This is one of the major advantages of this method compared to other methods.

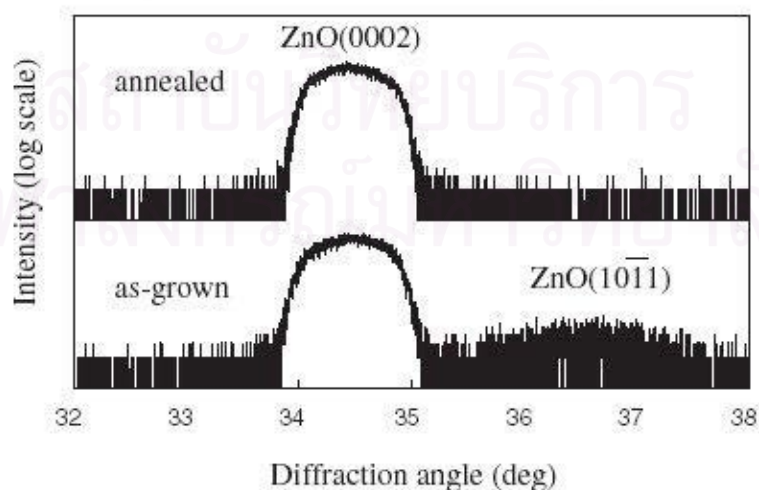


Figure 4.5 XRD  $2\theta$ - $\omega$  scan measurement of the as-grown and the annealed sample. The ZnO  $(10\bar{1}1)$  diffraction peak disappears upon annealing.

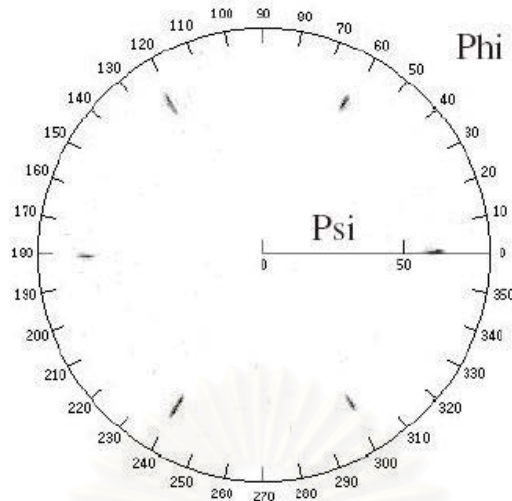


Figure 4.6  $\{10\bar{1}1\}$  XRD pole figure of the annealed sample. The sixfold symmetry about the surface normal is indicated. No rotational domain of ZnO (0001) exists in ZnO film.

Figure 4.7 shows the PL spectra of the as-grown and the annealed samples measured at 10 K. The as-grown sample shows a weak bound exciton emission at 3.360 eV and a very weak deep level emission at around 2.8 eV. The emission at 3.31 eV and its LO-phonon replica at 3.24 eV are peculiar to ZnO film grown on the Si (111) substrate. These emissions are probably due to an excitonic transition bound to the Si impurity and its LO-phonon replica. After annealing, PL characteristics are improved considerably. The bound exciton emission becomes dominant, and its peak intensity increases by a factor of ten. The full-width at half maximum (FWHM) of the bound exciton peak is lowered from 20 meV to 11 meV.

สถาบันวิทยบริการ  
จุฬาลงกรณ์มหาวิทยาลัย

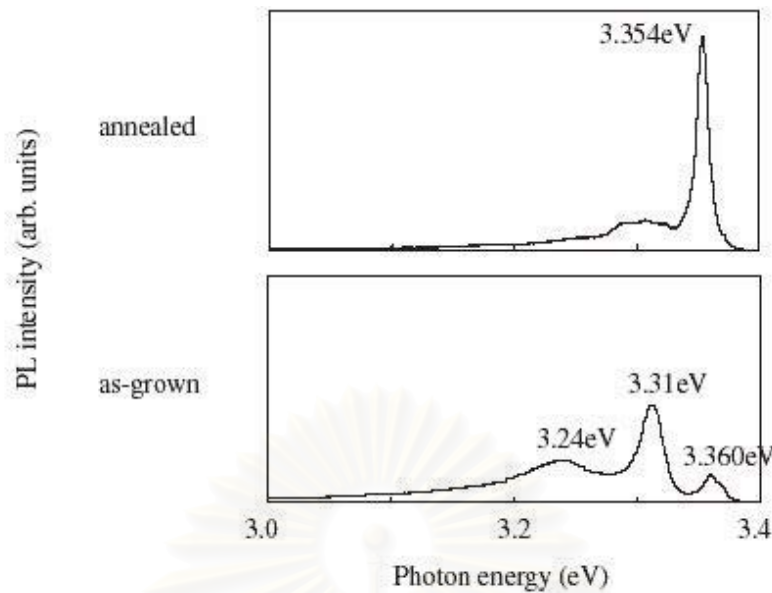


Figure 4.7 PL spectra of the as-grown and the annealed samples. The bound exciton emission becomes dominant after annealing. Its peak intensity increases by a factor of 10 upon annealing. The FWHM of the exciton peak changes from 20 meV to 11 meV after annealing.

#### 4.1.2 Initial Zn layer with oxygen plasma and LT-ZnO buffer layer

Even though an introduction of an initial Zn layer deposition followed by its oxidation is effective in hindering the oxidation of the Si substrate surface prior to the growth of ZnO by MBE using ozone as an oxygen source, there still remain some problems. Because of the low ozone concentration (2-3%), the growth rate is as low as 0.13  $\mu\text{m}/\text{h}$ . In addition, the ZnO layer is grown only at low substrate temperatures ( $\sim 200^\circ\text{C}$ ), which causes poor XRD characteristics. Then, the oxygen source is changed to oxygen plasma, which is more reactive than ozone. Therefore, the growth rate is expected to be higher, and the growth could be performed at high substrate temperature. The surface roughness of the initial layer, however, becomes more notable at high substrate temperature. To suppress this effect, Noriaki et al. proposes a low temperature (LT)-grown ZnO buffer layer applied before the growth of thick ZnO layers. The details is as the following

#### 4.1.2.1 Growth procedure

The preparation of the substrate prior to the insertion into the MBE chamber is the same as mentioned above of 4.1.1.1. After setting the substrate into the chamber, the temperature is increased to anneal at 750°C. After this surface cleaning process, the RHEED pattern showed a well-defined (7×7) reconstruction. Then, the substrate temperature is decreased to RT. An initial Zn layer is deposited at a Zn BEP of  $1 \times 10^{-7}$  Torr for 1 min. After the Zn deposition, oxygen is supplied to oxidize the initial Zn layer. At the same time, the substrate temperature is increased under oxygen supply. A 50 nm-thick LT ZnO buffer layer is grown at 350°C. The growth rate is 0.2  $\mu\text{m/h}$  with a Zn BEP of  $1 \times 10^{-6}$  Torr and an oxygen flow rate of 0.9 sccm. A 1  $\mu\text{m}$ -thick ZnO layer is then grown at 575°C. The growth rate is 0.5  $\mu\text{m/h}$  with a Zn BEP of  $3 \times 10^{-6}$  Torr and oxygen flow rate of 0.9 sccm.

#### 4.1.2.2 Experimental result

Since no ZnO growth occurs on the oxidized Si surface in the case of using ozone as an oxygen source, oxygen plasma is interesting because stable polycrystalline ZnO can be grown even on that oxidized one. Also, the crystallographic relationships among Si, Zn and ZnO grown using oxygen plasma are similar to those grown using ozone. Furthermore, the RHEED patterns during growth using oxygen plasma are similar to those using ozone. These indicate the favorable reactivity of oxygen plasma. In addition, oxygen plasma not only improves the growth rate of ZnO, but also makes the growth at high temperature possible.

The XRD result of a  $\phi$  scan for the (10 $\bar{1}$ 0) planes of the ZnO film grown using the initial Zn layer is shown in Figure 4.8. It clearly shows the sixfold symmetry about surface normal, indicating that no rotational domain of c-oriented ZnO exists. This sixfold symmetry is observed in samples with and without the LT ZnO buffer. A template may be formed by the oxidation of the initial Zn layer, which is useful in growing the epitaxial ZnO layer on Si substrates and suppresses the formation of rotational domains.

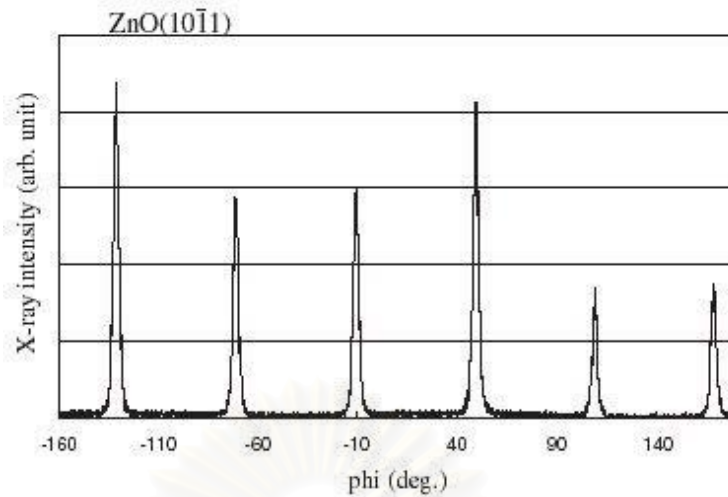


Figure 4.8 XRD result of a  $\phi$  scan of the (10 $\bar{1}$ 0) planes of the ZnO film with the initial Zn layer

The surface roughness of the oxidized initial Zn layer surface is shown in Figure 4.9. The RMS values estimated by AFM measurements are plotted as a function of growth temperature. While the substrate temperature increases, the RMS value of the oxidized initial Zn layer surface gradually increases owing to the larger grain size. However, at 575°C the surface roughness becomes very large. When an LT ZnO buffer is introduced, the surface roughness is considerably reduced and the grain size of ZnO decreases from 300 nm to 90 nm.

Figure 4.10 shows the rocking curves of the ZnO layers with and without the LT-ZnO buffer layer. The FWHM of the diffraction peak of ZnO (0002) is reduced from 0.94° to 0.23° by applying the LT-ZnO buffer layer. It may imply that the LT-ZnO layer reduces the mosaic structure of the epitaxial layers. Figure 4.11 shows the microscopic images of the films with and without the LT-ZnO layer. The straight cracks along the principal axes of the Si (111) surface, i.e., {1 $\bar{1}$ 0} directions, can be observed in the samples both with and without the LT-ZnO buffer layer, probably caused by the difference in thermal expansion coefficient between ZnO ( $475 \times 10^{-8} \text{ K}^{-1}$ ) and Si ( $256 \times 10^{-8} \text{ K}^{-1}$ ). The crack densities of the samples with and without LT-ZnO buffer layer are  $1.6 \times 10^2 \text{ cm}^{-1}$  and  $2.9 \times 10^2 \text{ cm}^{-1}$ , respectively. The ZnO films grown without the LT-ZnO buffer layer, however, tend to peel off along the cracks as shown in Figure 4.11(a). Furthermore, no crack is observed in polycrystalline ZnO films grown without initial Zn layers on Si substrates.

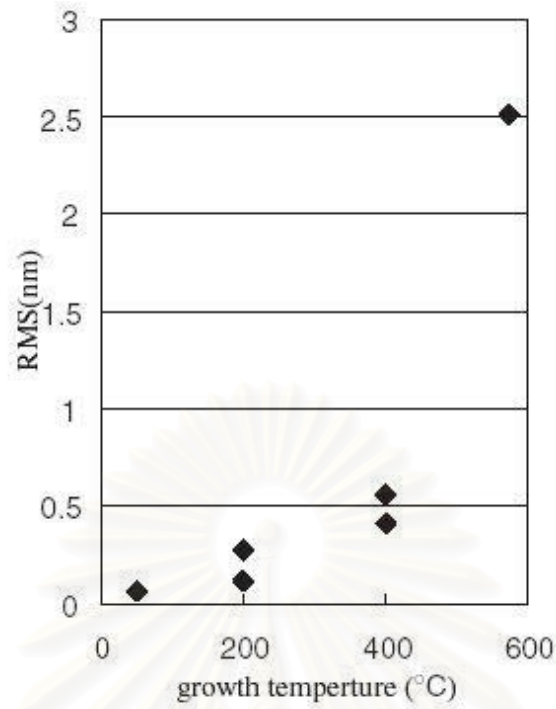


Figure 4.9 Surface roughness of oxidized initial Zn layer surface. The RMS values are plotted as a function of growth temperature.

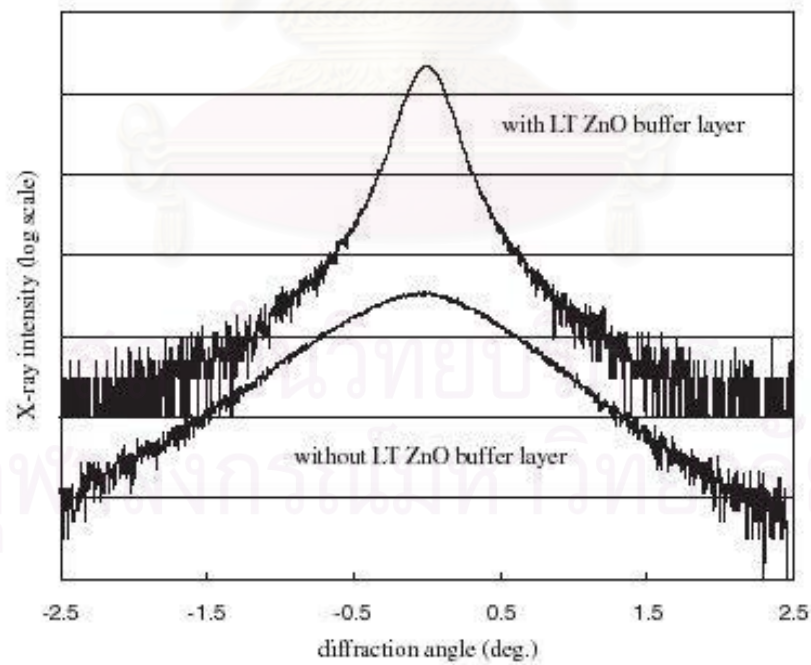
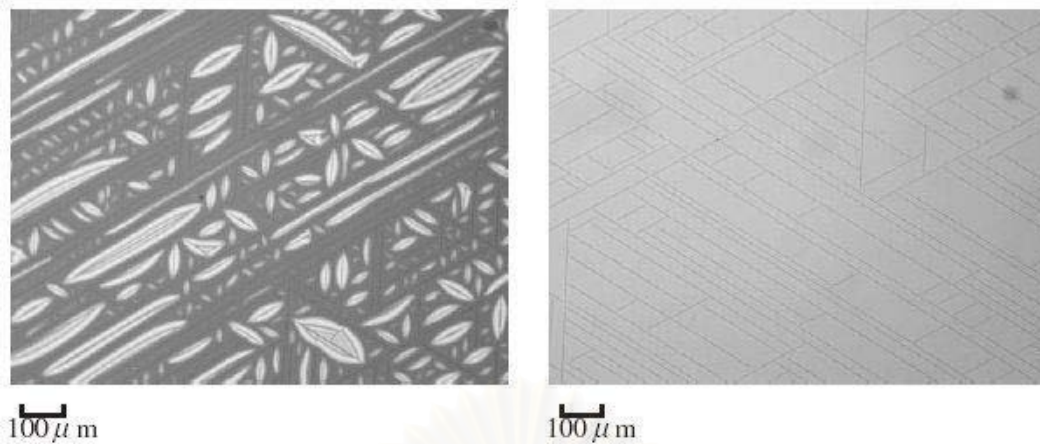


Figure 4.10 XRD rocking curves of the ZnO epitaxial layers with and without the LT-ZnO buffer layer.





(a) ZnO film without LT-ZnO buffer layer (b) ZnO film with LT-ZnO buffer layer

Figure 4.11 Microscopic images of the films with and without the LT-ZnO layer. Straight cracks along the principal axes of Si (111) surface can be clearly observed.

LT buffer layers have been generally applied for the highly mismatched heteroepitaxial layer growth to alleviate lattice strain and also act as a template for high temperature growth. In addition, the LT buffer layer is found to improve not only the crystal quality of subsequent ZnO layer, but also the surface morphology of the template. It also improves the adhesion of the ZnO epitaxial layer to the Si substrate, preventing the ZnO epitaxial layer from peeling off from the Si substrate.

Figure 4.12 shows the PL spectra of the ZnO films with and without the LT-ZnO buffer layer measured at 10 K. The film without the LT-ZnO buffer layer shows emissions at 3.317 eV and 3.28 eV, which are peculiar to ZnO films grown on the Si (111) substrate related to an excitonic transition bound to the Si impurity and its LO-phonon replica. A weak deep-level emission around 2.3 eV is also observed. The better PL characteristics can be observed in the samples with the LT-ZnO buffer layers. The neutral-donor-bound exciton emission at 3.365 eV becomes dominant and the PL peak intensity increases by a factor of 10. The FWHM is 6 meV. The weak deep-level emission almost disappears.

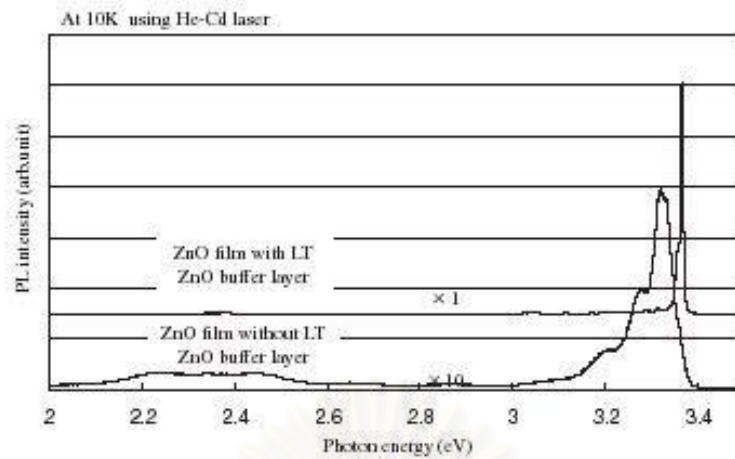


Figure 4.12 PL spectra of the ZnO film with and without the LT-ZnO buffer layer measured at 10 K.

### 4.1.3 MgO buffer layer

According to the useful initial Zn layer application both to protect the Si surface from being oxidized and to improve the crystal quality of a ZnO layer grown on it, the grown ZnO films suffer from high density of microcracks along the principal axes on the Si (111) surface probably caused by the difference in thermal expansion coefficients between ZnO and Si. Then, the effect of a thin MgO buffer layer deposited prior to the growth has been studied. This buffer layer is expected to alleviate the tensile strain imposed on the ZnO films. The improvement compared to the applied initial Zn layer method is obtained.

#### 4.1.3.1 Growth procedure

The preparation of the substrate prior to the insertion into the MBE chamber is the same as mentioned above of 4.1.1.1. After setting the substrate into the chamber, the temperature is increased to anneal at 750°C. After this surface cleaning process, the RHEED pattern showed a well-defined (7×7) reconstruction. Then, the substrate temperature is decreased to 350°C. The Si substrate is exposed to a Mg flux with a BEP of  $5 \times 10^{-7}$  Torr. After 2 min, oxygen gas supply is started at a flow rate of 0.9 sccm. This growth is continued until the grown MgO buffer layer thickness reaches approximately 20 nm. Then, 1- $\mu\text{m}$ -thick ZnO is grown at 575°C using Zn BEP of  $2 \times 10^{-6}$  Torr and an oxygen flow rate of 0.9 sccm. The growth rate of ZnO is

approximately 90 nm/min. The substrate temperature is reduced to RT at the rate of 6°C/min after growth, the same as the growth using the initial Zn layer.

#### 4.1.3.2 Experimental result

The RHEED patterns in the different stages of ZnO growth by using a thin MgO buffer layer are shown in Figure 4.13. After the surface cleaning process, a clear (7×7) pattern appears at 750°C as shown in Figure 4.13(a). While Mg is deposited on the Si (111) substrate, the RHEED pattern changes to a Si (1×6) pattern as shown in Figure 4.13(b). When MgO buffer layer growth start with supplying oxygen gas, a spotty pattern corresponding to MgO (1×1) with sixfold symmetry appears as shown in Figure 4.13(c). It implies that the grown MgO is (111)-oriented. The spotty pattern still remains during a whole ZnO growth. That means a ZnO (1×1) spotty pattern with sixfold symmetry as shown Figure 4.13(d).

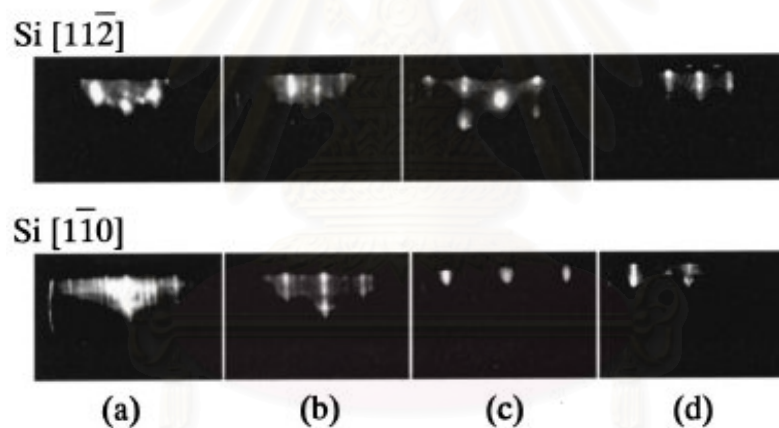


Figure 4.13 RHEED patterns along Si  $[11\bar{2}]$  and Si  $[1\bar{1}0]$  direction in different stages of ZnO growth by using a MgO buffer layer: (a) before growth, (b) a Mg evaporated surface, (c) a MgO buffer layer, and (d) a ZnO layer.

The RHEED patterns also show that both MgO and ZnO lattices are not rotated by 30° with respect to the Si surface, much improved compared to the applied initial Zn layer case. In other words, the  $[11\bar{2}0]$  direction of ZnO and the  $[11\bar{2}]$  direction of MgO are parallel to the  $[11\bar{2}]$  direction of the Si surface, and the  $[1000]$

direction of ZnO and  $[\bar{1}\bar{1}0]$  direction of MgO is parallel to the  $[\bar{1}\bar{1}0]$  direction of the Si surface.

Figure 4.14 show the microscopic images of the ZnO films grown by using the initial Zn layer and MgO buffer layer. For the initial Zn layer case, the straight cracks along the principal axes of the Si (111) surface, due to the difference of the thermal expansion coefficient between ZnO and Si as mentioned before, appear as shown in Figure 4.14(a). On the contrary, no cracks can be observed on the layers with a MgO buffer layer as shown in Figure 4.14(b). The thermal expansion coefficient of MgO is  $1040 \times 10^{-8} \text{ K}^{-1}$  at RT, which is larger than both Si and ZnO. Then, the insertion of MgO buffer layer may produce a compressive stress to the ZnO layer, alleviating the tensile strain from the Si substrate and the cracks on the ZnO surface considerably disappear.

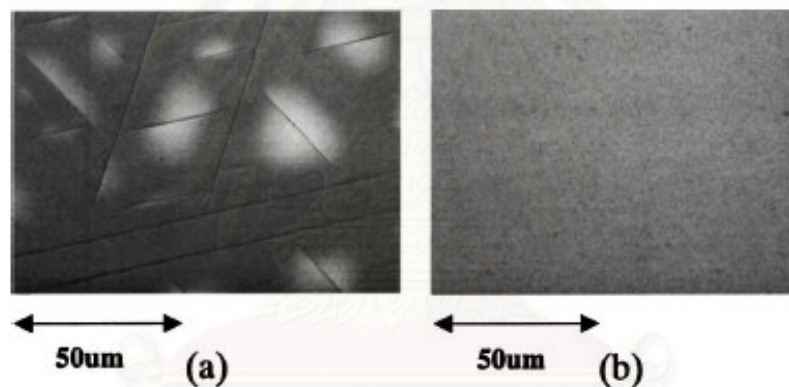


Figure 4.14 Microscopic images of the ZnO films grown by using (a) initial a Zn layer and (b) a MgO buffer layer.

The XRD  $2\theta$ - $\omega$  spectra of the ZnO (0002) peak with the initial Zn layer and with the MgO buffer layer are shown in Figure 4.15. The FWHM of the diffraction peak is improved when a MgO buffer layer is applied. The FWHM values of  $2\theta$ - $\omega$  and  $\omega$  scan, comparable to the ZnO films grown on sapphire substrates, are  $0.038^\circ$  and  $0.26^\circ$ , respectively. This indicates that the MgO buffer layer reduces the mosaic structure of the epitaxial layers.

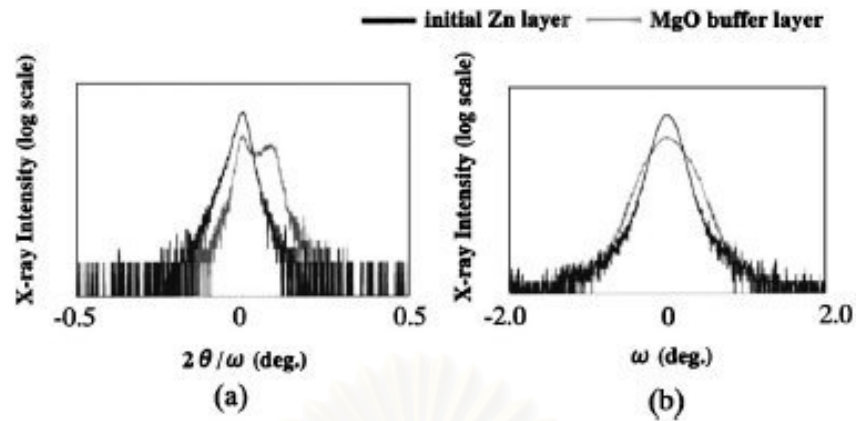


Figure 4.15 Comparison of ZnO (0002) XRD spectra for the samples grown by using an initial Zn layer and a MgO buffer layer (a)  $2\theta$ - $\omega$  scan spectra and (b)  $\omega$  scan spectra.

Figure 4.16 shows the PL spectra of the ZnO films grown with an initial Zn layer and with a MgO buffer layer. The measurement is carried out at 10 K. All samples show PL spectra due to bound excitons in the range of 3.35-3.37 eV and also near 3.31 eV. However, the PL intensity is improved by applying MgO buffer layer.

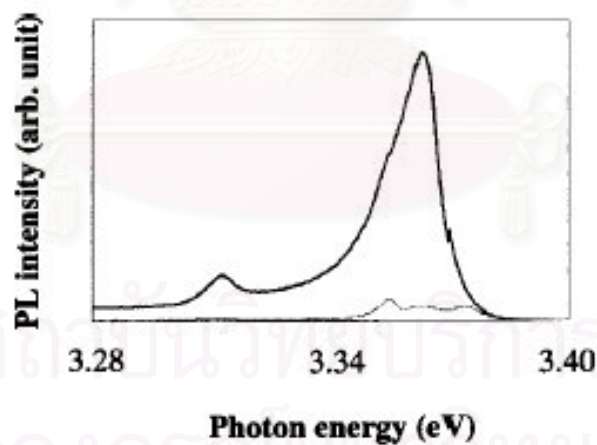


Figure 4.16 PL spectra of ZnO films grown by using an initial Zn layer and a MgO buffer layer.

## 4.2 ZnO film on sapphire substrate

Recently, wide band gap semiconductors including ZnO have been studied because of the applications in blue and UV optical device. Owing to the high exciton binding energy of ZnO, roughly three times higher than that of ZnSe and GaN, it is considered to be a promising material for novel exciton-related devices, such as low threshold optical devices. Then, high-quality ZnO films with p- as well as n-type conductivity are indispensable. However, there have been only a few reports on p-type ZnO. As-grown undoped ZnO epitaxial films normally exhibit strong n-type conductivity due to intrinsic defects such as interstitial Zn and oxygen vacancy. These lead to the difficulty to succeed low-resistivity p-type ZnO. Then, Tomohiko et al. proposes the method to reduce these defects in undoped ZnO films, which is the most crucial issue toward device applications.

### 4.2.1 Growth procedure

Epitaxial ZnO films are grown on Al<sub>2</sub>O<sub>3</sub> (0001) substrate by MBE with an oxygen source supplied from a radio-frequency-activated plasma cell (RF-MBE). In order to clean the substrate surface, the Al<sub>2</sub>O<sub>3</sub> substrate is first degreased in organic solution and etched in 3:1 of CH<sub>3</sub>OH:HF solution. Then, it is annealed at 800°C for 10 min in an ultrahigh-vacuum chamber, and exposed to an oxygen beam at 600°C for 10 min. After the cleaning surface, the substrate temperature is decreased to a growth temperature in the range of 315-575°C. The oxygen flow rate is fixed at 1.0 sccm with an RF power of 400 W. The Zn BEP is in the range of  $1.7 \times 10^{-6}$ - $6.0 \times 10^{-6}$  Torr. Thermal annealing after growth is performed in O<sub>2</sub> or N<sub>2</sub> atmosphere. The annealing temperature is varied between 600°C and 1000°C.

### 4.2.2 Experimental result

Figure 4.17 shows the growth rate of ZnO films as a function of Zn BEP at 575°C. With increasing Zn BEP, the growth rate first increases in proportion of BEP, called oxygen-enriched condition. Then, the growth rate deviates and finally

decreases at very high BEP. The sample grown at the high BEP of  $6 \times 10^{-6}$  Torr shows a rather rough surface.

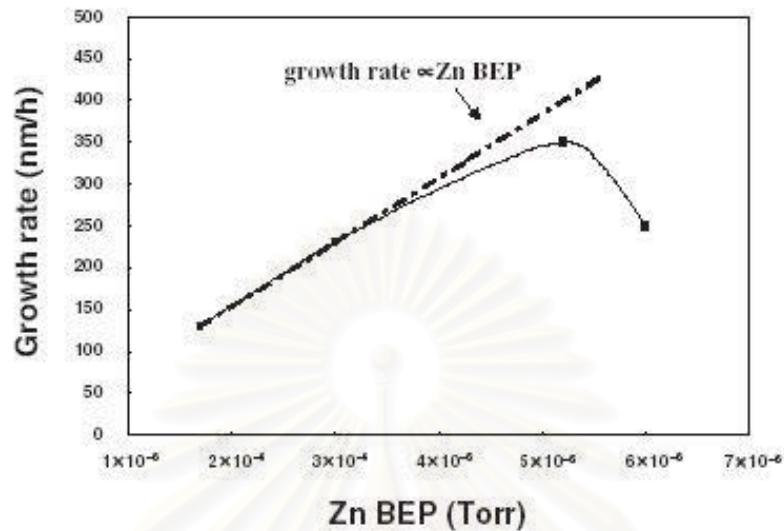


Figure 4.17 Growth rate as a function of Zn BEP for the samples grown at  $575^\circ\text{C}$ . The straight line indicates the linear relationship.

To investigate the purity of as-grown ZnO films, Auger electron spectroscopy (AES) and secondary ion mass spectroscopy measurements (SIMS) are carried out on the films grown at  $575^\circ\text{C}$ . The depth profiles of host and impurities measured by AES are shown in Figure 4.18. The Al signal in the layer is caused by noise in the AES spectrum. This result indicates that no impurity is present in high concentration. The depth profile measured by SIMS indicates that there are small amounts of Mg and Al as shown in Figure 4.19. Al contamination from the substrate is possible. However, the measured level is at the background level. Thus, the Al impurity may be ignored. On the other hand, Mg is also used to grow MgO and ZnMgO in the same MBE chamber. Therefore, Mg contamination is unavoidable. Although Mg produces no donors or acceptors in the lattice site, it may act as a donor in the interstitial site. However, the vapor pressure of Mg is much lower than that of Zn at any given temperature. It is tenable to assume that the Zn interstitial is more sensitive to temperature than Mg interstitial. Then, the intrinsic defects, Zn interstitial and O vacancy, are mainly considered.

The PL spectra of as-grown ZnO films vary according to the growth conditions. However, the free excitonic spectra at 3.376 eV with up to second-excited

states can be observed as shown in Figure 4.20. This implies the fairly good crystal-quality of as-grown films.

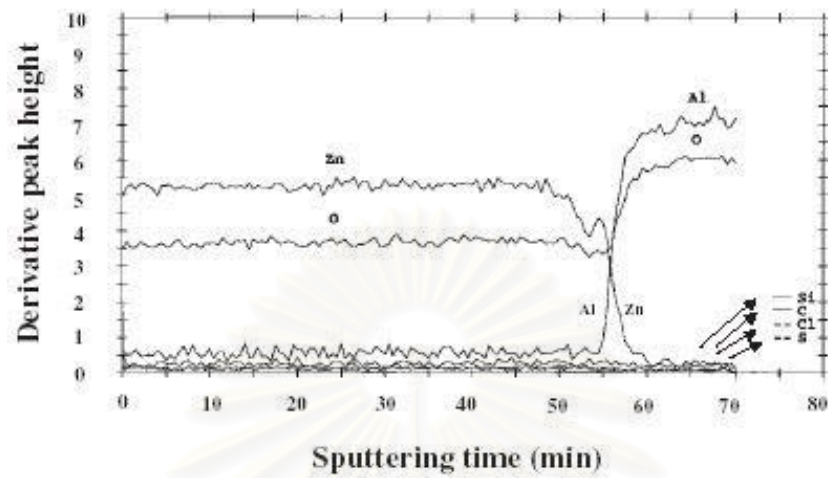


Figure 4.18 Depth profiles of Zn, O, and other impurities measured by AES. Al peak is caused by noise.

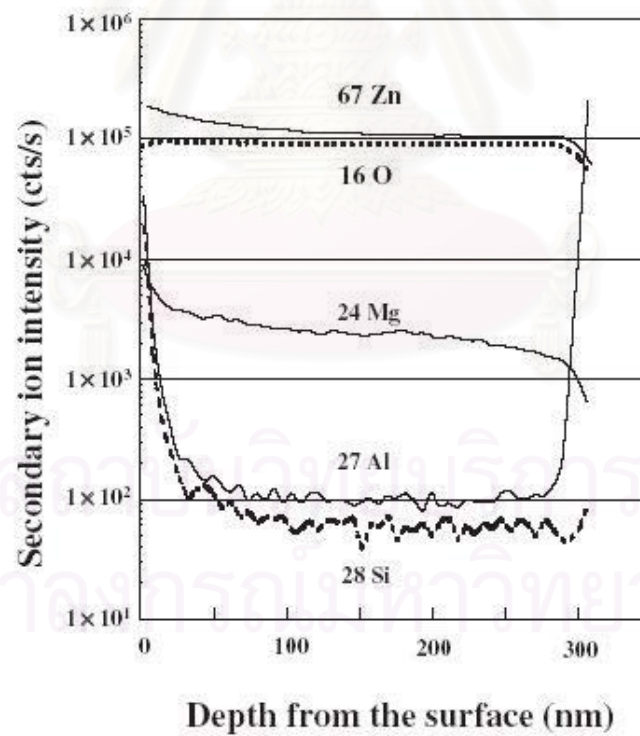


Figure 4.19 Depth profiles measured by SIMS. Both Al and Si in the layer are at the background level.



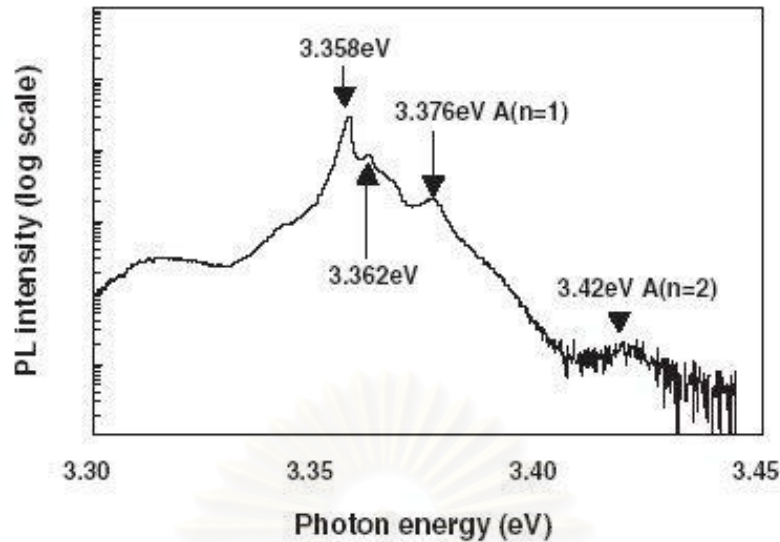


Figure 4.20 The typical PL spectrum of ZnO film measured at 10 K. The PL peaks at 3.358 eV and 3.362 eV are caused by the donor-bound excitons. Emissions due to free exciton and their second excited state are observed at 3.376 and 3.42 eV, respectively.

For the electrical characteristics, as-grown ZnO films exhibit n-type conductivity in the range of  $6.5 \times 10^{16}$ - $1.2 \times 10^{19}$   $\text{cm}^{-3}$ . The electron concentration is sensitive to postgrowth annealing under either  $\text{N}_2$  or  $\text{O}_2$  atmosphere. Figure 4.21 shows the variation of electron concentration as a function of the temperature in annealing for 5 min in  $\text{O}_2$  at atmospheric pressure. The electron concentration first decreases, but increases again when the annealing temperature exceeds  $800^\circ\text{C}$ . However, annealing at  $600^\circ\text{C}$  in  $\text{O}_2$  atmosphere makes the electron concentration lower. On the other hand, the opposite result is obtained when annealing is performed in  $\text{N}_2$  atmosphere. When the sample with an electron concentration of  $9.9 \times 10^{17}$   $\text{cm}^{-3}$  is annealed in  $\text{N}_2$  atmosphere at  $700^\circ\text{C}$  for 5 min, the electron concentration increases to  $6.0 \times 10^{18}$   $\text{cm}^{-3}$ . This sample is further annealed under two different conditions: in  $\text{N}_2$  and  $\text{O}_2$  atmosphere at  $600^\circ\text{C}$  for 5 min. The electron concentration increases slightly to  $6.6 \times 10^{18}$   $\text{cm}^{-3}$  when annealed in  $\text{N}_2$  atmosphere, while it decreases to  $5.3 \times 10^{18}$   $\text{cm}^{-3}$  when annealed in  $\text{O}_2$  atmosphere. Also, the electron concentration increases with annealing time when annealing is performed at  $1000^\circ\text{C}$  in  $\text{O}_2$  atmosphere.

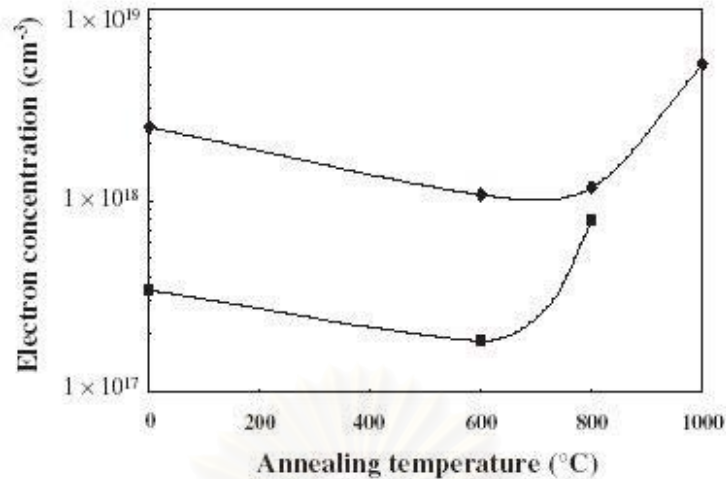


Figure 4.21 Electron concentrations as a function of annealing temperature when ZnO films are annealed in O<sub>2</sub> atmosphere (1 atm) for 5 min. The electron concentration is measured at room temperature.

Annealing is also performed in Ar atmosphere instead of N<sub>2</sub> for as-grown films. The results are similar to those obtained by annealing in N<sub>2</sub> atmosphere, which indicates that almost no reaction occurs between ZnO and N<sub>2</sub> ambient during annealing. Since the O vacancy acts as a donor, these results imply that thermal annealing in N<sub>2</sub> atmosphere increases O vacancy due to the evaporation of oxygen from ZnO films, and that annealing at 600°C in O<sub>2</sub> atmosphere decreases O vacancy. Annealing in O<sub>2</sub> atmosphere at 1000°C may also increase O vacancy, probably due to the fact that the oxygen pressure during annealing is too low to maintain the stoichiometric composition. In addition, no change is observed in the sample thickness and the XRD spectrum, even with 1000°C annealing as long as the annealing time is less than 10 min.

For the PL results, the typical near-band-edge spectra of as-grown samples with Zn BEP of  $1.7 \times 10^{-6}$  Torr are shown in Figure 4.22. The sample grown at 575°C shows an emission band peak at 3.358 eV, while the spectrum of the sample grown at 315°C is dominated by the emission at 3.362 and 3.323 eV including a weak shoulder near 3.358 eV. Since the intensities of the PL peak at 3.358 and 3.362 eV depend strongly on the growth temperature, the defects depending on these spectra are also sensitive to the temperature.

Figure 4.23 shows the PL spectrum of the sample grown at 315°C and those measured after thermal annealing in N<sub>2</sub> atmosphere at 700°C for 10 and 20 min.

Before annealing, the PL peak appears at 3.362 eV with a very weak intensity as shown in Figure 4.23. When the sample is annealed, the PL intensity dramatically increases, and the peak at 3.358 eV becomes more dominant than the original peak of 3.362 eV. This implies that thermal annealing in  $N_2$  atmosphere at  $700^\circ\text{C}$  increases the defects related to the emission at 3.358 eV. In contrast, the sample annealed in  $O_2$  atmosphere at  $600^\circ\text{C}$  for 5 min exhibits no peak at 3.358 eV. Instead, the PL intensity of 3.362 eV increases upon annealing as shown in Figure 4.24. Owing to the decrease of the electron density with  $O_2$  annealing at  $600^\circ\text{C}$ , it indicates that the emission at 3.358 eV may relate to the O vacancy.

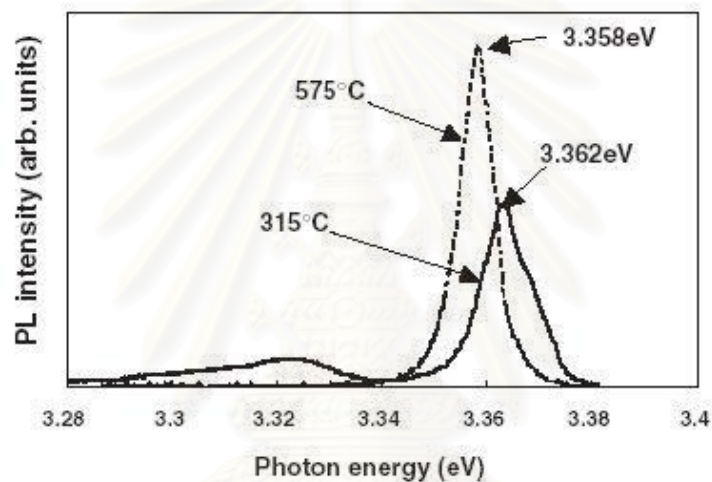


Figure 4.22 The typical PL spectra measured at 10 K for the samples grown at  $315^\circ\text{C}$  and  $575^\circ\text{C}$ .

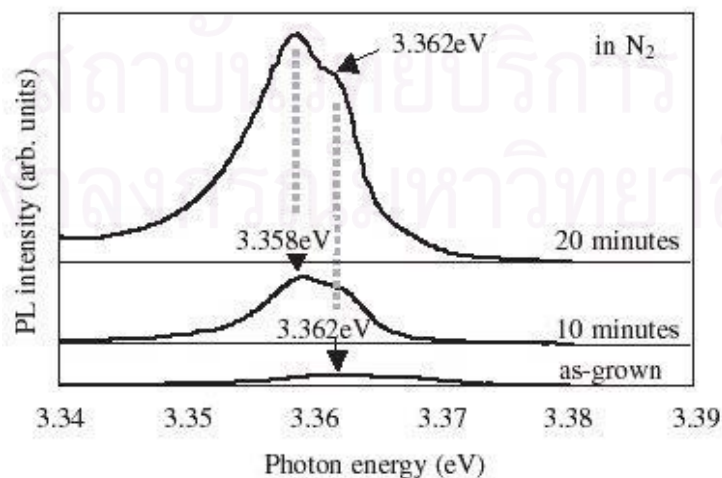


Figure 4.23 The PL spectra of the sample grown at  $315^\circ\text{C}$  and those measured after thermal annealing in  $N_2$  atmosphere at  $700^\circ\text{C}$  for 10 min and 20 min.

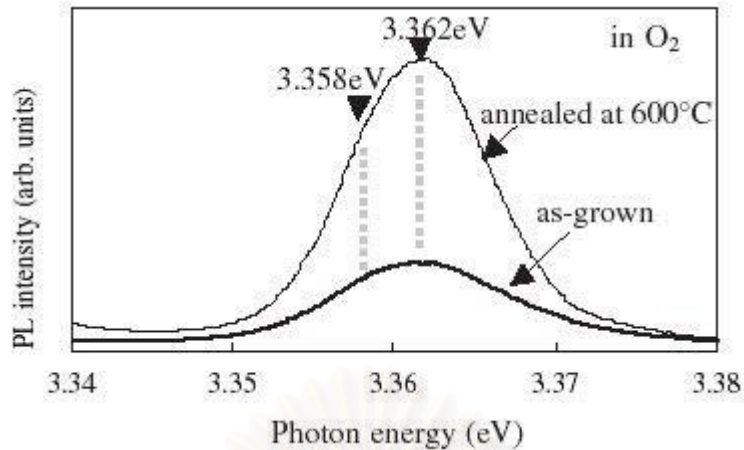


Figure 4.24 The PL spectra of the sample grown at 315°C, and that measured after thermal annealing in O<sub>2</sub> atmosphere at 600°C for 5 min.

The near-band-edge emission spectra of the ZnO film grown at 575°C and that annealed in O<sub>2</sub> atmosphere at 1000°C for 10 min are shown in Figure 4.25. The intensity of the peak at 3.358 eV increases dramatically upon annealing in O<sub>2</sub> atmosphere at 1000°C for 10 min.

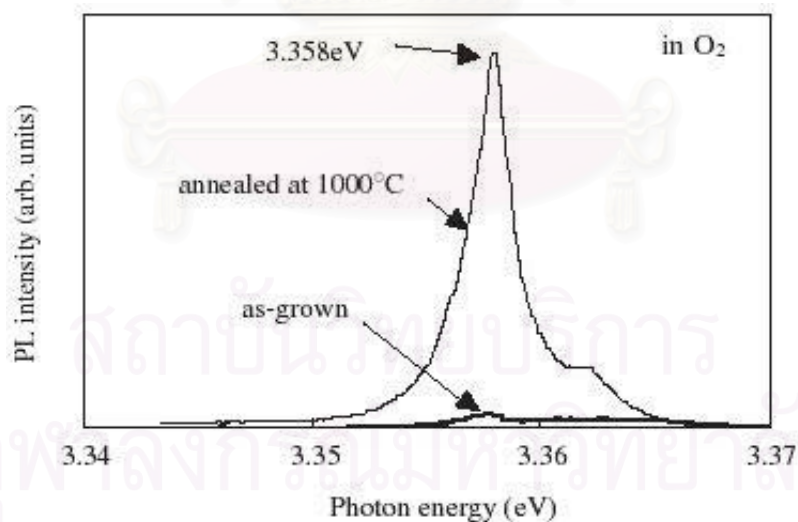


Figure 4.25 The PL spectra around band edge for as-grown and annealed samples. The annealing is performed in O<sub>2</sub> at 1000°C for 10 min.

The green-yellow emission band appears at around 2.3 eV in all the grown ZnO films. The intensity depends on the growth temperature. It increases when the growth temperature is lowered. The PL spectrum grown at 575°C is shown in

Figure 4.26. The intensity of this emission band drastically drops after annealing at 1000°C for 10 min. While the intensity of the emission peak at 3.358 eV increases with this annealing process as shown in Figure 4.25, the concentration of nonradiative recombination center probably decreases. On the other hand, the electron concentration increases with annealing time at 1000°C. Therefore, it can be referred that the 10 min of annealing at 1000°C in O<sub>2</sub> atmosphere reduces the defect centers due to the emission band around 2.3 eV, as well as nonradiative recombination center. Also, it makes the O vacancy increase. Furthermore, the defect centers related to the 2.3 eV emission cannot be caused by the O vacancy.

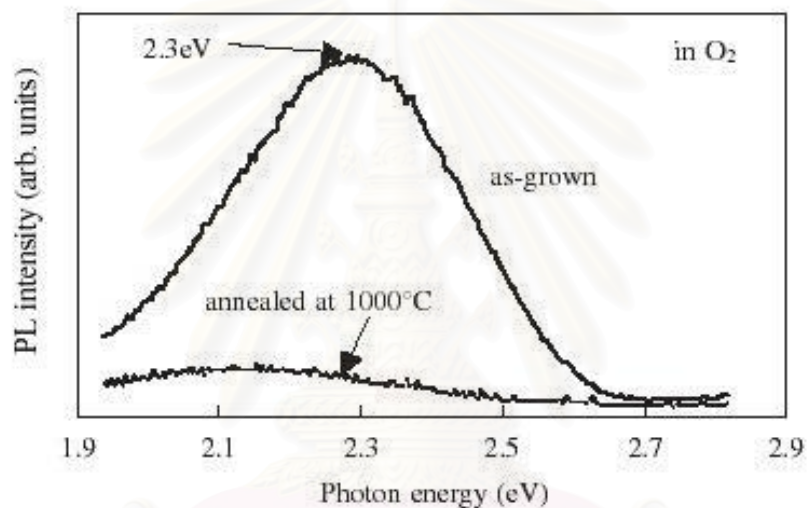


Figure 4.26 The PL spectra at around 2.3 eV for as-grown and annealed samples. The annealing is performed in O<sub>2</sub> at 1000°C for 10 min.

The ZnO films grown at 575°C are also annealed in N<sub>2</sub> atmosphere at 700°C for 5 min. The PL spectra at around 2.3 eV for as-grown and annealed samples are shown in Figure 4.27. The peak at around 2.3 eV almost disappears after annealing. The PL spectra at around 2.3 eV of ZnO films grown at 575°C under different Zn fluxes are shown in Figure 4.28. The PL intensity increases when the Zn flux intensity during growth increases. The sample with Zn BEP of  $5.2 \times 10^{-6}$  Torr may have more excess Zn atoms on the growing surface, compared to the sample with Zn BEP of  $1.7 \times 10^{-6}$  Torr. The PL intensity of the peak around 2.3 eV increases with Zn flux, also observed in the samples with the growth temperature of 435°C. This indicates that the PL emission at around 2.3 eV is probably related to the interstitial Zn.

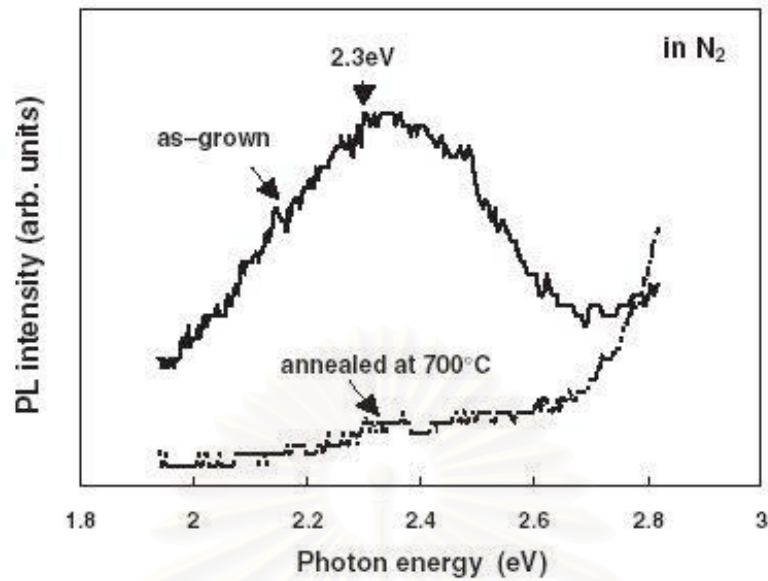


Figure 4.27 The PL spectra at around 2.3 eV for as-grown and annealed samples. The annealing is performed in  $N_2$  at  $700^\circ C$  for 5 min.

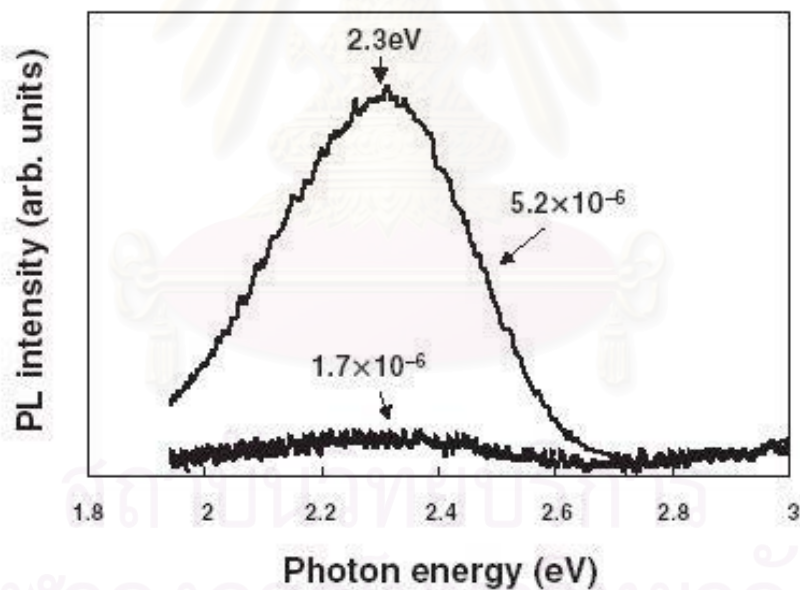


Figure 4.28 The PL spectra at around 2.3 eV for ZnO films grown at  $575^\circ C$  under different Zn fluxes.

As mentioned in this chapter that Si and  $Al_2O_3$  are good substrates for high quality ZnO film. However, in order to apply the ZnO optical devices into wide -area devices such as solar cells and TFTs, the previous mentioned substrates are not as good as glass in terms of cost and size with the commercial availability. Then, the

next chapter is provided the study of ZnO film deposited on amorphous glass substrate. The ZnO films grown on glass, however, suffer from high density of cracks because of the large mismatch in thermal expansion coefficients between ZnO and quartz glass.



สถาบันวิทยบริการ  
จุฬาลงกรณ์มหาวิทยาลัย

## CHAPTER V

### ZnO FILM ON GLASS SUBSTRATE

The experimental results on the ZnO growth on amorphous quartz glass substrate are shown in this chapter. By using RHEED observation, we can *in situ* monitor the crystal quality improvement of ZnO layer formation and by using optical microscopy, Field Emission-Scanning Electron Microscope (FE-SEM) and atomic force microscopy (AFM), the surface morphology after growth including the layer thickness can be investigated. The structural property of the samples can be characterized by X-ray diffraction measurement (XRD). The energy band gap can be estimated by absorption spectroscopy. Finally, with photoluminescence (PL) and Hall measurement, the optical and electrical properties of ZnO film can be investigated, respectively.

#### 5.1 Growth Parameter Optimization

According to the previous study, three main parameters during ZnO growth, which are composed of growth temperature, Zn flux and oxygen flow rate, that effect to the structural, optical and electrical properties of ZnO are optimized as the following.

##### 5.1.1 Growth Temperature

To reach the good crystal quality, ZnO layer has been grown by varying the growth temperature in order to seek the suitable heating condition. By *In-Situ* RHEED observation during growth, the sharp streaky pattern of ZnO grown on sapphire around 500°C is shown in Figure 5.1 (b). This pattern is clearer compared to the samples with higher and lower growth temperature as shown in Figure 5.1 (a) and (c). With other results such as surface morphology, structural and optical properties mentioned in the following sections, the growth temperature between 500 °C and



550 °C gives the better quality; however, there is no noticeable difference. Therefore, the growth temperature used in this work is around 530°C.

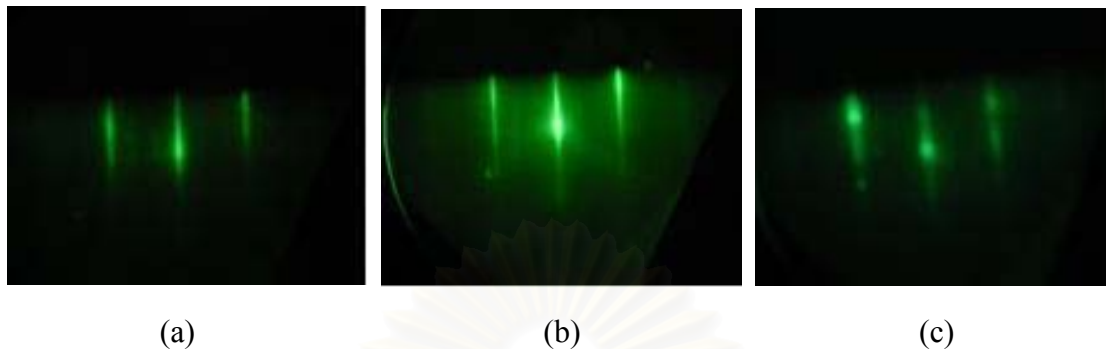


Figure 5.1 RHEED pattern of ZnO grown on sapphire (a) at 450°C (b) at 500°C (c) at 550°C.

### 5.1.2 Zn flux and Oxygen Quantity with Growth Rate

The big problems for the crystal quality of ZnO film are interstitial Zn and oxygen vacancy, which play important roles in the electrical property. Then, undoped and p-type ZnO are still a big problem to apply for the optoelectronic devices. The parameter, which directly effect is certainly Zn quantity. To control the growth mode, Zn-rich or O-rich mode, Zn Beam equivalent pressure (BEP) and oxygen volume are the main factor. In this research, oxygen volume is fixed. Then, only Zn flux is varied. In the case of Zn-rich condition, interstitial Zn easily happens whereas if oxygen quantity is too high, it is possible to have Zn vacancy. The suitable condition is a stoichiometric condition that the ratio of Zn and oxygen is nearly or equal to 1. The relation between ZnO growth rate on glass substrate and Zn BEP to decide the growth mode is shown in Figure 5.2. In the case of ZnO film grown on sapphire also show the similar result. The suitable Zn flux condition is around  $4.5 \times 10^{-6}$  Torr. Furthermore, the result of ZnO film on sapphire substrate with various Zn BEP due to some measurements also shows the improvement of the characteristic of the ZnO film around this region. The comparison of XRD and Hall measurement results, relating to the structural and electrical properties of ZnO film, are as shown in Figure 5.3 and 5.4, respectively. With the data as shown in Figure 5.3 due to the ZnO structural property, Zn BEP of  $4 \times 10^{-6}$  Torr offers the lowest FWHM compared to other positions,

implying the better orientation of the crystal structure. Furthermore, the quantities of Zn and oxygen impact directly to the electrical property of ZnO as mentioned above. Then, Hall mobility and carrier concentration are important to express the electrical property. As shown in Figure 5.4, Zn BEP of  $4 \times 10^{-6}$  Torr offers the highest Hall mobility and the lowest carrier concentration of undoped ZnO, however, the film still shows n-type conductivity. According to the results, the appropriate Zn BEP is around  $4 \times 10^{-6}$  Torr in a little O-rich growth mode. During the varying of Zn BEP, oxygen volume is kept constant at 1.07 sccm. It is not necessary to adjust oxygen quantity due to the match of Zn BEP at the fixed oxygen of 1.07 sccm. Therefore, Zn BEP and oxygen quantity in this work are kept constant at  $4 \times 10^{-6}$  Torr and 1.07 sccm, respectively.

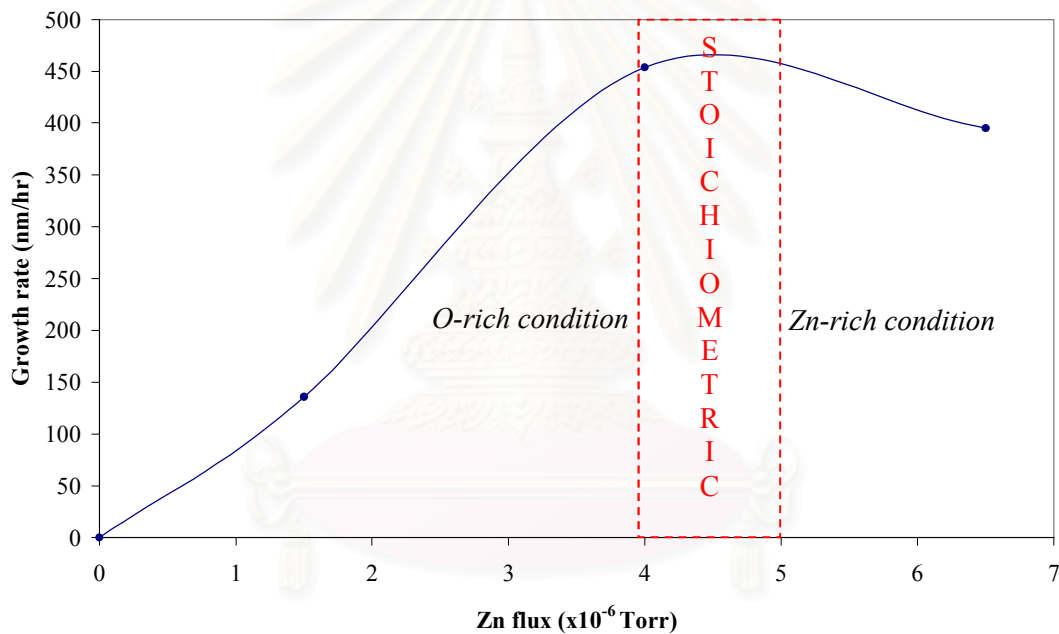


Figure 5.2 Relation between ZnO growth rate (nm/hr) on glass substrate and Zn BEP (Torr) with growth mode details.

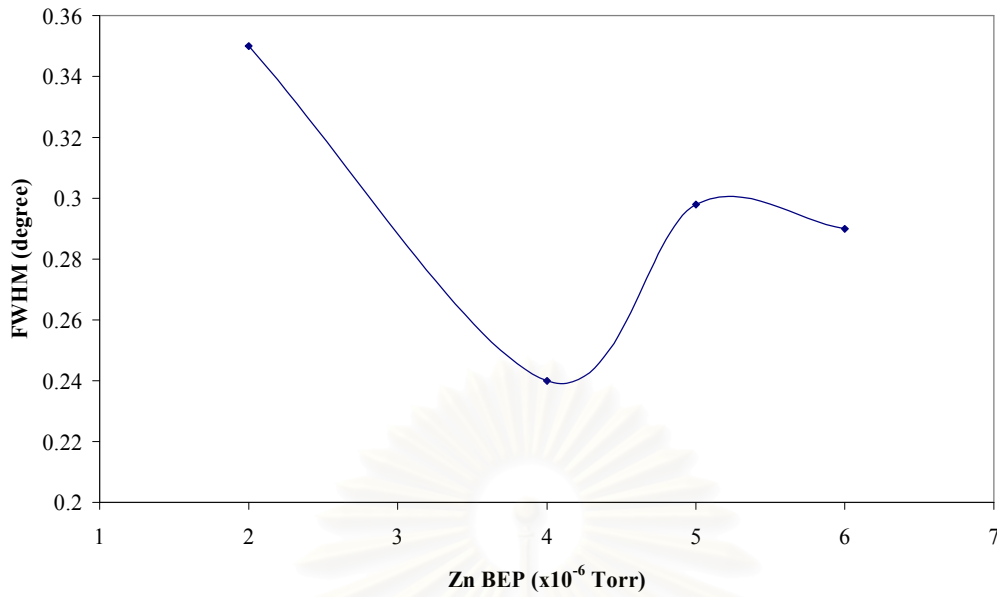


Figure 5.3 FWHM of ZnO film grown on sapphire substrate by XRD  $2\theta$ - $\omega$  scan with various Zn BEP.

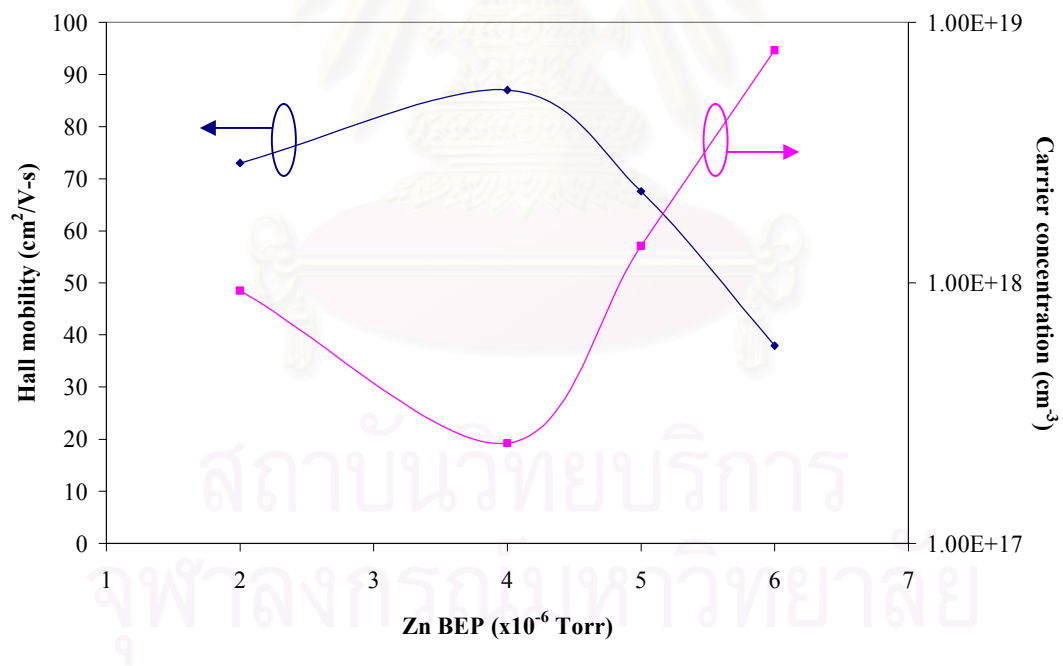


Figure 5.4 Hall mobility and Carrier concentration of ZnO film grown on sapphire substrate with various Zn BEP.

## 5.2 Growth Procedure

The detailed steps for sample preparation are as follows. First, a  $2 \times 2\text{-cm}^2$ -glass substrate surface is clean by chemical solution. The substrate is soaked in de-ion (DI) water, and then put in IPA and ethanol with ultrasonic for 10 min, respectively. The substrate is next soaked in DI water again. Finally, Nitrogen gas is blown to dry the substrate. The substrate is then mounted onto a molybdenum block by In attachment. Then, the substrate is inserted into the MBE chamber. Before growth, the sample is heated to decontaminate the substrate surface from water ( $\text{H}_2\text{O}$ ) at  $790^\circ\text{C}$  by pyrometer for 30 min. The RHEED pattern shows halo pattern due to amorphous substrate. After the desorption at  $790^\circ\text{C}$ , the substrate is cooled down to anneal at  $680^\circ\text{C}$  for 10 min in oxygen ambient with oxygen flow rate of 0.89 sccm for the oxygen polar before ramping down the substrate temperature to ZnO growth temperature of  $530^\circ\text{C}$ . Then, the approximately 800-nm ZnO layer is grown with the growth rate of 7 nm/min by applying oxygen plasma with oxygen flow rate of 1.07 sccm and Zn BEP of  $4.0 \times 10^{-6}$  Torr. The schematic of the sample structure grown in this work is shown in Figure 5.5.

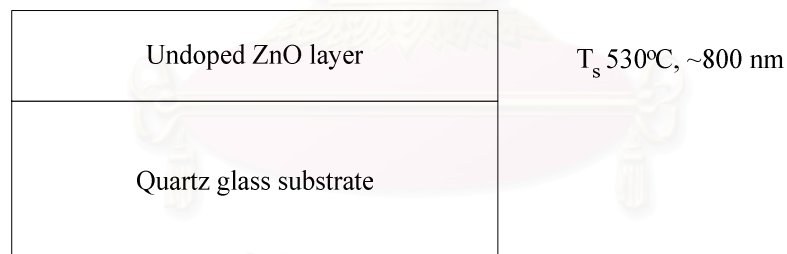


Figure 5.5 Schematic diagram of the sample structure grown in this work.

The growth conditions are given in the text.

### 5.3 *In Situ* RHEED Observation

RHEED patterns during the ZnO growth on amorphous glass substrate are shown in Figure 5.6(a), (b) and (c), respectively. Before ZnO growth, RHEED pattern shows halo pattern due to the amorphous substrate. Then, the halo keeps remaining around the very beginning of ZnO growth (around 10 nm), which implies the amorphous structure of the beginning ZnO layer. However, RHEED pattern develops to ring pattern and finally fixed spotty pattern. That means the crystal quality changes from amorphous to polycrystalline. During the growth of ZnO layer, the intensity signal gradually increases. Anyway, no significant difference of the intensity can be observed.

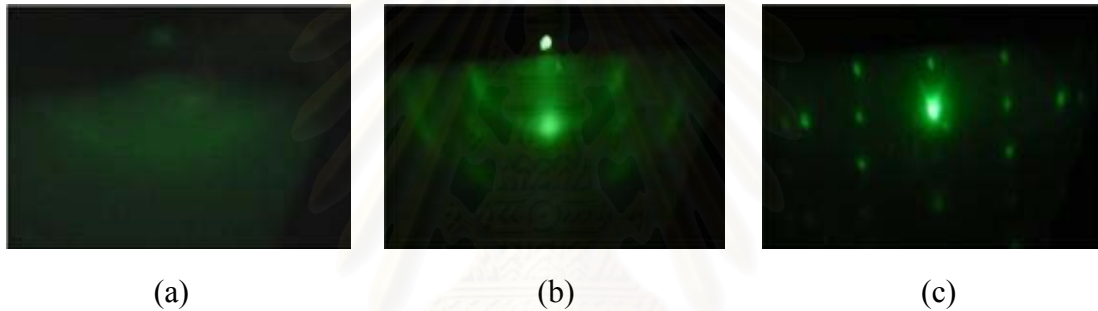


Figure 5.6 (a) RHEED pattern before ZnO growth (halo pattern),  
(b) RHEED pattern after 10-nm ZnO growth (ring pattern),  
(c) RHEED pattern after 800-nm ZnO growth (fixed-spotty pattern).

## 5.4 Surface Morphology

After *In Situ* observation by RHEED during growth, surface morphology of samples is observed by optical microscopy as shown in Figure 5.7. A high density of cracks can be easily observed. Regardless of the substrate temperature as well as the ramp rate of the substrate temperature after growth, surface cracks still appear. The origin of surface crack problem is the difference in the thermal expansion coefficients between ZnO ( $4.75 \times 10^{-6} \text{ K}^{-1}$ ) and quartz substrate ( $5.5 \times 10^{-7} \text{ K}^{-1}$ ). Tensile strain from the substrate affects the ZnO layer while the substrate is cooled down to room temperature after growth, which results in the formation of cracks as occur in the same condition of Si substrate ( $2.56 \times 10^{-6} \text{ K}^{-1}$ ). Therefore, the buffer layer seems to be one of the good method to alleviate this crack problem, which the details will be mentioned in chapter 5.

Furthermore, the surface of the sample and also the thickness are investigated by FE-SEM. The messy surface cracks can also be clearly observed as shown in Figure 5.8. Also, AFM is used to characterize the important data of the surface such as the RMS as shown in Figure 5.9 (a) and (b). The RMS value of ZnO film is 15.905 nm. The smaller RMS value, the better film surface is. For ZnO on other crystalline substrate such as sapphire ( $\text{Al}_2\text{O}_3$ ) and silicon (Si), the RMS value is less than 10 nm. However, because the interface ZnO layer is amorphous, the tendency of the poorer surface quality of ZnO on glass substrate is higher than those of the crystalline substrate. To improve the morphology, the growth mechanism have to be managed by, as mentioned in the previous paragraph, the buffer layer.

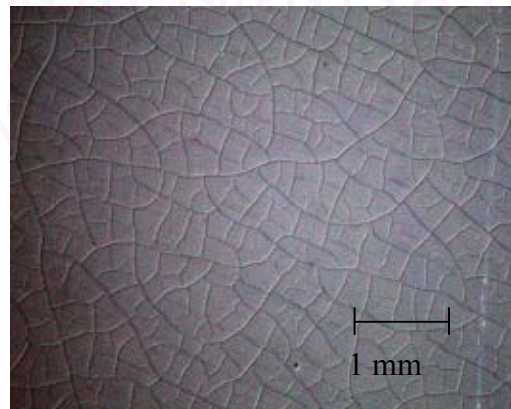


Figure 5.7 Surface morphology of undoped ZnO film grown on glass substrate without buffer layer.

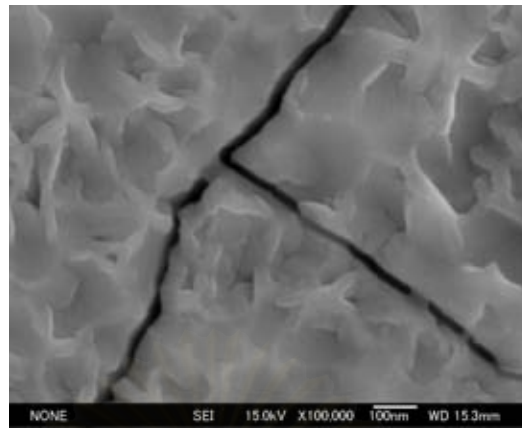
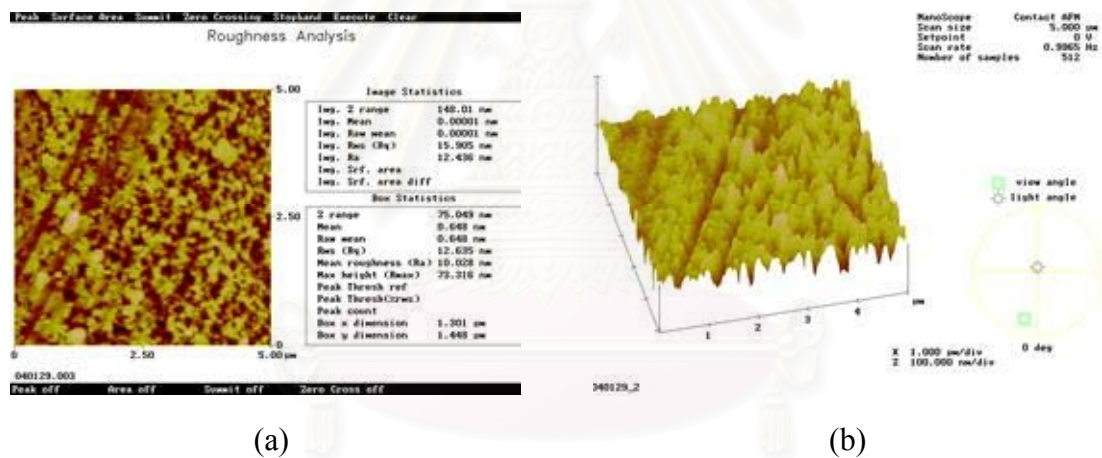


Figure 5.8 Surface investigation by FE-SEM.



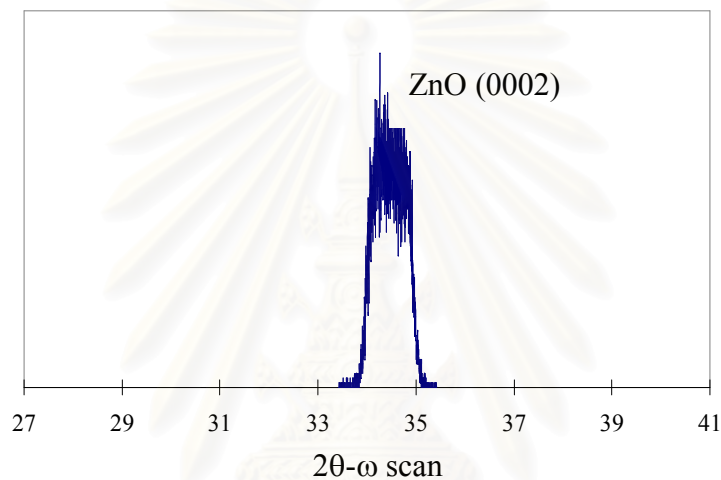
(a)

(b)

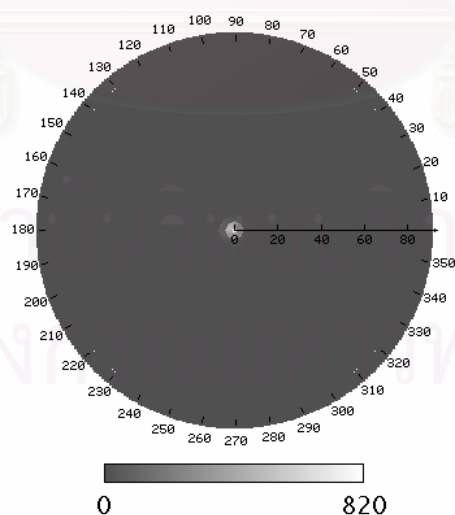
Figure 5.9  $5 \times 5 \mu\text{m}^2$  AFM images of undoped ZnO surface. (a) Surface roughness analysis (b) 3D image.

## 5.5 Structural Property

The crystal orientation of the as-grown films can be investigated using  $2\theta$ - $\omega$  scan and pole figure of XRD. The results are shown in Figure 5.10 (a) and (b). The ZnO (0002) peak at 34.42 degree appears in Figure 5.10 (a) indicating the c-orientation ZnO. Whereas Figure 5.10 (b) indicates the structure of the ZnO film with the grains having the same crystallographic axis (0002) parallel to the substrate surface normal, but having random rotational orientations about that axis.



(a)



(b)

Figure 5.10 (a) XRD spectral:  $2\theta$ - $\omega$  scan of ZnO film without buffer layer (b) XRD spectral: pole figure of ZnO film without buffer layer.



## 5.6 Optical Property

The interest of ZnO recently increases because of the outstanding optical property. Then, this characteristic is very important for the optoelectronic application. In this work, the optical property of ZnO film is measured by Absorption spectrometry and typical near-band-edge PL measurement.

To investigate the band gap of ZnO film at room temperature, the measurement method is as explained in the last chapter. The estimated band gap energy at room temperature of undoped ZnO grown on glass substrate is 3.209 eV as shown in Figure 5.11. This measurement is also necessary to observe the tensile-compressive strain within the film due to the different structural property between ZnO film and glass substrate. The details will be provided in the chapter 6.

Furthermore, the emission property is observed. The PL spectral response is shown in Figure 5.12. The emission lines located around 3.358 eV and 3.368 eV dominate the spectrum. The emission peaks at 3.358 eV and 3.368 eV are donor-bound exciton related to the oxygen vacancy and ionized donor-bound exciton, respectively. A shoulder peak at 3.375 eV is attributed to the free exciton emission with A-valence band. The lattice mismatch-induced inhomogeneous strain distribution results in a Stokes shift of  $< 5$  meV. However, the PL intensity of ZnO film grown on glass substrate is much lower than (0.01 time) that grown on sapphire and Si substrates. This is probably caused by ZnO crystal quality. The crystal quality of ZnO film grown on amorphous glass substrate is worse than those on single crystal substrate. To improve this optical property, the crystal quality including the reduction of the carrier trap should be decreased. To increase the thickness of the ZnO film may be a good idea to improve the crystal quality due to the strain relaxation. In this work, even though the ZnO film thickness is thicker ( $\sim 1$   $\mu\text{m}$ ), the PL intensity does not obviously improve. The emission peak and other results are similar to the thinner ZnO one. Then, to grow thicker ZnO film may be not a good idea to improve the film quality.

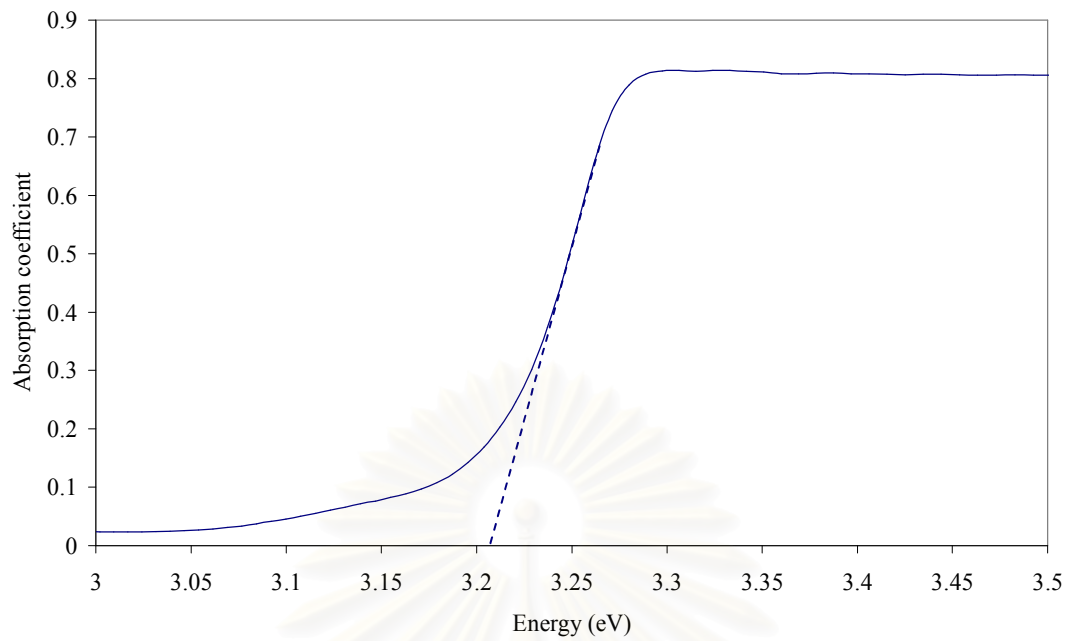


Figure 5.11 Energy band gap estimation measured at room temperature of undoped ZnO film grown on glass substrate.

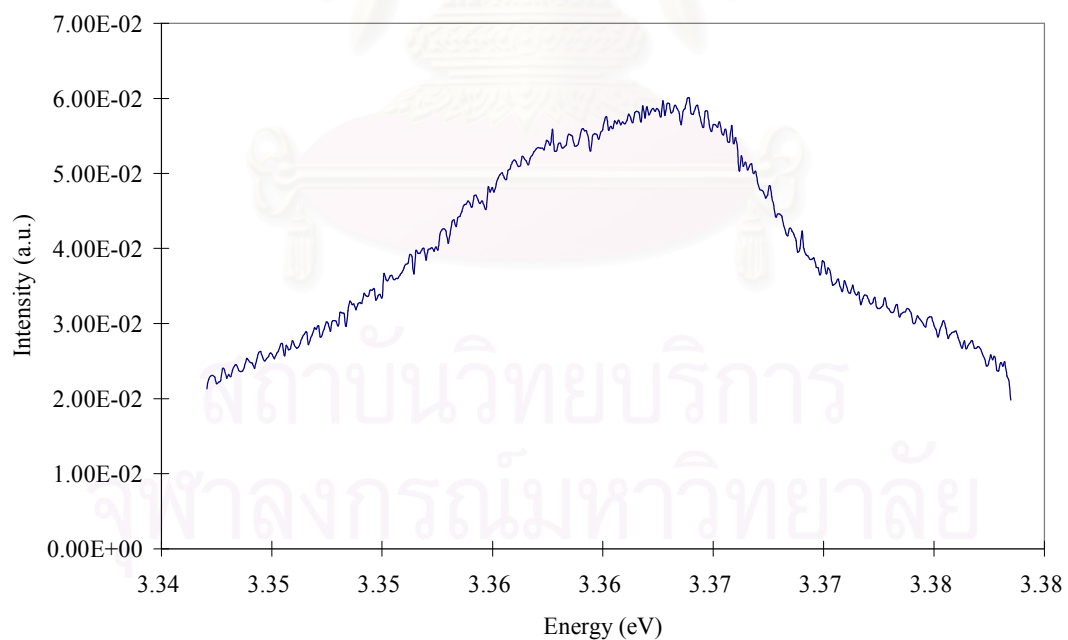


Figure 5.12 PL spectral response measured at 10 K of undoped ZnO film grown on glass substrate.

### 5.7 Electrical Property

Due to a high density of cracks clearly observed as shown in Section 5.4, the carrier concentration and Hall mobility cannot be observed because applied current cannot flow between poles via van der Pauw method. To investigate the characteristics including device application, this crack problem has to be solved.



สถาบันวิทยบริการ  
จุฬาลงกรณ์มหาวิทยาลัย

## 5.8 Nitrogen Doped Effect

According to a promising material for optoelectronic applications in the blue and ultraviolet regions, both n-type and p-type ZnO are very important to achieve this purpose. For ZnO, n-type conductivity is relatively easy to realize via excess Zn or with Al, Ga or In doping. However, with respect to p-type doping, ZnO displays significant resistance to the formation of shallow acceptor levels. Difficulty in achieving bipolar (n- and p-type) doping in a wide band gap material is not unusual.

The most promising dopants for p-type ZnO are the group-V elements, although theory suggests some difficulty in achieving shallow acceptor states. There have been several reports suggesting acceptor doping levels with group-V substitution. Most efforts on p-type doping of ZnO have focused on nitrogen doping. Therefore, we have studied the nitrogen doped effect due to the reason mentioned above. However, the investigated results with varying nitrogen gas show no sign of p-type ZnO. The details will be shown later. Anyway, a high density of cracks disappears. Then, we can solve the surface crack problem by this method. Also, the quality of ZnO film had better be improved. However, only crack problem can be arranged. The other properties show no significant difference as the following results.

### 5.8.1 Growth Procedure

All the growth parameters are kept the same as the case of undoped ZnO film grown on glass substrate excluding nitrogen quantity. Nitrogen plasma is generated and applied only during ZnO film growth. The quantity of nitrogen gas is also controlled by MFC, as that of oxygen, and varied from 0.1 to 0.5 sccm. The ZnO growth procedure, such as annealing process including cooling process, is also the same as explained in 5.2. The only different process is ZnO layer growth process. Before N-doped ZnO film growth, N<sub>2</sub> and O<sub>2</sub> gas are mixed and flow into the RF cell to generate N-plasma and O-plasma.

### 5.8.2 *In Situ* RHEED Observation

RHEED patterns during the N-doped ZnO growth with 0.1 sccm N<sub>2</sub> on amorphous glass substrate are shown in Figure 5.13 (a), (b) and (c), respectively. Before ZnO growth, RHEED pattern shows certainly halo pattern due to the amorphous substrate. Then, the halo keeps remaining around the very beginning of ZnO growth, which implies the amorphous structure of the beginning ZnO layer. However, RHEED pattern develops to ring pattern and finally fixed spotty pattern. That means the crystal quality changes from amorphous to polycrystalline. When nitrogen quantity increases, RHEED pattern changes. The samples with 0.1 and 0.3 sccm N<sub>2</sub> show similar improvement by RHEED observation, but the sample with 0.5 sccm N<sub>2</sub> shows a little difference around the end of the ZnO growth. RHEED pattern of the sample with 0.1 sccm N<sub>2</sub> changes from halo to ring pattern around 10 nm of ZnO thickness, whereas those of the sample with 0.3 and 0.5 sccm N<sub>2</sub> change around 20 nm of ZnO thickness. Furthermore, the sample with 0.5 sccm N<sub>2</sub> still shows poor ring RHEED pattern at the end of 2-hour ZnO growth as shown in Figure 5.14 (a) and (b). Then, when N<sub>2</sub> quantity is too high, the crystal quality of the sample gets poorer. Even the sample with 0.5 sccm N<sub>2</sub> was grown longer to let the chance of RHEED development, the ring pattern still keeps a little improvement to ring-to spot pattern as shown in Figure 5.14 (c).

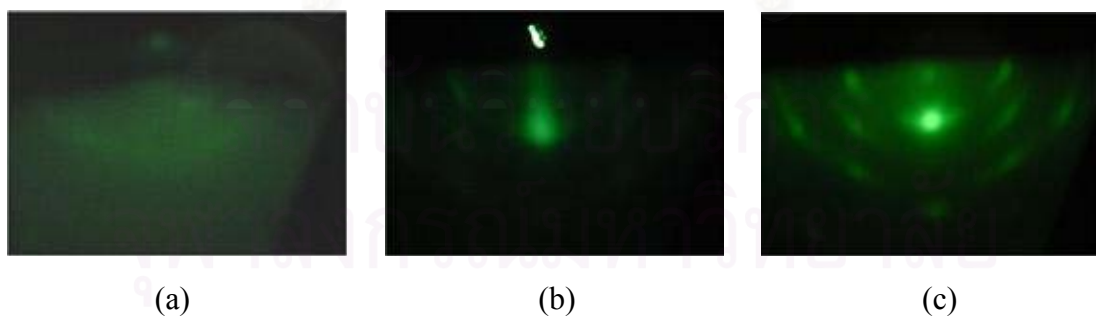


Figure 5.13 (a) RHEED pattern before ZnO with 0.1 sccm N<sub>2</sub> growth (hallo pattern),  
 (b) RHEED pattern after 10-nm ZnO growth (ring pattern),  
 (c) RHEED pattern after 600-nm ZnO growth (fixed-spotty pattern).

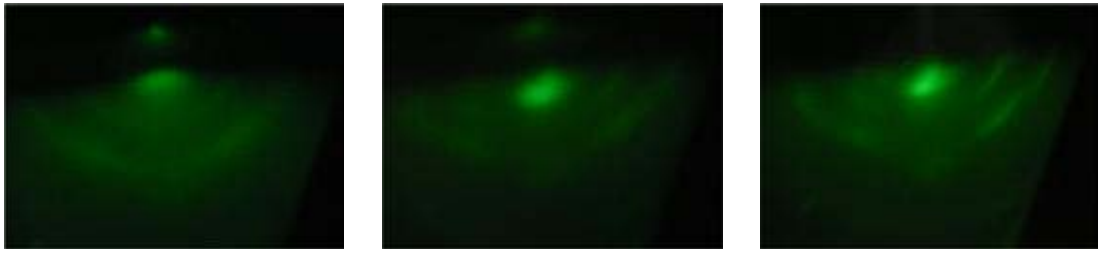


Figure 5.14 (a) RHEED pattern after 20-nm ZnO with 0.5 sccm N<sub>2</sub> growth (ring pattern),  
 (b) RHEED pattern after 600-nm ZnO growth (ring pattern),  
 (c) RHEED pattern after 900-nm ZnO growth (ring-to-spot pattern).

### 5.8.3 Surface Morphology

After ZnO growth, surface morphology of samples is observed by optical microscopy and FE-SEM. No cracks can be observed by both measurements. Surface morphology of the samples with 0, 0.3 and 0.5 sccm N<sub>2</sub> observed by FE-SEM is shown in Figure 5.15 (a), (b) and (c), respectively. The grain size decreases when N<sub>2</sub> quantity increases.

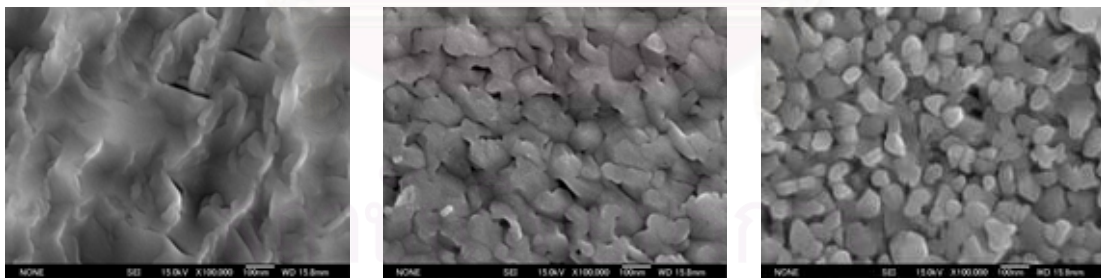


Figure 5.15 Surface morphology of ZnO film grown on glass substrate with N<sub>2</sub>  
 (a) 0 sccm (b) 0.3 sccm (c) 0.5 sccm.

Furthermore, the thickness of the sample is investigated by FE-SEM. Then, the growth rate of ZnO is shown in Figure 5.16. Due to the growth rate graph, ZnO growth rate reduces when N<sub>2</sub> quantity increases. N<sub>2</sub> might dilute the oxygen plasma not to bind with Zn flux and hinder ZnO growth instead of doping as expected,

however, we need some measurements to confirm that Nitrogen can be doped into ZnO layer, which the detail will be shown later.

AFM is used to characterize the important data of the surface such as the RMS. The RMS of the samples with N<sub>2</sub> doping is between 20 to 30 nm, higher value than ZnO without N<sub>2</sub>. There is no relation between N<sub>2</sub> quantity and RMS. Consequently, the surface morphology gets worse when N<sub>2</sub> is applied.

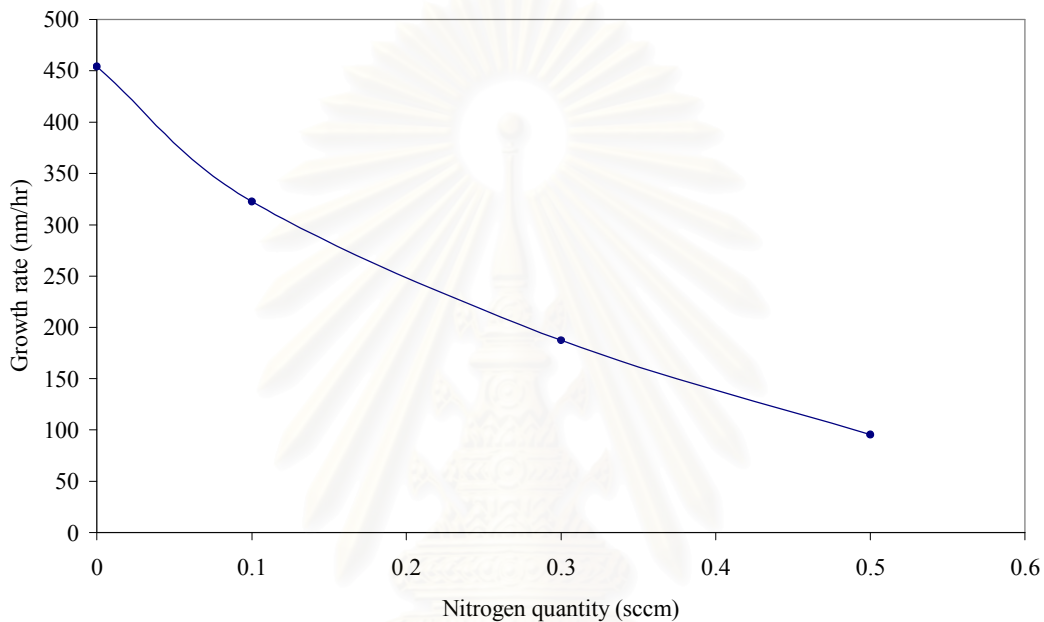


Figure 5.16 Growth rate of ZnO film grown on glass substrate with various N<sub>2</sub> quantities.

#### 5.8.4 Structural Property

The crystal orientation is investigated by 2 $\theta$ - $\omega$  scan of XRD. The results of ZnO films with 0, 0.1, 0.3 and 0.5 N<sub>2</sub> are shown in Figure 5.17. The ZnO (0002) peak at 34.42 degree appears in all samples also indicating the c-orientation ZnO. The highest intensity of (0002) peak was from the sample without nitrogen. The intensity of ZnO (0002) peak of XRD 2 $\theta$ - $\omega$  scan decreases when N<sub>2</sub> quantity increases as shown in Figure 5.18. The intensity of ZnO with 0.5 N<sub>2</sub> is a little lower compared to that of the sample with 0.3 sccm. Due to the result shown in Figure 5.18, when N<sub>2</sub>

quantity is more than 0.3 sccm, the intensity keeps almost constant. That means the structural quality of ZnO becomes worse when nitrogen increases.

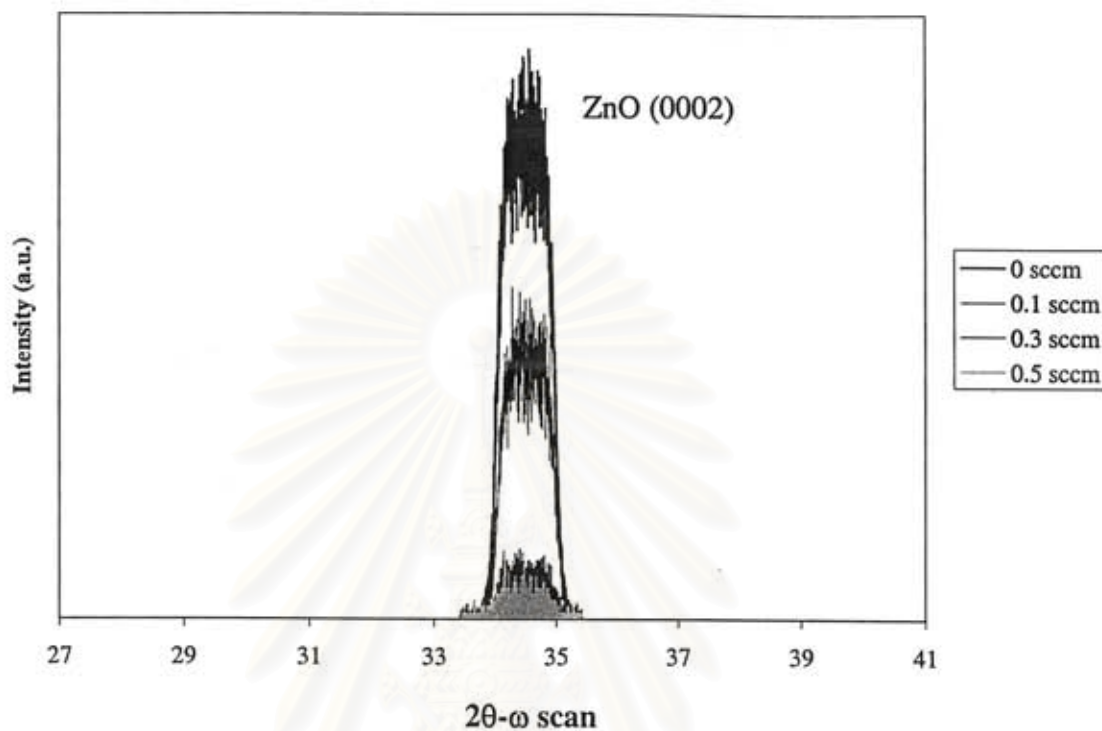


Figure 5.17 XRD  $2\theta$ - $\omega$  scan spectral response of ZnO film with  $N_2$  flow rate of 0, 0.1, 0.3 and 0.5 sccm.

Furthermore, the layer thickness of ZnO also decreases when  $N_2$  flow rate increases. Then, ZnO film with higher  $N_2$  volume cannot be improved compared to the film with lower  $N_2$  volume. If ZnO film with high  $N_2$  flow rate is grown longer, the structural property might get better, similar to RHEED result, as mentioned above. Anyway, the result is also similar to RHEED result, a little improvement can be observed. Therefore, this method may not be a good way to improve the surface morphology and the structural property of ZnO film.



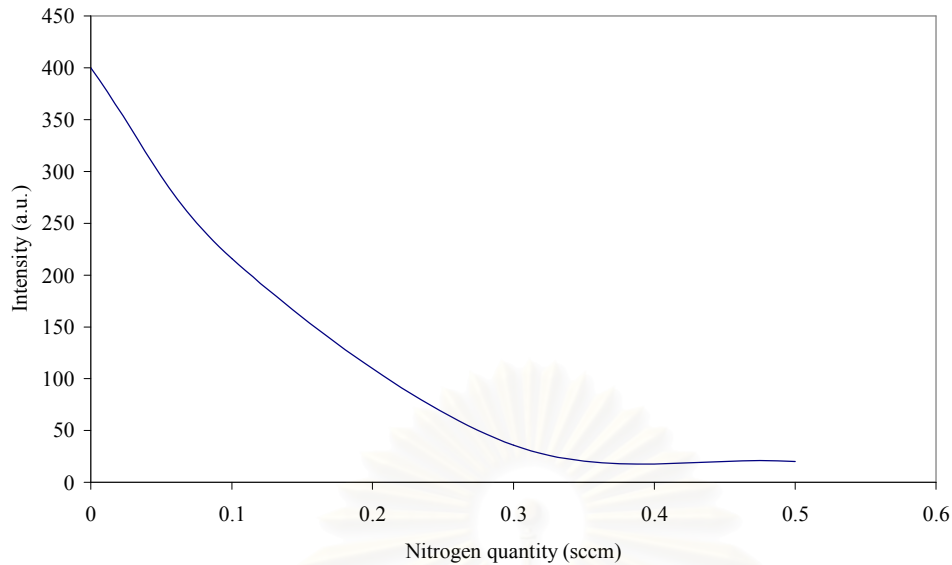


Figure 5.18 XRD  $2\theta$ - $\omega$  scan spectral response of ZnO film with  $N_2$  flow rate of 0, 0.1, 0.3 and 0.5 sccm.

### 5.8.5 Optical Property

The emission property is observed especially to investigate a shallow acceptor level due to the p-type ZnO requirement. The PL spectral response is shown in Figure 5.19 (a) and (b). The emission lines located around 3.358 eV and 3.368 eV dominate the spectrum, the same as ZnO without  $N_2$  doping, as shown in Figure 5.19 (a). The detail of both emission peaks at 3.358 eV and 3.368 eV are mentioned above. Anyway, a shoulder peak at 3.375 eV, related to the free exciton emission with A-valence band, cannot be observed. The PL spectral responses including the PL intensity of all the samples are pretty the same. There is no obviously change, implying no improvement of optical property of ZnO film even  $N_2$  is applied. Moreover, no new PL peak, expected to relate to the shallow acceptor level of nitrogen, cannot be investigated as shown in Figure 5.19 (b). This may imply that nitrogen might not be doped into ZnO film. To confirm about nitrogen impurity in ZnO film, another measurement is needed.

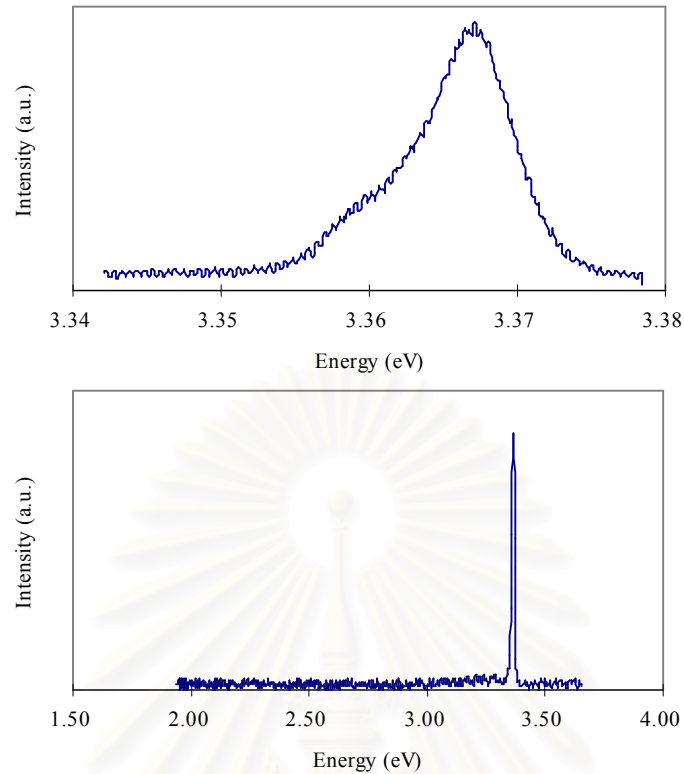


Figure 5.19 (a) PL spectral response around main peaks measured at 10 K of ZnO film with 0.3 sccm  $N_2$  grown on glass substrate (b) PL spectral response in wide range of the same sample measured at 10 K.

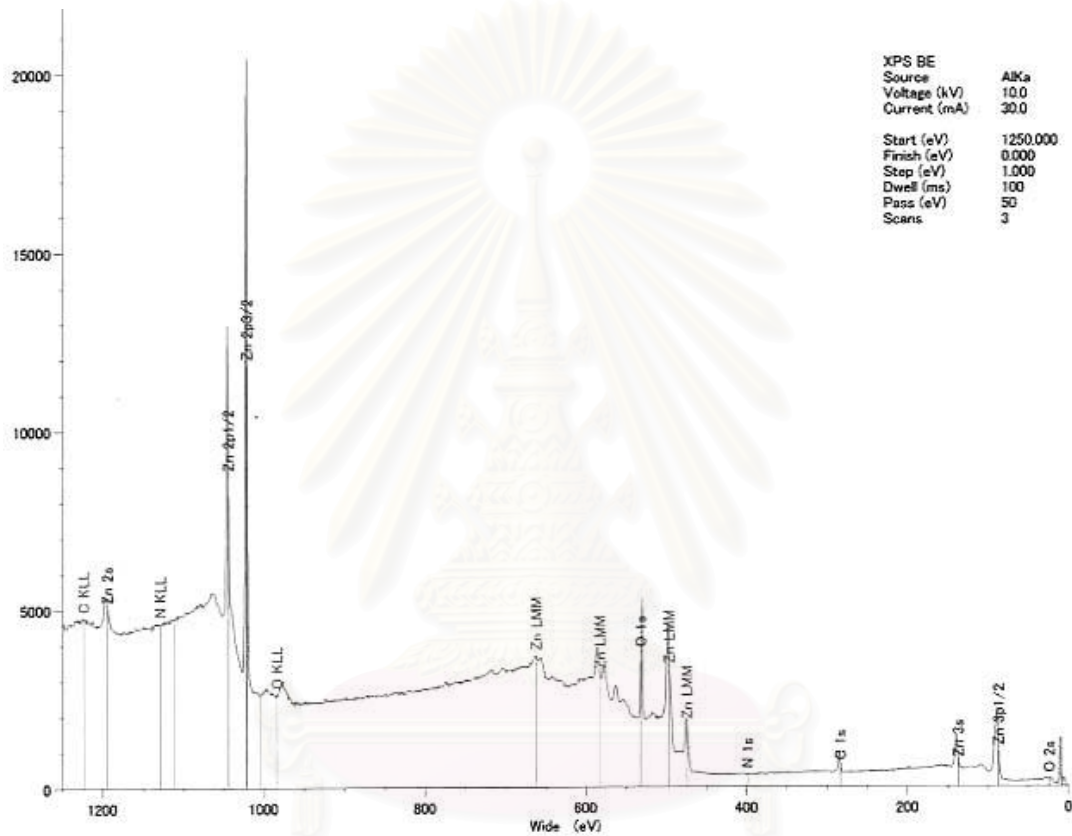
### 5.8.6 Impurity Measurement

According to p-type ZnO requirement, nitrogen is applied to be the shallow acceptor level in ZnO film. X-ray Photoelectron Spectroscopy (XPS) is one of the methods for impurity investigation. The samples with nitrogen doping are measured and the results are shown in Figure 5.20. No sign of nitrogen peak appears which means no nitrogen in ZnO film.

### 5.8.7 Electrical Property

Due to the samples without crack as mentioned above, the carrier concentration and Hall mobility of all samples with nitrogen adding can be

investigated via van der Pauw method. Due to XPS result, nitrogen cannot be doped into ZnO film. The electrical characteristics of all grown ZnO films in this condition exhibit n-type conductivity in the range of  $10^{17}$  and  $10^{18}$   $\text{cm}^{-3}$ . All these samples, however, show pretty low electron mobility ( $5 \text{ cm}^2/\text{V}\cdot\text{s}$ ). The observed resistivities are in the range of  $10^3$ - $10^5 \Omega\text{cm}$ .



(a)

สถาบันวิทยบริการ  
จุฬาลงกรณ์มหาวิทยาลัย

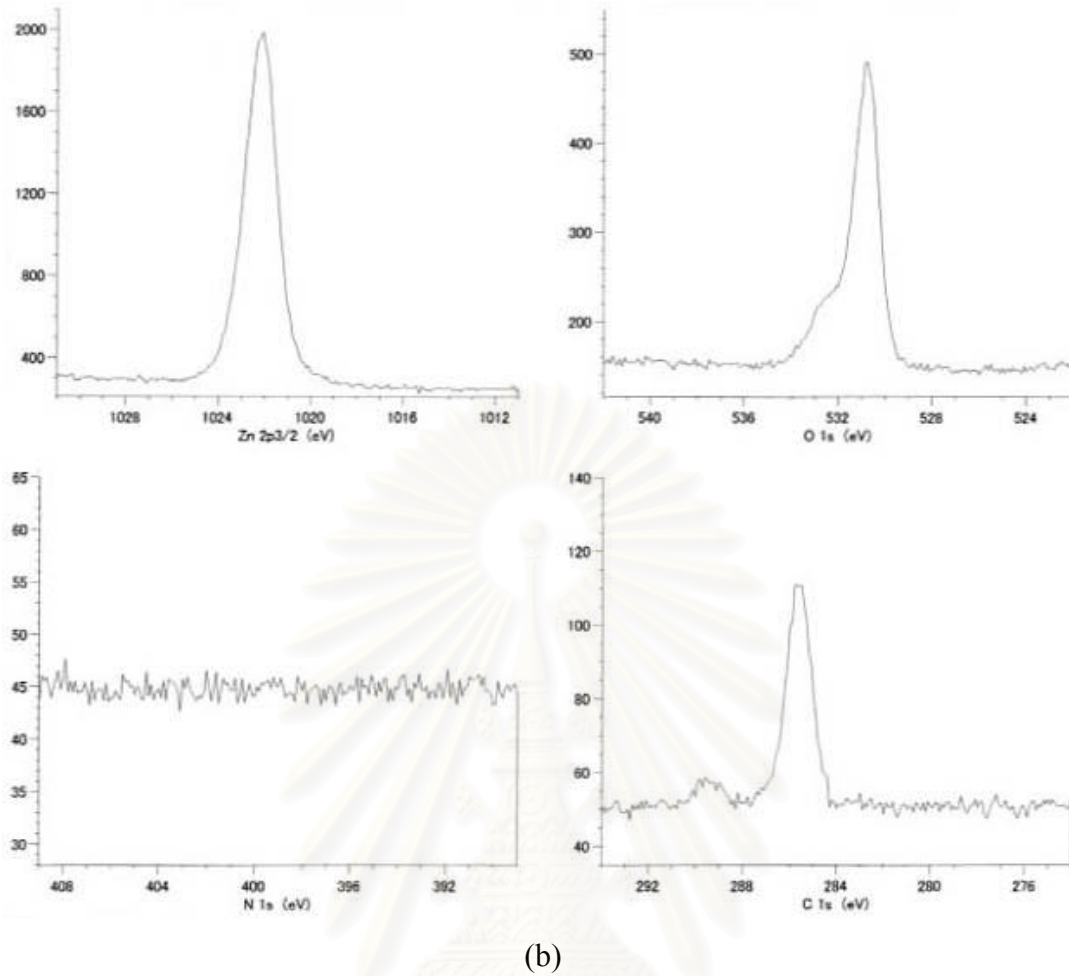


Figure 5.20 XPS result of ZnO film with 0.3 sccm applied nitrogen (a) all material in the film (b) Zn, O, N and C components.

Then, the next chapter provides another method, buffer layer application, that relieves the surface crack problem because of the ineffective method explained in this chapter, nitrogen doping. MgO buffer layer is proposed to make the improvement of the ZnO film grown on glass substrate.

## CHAPTER VI

### MgO BUFFER LAYER EFFECT

To handle the surface crack problem as mentioned in chapter 5, a method of an applied MgO buffer layer is presented in this chapter. ZnO films grown directly on glass substrates, however, result in a high density of cracks due to the thermal expansion coefficient mismatch between ZnO film and the quartz glass substrate as mentioned in Chapter 5. Therefore, a buffer layer between the ZnO layer and the glass substrate may be a possible method of preventing cracks. To select the proper buffer layer for this purpose, the buffer material should be from II-VI compounds to avoid impurity problems. Furthermore, the correct thermal expansion coefficient of the buffer layer is also necessary to solve this problem since it is the tensile strain from the glass substrate affecting the ZnO films that results in many cracks. The compressive stress of the ZnO film, a consequence of the buffer-layer insertion, must then balance this tensile strain in ZnO films. When the material selected for use as a buffer layer has a thermal expansion coefficient smaller than those of both ZnO and the glass, tensile strain, even though compressive stress is generated, will appear at the interface between the buffer layer and ZnO and may lead to the appearance of some cracks. With a buffer material with a thermal expansion coefficient lying between those of ZnO and glass, only tensile strain will remain, but it will be lower than that without a buffer layer. Thus, the required buffer layer should have a higher thermal coefficient than both ZnO and the quartz glass substrate. MgO is one of the best choices using these selection rules.

The MgO buffer layer is applied with varying its thickness before growing ZnO film. Owing to MgO buffer layer, crack problem can be controlled. The structural property including surface morphology shows noticeable difference. The optical property shows significant improvement. Anyway, the electrical property still keeps unchanged with n-type conductivity as the following results.

## 6.1 Growth Procedure

The detailed steps for sample preparation are as follows. First, a 2×2-cm<sup>2</sup>-glass substrate surface is clean by chemical solution, the same procedure as mentioned in chapter 5. The substrate is then mounted onto a molybdenum block by In attachment. Next, the substrate is inserted into the MBE chamber. Before growth, the sample is heated to decontaminate the substrate surface from water (H<sub>2</sub>O) at 790°C by pyrometer for 30 min. The RHEED pattern shows halo pattern due to amorphous substrate. After the desorption at 790°C, the substrate is cooled down and MgO buffer layer is grown at 450°C with applying oxygen plasma with oxygen flow rate of 0.89 sccm and Mg BEP of  $1.2 \times 10^{-6}$  Torr to adjust the interface stress and flatten the surface. The MgO growth rate is around 11 nm/min. The ring RHEED pattern is continuously observed since the growth of this buffer layer started. The ring pattern becomes clearer during the proceeding of the growth. After the buffer layer growth, the substrate temperature is increased to anneal the buffer layer at 680°C for 10 min in oxygen ambient with oxygen flow rate of 0.89 sccm for the surface improvement before ramping down the substrate temperature to ZnO growth temperature of 530°C. Then, the approximately 800-nm ZnO layer is grown with the growth rate of 7 nm/min by applying oxygen plasma with oxygen flow rate of 1.07 sccm and Zn BEP of  $4.0 \times 10^{-6}$  Torr. For all samples, the growth temperature is fixed at 530°C, other parameters also unchange. Only MgO buffer layer thickness is varied. Schematic diagram of the sample structure grown in this work is shown in Figure 6.1. The samples with varying MgO buffer layer thickness are composed of 0, 100, 120, 130, 145, 170, 240 and 300 nm by changing the MgO growth period, keeping other parameters constant.

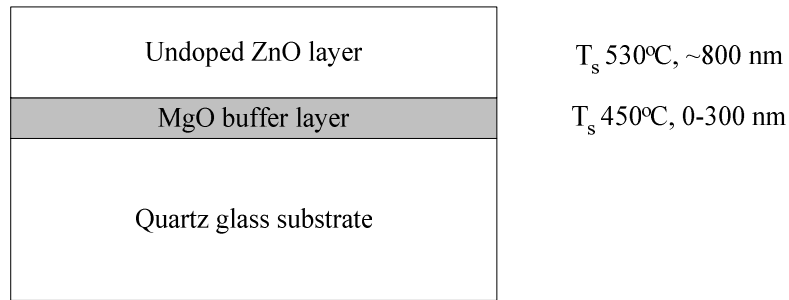


Figure 6.1 Schematic diagram of the sample structure grown in this work.  
The growth conditions are given in the text.

Furthermore, oxygen annealing after MgO buffer layer growth is studied. This procedure is performed before the ZnO film growth with oxygen annealing to improve the initial stage of ZnO film. Then, the sample without oxygen annealing and the other with oxygen annealing are grown and investigated the result. Most of all results including the RMS of AFM are not sufficiently different, however, the PL intensity of the sample with oxygen annealing is higher than the other one without oxygen annealing as shown in Figure 6.2. Consequently, the oxygen annealing procedure should be applied before the ZnO film growth; however, the annealing period is also important. We have observed the samples with short (10 min) and long (40 min) oxygen annealing periods. The RHEED patterns are not obviously different. However, the AFM and PL results become worse with the long annealing time. The RMS value of the long oxygen annealed sample is 26.917 nm, 2 times higher than the short annealed one (13.025 nm). Moreover, the dominant emission peaks at 3.358 eV and 3.368 eV, owing to the donor-bound exciton and ionized donor-bound exciton, disappear. Also, other donor-bound excitons around 3.3 eV disappear. The deep level emission near 2.9 eV emerges in place, implying the poorer quality the film is. The PL spectra of the samples with short and long period oxygen annealing are shown in Figure 6.3.

The surface morphology investigated by FE-SEM is also different. With 10-min oxygen-annealed buffer layer, the dot-like surface is clearly observed, whereas the sample with long period oxygen-annealed buffer layer shows totally different as shown in Figure 6.4 (a) and (b), respectively. This may relate to the optical property, which will be discussed later.

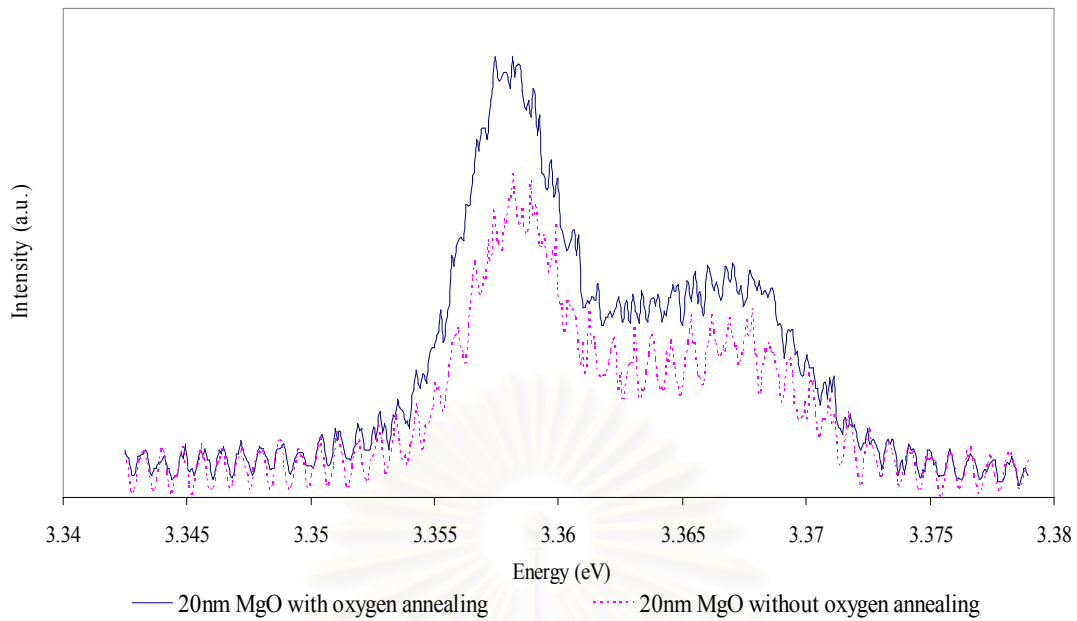


Figure 6.2 Comparison of PL spectra of the ZnO films with oxygen annealing and without oxygen annealing after 20-nm MgO buffer layer growth.

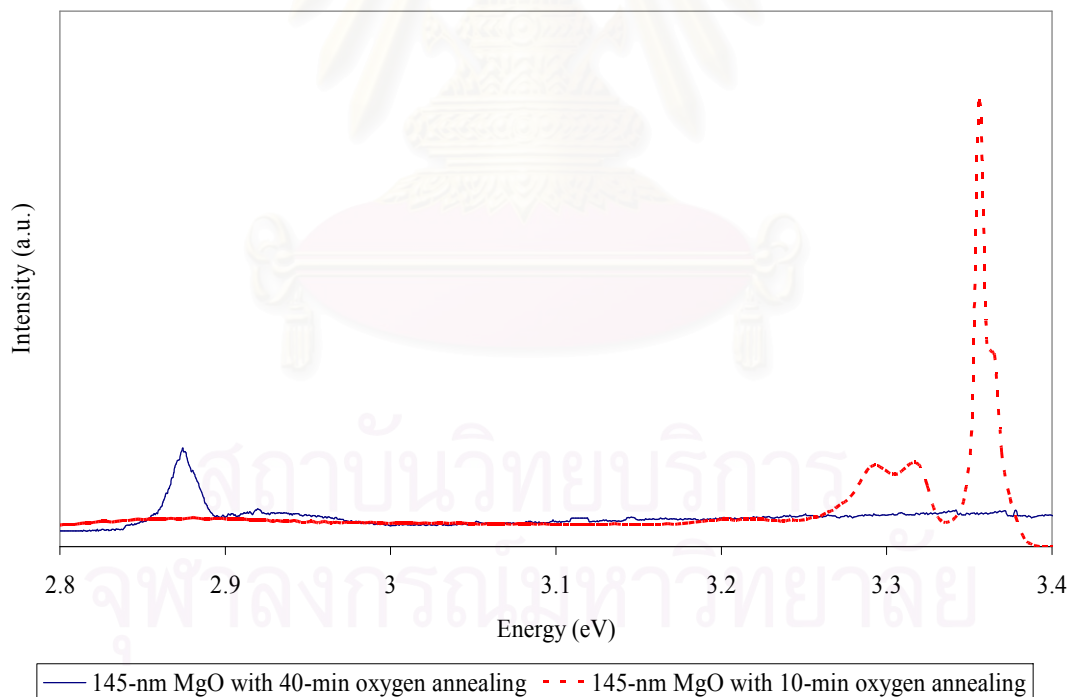
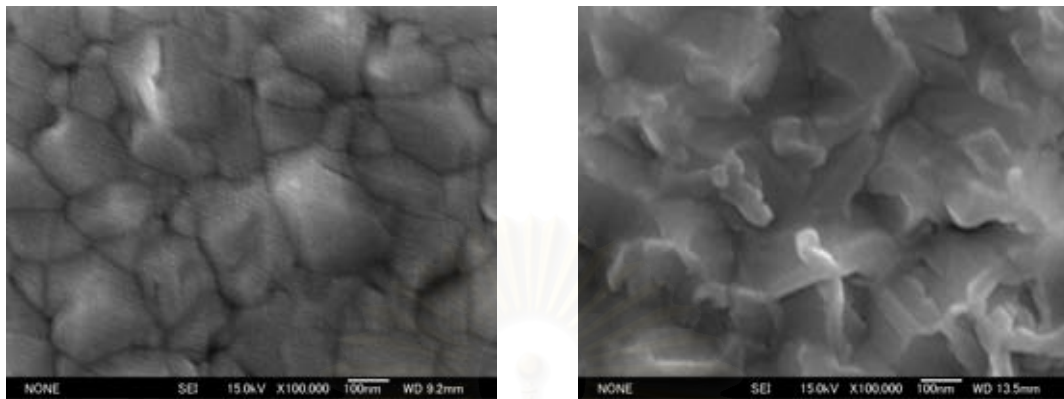


Figure 6.3 Comparison of PL spectra of the ZnO films with 10-min and 40-min oxygen annealing after 145-nm MgO buffer layer growth.

According to the above results, the oxygen annealing procedure after the MgO buffer layer growth is necessary to improve the thin film property. However, long



period anneal makes the property of the film poorer. Therefore, the 10-min oxygen annealing process is essential for the better quality.



(a)

(b)

Figure 6.4 Surface morphology by 100,000-time FE-SEM as a function of the oxygen annealing period of 145-nm MgO buffer layer: (a) 10 min (b) 40 min.

## 6.2 *In Situ* RHEED Observation

The surface of all samples during the growth is *in situ* observed by RHEED. The starting pattern before the growth of both MgO and ZnO layers is halo pattern of glass substrate as usual. Anyway, the ring pattern easily appears from the very beginning of the MgO growth. Then, the ring pattern becomes clear during growth and finally changes into ring-to-spot pattern. The fixed pattern emerges during the growth for all samples. This may imply that very thin MgO layer is disorderly amorphous, whereas the structure of most MgO buffer layer and a whole ZnO are polycrystalline. RHEED patterns during growth of ZnO with 20-nm MgO buffer layer grown on glass substrate are shown in Figure 6.5. Also, the different result due to various MgO buffer layer thicknesses can be noticed. When MgO buffer layer thickness changes, RHEED pattern development including the final pattern are also different, which mean the structural development might be different. RHEED patterns after ZnO growth of all samples are shown in Figure 6.6. Without MgO buffer layer, RHEED pattern shows fixed spotty pattern as mentioned in chapter 5. The samples with MgO buffer layer, however, shows the fixed ring-to-spot patterns. Among these samples, the RHEED patterns of 130-nm, 145-nm and 170-nm MgO buffer layer samples, as shown in Figure 6.6 (e)-(g), look nearly ring pattern indicating the higher disorder of the crystal quality.

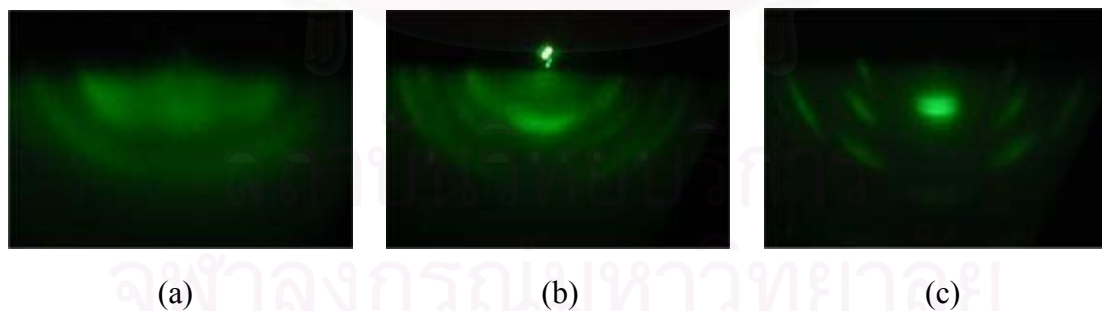


Figure 6.5 (a) RHEED pattern of MgO buffer layer growth start (ring pattern),  
 (b) RHEED pattern of 10-nm ZnO growth (ring pattern),  
 (c) RHEED pattern of 800-nm ZnO growth (fixed-spotty pattern).

### 6.3 Surface Morphology

Surface morphology of samples is observed by optical microscopy and FE-SEM after growth. With the thin MgO buffer layer ( $< 170$  nm), no cracks can be observed by both measurements. Whereas the crack can be easily observed on the surface of the samples with thick MgO buffer layer ( $\geq 170$  nm), however, low density of crack-compared to the sample without buffer layer. This means the samples with MgO buffer layer may create some mechanism to alleviate the crack problem. The ZnO surface images of the samples without MgO buffer layer, with a thin 145-nm MgO and with a thick 170-nm MgO observed by optical microscope are shown in Figure 6.7 (a), (b) and (c), respectively. The surface morphology of the samples without MgO buffer layer, with a thin 145-nm MgO and with a thick 300-nm MgO investigated by FE-SEM is shown in Figure 6.8 (a), (b) and (c), respectively. We can notice that the grain size and surface feature of the samples also change when MgO buffer layer thickness change.

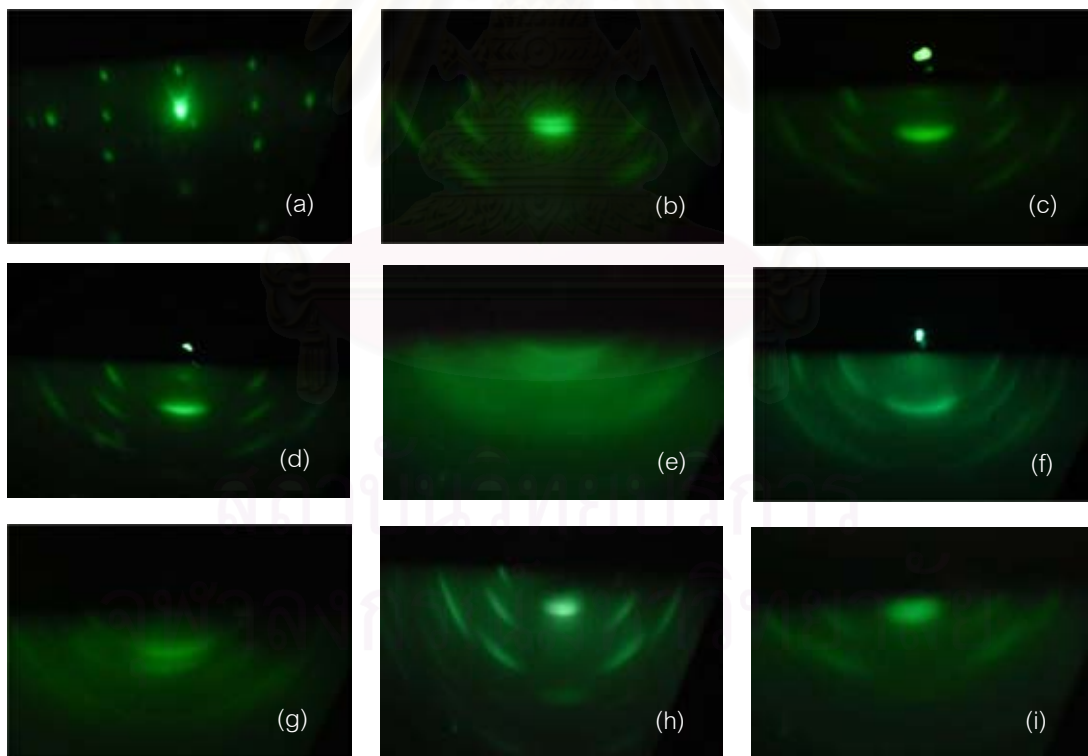


Figure 6.6 RHEED patterns of the ZnO films as a function of the MgO buffer layer thickness: (a) 0 nm (b) 20 nm (c) 100 nm (d) 120 nm (e) 130 nm (f) 145 nm (g) 170 nm (h) 240 nm and (i) 300 nm.

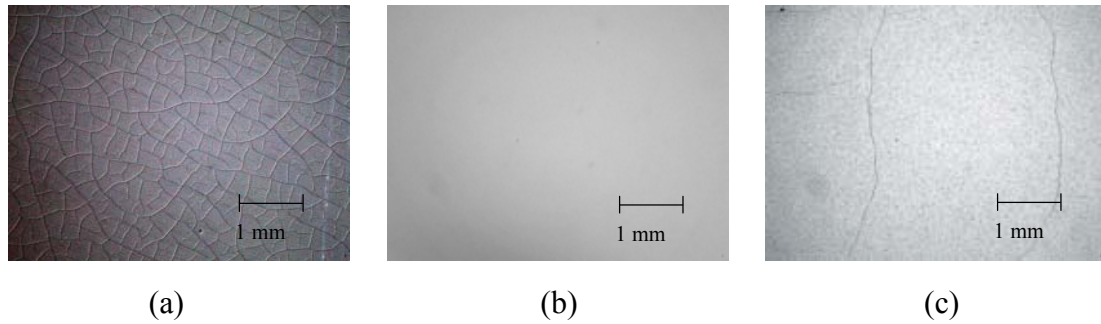


Figure 6.7 ZnO surface images by optical microscope: (a) without MgO buffer layer (b) 145-nm MgO buffer layer (c) 170-nm MgO buffer layer.

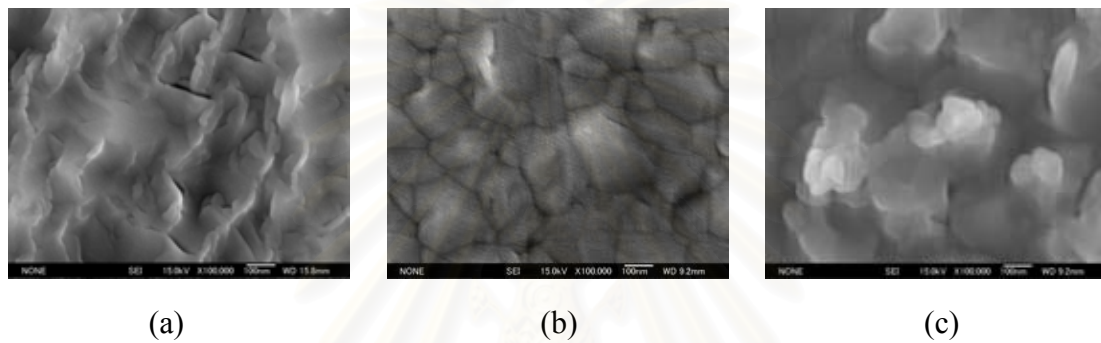


Figure 6.8 Surface morphology by 100,000-time FE-SEM as a function of the MgO buffer layer thickness: (a) 0 nm (b) 145 nm (c) 300 nm.

The surface morphology of the samples without MgO buffer layer and with MgO buffer layer thinner than 130 nm looks similar as shown in Figure 6.8 (a). With 130-nm, 145-nm and 170-nm buffer layers, the surface looks like dot combination as shown in Figure 6.8 (b). The other samples with MgO layer thicker than 170 nm, as shown in Figure 6.8 (c), show rough surface morphology without dot-like. This phenomenon may relate to the compressive-tensile stress balance by applying the various MgO buffer layer thicknesses. Without MgO buffer layer, only tensile strain at the interface, caused by the mismatch of thermal expansion coefficients between the ZnO film and the glass substrate as mentioned in chapter 5, affects the ZnO layer and causes a high density of cracks. When MgO layer thinner than 130 nm is grown on the substrate prior to the ZnO film growth, the compressive stress at the interface of MgO and ZnO is equal to or a little higher than the tensile strain from the substrate. Hence, no crack appears. In the condition of medium MgO buffer layer thickness ( $130 \text{ nm} \leq \text{MgO thickness} \leq 170 \text{ nm}$ ), the compressive stress is then comparatively higher than the tensile strain, which effects to the morphology with dot-like surface to

reduce some stress. However, when MgO buffer layer is very thick ( $> 170$  nm), the compressive stress is much less than the strain from the substrate, which causes the appearance of few cracks. We may refer that the compressive stress related to Stoney's equation is reduced by the partly stress relaxation in the dislocation form.

Furthermore, the thickness of the sample was investigated by FE-SEM. The ZnO growth rate after 2-hour growth is shown in Figure 6.9. We can notice that the growth rate of the sample with dot-like surface show lower growth rate. There will be some mechanism influence the sample during growth such as the crystal structure or the polarity of the structure. To find out the root cause, some new measurements are needed due to the amorphous substrate and polycrystal ZnO layer.

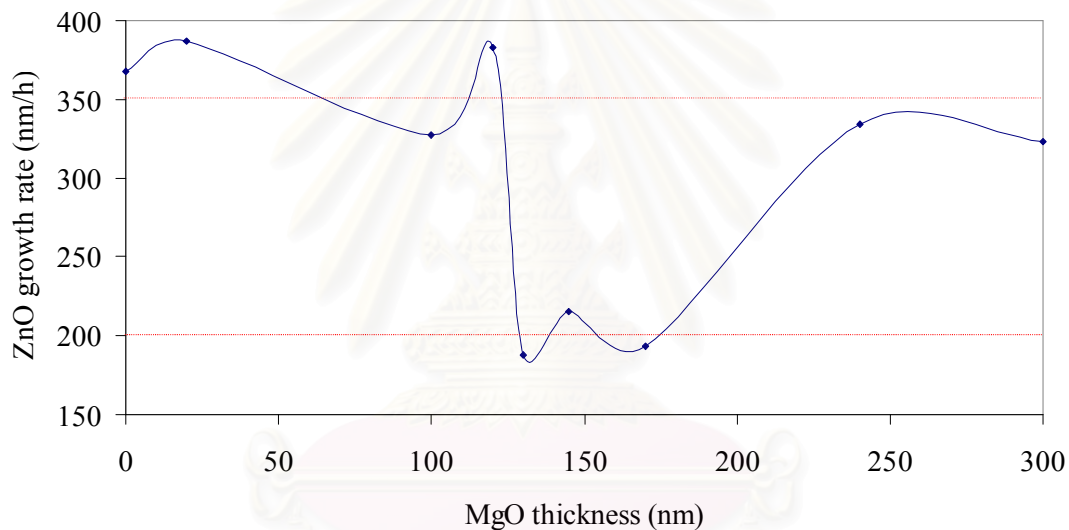


Figure 6.9 Relation of ZnO growth rate and MgO buffer layer thickness grown on glass substrate.

AFM is used to characterize the important data of the surface such as RMS. The AFM result of the sample with 130-nm MgO buffer layer thickness showed small dot combination as shown in Figure 6.10. Also, the relation between RMS of the samples and the thickness of the MgO buffer layer is shown in Figure 6.11. The RMS value increased with the thickness of MgO buffer layer. We can notice that the RMS value of the samples with dot-like surface is pretty low compared to the trend of the relation.

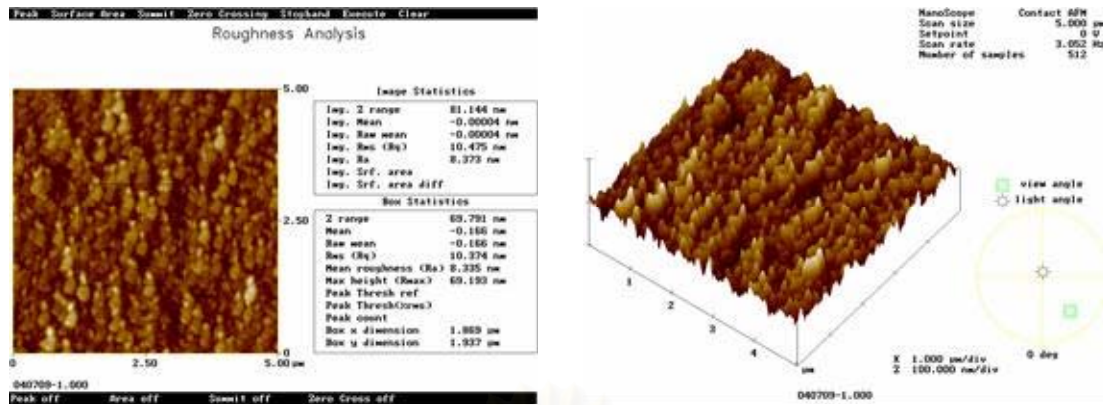


Figure 6.10  $5 \times 5 \mu\text{m}^2$  AFM images of ZnO surface with 130-nm MgO buffer layer. (a) Surface roughness analysis (b) 3D image.

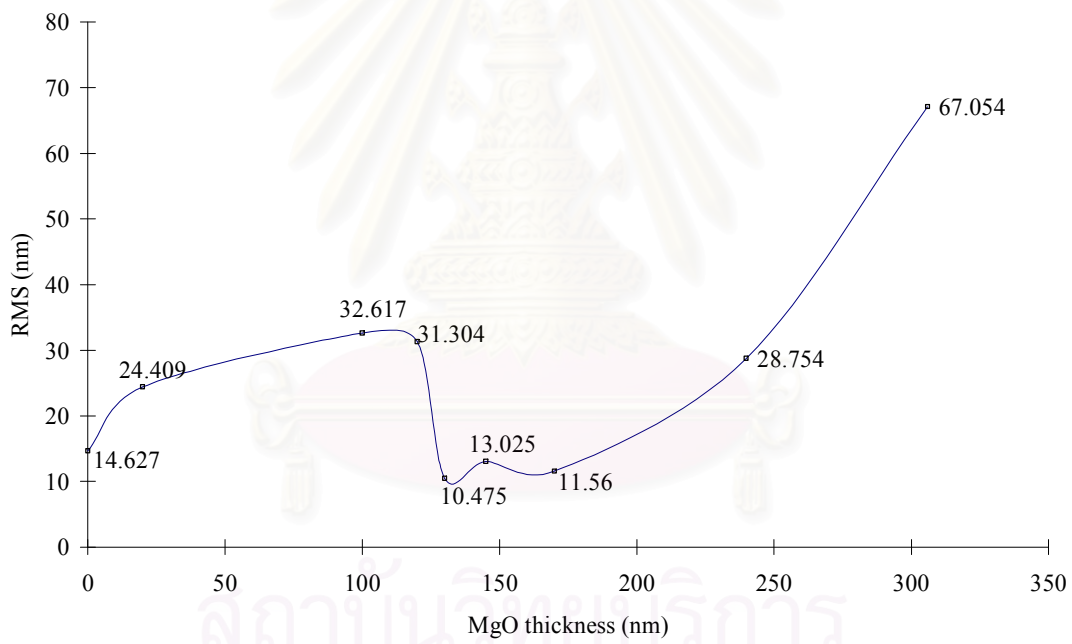


Figure 6.11 RMS value of surface roughness of the samples with various MgO buffer layer thickness.

## 6.4 Structural Property

Also, the crystal orientation of all samples is investigated by  $2\theta$ - $\omega$  scan and pole figure of XRD. The results of ZnO films can be separated in 2 groups. The first group is composed of the sample without buffer layer and the samples with MgO buffer layer thinner than 130-nm,  $\text{MgO} < 130 \text{ nm}$ , including the samples with MgO buffer layer thicker than 170-nm,  $\text{MgO} > 170 \text{ nm}$ , (normal surface group). The other group is composed of the samples with MgO buffer layer from 130-nm to 170-nm,  $130 \text{ nm} \leq \text{MgO} \leq 170 \text{ nm}$ , (dot-like surface group). The  $2\theta$ - $\omega$  scan XRD results of both group are shown in Figure 6.12. The ZnO (0002) peak appears in all the samples of the normal surface group indicating the c-orientation. On the other hand, all samples with dot-like morphology (dot-like surface group) show no appearance of the (0002) peak indicating no c-orientation with small grain size. The pole figures of c-axis oriented ZnO films deposited on glass substrates with the 120-nm and 145-nm MgO buffer layers are also shown in Figure 6.13 (a) and (b), respectively. Figure 6.13(a) indicates the structure of the ZnO film with the grains having the same crystallographic axis (0002) parallel to the substrate surface normal, but having random rotational orientations about that axis. On the other hand, Figure 6.13 (b) indicates the microstructure of the film without c-orientation, but only random rotational-oriented grains.

Furthermore, the intensity of  $2\theta$ - $\omega$  scan XRD of ZnO in normal surface group decreases when MgO buffer layer thickness increases as shown in Figure 6.14. The highest intensity result comes from the ZnO film without MgO buffer layer. This may imply that the sample surface in the normal surface group becomes worse when MgO buffer layer is applied thicker which we can notice from the RMS result of AFM in Figure 6.11 due to the compressive and tensile strain which accumulated more with MgO buffer layer thickness.

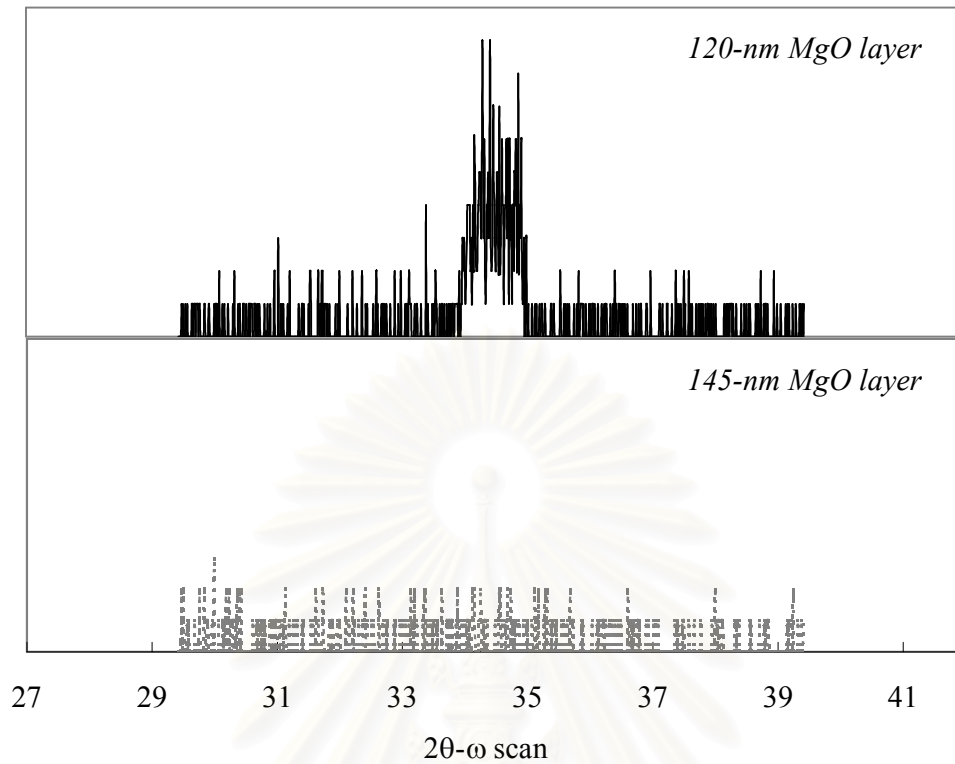


Figure 6.12 XRD  $2\theta$ - $\omega$  scan spectral response of ZnO film with 120-nm MgO buffer layer (normal surface group) and with 145-nm MgO buffer layer (dot-like surface group).

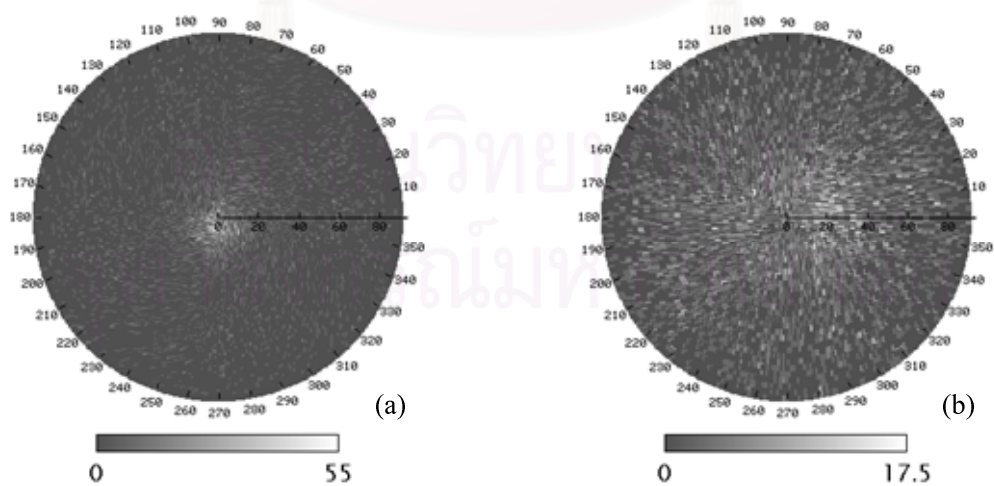


Figure 6.13 XRD pole figure spectral response of ZnO film with 120-nm MgO buffer layer (normal surface group) and with 145-nm MgO buffer layer (dot-like surface group).



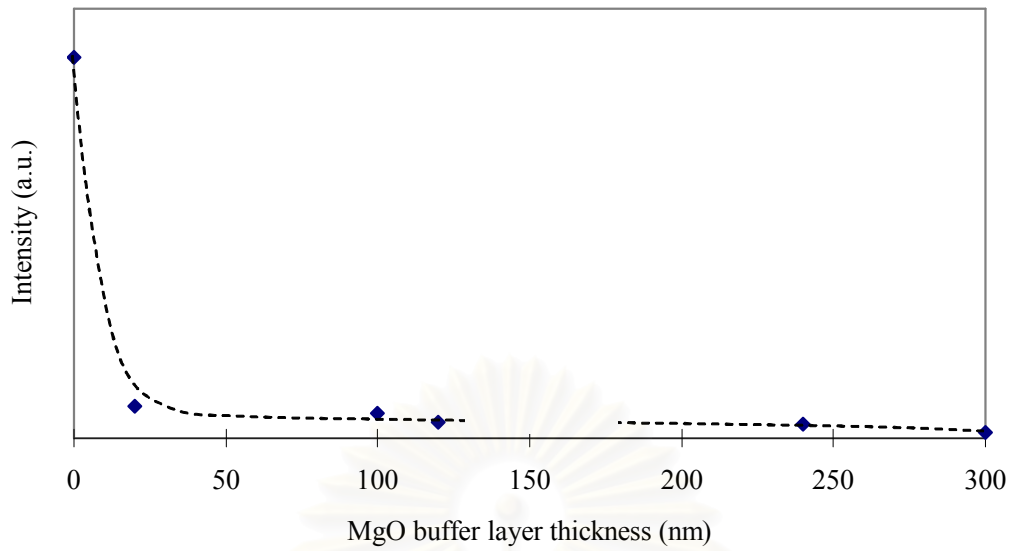


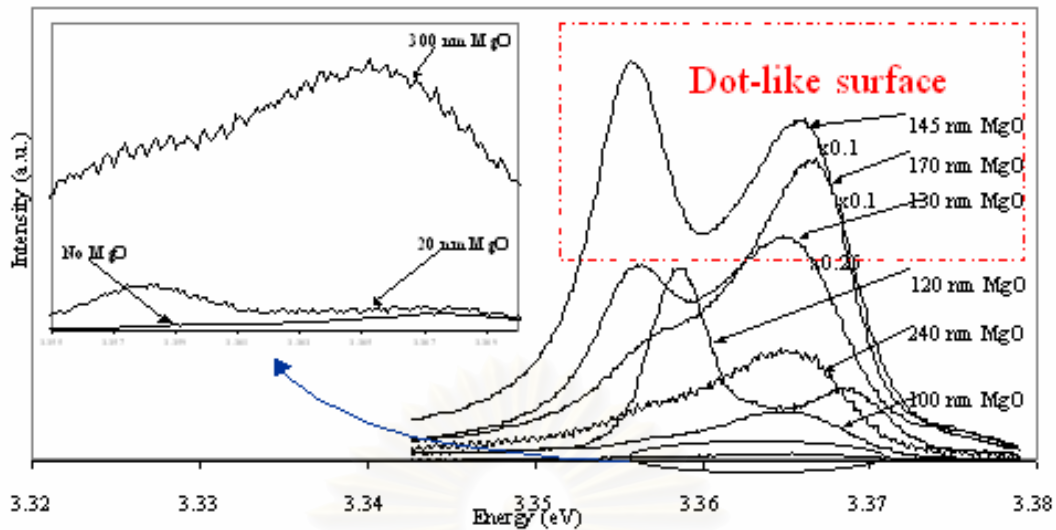
Figure 6.14 Intensity of  $2\theta$ - $\omega$  scan spectral response of ZnO film with various MgO buffer layer thicknesses in normal surface group.

สถาบันวิทยบริการ  
จุฬาลงกรณ์มหาวิทยาลัย

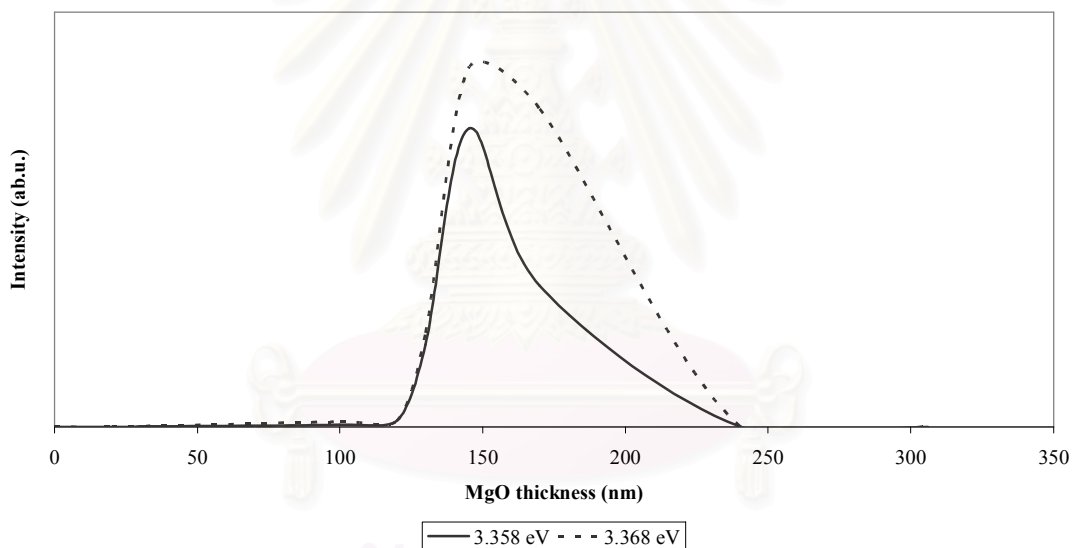
## 6.5 Optical Property

All the ZnO thin films are observed by PL measurement to investigate the optical property of the films influenced by MgO buffer layer. The PL spectra of the annealed MgO buffer layer samples with various buffer layer thicknesses are shown in Figure 6.15 (a). The inset of Figure 6.15 (a) also shows PL spectra of three samples, which are the samples without the buffer layer, with a thin (20 nm) buffer layer, and with a thick (300 nm) buffer layer. The typical near-band-edge PL measurement indicates that the PL intensity of these three samples is pretty weak, compared to the other samples. The minimum intensity of PL spectra is from the sample without the MgO buffer layer. The emission lines located at 3.358 eV and 3.368 eV dominate the spectrum in all samples. The emission peaks at 3.358 eV and 3.368 eV are donor-bound exciton related to the oxygen vacancy and ionized donor-bound exciton, respectively. A shoulder peak at 3.375 eV is attributed to the free exciton emission with A-valence band. The lattice mismatch-induced inhomogeneous strain distribution results in a Stokes shift of less than 5 meV. Figure 6.15 (b) shows the relationship of the PL intensity of both dominant emission peaks with the different MgO buffer layer thickness. The PL intensity of donor-bound exciton emissions increases with the buffer layer thickness until it reaches the optimum value of approximately 150 nm with the strongest PL intensity among all the samples. Then, the PL intensity starts decreasing when the MgO thickness exceeds 170 nm including few-crack appearance presumably caused by the relatively poor crystalline quality as shown in Figure 6.7 and Figure 6.8. Therefore, the optimum buffer layer thickness probably lies around 150 nm. It should be pointed out that the decrease of PL intensity and the formation of surface cracks occur at the same MgO buffer layer thickness. However, the PL intensity of the samples with the dot-like surface is much higher than those of the others implying this smaller grain size may cause the band bending and partly carrier confinement with piezoelectric field effect, which likely leads to the emission intensity stronger than that of c-oriented crystalline ZnO.

Figure 6.16 shows the comparison of the results of the RMS result by AFM and PL intensity of both dominant peaks of all samples with MgO buffer layer thickness. We can notice that the samples with the dot-like surface exhibited the smoother surface and emission-property improvement.



(a)



(b)

Figure 6.15 (a) PL spectra of the annealed MgO buffer layer samples with various buffer layer thicknesses. (b) Relationship of the PL intensity of emission peaks at 3.358 eV and 3.368 eV.

To investigate the influence of MgO buffer layer to the band gap of ZnO film, the absorption coefficient of samples is measured at room temperature. The measurement method is explained in chapter 3. The absorption coefficient spectral, which used to estimate band gap energy at room temperature of undoped ZnO grown

on glass substrate with various MgO buffer layer thicknesses, is shown in Figure 6.17. Also, Figure 6.18 shows the estimated energy band gap of ZnO thin films with several MgO buffer layer thicknesses. This result can imply to the tensile-compressive strain within the film due to the different structural property between ZnO film and glass substrate.

With the estimated energy band gap of ZnO thin films in Figure 6.18, we can easily separate the trend of the ZnO band gap into 3 groups. The first group of the samples with MgO buffer layer thinner than 130 nm shows narrow energy gap of ZnO with MgO buffer layer thickness, however, the estimated energy band gap increases with the MgO buffer layer thickness. The second group is composed of the samples with dot-like surface,  $130 \text{ nm} \leq \text{MgO} \leq 170 \text{ nm}$ . We can observed that the estimated energy band gap of ZnO with the dot-like surface show higher value, approximately 3.25 eV. The last group is composed of the samples with MgO buffer layer thicker than 170 nm with low energy band gap. This might be the result of the strain in the layer effected both the valence band and conduction bands of ZnO including quantization effect. The strain, due to the lattice mismatch including the thermal expansion coefficient mismatch, has relatively little effect on the conduction band of direct-gap semiconductors but splits the degeneracy of the valences band maximum, so significantly affecting its properties. Without MgO buffer layer, only tensile strain due to the thermal expansion coefficient mismatch between the glass substrate and ZnO thin film affects the thin film, the high density of cracks then appears to relieve this force. When MgO is applied to be the buffer layer, the tensile strain of glass substrate and MgO buffer layer is alleviated by the compressive strain between MgO buffer layer and ZnO thin film. Then, the cracks disappear even though MgO buffer layer is very thin. When the MgO buffer layer is thicker, the compressive strain is higher. This effects to the mean band gap increase and the valence band split, which make the highest band, is that of heavy hole along strain axis. Therefore, the trend of the energy band gap of the samples in the first group with thin MgO buffer layer increases with MgO buffer layer thickness. The next group with dot-like surface shows a little change of ZnO energy gap. In this group, the compressive strain, relating to the lattice mismatch between MgO and ZnO including the different thermal expansion coefficient between both materials, might effect the ZnO layer to form the dot-like surface morphology to relax some stress. Also, the compressive strain makes

the band edge shift for the conduction and valence bands, then the energy band gap, compared to the first group, increases. On the other hand, the last group with of the ZnO films with thicker MgO buffer layer shows reverse. When the MgO buffer layer is thicker, the compressive strain increases until a limit, and then reduces because of the relaxation as mentioned above in the dot-like surface group. However, the dislocations may occur due to the large mismatch and the compressive strain reduces. Then, the tensile strain from the substrate dominate again and affect the ZnO film with some cracks. This effects to the mean band gap decrease and the valence band splits, which made the highest band, is that of lightly hole along strain axis. Therefore, the trend of the energy band gap of the samples in the last group with thick MgO buffer layer reversibly decreases with MgO buffer layer thickness.

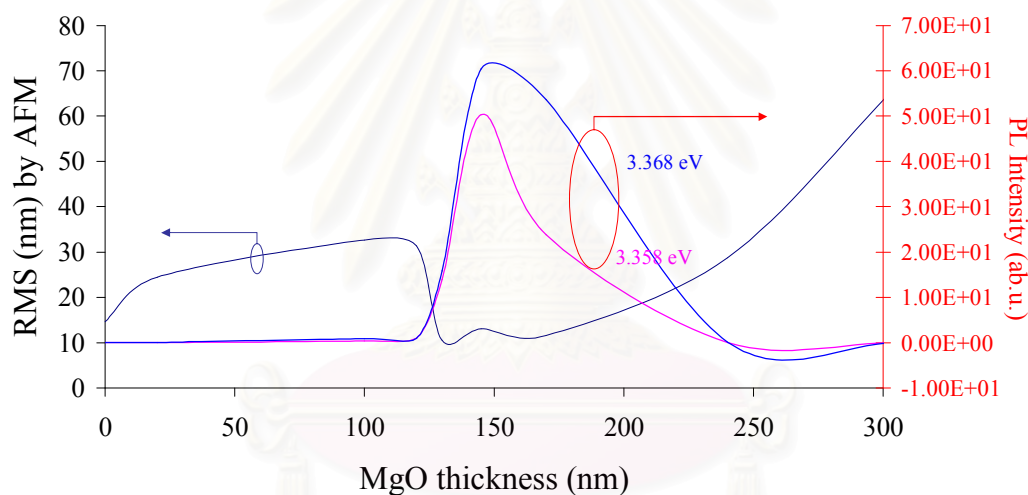


Figure 6.16 RMS result by AFM and PL intensity of both dominant peaks, 3.358 eV and 3.368 eV, with various MgO buffer layer thickness.

จุฬาลงกรณ์มหาวิทยาลัย

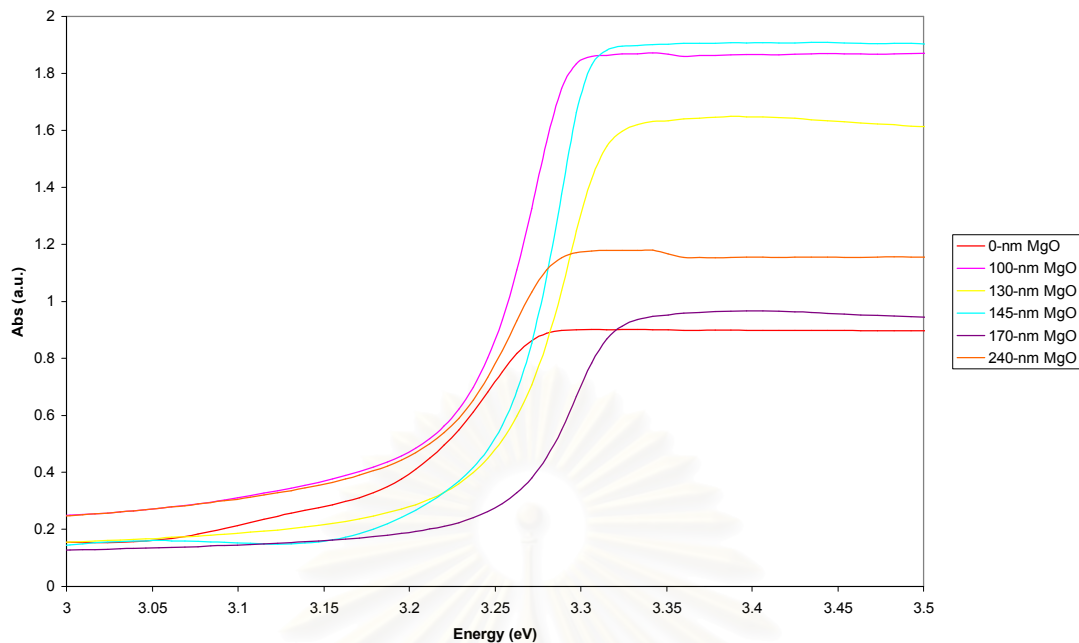


Figure 6.17 Absorption coefficient spectral response of ZnO thin films with various MgO buffer layer measured at room temperature.

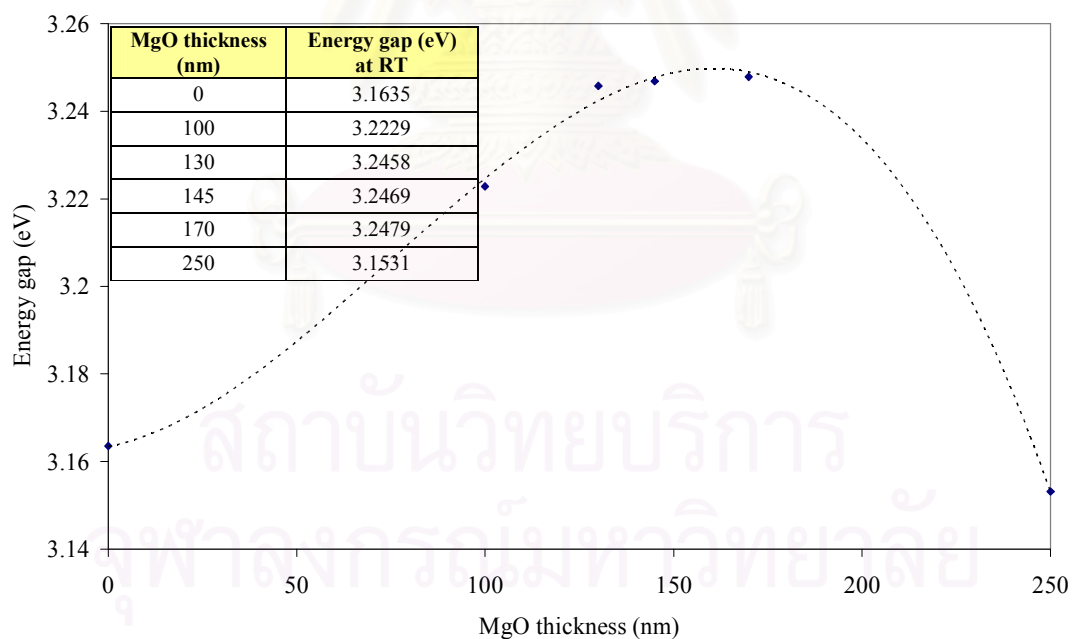


Figure 6.18 Estimated energy band gap of ZnO films with MgO buffer layer thickness at room temperature.

## 6.6 Electrical Property

The carrier concentration and Hall mobility of all samples without crack resulting from MgO buffer layer thinner than 170 nm are investigated via van der Pauw method. The electrical characteristics of all grown ZnO films in this condition exhibit n-type conductivity in the range of  $10^{17}$  and  $10^{18}$   $\text{cm}^{-3}$ , similar to those of N-doped ZnO film as mentioned in the previous chapter. All these samples, however, show pretty low electron mobility ( $5 \text{ cm}^2/\text{V}\cdot\text{s}$ ). The observed resistivities are in the range of  $10^3$ - $10^5$   $\Omega \text{ cm}$ . No improvement of the electrical property can be observed. The measurement result of the ZnO film with 20-nm MgO buffer layer is shown in Figure 6.19.

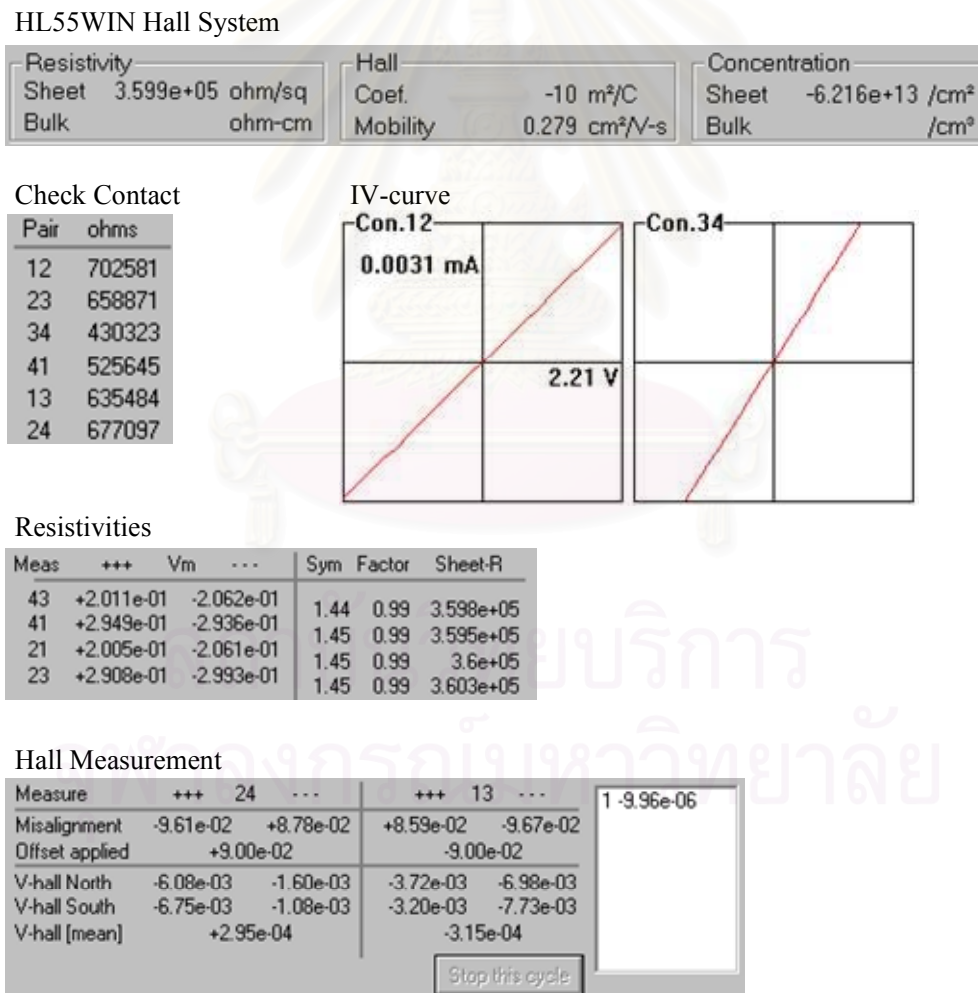


Figure 6.19 Hall measurement result of the ZnO thin film with 20-nm MgO buffer layer.

## 6.7 ZnO Quality Improvement

According to the MgO thickness adjustment, we can find the optimum thickness around 130 nm, which show no crack and high PL intensity including lower growth rate as well as low RMS. However, these samples show only random rotational-oriented grains without c-orientation due to the small grain size. The lower growth rate appears naturally in the samples with MgO buffer layer thickness in between 130 nm and 170 nm even though all the parameters are fixed. We found that the qualities of ZnO layer seem relate to the growth rate. Therefore, we tried to reduce the ZnO growth rate more in order to improve ZnO property including structural property by varying three parameters, which are O<sub>2</sub> flow rate, Zn flux and ZnO growth temperature, at 130 nm optimum MgO buffer layer.

### 6.7.1 O<sub>2</sub> flow rate variation

At the optimum growth condition, O<sub>2</sub> flow rate is set at 1.07 sccm. Then, we try to reduce ZnO growth rate by reducing O<sub>2</sub> flow rate to 0.7 sccm. After growth, the ZnO surface shows no crack via optical microscope and FE-SEM. The surface morphology is shown in Figure 6.20, which is similar to dot-like surface. The grain size looks not various but pretty rough. The ZnO thickness is also observed and indicated that the ZnO growth rate cannot be reduced by reducing O<sub>2</sub> amount. Furthermore, a result measured by AFM, Figure 6.21, shows rougher surface with RMS of 26.281 nm, much higher than that of the optimum sample.

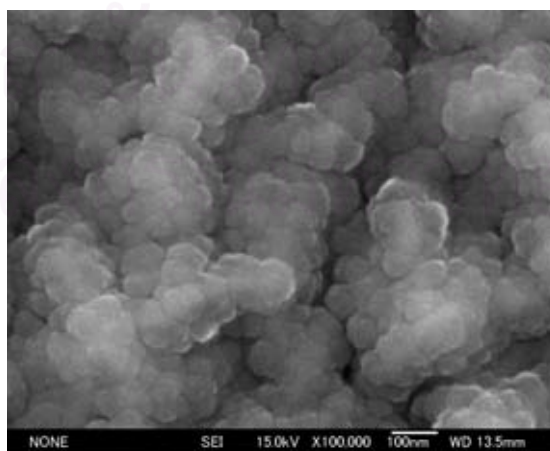


Figure 6.20 Surface morphology by 100,000-time FE-SEM of the ZnO film with 0.7 sccm oxygen flow rate.



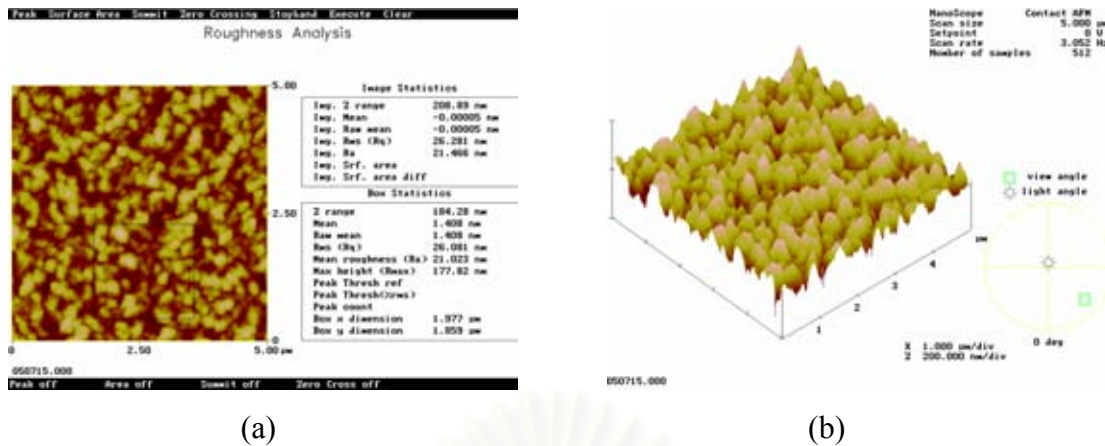


Figure 6.21  $5 \times 5 \mu\text{m}^2$  AFM images of ZnO surface with 130-nm MgO buffer layer in the growth condition of low oxygen flow rate. (a) Surface roughness analysis (b) 3D image.

For the structural property of ZnO film, The ZnO (0002) peak can be observed even though the MgO layer thickness is 130 nm as shown in Figure 6.22. This implies the improvement of the structural property.

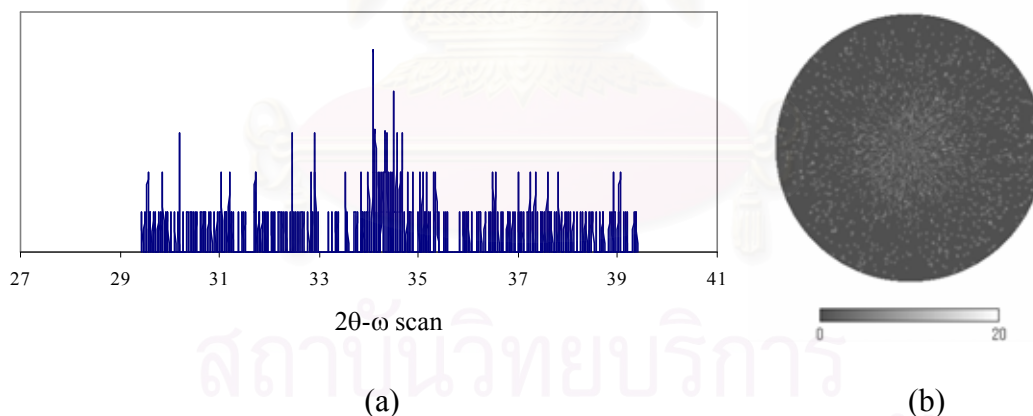


Figure 6.22 XRD spectral response of ZnO film with 130-nm MgO buffer layer in the growth condition of low oxygen flow rate. (a) 2θ-ω scan (b) pole figure.

To investigate the optical property, the sample is measured by PL. For the ZnO sample with 130-nm MgO buffer layer, the high PL intensity is shown in Figure 6.15. However, the sample with low oxygen flow rate shows low PL intensity with several peaks including the donor-bound exciton peak of 3.358 eV as shown in

is varied as mention in chapter 5. Then, we vary the Zn flux to investigate the characteristics of the ZnO film in the conditions of both oxygen rich, Zn flux of  $2 \times 10^{-6}$  Torr, and zinc rich, Zn flux of  $5 \times 10^{-6}$  Torr. After thin film growth, the ZnO surface shows no crack via optical microscope and FE-SEM. The surface morphology is shown in Figure 6.24, which is similar to dot-like surface. The grain size looks not various but pretty rough. The ZnO thickness is also observed and indicated that the ZnO growth rate cannot be changed by changing Zn quantity. Furthermore, a result measured by AFM, Figure 6.25, shows rougher surface with RMS of 33.755 and 33.761 nm, respectively. These values are much higher than that of the optimum sample, around 10 nm.

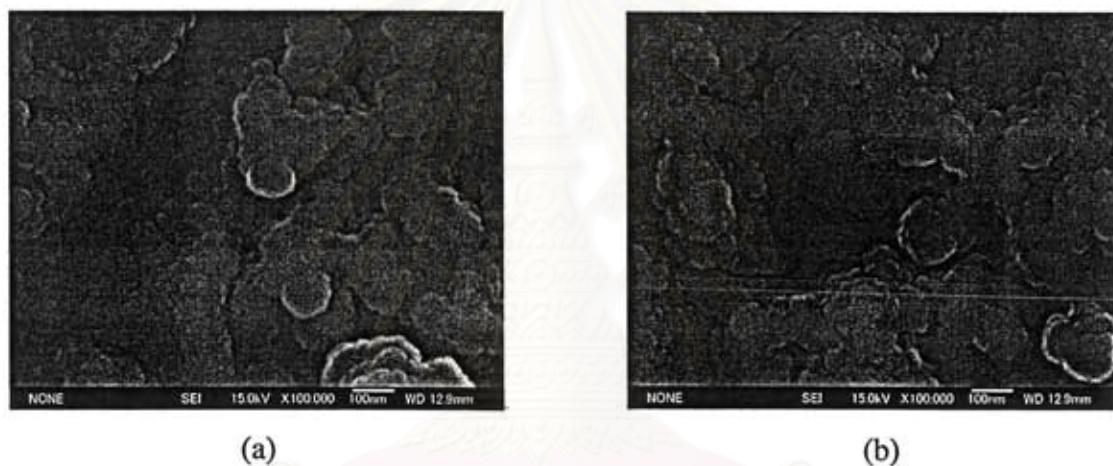


Figure 6.24 Surface morphology by 100,000-time FE-SEM of the ZnO film with Zn flux of (a)  $2 \times 10^{-6}$  Torr (b)  $5 \times 10^{-6}$  Torr.

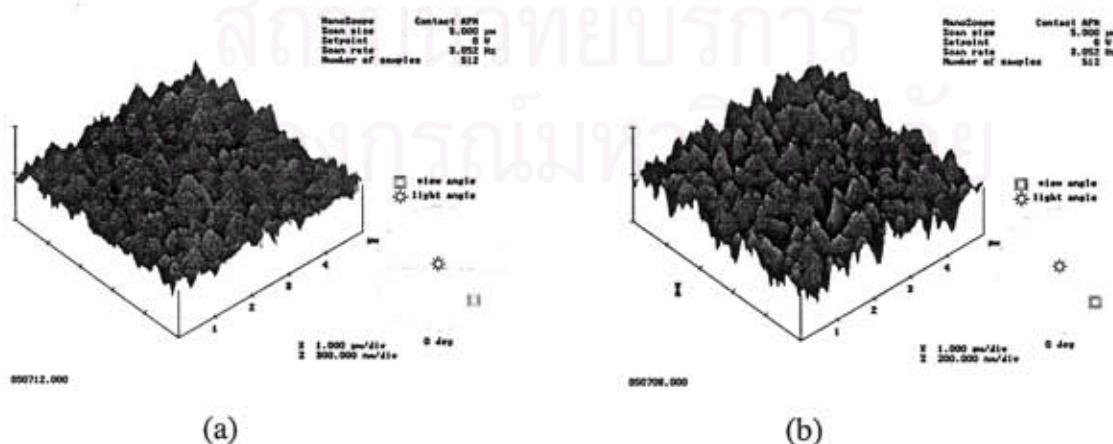


Figure 6.25 3D images of  $5 \times 5 \mu\text{m}^2$  ZnO surface with 130-nm MgO buffer layer in the growth condition of Zn flux (a)  $2 \times 10^{-6}$  Torr (b)  $5 \times 10^{-6}$  Torr.

Figure 6.23. The emission peaks around 2.4 eV and 2.8 eV show the deep-level emission. The defects due to the lack of oxygen may cause these peaks; however, the real cause is still unknown.

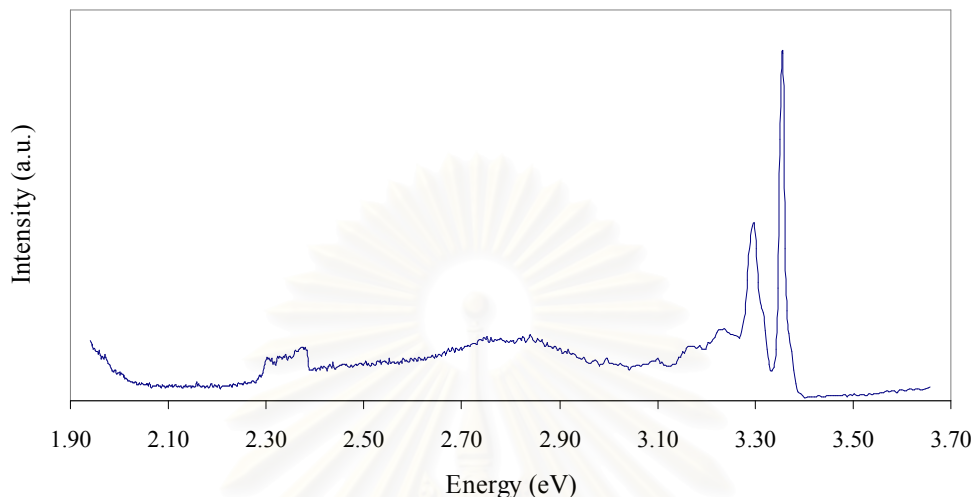


Figure 6.23 PL spectra of the ZnO with 130-nm MgO buffer layer in the growth condition of low oxygen flow rate.

The electrical characteristics of the ZnO film in this condition exhibit n-type conductivity in the range of  $10^{17} \text{ cm}^{-3}$  with very low electron mobility ( $3 \text{ cm}^2/\text{V}\cdot\text{s}$ ). No improvement compared to all samples with higher oxygen flow rate can be investigated.

Even though the structural property of ZnO film can be improved by reducing oxygen flow rate, the surface roughness and optical property get worse. Also, the growth rate of ZnO can not be changed. Then, the study of Zn flux may be a good way to improve the ZnO film, which is described next.

### 6.7.2 Zn flux variation

According to all experiment, Zn flux during ZnO film growth is fixed at  $4 \times 10^{-6}$  Torr in order to grow ZnO layer in the stoichiometric condition with oxygen-

For the structural property of ZnO film, The ZnO (0002) peak can be observed even though the MgO layer thickness is 130 nm in the condition of high Zn flux,  $5 \times 10^{-6}$  Torr, as shown in Figure 6.26. This indicates the structural property improvement with the c-orientation of ZnO film.

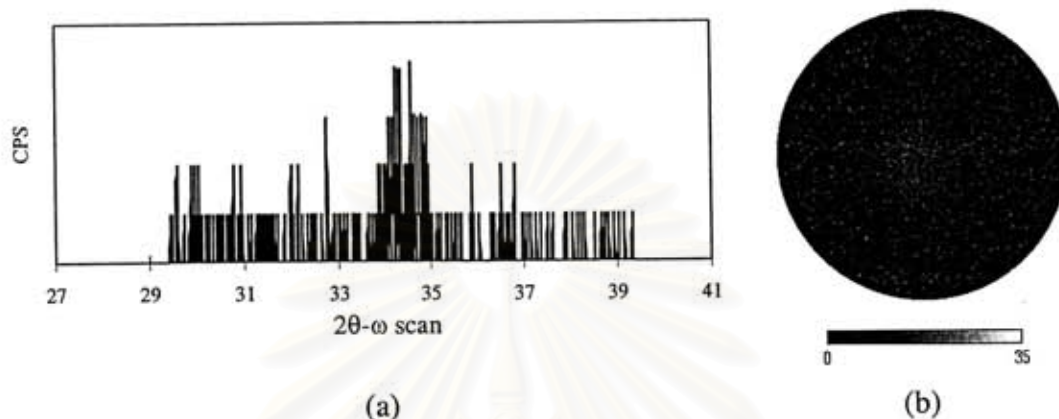


Figure 6.26 XRD spectral response of ZnO film with 130-nm MgO buffer layer in the growth condition of high Zn flux ( $5 \times 10^{-6}$  Torr). (a)  $2\theta$ - $\omega$  scan (b) pole figure.

For the optical property observation, the samples are measured by PL. All the ZnO films with various Zn flux show comparatively high PL intensity as shown in Figure 6.27. The emission lines located at 3.358 eV and 3.368 eV dominate the spectrum in all samples. Furthermore, the emission peak around 3.300 eV, which is also donor bound exciton, can be clearly observed. In the condition of high Zn flux, the intensity of 3.358 eV and 3.300 eV is comparative. Also, the emission peak at 3.300 eV, which may be donor-bound exciton, appears in all samples. All the emission peaks are a little blue-shift with Zn flux. Anyway, all samples except the sample with Zn flux of  $4 \times 10^{-6}$  Torr show no emission peaks around 2.4 eV and 2.8 eV, the deep-level emission. This might refer to the lower amount of defect in the films.

The electrical characteristics of the ZnO films with various Zn flux exhibit n-type conductivity in the range of  $10^{17} \text{ cm}^{-3}$  with very low electron mobility ( $3 \text{ cm}^2/\text{V}\cdot\text{s}$ ). No improvement can be observed even though the Zn flux was changed.

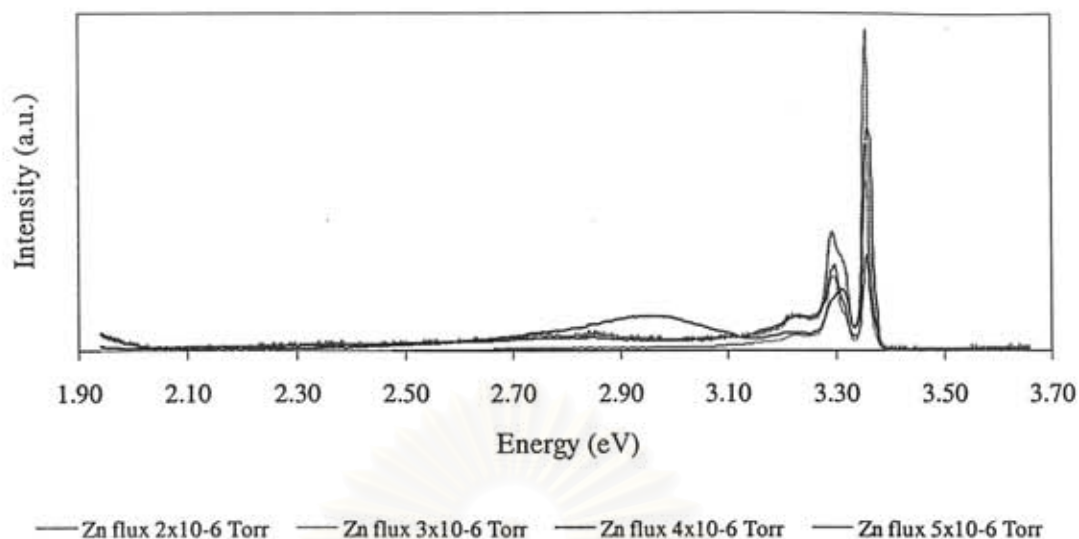


Figure 6.27 PL spectra of the ZnO with 130-nm MgO buffer layer in the growth condition of various Zn flux.

The structural property of ZnO film can be improved with the c-orientation by increasing the Zn flux for ZnO growth, however, the surface roughness gets worse. The optical and electrical properties keep unchanged. Also, the growth rate of ZnO can not be changed. To improve the quality of ZnO film, the study of ZnO growth temperature is an interesting parameter, which is mentioned next.

### 6.7.3 ZnO growth temperature variation

Relating to ZnO crystal quality, ZnO growth temperature is an important parameter. For our knowledge, high temperature growth generally enhances diffusion of adatoms on growing surface leading to a high-quality crystal growth. This might let an atom settle at a suitable position. However, high ZnO growth temperature may affect the crack problem due to the different thermal expansion coefficient as mentioned in chapter 5. According to the suitable growth temperature of ZnO on sapphire substrate, all ZnO layers are grown at 530°C. In order to investigate the ZnO growth temperature, we vary to the higher growth temperatures at 600°C and 680°C (oxygen annealing temperature). After thin film growth, the ZnO surface shows no crack via optical microscope and FE-SEM at the ZnO growth temperature of 600°C whereas there are a few cracks of the sample grown at 680°C as shown in Figure 6.28.

The surface morphology is shown in Figure 6.29, which is similar to dot-like surface. The grain size looks not various but pretty rough. The ZnO thickness is also observed and indicated that the ZnO growth rate increases with ZnO growth temperature as shown in Figure 6.30. Furthermore, a result measured by AFM, Figure 6.31, shows rougher surface with higher ZnO growth temperature.

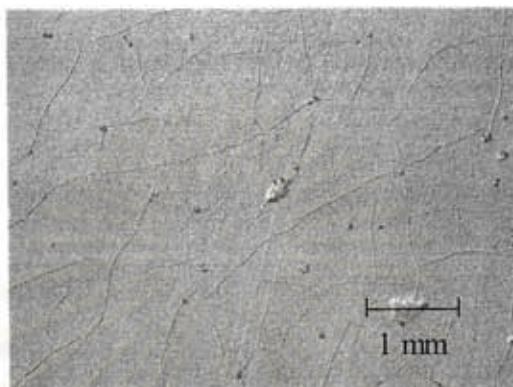


Figure 6.28 ZnO surface images by optical microscope. The ZnO growth temperature is 680 °C.

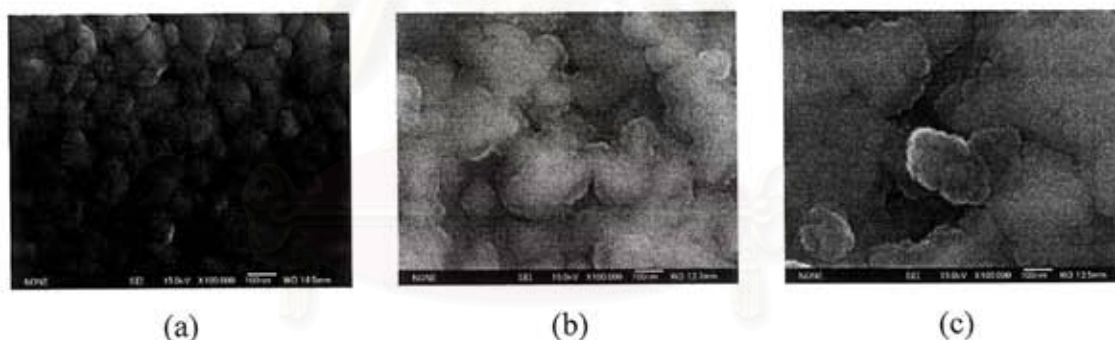


Figure 6.29 Surface morphology by 100,000-time FE-SEM of the ZnO film with Zn flux of (a) 530 °C (b) 600 °C (c) 680 °C.

For the structural property of ZnO film, The ZnO (0002) peak can be observed even though the MgO layer thickness is 130 nm in the condition of higher ZnO growth temperature, as shown in Figure 6.32. This indicates the structural property improvement with the c-orientation of ZnO film.

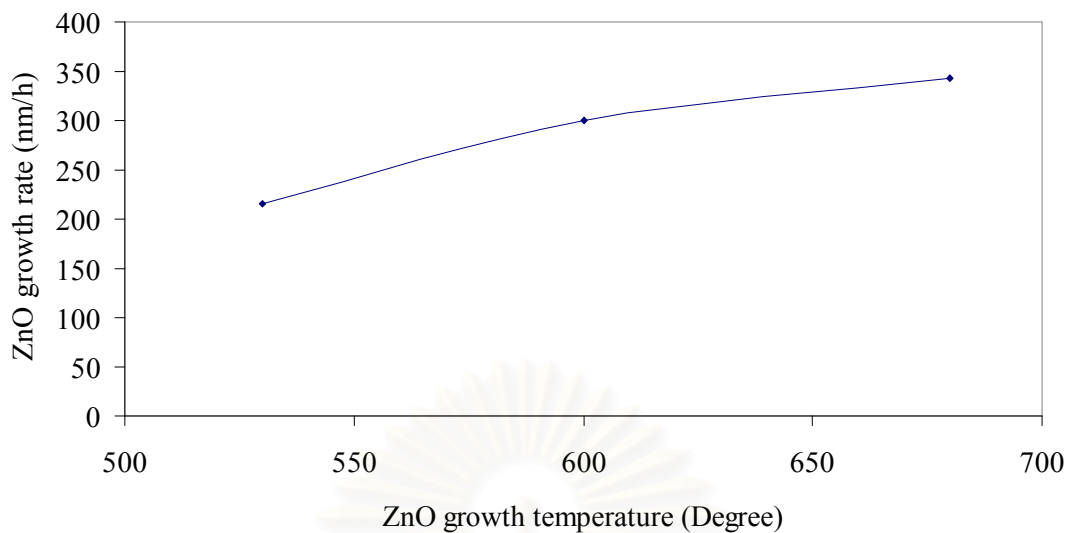


Figure 6.30 Relation of ZnO growth rate and ZnO growth temperature with 140-nm MgO buffer layer thickness grown on glass substrate.

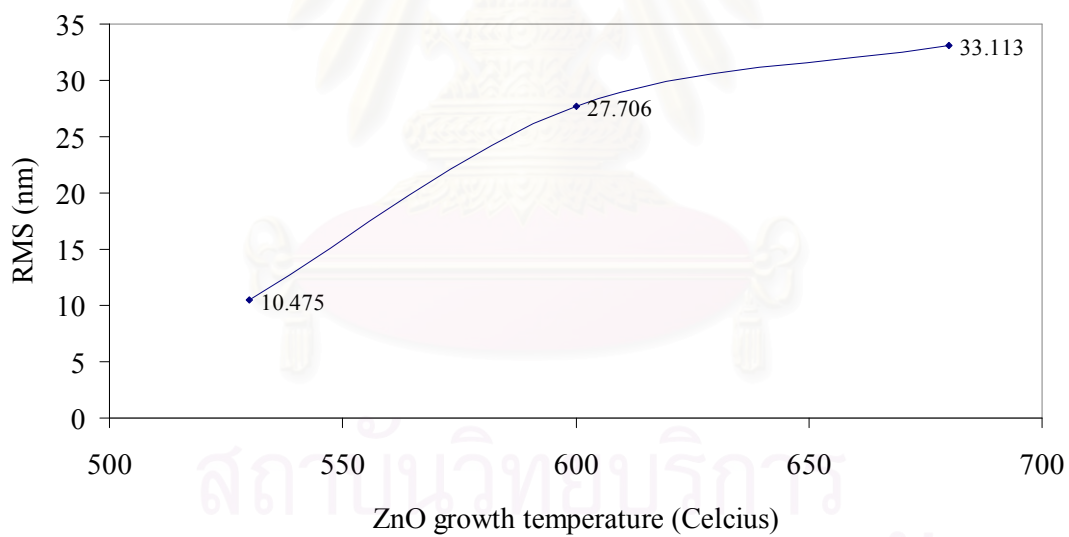


Figure 6.31 RMS value of surface roughness of the samples with various ZnO growth temperatures.

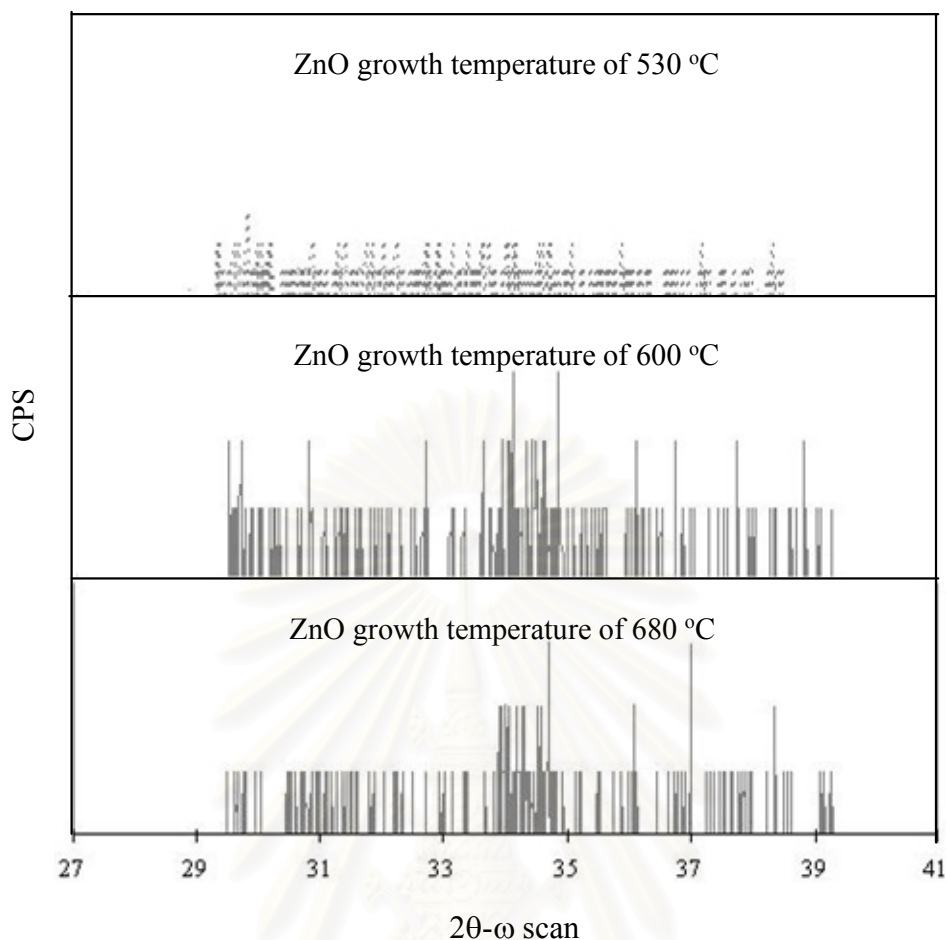


Figure 6.32  $2\theta$ - $\omega$  scan XRD spectral response of ZnO film with 130-nm MgO buffer layer in the condition of different ZnO growth temperature.

For the optical observation of the samples, they are measured by PL at 10 K. The ZnO films with the growth temperature of 530 °C and 600 °C, which no crack can be observed, show comparatively high PL intensity, whereas the sample with higher ZnO growth temperature of 680 °C, which a few cracks emerge, show pretty low PL intensity as shown in Figure 6.33. The emission lines located at 3.358 eV and 3.368 eV dominate the spectrum when the growth temperature is 530 °C. However, the sample with the growth temperature of 600 °C show both the donor-bound excitation peaks at 3.358 eV and 3.368 eV including some new peaks, 3.361 eV and 3.372 eV. Furthermore, only the new emission peaks at 3.361 eV and 3.372 eV dominate the spectrum when the ZnO layers are grown at high temperature of 680 °C with much lower PL intensity. The origins of these new peaks have not been found out yet. Also, there are some new PL peaks at 3.106 eV, 3.174 eV and 3.242 eV as shown in Figure 6.34. These may be the result of LO phonon scattering due to the different of



68 meV. The small emission peak around 3.220 eV, which may be the donor-acceptor bound exciton, can be observed in the samples with the growth temperature of 530 °C and 600 °C. The emission peak around 3.300 eV, which is also donor bound exciton, can be clearly observed in all samples. Anyway, all samples show the small emission peaks around 2.4 eV and 2.8 eV, the deep-level emission.

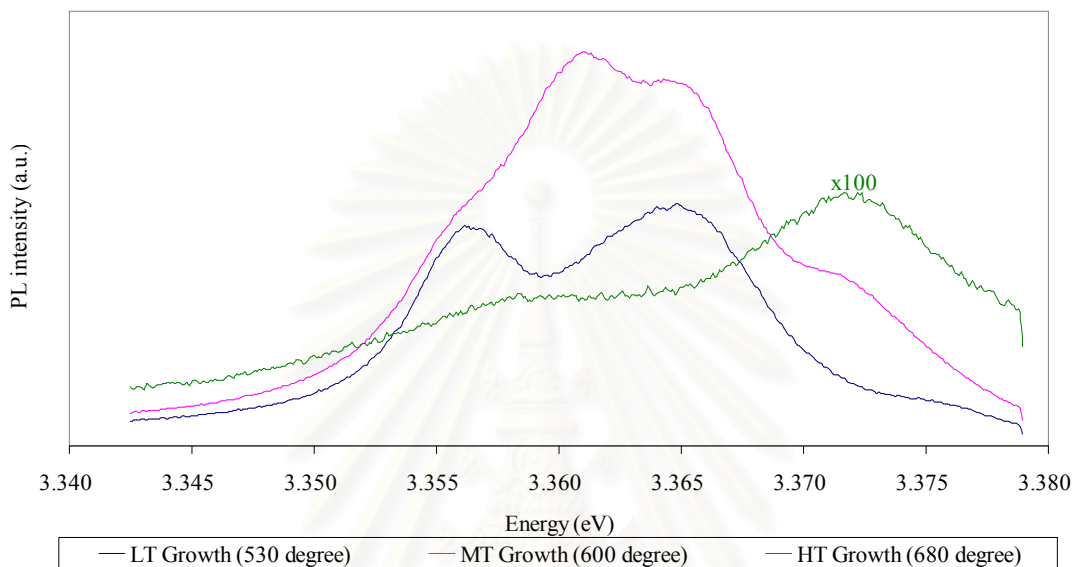


Figure 6.33 PL spectra around 3.340 eV to 3.380 eV of the ZnO with 130-nm MgO buffer layer in the various ZnO growth temperatures.

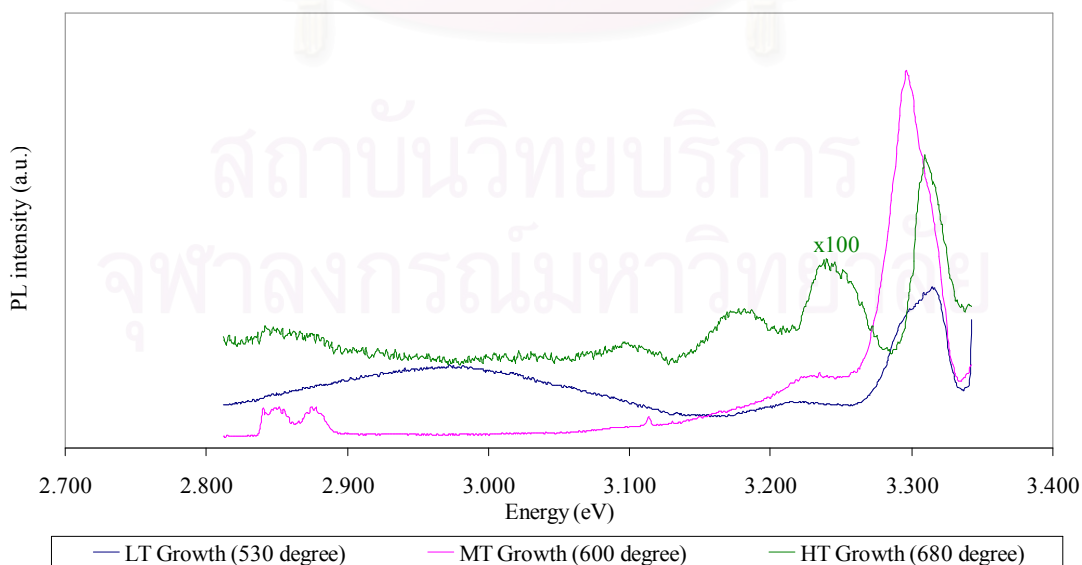


Figure 6.34 PL spectra around 2.800 eV to 3.340 eV of the ZnO with 130-nm MgO buffer layer in the various ZnO growth temperatures.

To improve the ZnO thin film grown on glass substrate, we succeed with higher Zn flux of  $5 \times 10^{-6}$  Torr and higher ZnO growth temperature of 600 °C including MgO buffer layer thickness of around 130 nm. At this point, not only optical property of the ZnO film is good, but also the good structural property with c-orientation can be successful. Anyway, the study about the electrical property is necessary to the further application. Then, it is better to find out the method to improve this property with higher mobility and lower the carrier concentration in undoped film.



สถาบันวิทยบริการ  
จุฬาลงกรณ์มหาวิทยาลัย

## CHAPTER VII

### CONCLUSIONS

This work presents ZnO film growth by MBE technique. The ZnO films grown on various substrates, which are Si, Al<sub>2</sub>O<sub>3</sub> and glass, have been studied; however, it mainly demonstrates the ZnO grown on amorphous glass substrate.

First, a brief overview on the basic knowledge of ZnO crystal structure including the ZnO properties was given. According to material considerations, ZnO is interesting to the optoelectronic applications in the blue and UV regions. To grow high-quality ZnO layer, ZnO substrate is certainly the best choice, however, the price of the ZnO substrate is very expensive. Other cheaper substrates such as Si and Al<sub>2</sub>O<sub>3</sub> with acceptable lattice mismatch are necessary. Therefore, the basic theory of strain of epilayers were reviewed, especially the variation strain with the layer thickness.

*In situ* RHEED observations were used to investigate the crystal quality of the ZnO films grown on various substrates. The structural properties and the surface morphology were characterized by *ex situ* AFM, FE-SEM and XRD. Furthermore, the optical properties and electrical properties were observed by 10K PL and Hall measurement, respectively.

There are many researches about ZnO growth on Si and Al<sub>2</sub>O<sub>3</sub> substrates. Our group has also studied these stories. However, to apply the ZnO optical devices into wide-area devices such as solar cells and TFTs, Si and Al<sub>2</sub>O<sub>3</sub> substrates are not as good as glass in terms of cost and size with the commercial availability. Therefore, the characteristics of ZnO films growth on glass substrates were investigated. The ZnO films grown on glass, however, suffered from high density of cracks because of the large mismatch in thermal expansion coefficients between ZnO and quartz glass. To avoid these problematical cracks, we proposed 2 methods in this work, which are nitrogen doped ZnO flim and MgO-buffer-layer application. To avoid the crack problem via N-doped ZnO, there was no improvement in entire ZnO properties. Also, the nitrogen could not be doped into the film even though the amount of nitrogen gas was increased. Then, the p-type ZnO film could not be fabricated.

The other method proposed to manage the crack problem was MgO buffer layer. The growth of low-temperature MgO buffer layer prior to the growth of ZnO

film is to balance the tensile strain between the grown ZnO film and the glass substrate. Since MgO belongs to II-VI oxide compounds, there is no need to use additional chamber to grow the buffer layer or to develop some special surface protection process. Also, there is no additional problem in device design caused by the buffer layer, which is completely transparent at the wavelength where ZnO based devices work. The surface crack problem was greatly alleviated and at the same time, photoluminescence (PL) characteristics and the roughness of ZnO films with optimum MgO buffer layer thickness were considerably improved. However, the structural property showed no c-orientation.

To improve the quality of the ZnO film grown on glass substrate, other parameters, which are zinc flux, oxygen flow rate and ZnO growth temperature, were considered at the point of the optimum MgO buffer layer thickness. With higher oxygen flow rate, the property of ZnO got worse even though the MgO buffer layer thickness was optimum, 130 nm. On the other hand, the c-orientation including the good properties showed when the Zn flux increased. In additions, the growth temperature effected to the properties of the ZnO film. To grow ZnO film at higher temperature, 600°C, the c-orientation of ZnO film also showed. However, ZnO film grown at very high temperature, 680°C, and the cracks emerged again and the properties got worse. Furthermore, the new peak of PL measurement appeared.

## REFERENCES

- Almamun Ashrafi, A. B. M., Suemune, I., Kumano, H., and Tanaka, S. 2002. Nitrogen-doped p-type ZnO layers prepared with H<sub>2</sub>O vapor-assisted metalorganic molecular-beam epitaxy. Japanese Journal of Applied Physics 41: L1281-L1284.
- Almamun Ashrafi, A. B. M., Zhang, B. P., Binh, N. T., Wakatsuki, K., and Segawa, Y. 2004. High-quality ZnO layers grown on 6H-SiC substrates by metalorganic chemical vapor deposition. Japanese Journal of Applied Physics 43: 1114-1117.
- Arakawa, Y., and Sakaki, H. 1982. Multidimensional quantum well laser and temperature dependence of its threshold current. Applied Physics Letters 40: 939-941.
- Ben, G. S., 1995. Solid State Electronic Devices. Prentice Hall International
- Binh, N. T., Zhang, B. P., Liu, C. Y., Wakatsuki, K., and Segawa, Y., Usami, N., Yamada, Y., Kawasaki, M., and Koinuma, H. 2004. Structural and optical properties of ZnO epitaxial films grown on Al<sub>2</sub>O<sub>3</sub> (11 $\bar{2}$ 0) substrates by metalorganic chemical vapor deposition. Japanese Journal of Applied Physics 43: 4110-4113.
- Charles, M. W., Nick H. Jr., and Gregory E. S. 1989. Physical Properties of Semiconductors. Prentice Hall International
- Chen, S. J., Liu, Y. C., Ma, J. G., Lu, Y. M., Zhang, J. Y., Shen, D. Z., and Fan, X. W. 2003. Effects of thermal treatment on the properties of ZnO films deposited on MgO-buffered Si substrates. Journal of Crystal Growth 254: 86-91.
- Chen, Y., Bagnall, D., and Yao, T. 2000. ZnO as a novel photonic material for the UV region. Materials Science and Engineering B75: 190-198.
- Chen, Y., Hong, S. K., Ko, H. J., Kirshner, V., Wensch, H., Yao, T., Inaba, K., and Segawa, Y. 2001. Effects of an extremely thin buffer on heteroepitaxy with large lattice mismatch. Applied Physics Letters 78: 3352-3354.
- Chen, Y., Ko, H. J., Hong, S. K., and Yao, T. 2000. Layer-by-layer growth of ZnO epilayer on Al<sub>2</sub>O<sub>3</sub> (0001) by using a MgO buffer layer. Applied Physics Letters 76: 559-561.

- Chen, Y., Ko, H. J., Hong, S. K., Yao, T., and Segawa, Y. 2000. Two-dimensional growth of ZnO films on sapphire (0001) with buffer layers. Journal of Crystal Growth 214/215:87-91
- Chen, Y., Tuan, N. T., Segawa, Y., Ko, H. J., Hong, H. K., Yao, T. 2001. Stimulated emission and optical gain in ZnO epilayers grown by plasma-assisted molecular-beam epitaxy with buffers. Applied Physics Letters 78: 1469-1471.
- Choi, H. K. 2004. Long-wavelength infrared semiconductor lasers : Wiley series in lasers and applications
- Choi, J. H., Tabata, H., and Kawai, T. 2001. Initial preferred growth in zinc oxide thin films on Si and amorphous substrates by a pulse laser deposition. Journal of Crystal Growth 226: 493-500.
- Fujihara, S., Sasaki, C., and Kimura, T. 2001. Crystallization behavior and origin of *c*-axis orientation in sol-gel-derived ZnO:Li thin films on glass substrates. Applied Surface Science 180: 341-350.
- Fujita, M., Kawamoto, N., Sasajima, M., and Horikoshi, Y. 2004. Molecular beam epitaxy growth of ZnO using initial Zn layer and MgO buffer layer on Si (111) substrates. Journal Vacuum Science and Technology B 22: 1484-1486.
- Fujita, M., Kawamoto, N., Tatsumi, T., Yamamgishi, K., and Horikoshi, Y. 2003. Molecular beam epitaxial growth of ZnO on Si substrate using ozone as an oxygen source. Japanese Journal of Applied Physics 42: 67-70.
- Fused Quartz Catalogue Q-7A, General Electric Co.  
<http://encyclopedia.thefreedictionary.com>
- Ghosh, R., Basak, D., and Fujihara, S. 2004. Effects of substrate-induced strain on the structural, electrical, and optical properties of polycrystalline ZnO thin films. Journal of Applied Physics 96: 2689-2692.
- Hayamizu, S., Tabata, H., Tanaka, H., and Kawai, T. 1996. Preparation of crystallized zinc oxide films on amorphous glass substrates by pulsed laser deposition. Journal of Applied Physics 80: 787-791.
- Herman M. A., and Sitter H. 1989. Molecular Beam Epitaxy Fundamentals and Current Status. Springer-Verlag
- Hoffman, R. W. 1975. Stresses in thin films: The relevance of grain boundaries and impurities. Thin Solid Films 34: 185-190.

- Hong, S. K., Chen, Y., Wenisch, H., Hanada, T., and Yao, T. 2001. ZnO and related materials: plasma-assisted molecular beam epitaxial growth, characterization, and application. Journal of Electronic Materials 30: 647-658.
- Hong, S. K., Ko, H. J., Chen, Y., and Yao, T. 2000. Defect characterization in epitaxial ZnO/epi-GaN/Al<sub>2</sub>O<sub>3</sub> heterostructures: transmission electron microscope and triple-axis X-ray diffractometry. Journal of Crystal Growth 209: 537-541.
- Iwata, K., Fons, P., Niki, S., Yamada, A., Matsubara, K., Nakahara, K., Tanabe, T., and Takasu, H. 2000. ZnO growth on Si by radical source MBE. Journal of Crystal Growth 214/215: 50-54.
- John, D. B. 2004. Wide bandgap semiconductor substrates: Current status and future trends. The International Conference on Compound Semiconductor Manufacturing Technology
- Kato, H., Miyamoto, K., Sano, M., and Yao, T. 2004. Polarity control of ZnO on sapphire by varying the MgO buffer layer thickness. Applied Physics Letters 84:4562-4564.
- Kato, H., Sano, M., Miyamoto, K., and Yao, T. 2002. Growth and characterization of Ga-doped ZnO layers on a-plane sapphire substrates grown by molecular beam epitaxy. Journal of Crystal Growth 237-239: 538-543.
- Kawamoto, N., Fujita, M., Tatsumi, T., and Horikoshi, Y. 2003. Growth of ZnO on Si substrate by plasma-assisted molecular beam epitaxy. Japanese Journal of Applied Physics 42: 7209-7212.
- Kim, K. S., Kim, H. W., and Kim, N. H. 2003. Structural characterization of ZnO films grown on SiO<sub>2</sub> by the RF magnetron sputtering. Physica B 334: 343-346.
- Kim, K. S., Kim, H. W., and Lee, C. M. 2003. Effect of growth temperature on ZnO thin film deposited on SiO<sub>2</sub> substrate. Materials Science and Engineering B 98: 135-139
- Kim, S. W., Fujita, S., and Fujita, S. 2002. Self-organized ZnO quantum dots on SiO<sub>2</sub>/Si substrates by metalorganic chemical vapor deposition. Applied Physics Letters 81:5036-5038.
- Klein, C. A. 2000. How accurate are Stoney's equation and recent modifications. Journal Applied Physics 88: 5487-5489.

- Li, B. S., Liu, Y. C., Shen, D. Z., Zhang, J. Y., Lu, Y. M., and Fan, X. W. 2003. Effects of RF power on properties of ZnO thin films grown on Si (001) substrate by plasma enhanced chemical vapor deposition. Journal of Crystal Growth 249: 179-185.
- Look, D. C. 2001. Recent advances in ZnO materials and device. Material Science and Engineering B 80: 383-387.
- Look, D. C., Coskun, C., Claffin, B., and Farlow, G. C. 2003. Electrical and optical properties of defects and impurities in ZnO. Physica B 340-342: 32-38.
- Look, D. C., Hemsley, J. W., and Sizelove, J. R. 1999. Residual native shallow donor in ZnO. Physical Review Letters 82: 2552-2555.
- Madelung, O. 1982. Numerical Data and Functional Relationships in Science and Technology New Series Group III Crystal and Solid State Physics. Springer, Heidelberg
- Markoc, H., Strite, S., Gao, G. B., Lin, M. E., Sverdlov, B., and Burns, M. 1994. Large-band-gap SiC, III-V nitride, and II-VI ZnSe-based semiconductor device technologies. Journal of Applied Physics 76: 1363-1398.
- Meyer, B. K., Alves, H., Hofmann, D. M., Kriegseis, W., Forster, D., Bertram, F., Christen, J., Hoffmann, A., Straburg, M., Dworzak, M., Haboek, U., and Rodina, A. V. 2004. Bound exciton and donor-acceptor pair recombinations in ZnO. Physical Status Solidi (b) 241: 231-260.
- Miyamoto, K., Sano, M., Kato, H., and Yao, T. 2002. Effects of ZnO/MgO double buffer layers on structural quality and electron mobility of ZnO epitaxial films grown on c-plane sapphire. Japanese Journal of Applied Physics 41: L1203-L1205.
- Natsume, Y., and Sakata, H. 2000. Zinc oxide films prepared by sol-gel spin-coating. Thin Solid Films 372: 30-36.
- Neumark, G. F. 1997. Defects in wide band gap II-VI crystal. Materials Science and Engineering R21: 1-46.
- Nishinaga, T., Nishioka, K., Harada, J., Sasaki, A., and Takei, H. 1997. Advances in the Understanding of Crystal Growth Mechanisms. Elsevier Science Amsterdam
- O'Reilly, E. P. 1989. Valence band engineering in strained-layer structures. Semiconductor Science and Technology 4: 121-137.



- Ozpineci, B., Tolbert, L. M., Islam, S. K., Chinthavali, M., 2003. Wide Bandgap Semiconductors for Utility Applications. IASTED International Conference on Power and Energy Systems (PES)
- Pallab, B. 1997. Semiconductor Optoelectronic Devices. Prentice Hall International
- Pearson, S. J., Abernathy, C. R., Overberg, M. E., Thaler, G. T., Norton, D. P., Theodoropoulou, N., Hebard, A. F., Park, Y. D., Ren, F., Kim, J., and Boatner, L. A. 2002. Wide band gap ferromagnetic semiconductors and oxides. Applied Physics Reviews-Focus Review 93: 1-13.
- Phillips, M. C., Wang, M. W., Swenberg, J. F., McCaldin, J. O., and McGill, T. C. 1992. Proposal and verification of a new visible light emitter based on wide band gap II-VI semiconductors. Applied Physics Letters 61:1962-1964.
- Pinardi, K., Jain, U., Jain, S. C., Maes, H. E., Overstraeter, R. V., and Willander, M. 1998. Critical thickness and strain relaxation in lattice mismatched II-VI semiconductor layers. Journal of Applied Physics 83: 4724-4733.
- Riemann, T., Christen, J., Kaczmarczyk, G., Kaschner, A., Hoffmann, A., Zeuner, A., Hofmann, D., and Meyer, B. K. 2002. Microscopic analysis of high quality thick ZnO CVD layers: Imaging of growth domains, strain relaxation, and impurity incorporation. Physical Status Solidi (b) 229: 891-895.
- Schildknecht, A., Sauer, R., and Thonke, K. 2003. Donor-related defect states in ZNO substrate material. Physica B 340-342: 205-209.
- Setiawan, A., Ko, H. J., Hong, S. K., Chen, Y., and Yao, T. 2003. Study on MgO buffer in ZnO layers grown by plasma-assisted molecular beam epitaxy on Al<sub>2</sub>O<sub>3</sub> (0001). Thin Solid Films 445: 213-218.
- Setiawan, A., Ko, H. J., Hong, S. K., Chen, Y., and Yao T. 2003. Study on MgO buffer in ZnO layers grown by plasma-assisted molecular beam epitaxy on Al<sub>2</sub>O<sub>3</sub> (0001). Thin Solid Films 445: 213-218.
- Shan, F. K., and Yu, Y. S. 2003. Optical properties of pure and Al doped ZnO thin films fabricated with plasma produced by excimer laser. Thin Solid Films 435: 174-178.
- Spaepen, F. 2000. Interfaces and stresses in thin films. Acta Material 48: 31-42.
- Srikant, V., and Clarke, D. R. 1997. Optical absorption edge of ZnO thin films: The effect of substrate. Journal of Applied Physics 81: 6357-6364.
- Strassburg, M., Rodina, A., Dworzak, M., Habocek, U., Krestnikov, I. L., Hoffmann, A., Gelhausen, O., Phillips, M. R., Alves, H. R., Zeunar, A., Hofmann, D. M.,

- and Meyer, B. K. 2004. Identification of bound exciton complexes in ZnO. Physical Status Solidi (b) 241: 607-611.
- Suresh, J., Magnus W., and Van, R. 2000. Compound Semiconductors Strained Layers and Devices. Kluwer Academic Publisher
- Tatsumi, T., Fujita, M., Kawamoto, N., Sasajima, M., and Horikoshi, Y. 2004. Intrinsic defects in ZnO films grown by molecular beam epitaxy. Japanese Journal of Applied Physics 43: 2602-2606.
- Townsend, P. H., Barnett, D. M., and Brunner, D. A. 1987. Elastic relationships in layered composite media with approximation for the case of thin films on a thick substrate. Journal of Applied Physics 62: 4438-4444.
- Vipute, R. D., Talyansky, V., Choopun, S., Sharma, R. P., Venkatesan, T., He, M., Tang, X., Halpern, J. B., Spencer, M. G., Li, Y. X., Salamanca-Riba, L. G., Iliadis, A. A., and Jones, K. A. 1998. Heteroepitaxy of ZnO on GaN and its implications for fabrication of hybrid optoelectronic devices. Applied Physics Letters 73: 348-350.
- Wang, Z., Zhang, H., Zhang, L., Yuan, Y., Yan, S., and Wang, C. 2003. Structure and strong ultraviolet emission characteristics of amorphous ZnO films grown by electrophoretic deposition. Journal of Materials Research 18: 151-155.
- Yamauchi, S., Goto, Y., and Hariu, T. 2004. Photoluminescence studies of undoped and nitrogen-doped ZnO layers grown by plasma-assisted epitaxy. Journal of Crystal Growth 260: 1-6.
- Yoshino, Y., Makino, T., Katayama, Y., and Hata, T. 2000. Optimization of zinc oxide thin film for surface acoustic wave filters by radio frequency sputtering. Vacuum 59: 538-545.
- Zeuner, A., Alves, H., Hofmann, D. M., Meyer, B. K., Hoffmann, A., Habocek, U., Strassburg, M., and Dworzak, M. 2002. Optical properties of the nitrogen acceptor in epitaxial ZnO. Physical Status Solidi (b) 234: R7-R9.
- Zhao, J. H., Du, Y., Morgan, M., and Ho, P.S. 1999. Simultaneous measurement of Young's modulus, Poisson ratio, and coefficient of thermal expansion of thin films on substrates. Journal of Applied Physics 87: 1575-1577.



**APPENDIX**

สถาบันวิทยบริการ  
จุฬาลงกรณ์มหาวิทยาลัย

## List of Publications

### 1. International Journals and International Conferences

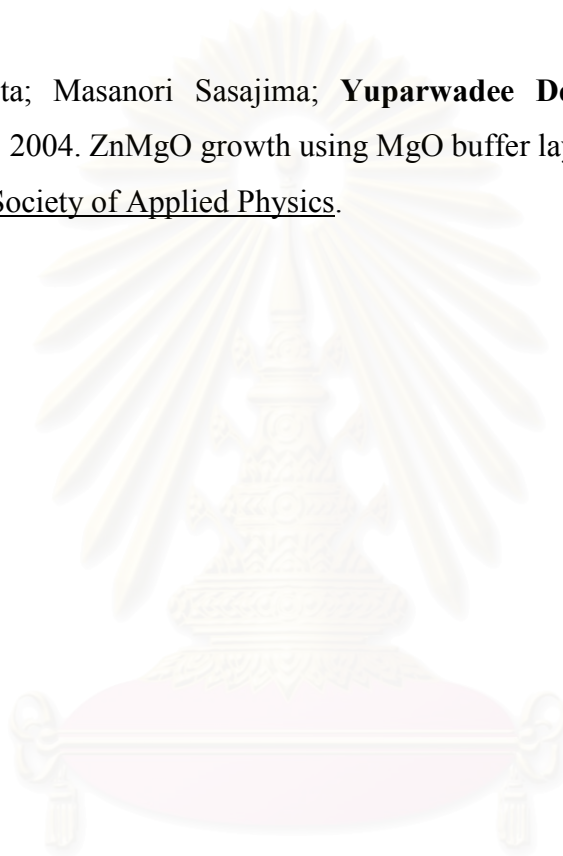
1. **Yuparwadee Deesirapiat**; Choopol Antarasena; Miki Fujita; Masanori Sasajima; Ryotaro Suzuki; and Yoshiji Horikoshi. 2004. Crack-free ZnO layer growth on glass substrate by MgO buffer layer. Compound Semiconductors 184: 304-307.
2. **Yuparwadee Deesirapiat**; Miki Fujita; Masanori Sasajima; Ryotaro Suzuki; Choopol Antarasena; and Yoshiji Horikoshi. 2005. Effects of the MgO-buffer layer on surface morphology with structural and optical properties of polycrystalline ZnO films grown on glass substrate. Japanese Journal of Applied Physics 44: 5150-5155.
3. Miki Fujita; Masanori Sasajima; **Yuparwadee Deesirapiat**; and Yoshiji Horikoshi. 2004. ZnMgO growth using MgO buffer layers on Si (111) substrates. Journal of Crystal Growth 278: 293-298.

### 2. Domestic Journals and Domestic Conferences

1. **Yuparwadee Deesirapiat**; Dasapich Thongnopnua; Supachok Thainoi; Songphol Kanjanachuchai; Somchai Ratanathammaphan; and Choopol Antarasena. 2003. Fabrication of the Symmetrical Emitter-Collector Zinc-doped Planar GaAlAs/GaAs Double Heterojunction Bipolar Transistors Using Two-stage LPE. Proceedings of RGJ-Ph.D. Congress IV.
2. **Yuparwadee Deesirapiat**; Dasapich Thongnopnua; Supachok Thainoi; Songphol Kanjanachuchai; Somchai Ratanathammaphan; and Choopol Antarasena. 2002. Fabrication of the Symmetrical Emitter-Collector Zinc-doped

Planar GaAlAs/GaAs Double Heterojunction Bipolar Transistors Using Two-stage LPE. Proceedings of the 25rd Electrical Engineering Conference.

3. **Yuparwadee Deesirapiat**; Choopol Antarasena; Miki Fujita; Masanori Sasajima; Ryotaro Suzuki; and Yoshiji Horikoshi. 2004. Crack-free ZnO layer growth on glass substrate by MgO buffer layer. Japanese Society of Applied Physics.
4. Miki Fujita; Masanori Sasajima; **Yuparwadee Deesirapiat**; and Yoshiji Horikoshi. 2004. ZnMgO growth using MgO buffer layers on Si (111) substrates. Japanese Society of Applied Physics.



สถาบันวิทยบริการ  
จุฬาลงกรณ์มหาวิทยาลัย

## List of Presentations

### 1. International Presentations

- *Oral presentation*

**Yuparwadee Deesirapiat**; Choopol Antarasena; Miki Fujita; Masanori Sasajima; Ryotaro Suzuki; and Yoshiji Horikoshi. Crack-free ZnO layer growth on glass substrate by MgO buffer layer. 31<sup>st</sup> International Symposium on Compound Semiconductor (ISCS), Seoul, South Korea, Sep 12-16 (2004).

- *Oral presentation*

**Yuparwadee Deesirapiat**; Choopol Antarasena; Miki Fujita; Masanori Sasajima; and Yoshiji Horikoshi. Crack-free ZnO layer growth on glass substrate by MgO buffer layer. 2<sup>nd</sup> Fieldwise Seminar on Nanoelectronics and Photonics, Hanoi, Vietnam, Nov 14-15 (2005).

- *Poster presentation*

Miki Fujita; Masanori Sasajima; **Yuparwadee Deesirapiat**; and Yoshiji Horikoshi. ZnMgO growth using MgO buffer layers on Si (111) substrates. The 13<sup>th</sup> International Conference on Molecular Beam Epitaxy. Edinberg, Scotland, Sep 25-28 (2004).

- *Poster presentation*

Miki Fujita; Ryotaro Suzuki; Masanori Sasajima; Tomohiro Kosaka; **Yuparwadee Deesirapiat**; and Yoshiji Horikoshi. 2005. ZnMgO/ZnO/ZnMgO single quantum well structure on Si (111) substrate. 23<sup>rd</sup> North American Conference on Molecular Beam Epitaxy. Santa Barbara, USA, Sep 11-14 (2005).

## 2. Domestic Presentations

- *Oral presentation*

**Yuparwadee Deesirapipat**; Dasapich Thongnopnua; Supachok Thainoi; Songphol Kanjanachuchai; Somchai Ratanathammaphan; and Choopol Antarasena. 2002. Fabrication of the Symmetrical Emitter-Collector Zinc-doped Planar GaAlAs/GaAs Double Heterojunction Bipolar Transistors Using Two-stage LPE. Proceedings of the 25<sup>rd</sup> Electrical Engineering Conference, Songklanakarin University, Songkla, Thailand, Nov 21-22 (2002).

- *Oral presentation*

**Yuparwadee Deesirapipat**; Dasapich Thongnopnua; Supachok Thainoi; Songphol Kanjanachuchai; Somchai Ratanathammaphan; and Choopol Antarasena. 2003. Fabrication of the Symmetrical Emitter-Collector Zinc-doped Planar GaAlAs/GaAs Double Heterojunction Bipolar Transistors Using Two-stage LPE. Proceedings of RGJ-Ph.D. Congress IV, Jomtien Palm Beach Hotel, Chonburi, Thailand, Apr 25-27 (2003).

- *Oral presentation*

**Yuparwadee Deesirapiat**; Choopol Antarasena; Miki Fujita; Masanori Sasajima; Ryotaro Suzuki; and Yoshiji Horikoshi. 2004. Crack-free ZnO layer growth on glass substrate by MgO buffer layer. Japanese Society of Applied Physics, Tohoku University, Sendai, Japan, Sep 1-4 (2004).

- *Oral presentation*

Miki Fujita; Masanori Sasajima; **Yuparwadee Deesirapipat**; and Yoshiji Horikoshi. 2004. ZnMgO growth using MgO buffer layers on Si (111) substrates. Japanese Society of Applied Physics, Tohoku University, Sendai, Japan, Sep 1-4 (2004).

- *Poster presentation*

**Yuparwadee Deesirapiat**; Choopol Antarasena; Miki Fujita; Masanori Sasajima; Ryotaro Suzuki; and Yoshiji Horikoshi. 2004. Crack-free ZnO layer

growth on glass substrate by MgO buffer layer. Center of Excellence (COE) Program, Waseda University, Tokyo, Japan, Dec 21-22 (2004).

- *Poster presentation*

Miki Fujita; Masanori Sasajima; **Yuparwadee Deesirapipat**; and Yoshiji Horikoshi. 2004. ZnMgO growth using MgO buffer layers on Si (111) substrates. Center of Excellence (COE) Program, Waseda University, Tokyo, Japan, Dec 21-22 (2004).



สถาบันวิทยบริการ  
จุฬาลงกรณ์มหาวิทยาลัย



## VITAE

Yuparwadee Deesirapipat was born in Bangkok, Thailand on November 17, 1976. In June 1994, she entered into Chulalongkorn University and received the Bachelor of Engineering in Electrical Engineering Program in May 1998. She continued studying the Graduate School of Chulalongkorn University in June 1998, as a Master student. Her work is financial supported by National Science and Technology Development Agency (NSTDA) through “Sis Kon Kut” Program.

After her Master graduation, she worked at FabriNET as a process engineer. Since June 2002, she returned to the Graduate School of Chulalongkorn University, as a Ph.D. student and received Royal Golden Jubilee Scholarship from Thailand Research Fund.

Between October 2003 and March 2005, she received the Waseda Student Exchange Scholarship and worked in Horikoshi Laboratory, the School of Science and Engineering, Waseda University, Tokyo, Japan. Her research activity there is the study of ZnO film grown on amorphous glass substrate by molecular beam epitaxy. Between June 2005 and September 2005, she received the RGJ Scholarship for doing a short research program, which relates to her previous research, at the same laboratory in Waseda University.

สถาบันวิทยบริการ  
จุฬาลงกรณ์มหาวิทยาลัย

## Crack-free ZnO layer growth on glass substrates by MgO-buffer layer

Y Deesirapipat, C Antarasena

Department of Electrical Engineering, Chulalongkorn University,  
Bangkok, 10330, Thailand

M Fujita, M Sasajima, R Suzuki, Y Horikoshi

School of Science and Engineering, Waseda University, 3-4-1 Okubo,  
Shinjuku-ku, Tokyo, 169-0051, Japan

**Abstract.** ZnO grown on glass substrates by various thickness of MgO buffer layer has been investigated. All the layers are deposited by plasma-assisted molecular beam epitaxy. Without the MgO buffer layer, the surface cracks, due to the difference in the thermal expansion coefficients between ZnO and glass, are clearly observed. These cracks are drastically decreased with the MgO insertion. The photoluminescence emission intensity is also improved by increasing the buffer layer thickness until the optimum MgO thickness of 145 nm is reached. Few cracks start appearing with the reduction of the PL intensity when the buffer layer thickness is more than the optimised one. All of as-grown ZnO films without cracks exhibit n-type conductivity.

### 1. Introduction

Recently, ZnO is receiving a great deal of attention as a promising material for the optoelectronic applications to the blue and ultraviolet regions because of its wide direct bandgap of 3.37 eV at room temperature and high exciton binding energy of 60 meV which opens the possibility of exploiting excitonic effects in room temperature devices. ZnO has been grown on various substrates such as ScAlMgO<sub>4</sub> [1], Al<sub>2</sub>O<sub>3</sub> [2,3], Si [4], CaF<sub>2</sub> [5], and etc. However, to apply the ZnO optical devices into wide-area devices such as solar cells and TFTs, they are not as good as glass in terms of cost and size with the commercial availability. Therefore, the study of the ZnO growth on glass substrate is useful. The ZnO films grown on glass, however, suffer from high density of cracks because of the large mismatch in thermal expansion coefficients between ZnO and quartz glass.

To avoid these problematical cracks, we propose the growth of low-temperature (LT) MgO buffer layer prior to the growth of ZnO for balancing the tensile strain between the grown ZnO film and the glass substrate. Furthermore, since MgO belongs to II-VI oxide compounds, there is no need to use additional chamber to grow the buffer layer or to develop some special surface protection process. Also, there is no additional problem in device design caused by the buffer layer, which is completely transparent at the wavelength where ZnO based devices work [2]. The surface crack problem is

greatly alleviated and at the same time, photoluminescence (PL) characteristics are considerably improved.

## 2. Experiment

Epitaxial ZnO films are grown on amorphous glass substrates by plasma-assisted molecular beam epitaxy (MBE) with employing a MgO buffer layer. Elemental Zn (6N) and Mg (4N) are evaporated using a conventional effusion cell. Pure oxygen (5N) is used as the oxygen source and oxygen plasma is supplied by a radio-frequency (RF) activated plasma cell. First, the glass substrate is degreased in acetone and ethanol in an ultrasonic cleaner followed by rinsing in DI-water. Prior to growth, the clean substrate is inserted into an ultrahigh-vacuum chamber and annealed at 790°C for half an hour. Then, the substrate temperature is decreased to grow the LT-MgO buffer layer by oxygen plasma at 450°C. The LT-MgO buffer layer is then annealed at 680°C for 10 minutes in oxygen ambient. After this annealing process, the substrate temperature is decreased to the ZnO growth temperature of 530°C. The ZnO growth is performed at a growth rate of 7 nm/min for 2 hours under oxygen-enriched condition. The oxygen flow rate is fixed at 1.07 sccm with an RF power of 350 W. The beam equivalent pressure (BEP) of Zn is  $4.0 \times 10^{-6}$  Torr. The buffer layer thickness is varied from 0 to 300 nm. The surface morphology measurement is performed by optical microscope and FE-SEM. The optical property is investigated by PL measurement at 10 K using a He-Cd laser (325 nm) as an excitation source. The electrical property is investigated by Hall measurement with van der Pauw method.

## 3. Results and discussions

ZnO films directly grown on the glass substrates exhibit high density of cracks is clearly observed by both optical microscope and FE-SEM. Figure 1 shows the surface morphology of the ZnO with and without MgO buffer layer observed by an optical microscope. Without MgO buffer layer, surface cracks appear as shown in figure 1 (a). This phenomenon appears regardless of the substrate temperature as well as the ramp rate of the substrate temperature after growth. Thus, the cracks are probably caused by the difference in the thermal expansion coefficient between the quartz glass ( $5.5 \times 10^{-7} \text{ K}^{-1}$ ) [6] and ZnO ( $4.75 \times 10^{-6} \text{ K}^{-1}$ ) [7]. While the substrate is cooled down to room temperature after growth, tensile strain from the substrate affects the ZnO layer, which results in the formation of cracks as occur in the same condition of Si substrate ( $2.56 \times 10^{-6} \text{ K}^{-1}$ ) [4]. When the LT-MgO buffer layer is inserted, the surface cracks disappear almost completely as shown in figure 1 (b). The thermal expansion coefficient of MgO is  $1.04 \times 10^{-5} \text{ K}^{-1}$  [7], which is much larger than both glass and ZnO. Thus, the tensile strain from the glass substrate is relaxed by the compressive stress component due to the buffer layer implement to the ZnO layer [4]. When the MgO buffer layer is approximately 170 nm and thicker, few cracks still remain. However, they disappear by using the thin buffer layers of 145 nm and thinner. Therefore, the surface crack free ZnO films are grown on glass substrates by optimising the MgO buffer layer thickness.

To investigate the optical property of ZnO film grown by using a MgO buffer layer, PL measurement is carried out and compared with those obtained in the samples with various MgO buffer layer thickness including the samples directly grown on the substrate without the buffer layer. The typical near-band-edge PL measurement indicates that the samples with annealed MgO buffer layer show higher intensity than those without annealed buffer layer. The emission lines located at 3.358 eV and 3.368 eV dominate the spectrum in all samples. The emission peak at 3.358 eV is the donor-bound exciton related to the oxygen vacancy [3], whereas the emission peak at 3.368 eV

is the ionized donor bound exciton emission [8]. The PL characteristics of ZnO films are improved considerably by using annealed MgO buffer layer.

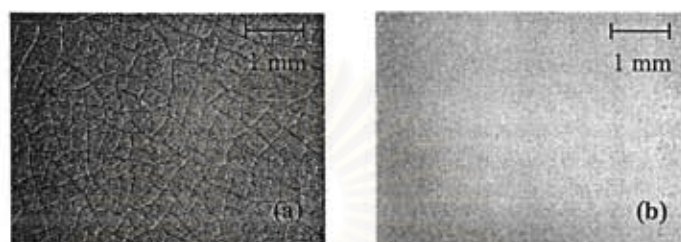


**Figure 1.** ZnO surface images by optical microscope: (a) without LT-MgO buffer layer (b) 145-nm LT-MgO buffer layer.

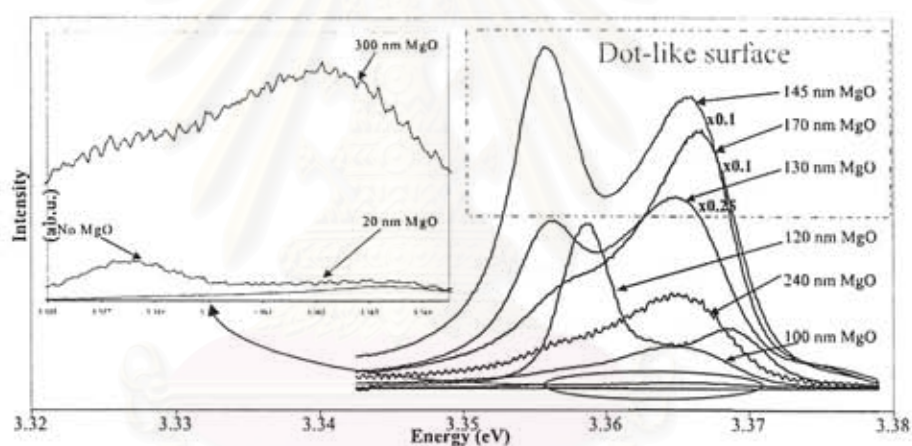


**Figure 2.** PL spectra of the annealed MgO buffer layer samples with various buffer layer thickness.

The PL spectra of the annealed MgO buffer layer samples with various buffer layer thickness are shown in figure 2. The inset of figure 2 also shows the PL spectra of the samples without MgO buffer layer, with thin (20-nm) buffer layer, and with thick (300-nm) MgO layer. The intensity of these three samples is pretty weak, compared to the other samples. The lattice mismatch-induced inhomogeneous strain distribution results in a Stokes shift of  $< 5\text{meV}$ . The minimum PL intensity is from the sample without the MgO buffer layer. The intensity of the donor-bound excitonic emission increases with the buffer layer thickness until it reaches 145 nm when the strongest PL intensity is observed among all the samples. However, the PL intensity starts decreasing for further increase of MgO buffer layer thickness. Therefore, the optimum buffer layer thickness probably lies around 145 nm. It should be pointed out that the decrease of PL intensity and the formation of surface cracks occur at the same MgO buffer layer thickness.

When the MgO buffer layer thickness is 145 nm and thinner, crack-free ZnO films are grown. The electrical characteristics of all grown ZnO films without cracks exhibit n-type conductivity in the range of  $2.17 \times 10^{17}$ - $1.76 \times 10^{18}$  cm<sup>-3</sup>. All these samples, however, show pretty low electron mobility (5 cm<sup>2</sup>/V-s). The observed resistivities are in the range of  $10^3$ - $10^5$  Ωcm.

#### 4. Summary

Epitaxial ZnO films with various MgO buffer layer thickness have been grown on glass substrates by plasma-assisted molecular beam epitaxy. The directly grown ZnO film on the glass substrate results in a high density of cracks, caused by the thermal expansion coefficient mismatch between ZnO and glass. It is found that these cracks disappear by applying the thin MgO buffer layer prior to the growth of ZnO. This crack-free condition also enhances the PL intensity of grown ZnO layer. The optimum MgO layer thickness in the present study is approximately 145 nm. The crack-free samples exhibit n-type conductivity.

#### Acknowledgements

This work is partly supported by the Thailand Research Fund (TRF) through His Majesty the King's Golden Jubilee Ph.D. program, by a Grant-in-Aid for Scientific Research on Priority Areas program "Photonics Based on Wavelength Integration and Manipulation", by the COE Program "Molecular Nano-Engineering", and by the 21<sup>st</sup> century COE "Practical Nano-Chemistry" from the Ministry of Education, Culture, Sports, Science, and Technology, Japan.

#### References

- [1] Y.F. Chen, S.K. Hong, H.J. Ko, M. Nakajima, T. Yao, and Y. Segawa 2000 *Appl. Phys. Lett.* 76 245-247
- [2] A. Setiawan, H.J. Ko, S.K. Hong, Y. Chen, and T. Yao 2003 *Thin Solid Films* 445 213-218
- [3] T. Tatsumi, M. Fujita, N. Kawamoto, M. Sasajima and Y. Horikoshi 2004 *JJAP* Vol. 43 No. 5A 2602-2606
- [4] M. Fujita, N. Kawamoto, M. Sasajima, and Y. Horikoshi 2004 *J. Vac. Sci. Technol.* B22 (3) 1-3
- [5] H.J. Ko, Y.F. Chen, J.M. Ko, T. Hanada, Z. Zhu, T. Fukuda, and T. Yao 1999 *J. Cryst. Growth.* 207 87-94
- [6] Fused Quartz Catalogue Q-7A, General Electric Company <http://encyclopedia.thefreedictionary.com>
- [7] O. Madelung 1982 *Numerical Data and Functional Relationships in Science and Technology New Series Group III Crystal and Solid State Physics Vol.22 Subvolumn a 14-15* 44-45
- [8] B.K. Meyer, H. Alves, D.M. Hofmann, W. Kriegseis, D. Forster, F. Bertram, J. Christen, A. Hoffmann, M. Dworzak, U. Habocek, and A.V. Rodina 2004 *phys. stat. sol. (b)* 241 No. 2 231-260

## Effects of MgO-Buffer Layer on the Structural and Optical Properties of Polycrystalline ZnO Films Grown on Glass Substrate

Yuparwadee DEESIRAPIPAT<sup>1,2\*</sup>, Miki FUJITA<sup>1</sup>, Masanori SASAJIMA<sup>1</sup>, Ryotaro SUZUKI<sup>1</sup>, Choompol ANTARASENA<sup>2</sup> and Yoshiji HORIKOSHI<sup>1</sup>

<sup>1</sup>*School of Science and Engineering, Waseda University, 3-4-1 Okubo, Shinjuku-ku, Tokyo 169-0051, Japan*

<sup>2</sup>*Department of Electrical Engineering, Chulalongkorn University, Bangkok 10330, Thailand*

(Received September 27, 2004; accepted March 29, 2005; published July 8, 2005)

Characteristics of ZnO films grown on glass substrates with various MgO buffer layer thicknesses have been investigated. All the layers are deposited by plasma-assisted molecular beam epitaxy. Without the MgO buffer layer, surface cracks due to the difference in the thermal expansion coefficients between ZnO and the quartz substrate are easily observed. With the MgO buffer layer, the cracks drastically decrease. The surface morphology changes with different MgO buffer layer thicknesses due to the compressive-tensile stress balance. The ZnO films with a medium MgO buffer layer thickness show a dotlike surface. All samples except those with the dotlike surface exhibit *c*-axis oriented polycrystalline structures. The photoluminescence emission intensity is also improved by increasing the buffer layer thickness until the optimum MgO buffer layer thickness of approximately 150 nm is reached. Few cracks appear with the reduction of the photoluminescence (PL) intensity when the buffer layer thickness is more than the optimum value. All of the as-grown ZnO films without cracks exhibit *n*-type conductivity. [DOI: 10.1143/JJAP.44.5150]

KEYWORDS: crack, polycrystalline ZnO, LT-MgO buffer layer, MBE, dotlike surface

### 1. Introduction

The increased interest in ZnO due to its outstanding excitonic properties, wide direct band gap of 3.37 eV at room temperature, and high exciton binding energy of 60 meV has recently stimulated the investigation of its characteristics as a promising material for optoelectronic applications in the blue and ultraviolet regions. ZnO films have been grown on a variety of substrates such as sapphire<sup>1,2)</sup> and silicon.<sup>3)</sup> However, for application ZnO films are not as good as glass in terms of cost, size, and commercial availability.

A number of different techniques have been utilized to prepare the ZnO thin films on glass substrates, such as the sol-gel method,<sup>4,5)</sup> metalorganic chemical vapour deposition (MOCVD),<sup>6)</sup> pulse laser deposition (PLD),<sup>7)</sup> and sputtering.<sup>8,9)</sup> However, molecular beam epitaxy (MBE) offers the precision to control parameters during growth, with ultrahigh-vacuum conditions and reliable measurements on a variety of complicated layer designs. An extremely thin layer can also be achieved, and better structural and optical properties can be obtained.

ZnO films grown directly on glass substrates, however, result in a high density of cracks due to the thermal expansion coefficient mismatch between ZnO film and the quartz glass substrate. Therefore, a buffer layer between the ZnO layer and the glass substrate may be a possible method of preventing cracks. To select the proper buffer layer for this purpose, the buffer material should be from II-VI compounds to avoid impurity problems. Furthermore, the correct thermal expansion coefficient of the buffer layer is also necessary to solve this problem since it is the tensile strain from the glass substrate affecting the ZnO films that results in many cracks. The compressive stress of the ZnO film, a consequence of the buffer-layer insertion, must then balance this tensile strain in ZnO films. When the material selected for use as a buffer layer has a thermal expansion

coefficient smaller than those of both ZnO and the glass, tensile strain, even though compressive stress is generated, will appear at the interface between the buffer layer and ZnO and may lead to the appearance of some cracks. With a buffer material with a thermal expansion coefficient lying between those of ZnO and glass, only tensile strain will remain, but it will be lower than that without a buffer layer. Thus, the required buffer layer should have a higher thermal coefficient than both ZnO and the quartz glass substrate. MgO is one of the best choices using these selection rules.

In this study, ZnO films are grown on glass substrates with various MgO buffer layer thicknesses. Low-temperature (LT) MgO is applied as a buffer layer prior to the ZnO growth to alleviate the cracking problem. Due to the characteristics of II-VI oxide compounds of MgO, there is no special need to use an additional chamber to grow the buffer layer or to develop a special surface protection process. Also, there are no additional problems in device design caused by the buffer layer, which is completely transparent at the wavelength where ZnO-based devices operate.<sup>1)</sup> The surface morphology, including the structural, optical and electrical properties, is investigated.

### 2. Experiment

ZnO epilayers are grown on amorphous glass substrates by plasma-assisted MBE employing a MgO buffer layer. Elemental Zn (6N) and Mg (4N) are evaporated using a conventional effusion cell. Pure oxygen (5N) is used as the oxygen source and oxygen plasma is supplied by a radio-frequency (RF)-activated plasma cell. First, the glass substrate is degreased in acetone and ethanol in an ultrasonic cleaner followed by rinsing in deion (DI)-water. Prior to growth, the clean substrate is inserted into an ultrahigh-vacuum chamber and annealed at 790°C for 30 min. Then, the substrate temperature is decreased to grow the LT-MgO buffer layer by oxygen plasma at 450°C. The LT-MgO buffer layer is then annealed at 680°C for 10 min in oxygen ambient. After this annealing process, the substrate temperature is decreased to the ZnO growth temperature of 530°C.

\*E-mail address: Yuparwadee.D@student.chula.ac.th

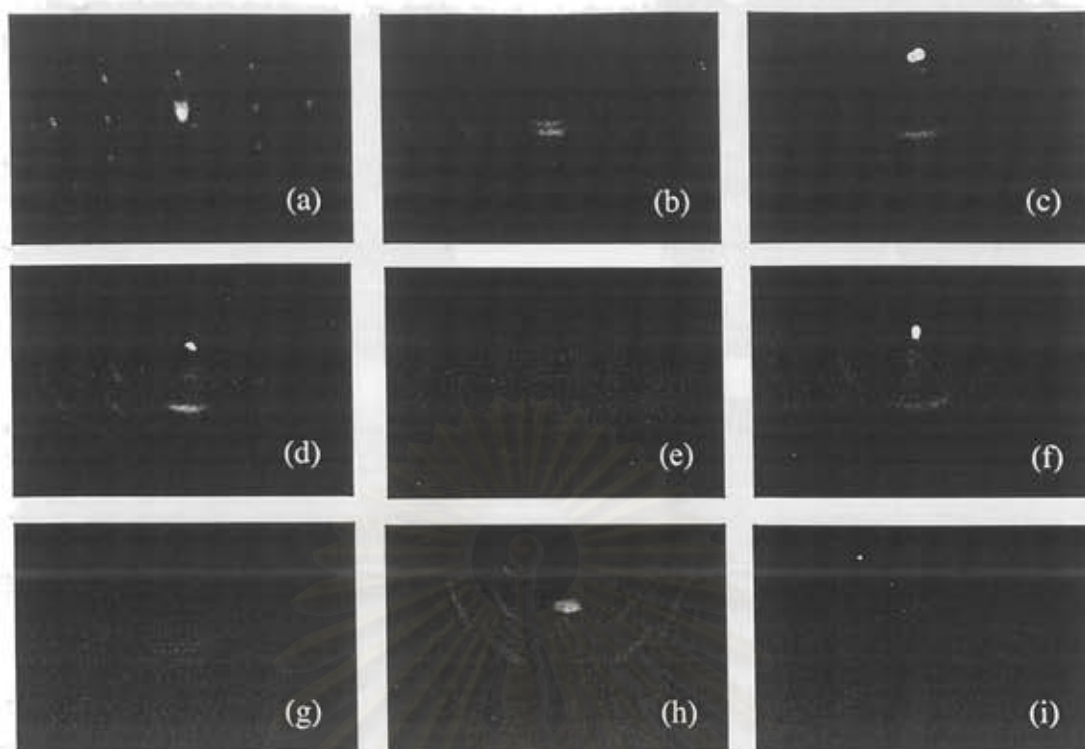


Fig. 1. RHEED patterns of the ZnO films as a function of the MgO buffer layer thickness: (a) 0 nm, (b) 20 nm, (c) 100 nm, (d) 120 nm, (e) 130 nm, (f) 145 nm, (g) 170 nm, (h) 240 nm, and (i) 300 nm.

ZnO growth proceeds at a growth rate of 7 nm/min for 2 h under oxygen-enriched conditions. The oxygen flow rate is fixed at 1.07 sccm with an RF power of 350 W. The beam equivalent pressure (BEP) of Zn is  $4.0 \times 10^{-6}$  Torr. The MgO buffer layer thickness is varied from 0 to 300 nm.

The morphology evolution is monitored in situ by reflection high-energy electron diffraction (RHEED). The surface morphology measurement is performed by optical microscopy, field-emission scanning electron microscopy (FE-SEM), and atomic force microscopy (AFM). The structural characterization is inspected using X-ray diffraction (XRD),  $2\theta$ - $\omega$  scan and pole figures. The optical property is investigated by photoluminescence (PL) measurement at 10 K using a He-Cd laser (325 nm) as an excitation source. The electrical property is investigated by Hall measurement applying the Van der Pauw method.

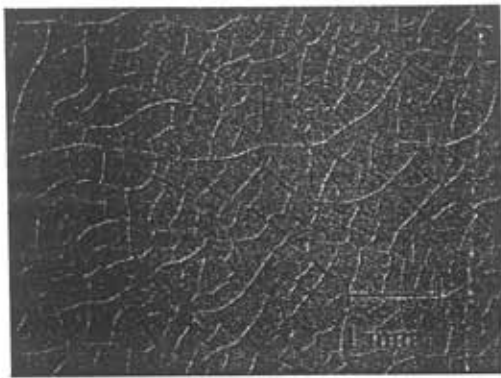
### 3. Results and Discussions

First, the ZnO crystal quality is examined with various thicknesses of the MgO buffer layer during growth by RHEED. Figure 1 shows RHEED patterns from the surface of ZnO epitaxial layers after 2-h (approximately 700 nm) growth with different MgO buffer layer thicknesses. Without the buffer layer, no RHEED pattern appears during the beginning of the growth. A ring pattern appears 10 min after the ZnO growth starts. Then, the pattern develops into the fixed spotty pattern shown in Fig. 1(a). With the MgO buffer layer, however, ring patterns appear from the very beginning of MgO growth. The ring patterns become clear during growth and finally change into ring-to-spot patterns, as shown in Figs. 1(b)–1(i). A fixed pattern emerged during growth for all samples, which implies a polycrystalline structure. Among these samples, the RHEED patterns of the

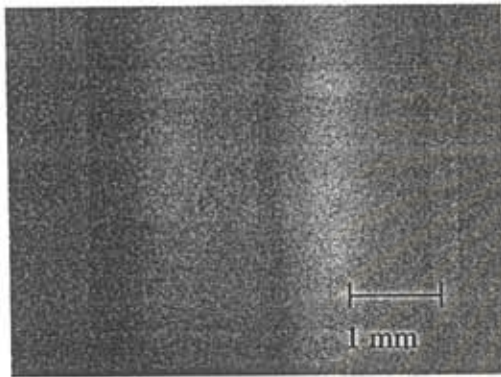
130-nm, 145-nm and 170-nm MgO buffer layer samples, as shown in Figs. 1(e)–1(g), respectively, appear ringlike, indicating a higher disorder in the crystal quality.

Surface morphology investigated by optical microscopy is shown in Fig. 2. A high density of cracks is clearly observed in the ZnO films directly grown on the glass substrates, as shown in Fig. 2(a), and drastically decreases when the MgO buffer layer is used, as shown in Fig. 2(b). Regardless of the substrate temperature and the ramp rate of the substrate temperature after growth, surface cracks always appear in the samples without the MgO buffer layer. The thermal expansion coefficient mismatch between the quartz glass ( $5.5 \times 10^{-7} \text{ K}^{-1}$ )<sup>10</sup> and ZnO ( $4.75 \times 10^{-6} \text{ K}^{-1}$ )<sup>11</sup> probably causes these cracks. Tensile strain from the substrate affects the ZnO layer while the substrate is cooled to room temperature after growth, which results in the formation of cracks, as occurs under the same conditions with a Si substrate ( $2.56 \times 10^{-6} \text{ K}^{-1}$ ).<sup>3</sup> The surface cracks are greatly alleviated when the LT-MgO buffer layer is inserted, as described above. The thermal expansion coefficient of MgO ( $1.04 \times 10^{-5} \text{ K}^{-1}$ )<sup>11</sup> is much larger than those of both glass and ZnO. Thus, the tensile strain from the glass substrate is relieved by the compressive stress component relating to the MgO buffer layer's effect on the ZnO layer.<sup>3</sup> For 170 nm and thicker MgO buffer layers, a few cracks remain. However, they disappear completely when a thinner MgO buffer layer ( $\leq 150$  nm) is used. Therefore, surface-crack-free ZnO films are grown on glass substrates by controlling the MgO buffer layer thickness.

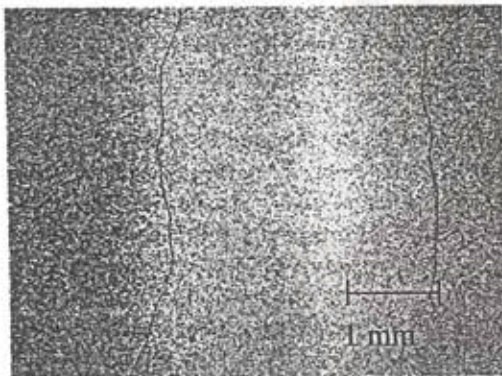
ZnO surface morphology can also be observed by FE-SEM, as shown in Fig. 3. The surface morphology of the samples without a MgO buffer layer and those with a MgO buffer layer thinner than 130 nm look similar, as shown in



(a)



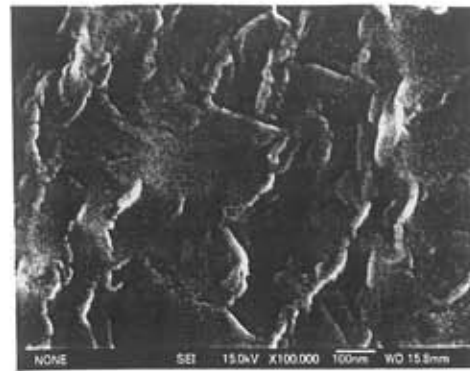
(b)



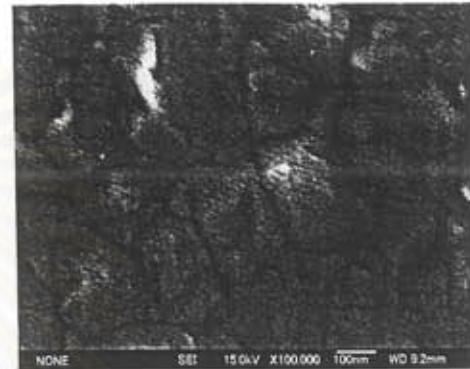
(c)

Fig. 2. ZnO surface images obtained using optical microscope: (a) without LT-MgO buffer layer, (b) 145-nm LT-MgO buffer layer, and (c) 170-nm LT-MgO buffer layer.

Fig. 3(a). With 130-nm, 145-nm and 170-nm buffer layers, the surface appears as dot combinations, as shown in Fig. 3(b). The samples with a MgO layer thicker than 170 nm, as shown in Fig. 3(c), show a rough surface morphology without the dotlike patterns. This phenomenon may be related to the compressive-tensile stress balance achieved by applying MgO buffer layers of various thicknesses. Without the MgO buffer layer, tensile strain at the interface, caused by the mismatch of thermal expansion coefficients between the ZnO film and the glass substrate, as mentioned above, affects the ZnO layer and causes a high density of cracks. When an LT-MgO layer thinner than 130 nm is grown on the substrate prior to ZnO film growth, the compressive stress at the interface of MgO and ZnO is equal to or slightly higher than the tensile strain from the substrate.<sup>12)</sup> Hence, no cracks appear. Under the condition of medium MgO buffer layer thickness ( $130 \text{ nm} \leq \text{MgO thick-}$



(a)



(b)



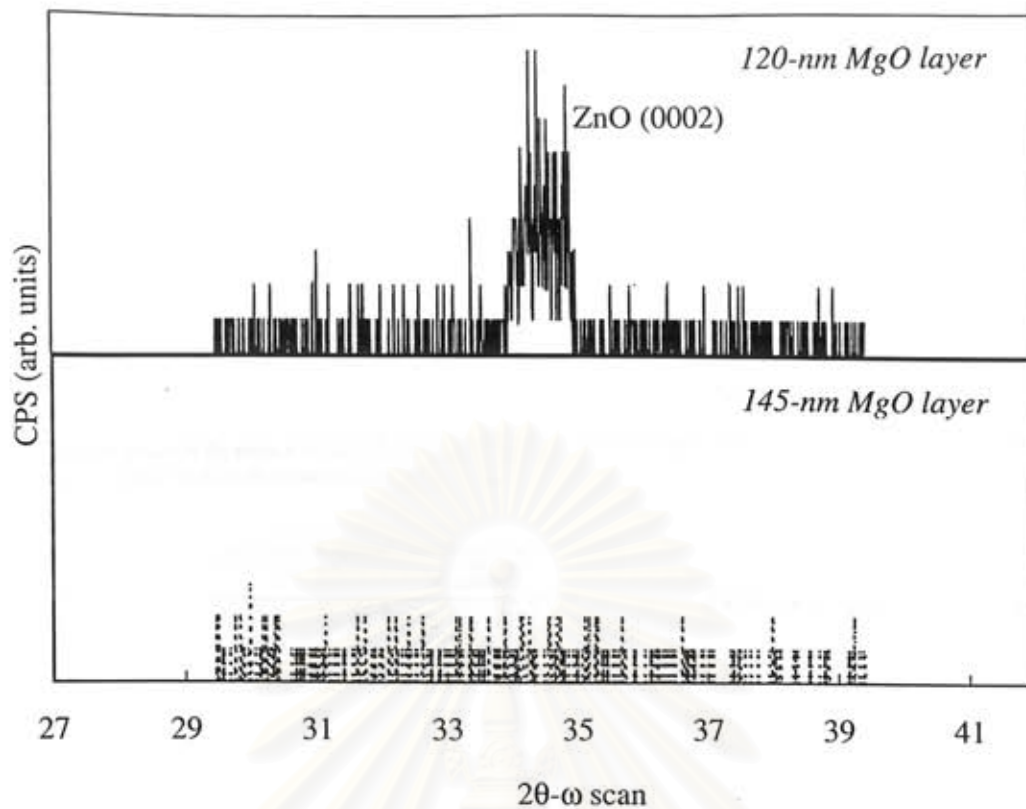
(c)

Fig. 3. Surface morphology by  $10^5 \times$  FE-SEM as a function of the MgO buffer layer thickness: (a) 0 nm, (b) 145 nm, and (c) 300 nm.

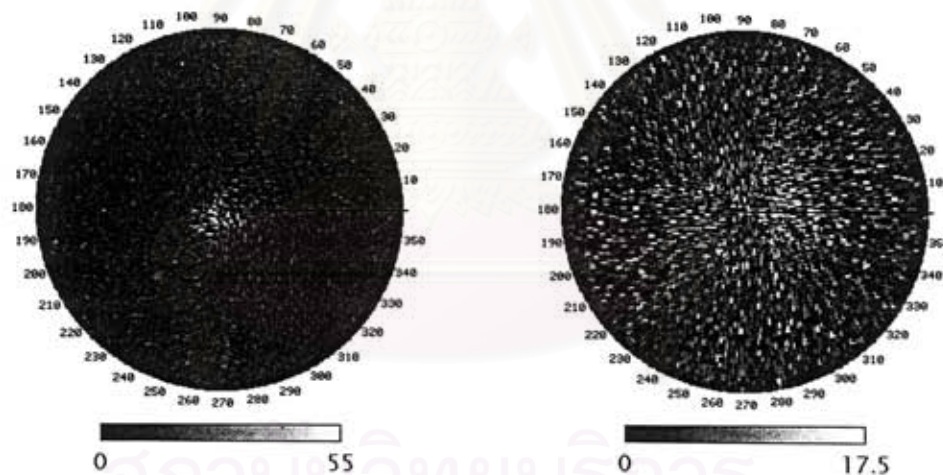
ness  $\leq 170 \text{ nm}$ ), the compressive stress is then less than the tensile strain due to elastic relaxation, which results in the morphology of a dotlike surface. However, when the MgO buffer layer is very thick ( $> 170 \text{ nm}$ ), the compressive stress is much less than the strain from the substrate, which causes the appearance of a few cracks. We may conclude that the compressive stress related to Stoney's equation<sup>13-15)</sup> is reduced partly by stress relaxation.<sup>16,17)</sup>

The crystal orientation of the as-grown films is investigated using a  $2\theta-\omega$  scan and a pole figure of XRD. Figure 4 shows XRD patterns of ZnO films on glass substrates with 120-nm and 145-nm MgO buffer layers. The ZnO(0002) peak appears in all the samples indicating  $c$ -axis orientation except the samples with a dotlike morphology. The pole figures of  $c$ -axis oriented ZnO films deposited on glass substrates with the 120-nm and 145-nm MgO buffer layers are also shown in Figs. 4(b) and 4(c), respectively. Figure 4(b) indicates the structure of the ZnO film with the grains having the same crystallographic axis (0002) parallel to the





(a)



(b)

(c)

Fig. 4. XRD spectra of ZnO films: (a)  $2\theta$ - $\omega$  scan of 120-nm and 145-nm buffer layer, (b) pole figure of 120-nm buffer layer, and (c) pole figure of 145-nm buffer layer.

substrate surface normal, but having random rotational orientations about that axis. On the other hand, Fig. 4(c) indicates the microstructure of the film with not  $c$ -axis orientation but only random rotationally oriented grains.<sup>18)</sup>

The surface morphology study using AFM indicates that the samples with a dotlike surface are smoother than those with lower values of root-mean-square roughness (RMS) due to the smaller grain size, as observed by FE-SEM. The data is shown in Fig. 5. The scan size is  $5 \times 5 \mu\text{m}^2$ .

The PL spectra of the annealed MgO buffer layer samples with various buffer layer thicknesses are shown in Fig. 6(a). The inset of Fig. 6(a) also shows PL spectra of three samples, which are the samples without the buffer layer,

with a thin (20 nm) buffer layer, and with a thick (300 nm) buffer layer. The typical near-band-edge PL measurement indicates that the PL intensity of these three samples is rather weak compared with the other samples. The minimum intensity of PL spectra comes from the sample without the MgO buffer layer. The emission lines located at 3.358 and 3.368 eV dominate the spectrum in all samples. The emission peaks at 3.358 and 3.368 eV are a donor-bound exciton related to the oxygen vacancy<sup>2)</sup> and an ionized donor-bound exciton,<sup>19)</sup> respectively. The shoulder peak at 3.375 eV is attributed to the free exciton emission with the A-valence band. The lattice-mismatch-induced inhomogeneous strain distribution results in a Stokes shift of  $<5$  meV.

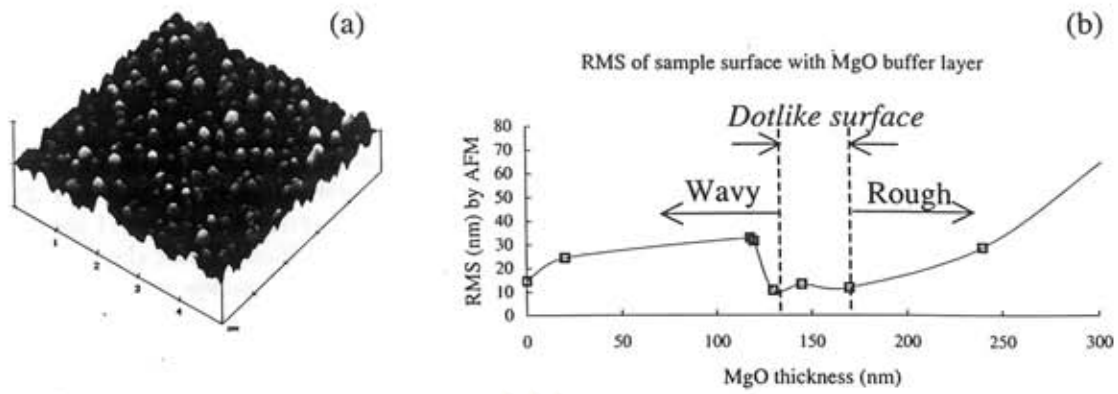


Fig. 5. (a) AFM image of the surface of the ZnO film with 145-nm MgO buffer layer. (b) Root mean square of surface roughness of the samples with various MgO buffer layer thicknesses.

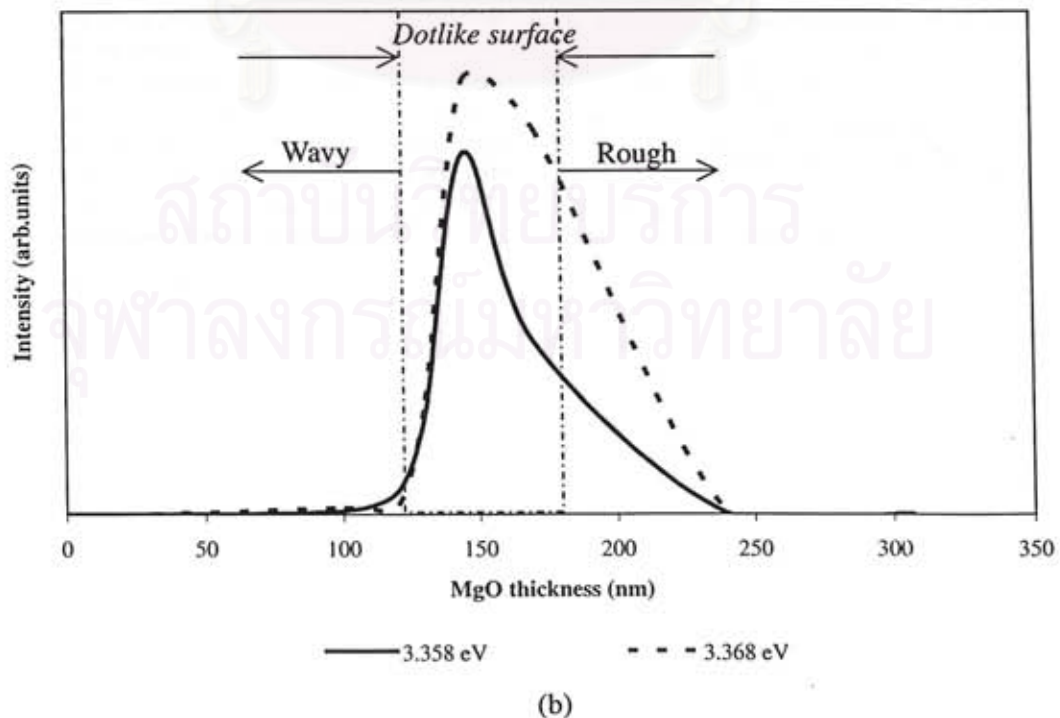
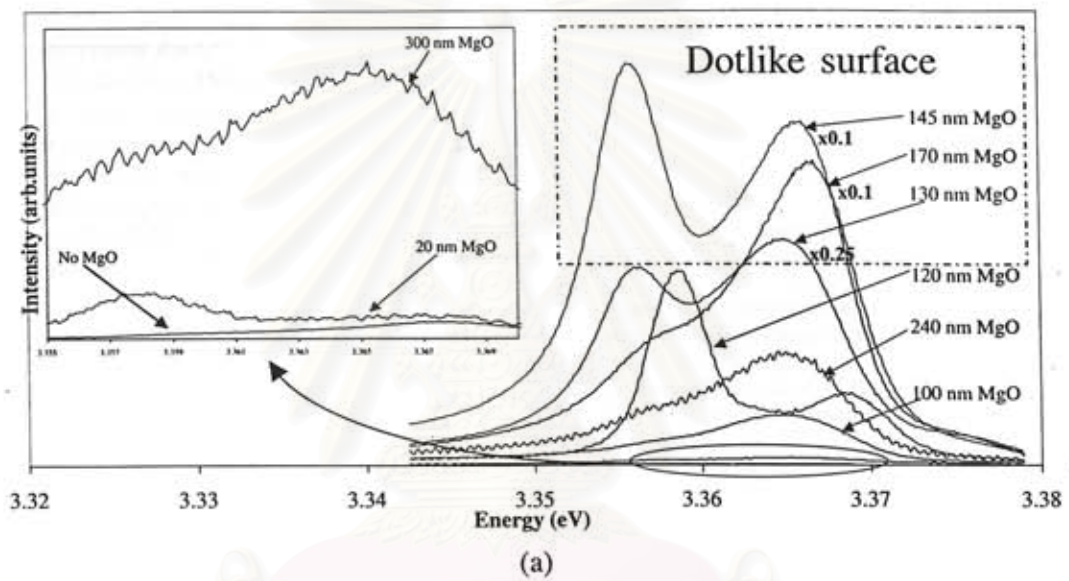


Fig. 6. (a) PL spectra of the annealed MgO buffer layer samples with various buffer layer thicknesses. (b) Relationship of the PL intensity of emission peaks at 3.358 and 3.368 eV to buffer layer thickness.

Figure 6(b) shows the relationship of the PL intensity of both dominant emission peaks with the MgO buffer layer thickness. The PL intensity of donor-bound exciton emissions increases with the buffer layer thickness up to the optimum thickness of approximately 150 nm, where the PL intensity becomes the strongest among all the samples. Then, the PL intensity begins to decrease when the MgO thickness exceeds 170 nm; a few cracks appear, presumably caused by the relatively poor crystalline quality, as shown in Fig. 3(c). Therefore, the optimum buffer layer thickness probably lies around 150 nm. It should be noted that the decrease of PL intensity and the formation of surface cracks begin at the same MgO buffer layer thickness. However, the PL intensity of the samples with the dotlike surface is much higher than those of the other samples, implying that the smaller grain size may cause band bending<sup>20</sup> and partial carrier confinement with the piezoelectric field effect, which likely leads to the stronger emission intensity than that of *c*-axis oriented crystalline ZnO.<sup>21</sup>

When the MgO buffer layer thickness is less than 150 nm, crack-free ZnO films are grown. The electrical characteristics of all ZnO films grown under this condition exhibit *n*-type conductivity in the range of  $2.17 \times 10^{17}$  to  $1.76 \times 10^{18}$  cm<sup>-3</sup>. All these samples, however, show relatively low electron mobility [5 cm<sup>2</sup>/(V s)]. The observed resistivities are in the range of 10<sup>3</sup> to 10<sup>5</sup> Ω cm.

#### 4. Conclusions

The polycrystalline ZnO epilayers are grown on amorphous glass substrates by plasma-assisted molecular beam epitaxy with various MgO buffer layer thicknesses. Without the MgO buffer layer, a high density of cracks due to the thermal expansion coefficient mismatch between ZnO and the quartz glass substrate is easily observed. The buffer layer thickness, however, affects the surface morphology, including the structural and optical properties. The applied thin MgO buffer layer not only prevents surface cracks, but also improves the optical property with a increasing buffer layer thickness. However, the samples with a very thick MgO layer (= 170 nm) show a few cracks. The optimum sample, a 150-nm MgO buffer layer, exhibits no cracks, a nonoriented polycrystalline structure, and the strongest PL intensity, with a dotlike surface due to the compressive-tensile stress balance. All samples exhibit *n*-type conductivity.

#### Acknowledgements

This work is partly supported by the Thailand Research Fund (TRF) through His Majesty the King's Golden Jubilee Ph.D. program, by a Grant-in-Aid for Scientific Research on the Priority Areas program "Photonics Based on Wavelength Integration and Manipulation", by the COE program "Molecular Nano-Engineering", and by the 21st Century COE program "Practical Nano-Chemistry" from the Ministry of Education, Culture, Sports, Science and Technology.

- 1) A. Setiawan, H. J. Ko, S. K. Hong, Y. Chen and T. Yao: *Thin Solid Films* **445** (2003) 213.
- 2) T. Tatsumi, M. Fujita, N. Kawamoto, M. Sasajima and Y. Horikoshi: *Jpn. J. Appl. Phys.* **43** (2004) 2602.
- 3) M. Fujita, N. Kawamoto, M. Sasajima and Y. Horikoshi: *J. Vac. Sci. Technol. B* **22** (2004) 1484.
- 4) Y. Natsume and H. Sakata: *Thin Solid Films* **372** (2000) 30.
- 5) S. Fujihara, C. Sasaki and T. Kimura: *Appl. Surf. Sci.* **180** (2001) 341.
- 6) K. S. Kim, H. W. Kim and C. M. Lee: *Mater. Sci. Eng. B* **98** (2003) 135.
- 7) F. K. Shan and Y. S. Yu: *Thin Solid Films* **435** (2003) 174.
- 8) K. S. Kim, H. W. Kim and N. H. Kim: *Physica B* **334** (2003) 343.
- 9) Y. Yoshino, T. Makino, Y. Katayama and T. Hata: *Vacuum* **59** (2000) 538.
- 10) Fused Quartz Catalogue Q-7A, General Electric Co. <http://encyclopedia.thefreedictionary.com>
- 11) O. Madelung: *Numerical Data and Functional Relationships in Science and Technology* (Springer, Heidelberg, 1982) Landolt-Börnstein, New Series, Group III, Crystal and Solid State Physics, Vol. 22, Subvol. a, p. 14.
- 12) F. Spaepen: *Acta Mater.* **48** (2000) 31.
- 13) P. H. Townsend, D. M. Barnett and T. A. Brunner: *J. Appl. Phys.* **62** (1987) 4438.
- 14) J. H. Zhao, Y. Du, M. Morgan and P. S. Ho: *J. Appl. Phys.* **87** (1999) 1575.
- 15) C. A. Klein: *J. Appl. Phys.* **88** (2000) 5487.
- 16) T. Nishinaga, K. Nishioka, J. Harada, A. Sasaki and H. Takei: *Advances in the Understanding of Crystal Growth Mechanisms* (Elsevier Science, Amsterdam, 1997) p. 429.
- 17) N. Y. Li, W. S. Wong, D. H. Tomich, K. L. Kavanagh and C. W. Tu: *J. Vac. Sci. Technol. B* **14** (1996) 2952.
- 18) J. H. Choi, H. Tabata and T. Kawai: *J. Cryst. Growth* **226** (2001) 493.
- 19) B. K. Meyer, H. Alves, D. M. Hofmann, W. Kriegseis, D. Forster, F. Bertram, J. Christen, A. Hoffmann, M. Dworzak, U. Habocek and A. V. Rodina: *Phys. Status Solidi B* **241** (2004) 231.
- 20) V. Srikant and D. R. Clarke: *J. Appl. Phys.* **81** (1997) 6357.
- 21) Z. Wang, H. Zhang, L. Zhang, Y. Yuan, S. Yan and C. Wang: *J. Mater. Res.* **18** (2003) 151.



# Molecular beam epitaxial growth of hexagonal ZnMgO films on Si(1 1 1) substrates using thin MgO buffer layer

Miki Fujita<sup>a,b,\*</sup>, Masanori Sasajima<sup>a,b</sup>, Yuparwadee Deesirapipat<sup>a,b</sup>, Yoshiji Horikoshi<sup>a,b</sup>

<sup>a</sup>*School of Science and Engineering, Waseda University, 3-4-1 Okubo, Shinjuku-ku, Tokyo 169-8555, Japan*

<sup>b</sup>*Kagami Memorial Laboratory for Materials Science and Technology, Waseda University, 2-8-26 Nishiwaseda, Shinjuku-ku, Tokyo 169-0051, Japan*

Available online 19 February 2005

## Abstract

The epitaxial growth of oxides such as ZnO and ZnMgO by molecular beam epitaxy (MBE) is known to be difficult because the Si substrate surface is easily oxidized in the initial stage of growth. However, we have succeeded in solving this problem by depositing a thin Mg buffer layer on the (7 × 7) reconstructed Si(1 1 1) surface prior to the growth of oxides. Good quality epitaxial ZnO layers are grown on such buffer layers.

Successful growth of hexagonal ZnMgO films on Si(1 1 1) substrates is demonstrated by using Mg layer followed by MgO growth as a buffer layer. All the layers are grown by MBE using a radio frequency radical cell. The results of the glow discharge optical emission spectroscopy measurement indicate that Zn<sub>1-x</sub>Mg<sub>x</sub>O films with Mg fraction *x* up to about 0.5 are obtained without phase separation. Moreover, these ZnMgO films are confirmed to be hexagonal c-oriented through the X-ray diffraction measurement and reflection high-energy electron diffraction observation. The lattice constant and cathodoluminescence peak energy are also investigated as a function of *x*.

© 2005 Elsevier B.V. All rights reserved.

PACS: 68.55.Nq; 81.05.Dz; 81.15.Hi; 82.80.Ms

Keywords: A1. Crystal structure; A2. Single-crystal growth; A3. Molecular beam epitaxy; B1. Alloy; B1. Oxides; B2. Semiconducting II–VI materials

## 1. Introduction

Recently, wide-band-gap semiconductors have been paid considerable attention for use in short-wavelength optical devices. Among these materials, ZnO is one of the most attractive materials due

\*Corresponding author. School of Science and Engineering, Waseda University, 3-4-1 Okubo, Shinjuku-ku, Tokyo 169-8555, Japan. Tel.: +81 3 5286 3176; fax: +81 3 3209 3450.  
E-mail address: [miki-f@ruri.waseda.jp](mailto:miki-f@ruri.waseda.jp) (M. Fujita).

to its direct wide band gap (3.37 eV at room temperature) and its large exciton binding energy (60 meV) [1,2]. In addition, in order to fabricate heterostructures for electronic and optical device applications,  $Zn_{1-x}Mg_xO$  alloys have also been investigated by many researchers. Although the crystal structures of ZnO and MgO are different (ZnO: wurtzite structure, MgO: rocksalt structure), and thermodynamic solubility limit of MgO in ZnO is only less than 4% according to the phase diagram of ZnO–MgO binary system, uniform  $Zn_{1-x}Mg_xO$  films with  $x$  values up to 0.5 have been grown by using molecular beam epitaxy (MBE) [3–5], metal organic chemical vapor deposition (MOCVD) [6,7], pulsed laser deposition (PLD) [8–12] and sputtering [13–15]. Most of these studies have adopted the sapphire substrates. However, since sapphire is an electrically insulating material, it introduces complexity to device fabrication processes especially when grown crystals are applied to injection-light-emitting devices. Electrically conductive Si substrates can relieve this problem. In addition, the crystal quality of the Si substrate is expected to be remarkably higher than that of the sapphire substrate.

Therefore, we have focused on the Si substrates for the growth of ZnO films [16–18]. The growth of epitaxial ZnO films on Si is, however, known to be a difficult task because the Si substrate surface is easily oxidized and the crystal quality of ZnO film grown on such a  $SiO_x$  layer is considerably deteriorated. In order to prevent the Si substrate surface from being oxidized in the initial growth stage of ZnO, and improve the crystal quality of ZnO films, we have used two methods: initial Zn layer deposition followed by its oxidation [16,17] and initial Mg layer deposition followed by MgO growth [18]. Although the grown ZnO films exhibit very high photoluminescence (PL) efficiency by using the former method, they suffer from high density of micro-cracks along the principal axes on the Si(111) surface probably caused by the difference in the thermal expansion coefficients between ZnO and Si. By introducing thin MgO buffer layer between ZnO and Si substrate using the latter method, these micro-cracks disappear and good quality epitaxial ZnO layers are successfully grown on Si substrates. Since the thermal

expansion coefficient of MgO is much larger than those of Si and ZnO, incorporation of MgO between Si substrate and ZnO may produce compressive stress to ZnO. This stress removes the cracks on the ZnO layers.

In this work, we investigate the characteristics of ZnMgO films grown on Si substrates by using thin MgO buffer layer. X-ray diffraction (XRD) measurement and glow discharge optical emission spectroscopy (GDOES) measurement show that uniform hexagonal  $Zn_{1-x}Mg_xO$  films with Mg  $x$  values up to 0.5 have been successfully grown.

## 2. Experimental procedure

ZnMgO films are grown on Si(111) substrates by MBE. Elemental Zn (6 N) and Mg (4 N) are evaporated using conventional effusion cells. Pure oxygen (5 N) is used for oxygen source and oxygen plasma is generated through a radio frequency (RF)-activated radical cell. The Si substrates are chemically etched in 5% HF solution. Then the Si substrates are inserted into an ultrahigh-vacuum chamber and annealed at 700 °C. After this surface cleaning process, the reflection high-energy electron diffraction (RHEED) pattern shows a well-defined ( $7 \times 7$ ) reconstruction. After confirming the ( $7 \times 7$ ) pattern, the substrate temperature is lowered to 350 °C. Then, the Si substrate is exposed to a flux of Mg in order to protect the Si surface from oxidation. Then, oxygen gas supply is started to grow MgO at a flow rate of 0.9 sccm without stopping the Mg supply. This MgO growth is continued until the thickness becomes about 3 nm. Then, 80-nm-thick ZnO layer is grown at 575 °C using a Zn BEP of  $3 \times 10^{-6}$  Torr and an oxygen flow rate of 0.9 sccm as a second buffer layer. Finally, ZnMgO (or ZnO) layer is grown at the same temperature using the same Zn BEP. The growth of ZnMgO is performed with different Mg BEP between  $1 \times 10^{-8}$  and  $7 \times 10^{-8}$  Torr. The total thickness of the films is 500–600 nm.

The crystalline quality of ZnMgO films is investigated by RHEED observation during growth, by XRD measurement and cathodoluminescence (CL) measurement. The compositions of

$\text{Zn}_{1-x}\text{Mg}_x\text{O}$  layers are evaluated by GDOES measurement.

### 3. Results and discussion

$\text{ZnMgO}$  layers are first grown after the growth of  $\text{MgO}$  buffer layer. In this experiment,  $\text{Mg}$  BEP is fixed at  $2.2 \times 10^{-8}$  Torr. However, no hexagonal diffraction peaks are observed in XRD  $2\theta/\omega$  scan chart. Instead, a clear (111) diffraction due to the cubic rocksalt structure appears as shown in Fig. 1 (curve b). Therefore, the  $\text{MgO}$  buffer layer probably provides a template of cubic rocksalt structure. In order to grow hexagonal  $\text{Zn}_{1-x}\text{Mg}_x\text{O}$ , the 2nd buffer layer ( $\text{ZnO}$ ) is needed on the original  $\text{MgO}$  buffer layer. The XRD  $2\theta/\omega$  scan chart observed in the sample with double buffer layer is shown as curve (a) in Fig. 1. As clearly indicated in the figure, hexagonal  $\text{ZnMgO}(0002)$  peak appears by using the  $\text{ZnO}/\text{MgO}$  double buffer layer.

Fig. 2 shows the TEM image taken around the  $\text{MgO}$  buffer layer on Si substrate. About 3-nm-thick  $\text{MgO}$  buffer layer is confirmed uniformly over the surface of  $\text{Si}(111)$  substrate. Fig. 3 shows the results of the XRD  $2\theta/\omega$  scan measurement of  $\text{ZnMgO}$  samples with different  $\text{Mg}$  BEP. With increasing the  $\text{Mg}$  BEP, diffraction peak of  $\text{ZnMgO}(0002)$  peak shifts to the higher angle,

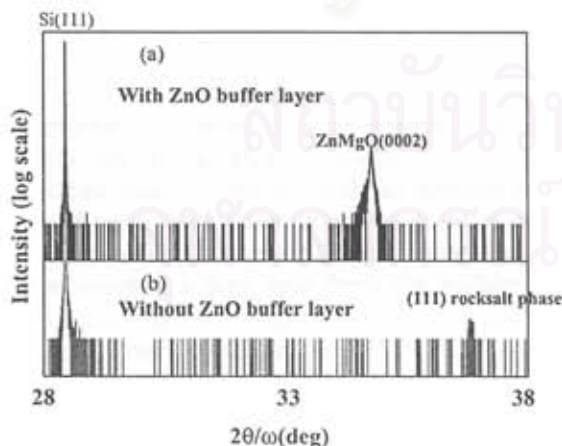


Fig. 1. The results of the XRD  $2\theta/\omega$  scan measurement with and without  $\text{ZnO}$  buffer layer.

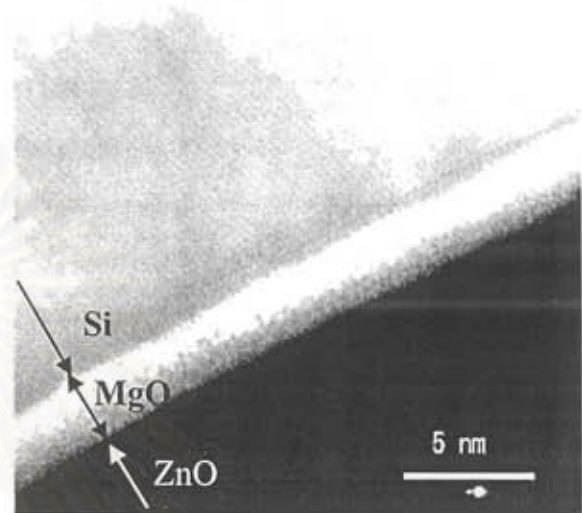


Fig. 2. TEM image of the  $\text{MgO}$  buffer layer between Si substrate and  $\text{ZnO}$  layer.

which indicates that the  $\text{Mg}$  content of  $\text{ZnMgO}$  layer increases with  $\text{Mg}$  BEP. However, when  $\text{Mg}$  BEP exceeds about  $5.0 \times 10^{-8}$  Torr, single hexagonal phase  $\text{ZnMgO}$  is no more obtained, and rocksalt  $\text{ZnMgO}(001)$  phase appears in addition to the hexagonal phase. This shows the onset of phase separation of  $\text{ZnMgO}$ . Although not shown here, RHEED observation has been performed during  $\text{ZnMgO}$  growth. The result on the grown surface is in good agreement with the XRD results.

Fig. 4 shows CL spectra of  $\text{ZnMgO}$  samples grown with different  $\text{Mg}$  BEP. The measurement is carried out at room temperature. The main CL peak shifts to the higher energy side with increasing  $\text{Mg}$  BEP. The sample grown at  $\text{Mg}$  BEP of  $5.7 \times 10^{-8}$  Torr shows the CL emission spectrum composed of three peaks, which might mean the phase separation. This phase separation is confirmed by the XRD measurement shown in Fig. 3. The XRD and CL measurements indicate that uniform hexagonal c-oriented  $\text{ZnMgO}$  layers are grown as far as the  $\text{Mg}$  BEP is less than approximately  $5.0 \times 10^{-8}$  Torr.

The  $\text{Mg}$  fraction  $x$  of  $\text{Zn}_{1-x}\text{Mg}_x\text{O}$  is evaluated by GDOES measurement (GDA750: RIGAKU). The measurements are performed only for homo-

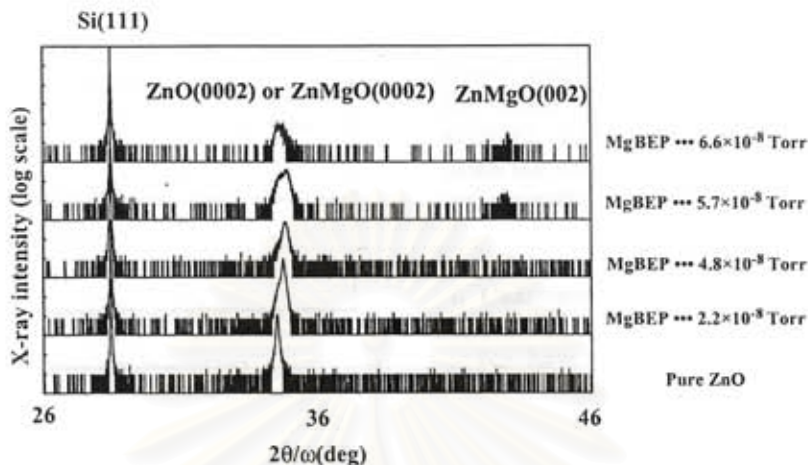


Fig. 3. The results of the XRD  $2\theta/\omega$  scan measurement of ZnMgO samples with different Mg BEP.

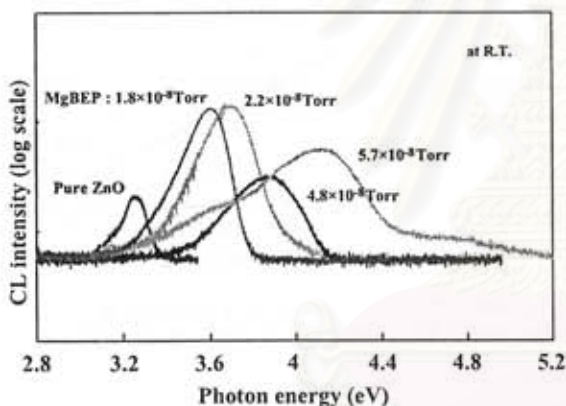


Fig. 4. CL spectra of ZnMgO samples grown with different Mg BEP measured at room temperature.

geneous alloys. GDOES is the method for analyzing amount and distribution of the elements in the sample by using glow discharge plasma. The detection limit of the method lies around a few tens of ppm. This value is not as good as SIMS measurement. However, GDOES is more suitable for examining a deep area from the surface than SIMS and the time needed for measurement is much shorter than that of SIMS. Argon glow discharge plasma is generated in vacuum and the surface of the sample is sputtered by this plasma. The atoms sputtered from the surface are excited by this plasma and radiate their own spectra. By dispersing the spectrum and measuring intensity,

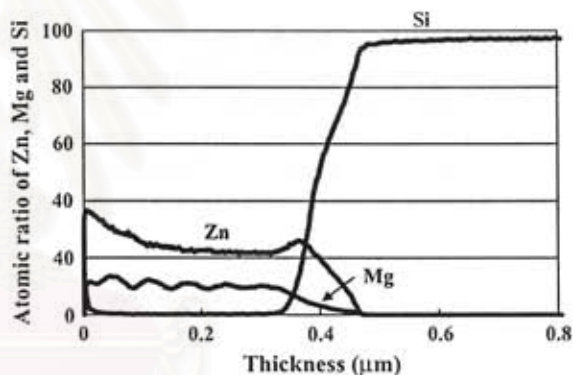


Fig. 5. The data of the GDOES measurement at Mg BEP of  $1.8 \times 10^{-8}$  Torr.

the information of the atomic concentrations and their depth profiles are easily obtained. In our samples, argon glow discharge plasma is stable and reliable measurements are performed in the range of single-phase compositions. The depth resolution is approximately 10 nm in our samples. The result of the GDOES measurement at Mg BEP of  $1.8 \times 10^{-8}$  Torr is shown in Fig. 5 as a typical data. We use the data at a depth of 200 nm from the surface in order to calculate the Mg fraction  $x$  because the surface of the sample could be affected by contamination.

The relationship of the Mg fraction  $x$  and the Mg BEP/(Zn BEP + Mg BEP) in  $Zn_{1-x}Mg_xO$  on Si substrates is shown in Fig. 6. Mg fraction  $x$

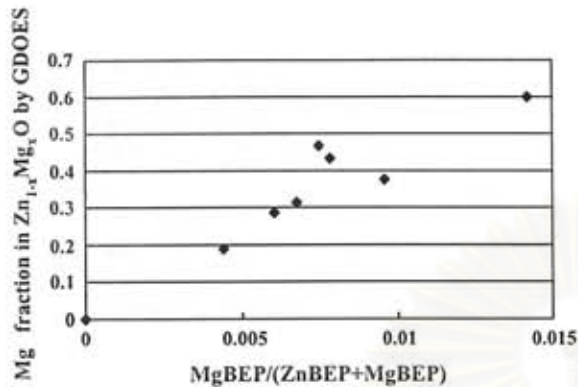


Fig. 6. The relationship of the Mg fraction  $x$  to the Mg BEP/(Zn BEP + Mg BEP).

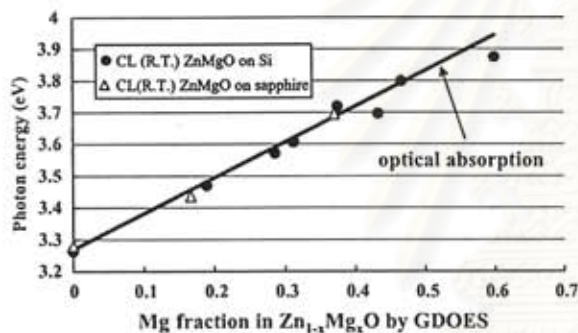


Fig. 7. The relationship between Mg fraction  $x$  and the CL peak photon energy. The line represents optical absorption data of our samples.

increases with Mg BEP/(Zn BEP + Mg BEP), as with the results of the XRD and CL measurements. The relationship of Mg fraction  $x$  and the CL peak photon energy shows linear characteristic as shown in Fig. 7, and coincides well with the optical absorption data of our samples. However, our CL peak plot lies a little below the optical absorption edge line reported in literature [5]. For example, the CL peak energy is 3.47 eV while the absorption energy is located at 3.62 eV. This discrepancy may be due to the methods used for the  $x$ -value estimation, i.e., the present results are estimated by GDOES, while the data in the literature was estimated by inductively coupled plasma (ICP) measurement. In order to see the difference between these two methods, both GDOES and ICP are applied to the same ZnMgO

samples grown on sapphire substrates. The  $x$  values estimated by GDOES are found to be larger than those estimated by ICP. For example, the sample whose  $x$  value is estimated to be 0.37 by GDOES is only 0.31 when the ICP method is used. Since the ICP method gives rather accurate values, our estimation by GDOES may be overestimated.

#### 4. Conclusion

We have grown hexagonal ZnMgO films on Si(111) substrates by using thin MgO layer. Mg evaporation followed by thin MgO buffer layer growth is very effective to prevent Si substrate from oxidation and obtain crack-free ZnO or ZnMgO film. XRD measurement shows that c-oriented hexagonal ZnMgO films are grown and ZnMgO peak is shifted to higher angle side with increase of Mg content. CL measurement also shows the similar results with XRD measurement. That is, the CL peak is shifted to higher-energy side with increase of Mg content. Judging from GDOES measurement, Zn<sub>1-x</sub>Mg<sub>x</sub>O, which is at least  $x = 0.5$  at maximum, is obtained without phase separation.

#### Acknowledgements

The author would like to thank to Mr. Okuda in Rigaku Industrial Corporation for measurement by GDOES and useful discussion about GDOES.

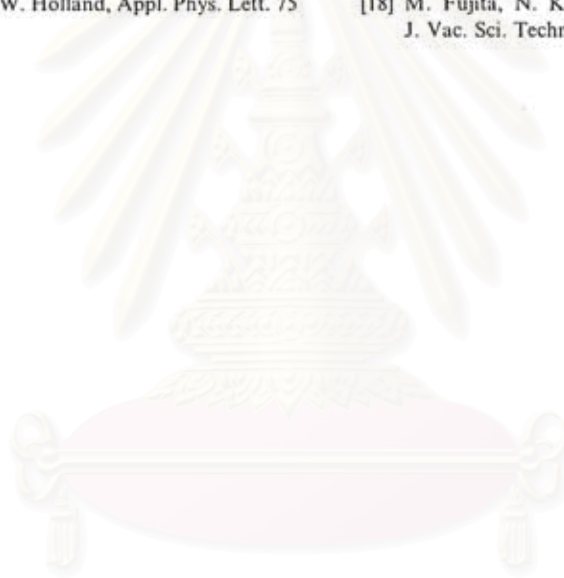
This work is partly supported by the Grant-in-Aid for Scientific Research on Priority Areas program "Photonics Based on Wavelength Integration and Manipulation," the Grant-in-Aid for Scientific Research (B) from Japan Society for the Promotion of Science (JSPS), and the COE Program "Molecular Nano-Engineering", 21 COE "Practical Nano-Chemistry" and the Open Research Center Project by the Ministry of Education, Culture, Sports, Science and Technology (MEXT), Japan.

#### References

- [1] Y. Segawa, A. Ohtomo, M. Kawasaki, H. Koinuma, Z.K. Tang, P. Yu, G.K.L. Wong, *Phys. Status Solidi B* 202 (1997) 669.



- [2] D.M. Bagnall, Y.F. Chen, Z. Zhu, T. Yao, M.Y. Shen, T. Goto, *Appl. Phys. Lett.* 73 (1998) 1038.
- [3] S.K. Hong, Y. Chen, H.J. Ko, H. Wenisch, T. Hanada, T. Yao, *J. Electron. Mater.* 30 (2001) 647.
- [4] K. Ogata, K. Koike, T. Tanite, T. Komuro, F. Yan, S. Sasa, M. Inoue, M. Yano, *J. Crystal Growth* 251 (2003) 623.
- [5] T. Takagi, H. Tanaka, S. Fujita, S. Fujita, *Jpn. J. Appl. Phys.* 42 (2003) L401.
- [6] W.I. Park, Gyu-Chui Yi, H.M. Jang, *Appl. Phys. Lett.* 79 (2001) 2022.
- [7] S. Muthukumar, J. Zhong, Y. Chen, Y. Lu, *Appl. Phys. Lett.* 82 (2003) 742.
- [8] A. Ohtomo, M. Kawasaki, T. Koida, K. Masubuchi, H. Koizuma, Y. Sakurai, Y. Yoshida, T. Yasuda, Y. Segawa, *Appl. Phys. Lett.* 72 (1998) 2466.
- [9] A.K. Sharma, J. Narayan, J.F. Muth, C.W. Teng, C. Jin, A. Kvit, R.M. Kolbas, O.W. Holland, *Appl. Phys. Lett.* 75 (1999) 3327.
- [10] S. Choopun, R.D. Vispute, W. Yang, R.P. Sharma, T. Venkatesan, *Appl. Phys. Lett.* 80 (2002) 1529.
- [11] J. Narayan, A.K. Sharma, A. Kvit, C. Jin, J.F. Muth, O.W. Holland, *Solid State Commun.* 121 (2002) 9.
- [12] W. Yang, S.S. Hullavarad, B. Nagaraj, I. Takeuchi, R.P. Sharma, T. Venkatesan, R.D. Vispute, H. Shen, *Appl. Phys. Lett.* 82 (2003) 3424.
- [13] T. Minemoto, T. Negami, S. Nishiwaki, H. Takakura, Y. Hamakawa, *Thin Solid Films* 372 (2000) 173.
- [14] G.J. Fang, D. Li, X. Zhao, *Phys. Status Solidi A* 200 (2003) 361.
- [15] D.K. Hwang, M.C. Jeong, J.M. Myoung, *Appl. Surf. Sci.* 225 (2004) 217.
- [16] M. Fujita, N. Kawamoto, T. Tatsumi, K. Yamagishi, Y. Horikoshi, *Jpn. J. Appl. Phys.* 42 (2003) 67.
- [17] N. Kawamoto, M. Fujita, T. Tatsumi, Y. Horikoshi, *Jpn. J. Appl. Phys.* 42 (2003) 7209.
- [18] M. Fujita, N. Kawamoto, M. Sasajima, Y. Horikoshi, *J. Vac. Sci. Technol. B* 22 (2004) 1484.



สถาบันวิทยบริการ  
จุฬาลงกรณ์มหาวิทยาลัย